UNIVERSITAT DE
BARCELONA

New technologies and their characterisation for nanostructured SnO₂ Gas sensor devices

Albert Cirera Hernández

Universitat de Barcelona

Departament d'Electrònica

New technologies and their characterisation

for nanostructured SnO_2 gas sensor devices

Memòria de Tesi doctoral presentada per n'Albert Cirera Hernández per a optar al títol de Doctor en Física.

Barcelona, setembre de 2000.

Universitat de Barcelona

Departament d'Electrònica

New technologies and their characterisation

for nanostructured SnO₂ gas sensor devices

Memòria de Tesi doctoral presentada per n'Albert Cirera Hernández per a optar al títol de Doctor en Física.
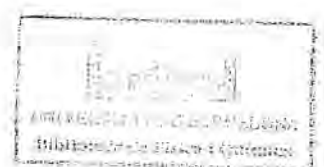
Barcelona, setembre de 2000.

Universitat de Barcelona

Facultat de Física

Departament d'Electrònica

NEW TECHNOLOGIES AND THEIR CHARACTERISATION FOR NANOSTRUCTURED SnO$_2$ GAS SENSOR DEVICES

Memòria presentada per a optar al títol de doctor en Ciències Físiques

Programa de doctorat: Enginyeria i Materials Electrònics i Òptica

Bienni: 1996-1998

Barcelona, setembre de 2000.

Autor: Albert Cirera Hernández

Director de tesi i tutor: Albert Cornet Calveras

N'Albert Cornet Calveras, Catedràtic de la Facultat de Física de la Universitat de Barcelona,

CERTIFICA:

que la memòria "**NEW TECHNOLOGIES AND THEIR CHARACTERISATION FOR NANOSTRUCTURED SnO$_2$ GAS SENSOR DEVICES**", que presenta n'Albert Cirera Hernández per a optar al grau de Doctor en Ciències Físiques, s'ha realitzat sota la seva direcció.

Barcelona, 5 de setembre de 2000.

Prof. Dr. Albert Cornet Calveras.

A ti, Sonia,
por tu cariño y apoyo durante estos años.

Contents

5. Applied characterisation for thin film based sensors___267

6. Conclusions, main findings and critic review ___319

1. Introduction

1.1 Scope

Nowadays the development of the *Information Society*, as last step of electronic revolution, requires the development and improvement of input devices (sensors) able to transform physical or chemical phenomena into electrical signal for further treatment in transducer systems.

Considering an easy analogy with sight and smelt, whereas when seeing we distinguish colours only evaluating the wavelength of the received photons, smelting consists in a more complicated recognition of atoms, atomic bonds and molecular structures. Therefore, in the field of sensor technology it is easier to develop *photon sensors* (cameras) than gas sensors. In comparison with other electronic devices or sensor systems, gas sensors are still not well developed nor understood.

Nevertheless our society requires of gas sensors for domestic, automotive and industrial application due to the implication of gases in environmental control or dangerous emissions. For gas monitoring different kinds of sensor systems can be used. Spectroscopic, Optic and Solid State are the three great families of gas sensors.

Spectroscopic systems are those based on the direct analysis of fundamental gas properties, such as molecular mass or vibrational spectrum. The most known systems are gas chromatography and mass spectrograph. These sensors measure quantitatively with high reliability and precision the amount of the different gas compounds. These systems are very expensive, usually more than 10000 €, and its use is limited for laboratory applications and very precise industrial procedures.

Optical sensor systems are based on the measurement of the absorption spectra after light stimulation. This kind of sensors needs a monochromatic excitation source as well as optical sensor for the analysis of absorbed spectra. Such devices and its corresponding electronics make optical sensors expensive for mass implementation. The

cost of these sensors is about 100 € and they are used mainly for industrial processes and environmental control.

The third kind of sensors, solid-state ones, is those based on the change of physical and/or chemical properties of its sensing material after gas exposure. These changes depend on the pair gas-sensing material and usually involve changes in electrical properties, as summarised in table 1.1. The final use of this kind of sensors covers very different fields (see table 1.2).

Electronic conductance and capacitance sensors	
Resistances R	$R = f(p_i)$
Capacitances C	$C = f(p_i)$
Frequency-dependent conductance Y	$|Y| = |G + i\omega C| = f(p_i)$
Field-effect sensors	
Potentials ΔV	$\Delta V = f(p_i)$
Source-drain current I_D	$I_D = f(p_i)$
Work function changes $\Delta\phi$	$\Delta\phi = f(p_i)$
Calorimetric sensors	
Heat of reactions Q_{react} per time	$\Delta V \sim Q_{react} \sim \Delta P \sim r\Delta H = f(p_i)$
Optochemical and photometric sensors	
Optical constants ε	$\varepsilon(\nu) = f(p_i)$
Function of frequency ν	
Intensity of light I	
Mass-sensitive sensors	
Masses Δm of ad- or absorbed particles	$\Delta f = -C_f f_0^2 / A \cdot \Delta m = f(p_i)$
Solid-state electrolyte sensors	
Voltages V	$V = (RT/nF)\ln a_i$
Currents I	$I = (nFADa_i)/\delta$

Table 1.1. Survey of solid state sensors [Göpel,97]

Applications

Environmental control and deposited particles (air, water, ground)
Working places measurements
Emission and outlets measurements (car exhausts, boilers exhausts)
Fire alarms and security control
Control and regulation of atmospheres (house, flights, cars)
Control and regulation of combustion
Control and regulation of process in industry
Chemical analysis
Biomedical applications
Food industry

Table 1.2. Main applications of solid state gas sensors [Oehme,89]

Technologies involved (printing, sintering, dipping) and an easy electronic signal conditioning make these sensors very cheap.

In fact, the mean price of these sensors (from 1 to 10 €) is very far away from the other kinds. This is the main reason of their commercial value in our society. In table 1.3 we can see economical impact of solid state sensors. The different kinds of solid state gas sensors exposed in tables 1.1 and 1.3 were reviewed in the work [Azad,92].

Use of sensor	1988	1990	1995	2000
Measurement of emission and storage in gases and air				
Electrochemical sensor	15	20	43	81
Semiconductor sensor	4	8	40	100
Physico-chemical sensors	42	52	75	90
Biosensors	-	-	2	4
Total	61	80	160	275
Residual water and environmental control				
Electrochemical sensor	10	12	33	65
Semiconductor sensor	-	3	7	35
Physico-chemical sensor	4	5	10	18
Biosensors	-	5	15	27
Total	14	25	65	145
Total of both	75	105	225	420

Table 1.3. World demand of sensors. Quantities in 10^6 € [Schröder,88]

1.2 Semiconductor gas sensors

As we can see in table 1.3, semiconductor gas sensors[1] are one of solid-state sensors with better presence in market. SGS are those sensors based on the change of resistivity after gas exposure. Sensor material is usually nanometric tin or titanium oxide, generally doped with palladium or platinum, but most of the other metal oxides exhibit this property, known since 50's years.

The property of change of conductivity after gas exposure that exhibits these materials is very weak at room temperatures. Maximum response temperature ranges from 200 to 800°C and depends on gas, sensor material and doping. Therefore, semiconductor gas sensors are composed by a sensing material, a substrate that holds sensing material, electrodes for resistance measuring, and a heater. See figure 1.1.

Al$_2$O$_3$ Substrate

Pt Heater

Sensing Layer
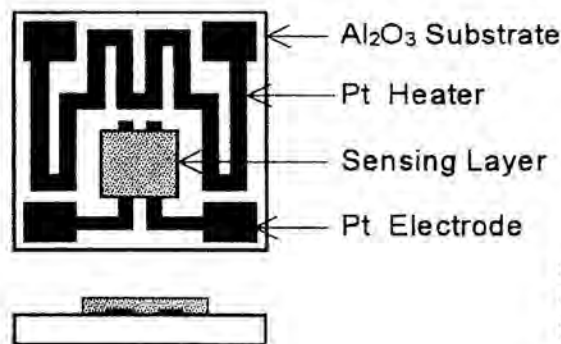
Pt Electrode

Figure 1.1. Alumina substrate with electrodes and heater resistance for gas sensors.

---

[1] Since this moment we will use the terminology Semiconductor Gas Sensors, or just SGS, nevertheless other names as chemical, conductive or resistance sensors are used with the same meaning. Recently it was introduced the acronym MOS (metal oxide sensor); under my view the use of this name is no very appreciated, specially when speaking about integrated silicon technology, where MOS has its own meaning.

Semiconductor gas sensors are usually mounted in a TO-socket covered by a charcoal filter. Sensor electrical output signal, as well as input (heating power) is processed by a whole sensor system that usually includes a microprocessor (see figure 1.2).
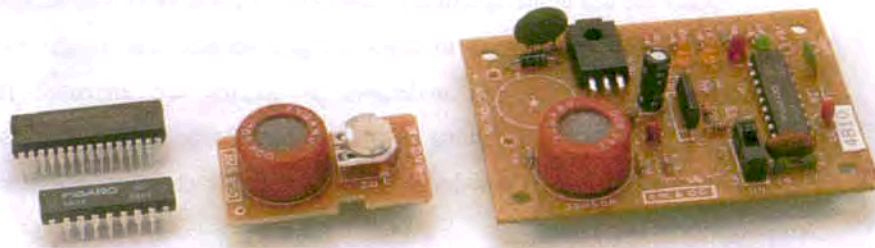
Figure 1.2. Gas sensor system that includes electronics for signal processing. Semiconductor Gas Sensor is inside the red socket in the centre of picture [Figaro,00]

Despite its simplicity and cheep production, SGS usually exhibit drifts and variation in its behaviour. Therefore SGS are not so well established and nor modelled like other electronic devices. These problems are related with structural parameters of the sensing material as well as device design. Nowadays these problems are known as *the four s*: sensitivity, selectivity, stability, and smart consumption.

1.2.1 Sensitivity

The first problem when making a sensor is to have sensitivity enough, with high signal to noise ratio. In this kind of sensor, where resistance varies with gas concentration, the sensitivity is defined for reducing gases and n-type sensing materials as,

$$S = \frac{R_{air}}{R_{gas}} \qquad \text{or} \qquad S = \frac{R_{air}}{R_{air} - R_{gas}} \qquad (1.1)$$

and for oxidising gases and n-type materials as,

$$S = \frac{R_{gas}}{R_{air}} \qquad \text{or} \qquad S = \frac{R_{gas} - R_{air}}{R_{air}} \qquad (1.2)$$

in the case of p-type materials the definitions are changed.

After the use of nanoparticles, sensitivity in gas sensors was improved. The use of nanoscaled materials enable to expose higher surface area to gas and hence the physicochemical reaction that undergoes at surface are increased [Shimizu,99]. Nevertheless, further understanding of grain size influence on sensitivity is much more complex and needs a deep knowledge on surface physic-chemical reactions, as we will introduce in the next chapter.

1.2.2 Selectivity

A second difficulty in the development of SGS consists on its low selectivity; this kind of sensors exhibits good sensitivity to a broad variety of gases, hence it is difficult to distinguish them. This problem, usually called *interfering discrimination* is extremely important because when detecting CH_4 in an explosion alarm, few ppm of CO can produce a similar signal in sensor that methane at level of explosion. The most part of gases (CO, CH_4, O_2, H_2,...) and volatile organic compounds –VOC- (methanol, ethanol, ...) can be detected with SGS. Four main approaches were developed to overcome this difficulty.

First, the use of filter allows distinguishing gases by means of the interception of interfering gas by filters –see figure 1.3-. Nowadays two families of filters are used. Passive filters consist in a porous media (like charcoal in domestic SGS or alumina in

automotive SGS) that inhibit diffusion of macromolecules (VOC, hydrocarbons) [Feng,94][Morooka,99][Schweizer-Berberich,99]. Only smaller molecules can get SGS-sensing surface. Catalytic metals (Pt, Pd) that burn volatile compounds (methane, methanol) compose active filters [Flingelli,97].

SB-50 (with active charcoal filter)

100 mesh
SUS 316 gauze

Active charcoal

Metal housing
(Nickel plated brass)
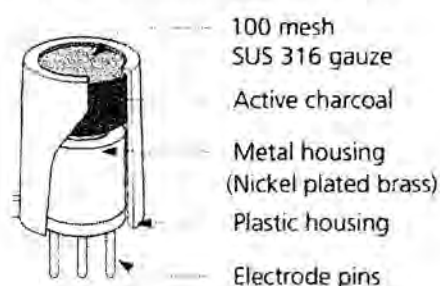
Plastic housing

Electrode pins

Figure 1.3. Encapsulated SGS with two passive filters, first stainless steel 100 mesh and active charcoal. This draw correspond to SB-50 model of Fis [Fis,00]

Another approach was the use of doped[2] sensing materials that are much more sensitive to one gas than others. This increase of selectivity will be reviewed and analysed in the next chapter.

The recent introduction of micromechanised substrates allows working in pulsed-mode heating. These substrates reach in milliseconds thermal stability. As the activation energy of gas/sensing-layer reaction different for every gas, maximum-temperature sensitivity is different too. We can improve hence the selectivity between

---

[2] Despite the word *doping* is widely used in the field of Semiconductor Gas Sensors, their meaning is only related with the addition of noble metal. Nevertheless, in physic electronics *doping* is understood as the modification of electronic levels in a semiconductor after the introduction of foreign atoms. Instead of *doping*, it has been suggested *catalytic additive* or just *additive* to reflect more accurately the actual working principle of these *foreign atoms*. Therefore, in the rest of the text we will use *additive* to reflect it more accurately. However, if we use *doping* it should be understood as SGS's *doping* and not electronic *doping*, except if it is specified.

two gases applying pulsed heating and detecting different gases at different temperatures.

One of the most studied features to improve selectivity is signal processing and pre-processing. In order to find the processing-signal algorithm it is necessary a good calibration. The output signal of transducer (SGS) and the information of composition and concentration of gas compounds must be related to each other. This implies the comparison of sensor outputs with former calibration data. By this way one knows the sensor response in relation with the gas concentration. This relation is known as *calibration function*.

Three man classifications describe the signal-processing algorithms. First the algorithms can be qualitative or quantitative, depending on the corresponding obtained information. *Qualitative* analysis is used to know the components of mixtures and it is very useful in food industry to distinguish for example Brazilian coffee and Arabian one. *Quantitative* algorithms are used when the knowledge of the gas concentration is required, i.e., in the automotive use oxygen sensors for combustion control (lambda probes).

Algorithms can be *model-based*, when the correlation between measurement data and gas concentration is described by a calibration function based on a physic-chemical model. *Model-free* algorithms use universal functions with parameters without physic-chemical meaning.

Last classification of algorithms corresponds to if these are supervised or not supervised. *Supervised* algorithms are those that need both sensor signal and gas concentration data for calibration, instead *not supervised* that only need sensor signal and classify it with respect to the existing differences and similarities.

In the table 1.4 can be found the most used algorithms and its classification [Šundić,98].

Algorithm	Quantitative/Qualitative	Model-#	Supervised
Principal Component Analysis (PCA)	*	Free	Not
Self Organising Maps (SOM)	*	Free	Not

Cluster Analysis (CA)	*			Free	Yes/Not
Backpropagation Networks (BPN)	*	/	*	Free	Yes
Polynomial Methods (PM)			*	Based	Yes
Multiple Linear Regression (MLR)			*	Based	Yes
Principal Component Regression (PCR)			*	Based	Yes
Partial Least-squares Regression (PLS)			*	Based	Yes
Radial Basis Function Networks (RBFN)			*	Free	Yes

Table I.4. Algorithms for signal processing in gas sensors.

As it can be seen, these algorithms are based on usual polynomial or lineal regression algorithms or in more recent neural networks. Although this thesis is not devoted to this subject, it is known that fuzzy-logic and genetic-algorithms are being used for gas sensor signal processing. An example of the use of some of the former algorithms can be found in [Marco,98].

1.2.3 Stability

One of the most desired characteristics in sensors is that these give a reproducible signal after use. As described, SGS are based on physic-chemical surface and bulk reactions on nanometric crystalline grains at working temperatures about 400°C. Such device is a complex system that usually exhibit great instabilities; key points for the understanding of leak of reproducibility are:

✓ physics and chemistry of surfaces still under development

✓ high working temperatures that enable gas/surface interaction

✓ exposure to poisoning (or oxidising/reducing) atmospheres that facilitate damaging chemical reactions at surface

✓ usual oxygen vacancy nanocrystalline structure that can be compensated/modulated with the oxygen partial pressure of the sensing atmosphere

In order to overcome these hard working conditions, different strategies were developed.

First, as the origin of the drifts is due to gas/sensing-material interaction, many efforts are devoted to improve material stability by means of reliable production procedures and appropriate annealing/firing treatments. The main idea is to apply thermal treatments —ranged from 400 to $1000°C$ during 1 to 8 hours- to avoid instabilities during working life continuously heated at $200-400°C$. Nevertheless this thermal treatments are time consuming and produce grain growth. As pointed out, this growth is not desired.

Another strategy to improve stability consists in applying surface treatments on sensing material. Several authors apply reducing treatments on surface before to start measurements, and some sensing materials, such as WO_3 [Williams,98], admit reset surface treatments consisting on applying a fast thermal treatment ($700°C$ during few minutes). In fact, most part of SGS manufacturer keep sensors continuously heating during about a week (or suggest to do) to avoid a first stage of instabilities [Mics,00][Fis,00][Figaro,00], as shown in figure 1.4.
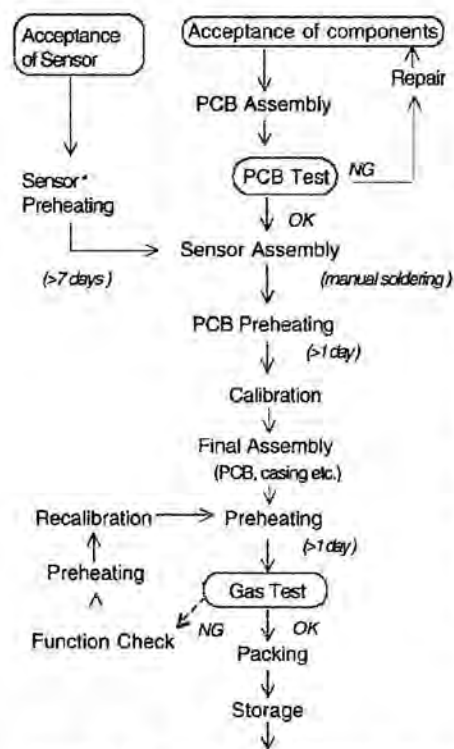
Figure 1.4. Manufacturing flowchart of Figaro SGS'. As seen, different heating stages are introduced to avoid instabilities. The factory recommends a minimum period of 2 days for sensor preheating, but for best results 7 days or longer preheating is strongly advised [Figaro,00].

1.2.4 Smart consumption

As seen above, SGS are devices that need to be heated continuously at very high temperatures. SGS use to be heated between 200 and 450°C consuming about 1W power. Nevertheless the use of sensors able to work with small portables batteries for domestic applications sensors would be more interesting. Different strategies are being developed to overcome this difficulty.

The use of dopants reduces the working temperatures in both cases. In SnO_2 domestic gas sensors for CO, maximum sensitivity temperature is reduced from 450°C to 250°C when doping with Pd [Schweizer-Berberich,96]. Such reduction of temperature approximately halves the power consumption.

Although this improvement is important, industrial developments of sensors trend to develop more intelligent substrate designs. Companies like Capteurs and Fis used smaller and thinner alumina substrates. This kind of sensors has a consumption about 0.4 W [Fis,00] [Capteurs,00]

Nevertheless, the most interesting approaches were developed by the introduction of both micromachined silicon substrates and bead designed sensors. As pointed out above, micromachined silicon substrates have a very small mass and hence the power required for heating it is strongly reduced. Advanced designs of micromachined substrates only consume about 30 mW [Mics,00]. Similar values are obtained by bead design of Fis [Fis,00]

1.3 Outline of the thesis

As described, although nowadays SGS constitute a well-established market with good perspectives, they are still under technological development. Under our view, such kind of sensors must be improved considering their final performances and problems in sensitivity, selectivity, stability and smart consumption. The deficiencies arising from these problems are related with a leak of knowledge of the main physical and chemical phenomena that undergoes at sensing material. Especially the phenomena related with:

✓ Surface physics and chemistry

✓ Nanocrystals properties of sensing materials

✓ Sensing principles of SGS

In my opinion, deeper knowledge of all this three points can –and must!- improve the deficiencies of present sensors.

Attending this consideration and the scope exposed in previous section, I started my PhD in September 96 in the group Enginyeria i Materials Electrònics of the Departament d'Electrònica of the Universitat de Barcelona leaded by Prof. Dr. Joan Ramon Morante i Lleonart and advised by Prof. Dr. Albert Cornet Calveras, supported by a CIRIT doctoral grant of the Generalitat de Catalunya (1997FI 00313) and involved in a Spanish CICYT project of the Ministerio de Educación y Ciencia (MAT96-1030-CO2-01). A year later I was also involved in the development of a technological project with the company FAE (Francisco Albero S.A.). During June-July 1999 I was in a research stage in the Center of Interface Analysis and Sensors of the Universität Tübingen leaded by Prof. Dr. Wolfgang Göpel[3].

As we will expose, this thesis contains the main results and innovative findings of the scientific research I was involved in, as well as the most interesting technological

---

[3] Prof. Dr. Wolfgang Göpel unfortunately deceased during my research stage.

designs and implementations, all of them related with semiconductor gas sensors. Table 1.5 summarises different parts of the work accepted for publication to different journals and congresses developed before the end of the thesis.

| *Papers* | | |
Title	Authors	Reference
New method to obtain stable small-sized SnO_2 powders for gas sensors	A. Cirera, A. Dieguez, R. Diaz, A. Cornet, J.R. Morante	Sensors and Actuators B 58 360-364 1999
Comparative structural study between sputered and pyrolysis nanocristaline SnO_2 samples	A. Cirera, A. Cornet, J.R. Morante, S.M. Olaizola, E. Castaño, J. Gracia	Materials Science & Engineering B 69-70 406-410 2000
Microwave processing for low cost and mass production of undoped and in-situ catalytic doped nanosized SnO_2 gas sensor powders	A. Cirera, A. Vilà, A. Diéguez, A. Cabot, A. Cornet, J.R. Morante	Sensors and Actuators B 64 65-69 2000
Characterisation of SnO_2 nanopowders obtained by liquid pyrolysis for gas monitoring	A. Vilà, A. Diéguez, A. Cirera, A. Cornet, J.R. Morante	Institute Physics Conference 164 153-156 1999
Nanocrystalline SnO_2 by liquid pyrolysis	J. Cerdà , A. Cirera , A. Vilà , R. Diaz , A. Cornet , J. R. Morante	Boletín de la Sociedad Española de Cerámica y Vidrio, 39 (4) 560-563 2000

| *Other Papers* | | |
Title	Authors	Reference
Low-cost differential scanning calorimeter	Ll. Mañosa, M. Bou, C. Calles, A. Cirera	American Journal of Physics 64 3 283-287 1996
Calorimetria diferencial de flux: la transició de fase sòlid-líquid de l'aigua	M. Bou, C. Calles, A. Cirera	Revista de física 1 1 20-27 1996

| *Communications* | | |
Title	Authors	Reference
Smart Multisensor Integrating Methane and Carbon Monoxide Gas Detection with Improved Selectivity by Signal Processing	A. Ortega, A. Pardo, S. Marco, A. Cirera, A. Cornet, J.R. Morante, R. Jané, S. Jiménez, E. Castaño, J.Gracia	IGRC (International Gas Research Congress) San Diego EEUU 4 278-291 1998
New method to obtain stable small-sized SnO_2 powders for gas sensors	A. Cirera, A. Diéguez, R. Díaz, A. Cornet, J.R. Morante	European Conference on Solid-State Tranducers (Eurosensors XII) Southampton UK 1 673- 676

		1998
Physics and Technology of SnO_2 nanocrystals for gas sensors improvement	A. Cirera, A. Diéguez, J.L. Alay, A. Vila, A. Romano, A. Cornet, J.R. Morante	SGS (International Seminar on Semiconductor Gas Sensors) Ustron Poloni 1998
Caracterisations structurales et optiques des nanostructures semiconductrices	A. Cornet, F. Peiró, J.C. Ferrer, A. Cirera, A. Diéguez, J.L. Alay, A. Vilà, A. Romano-Rodriguez, J.R. Morante	Materiaux et leurs applications aux dispositifs capteurs (MADICA) Monastir Tunes 1 26-26 1998
Characterisation of SnO_2 nanopowders obtained by liquid pyrolisis for gas monitoring	A. Vilà, A. Cirera, A. Cornet, J.R. Morante	Microscopy of Semiconductor Materials Oxford UK 1999
Obtención, procesado y control de SnO_2 nanocristalino mediante pirólisis líquida	A. Cirera, J. Cerdà, A. Vilà, R. Diaz, A. Cornet, J. R. Morante	Conferencia de la Sociedad Española de Materiales San Sebastian Spain 1999
Improvement of gas sensors devices using new nanometric SnO_2 developed by liquid pyrolisis	A. Cirera, A. Cornet, J.R. Morante	II Conferencia de Dispositivos Electrónicos Madrid Spain 1 463-467 1999
Fabrication process of methane selective gas sensors	S.M. Olaizola, A. Cirera, G. Garcia, A. Cornet, J.R. Morante, E. Castaño, F.J. Gracia	II Conferencia de Dispositivos Electrónicos Madrid Spain 1 79-82 1999
Microwave processing for low cost and mass production of undoped and in-situ catalytic doped nanosized SnO_2 gas sensors powders	A. Cirera, A. Vilà, A. Diéguez, A. Cabot, A. Cornet, J.R. Morante	10th International Conference on Solid-State Sensors and Actuators (Transducers) Sendai Japan 1 504-507 1999
Thermal Evolution of Nanosized SnO_2 for gas sensor applications	A. Cirera, A. Cornet, J.R. Morante, S.M. Olaizola, E. Castaño, J. Gracia	Aseva Summer School 1999 Avila Spain 1 6-7 1999
Comparative structural study between sputered and pyrolysis nanocristaline SnO_2 samples	A. Cirera, A. Cornet, J.R. Morante, S.M. Olaizola, E. Castaño, J. Gracia	European Material Research Society Spring meeting Luxemburg Belgium 1999
In-situ analysis of the conductance of SnO2 crystalline nanoparticles in the presence of oxidizing or reducing atmosphere by scanning tunneling microscopy	J. Arbiol, P. Gorostiza, A. Cirera, A. Cornet, J. R. Morante	Second International Conference on Scanning Probe Spectroscopy (SPS 2000) Hamburg Germany
CO-CH_4 selectivity enhancement by in-situ Pd-catalysed microwave SnO_2 nanoparticles for gas detectors	A. Cirera, A.Cabot, A. Cornet and J.R. Morante	European Conference on Solid-State Tranducers (Eurosensors XIV) Copenhaguen 2000 Dk

using active filter		
Innovative method of pulverization coating of previously stabilized nanopowders for mass production of gas sensors	I. Jiménez, A. Cirera, O. López, A. Cornet and J. R. Morante	European Conference on Solid-State Tranducers (Eurosensors XIV) Copenhaguen 2000 Dk
In-situ analysis of the conductance of SnO_2 crystalline nanoparticles in the presence of oxidizing or reducing atmosphere by scanning tunneling microscopy.	J. Arbiol, P. Gorostiza, A. Cirera, A. Cornet and J.R. Morante	European Conference on Solid-State Tranducers (Eurosensors XIV) Copenhaguen 2000 Dk
Properties of nancrystalline SnO_2 obtained by means of a microwave process.	A.Cirera, A. Cornet and J.R. Morante	European Material Research Society Spring meeting Luxemburg Belgium 2000
Deposition on micromachined silicon substrates of gas sensitive layers obtained by wet chemical route	J. Cerdà, A. Cirera, A. Vilà, A. Cornet and J.R. Morante.	Semiconductor Gas Sensor Seminar (SGS). Undstrom Poland 2000.
Gas sensitive layers from 0.2 μm to 10 μm obtained by pulverisation coating of nanoparticles	I. Jiménez, A. Cirera, A. Cornet and J.R. Morante	Semiconductor Gas Sensor Seminar (SGS). Undstrom Poland 2000.
Raman and FTIR analysis of tin dioxide nanoparticles catalysed with noble metals.	A.Cabot, J.Arbiol, A.Cirera, A.Cornet and J.R.Morante.	Semiconductor Gas Sensor Seminar (SGS). Undstrom Poland 2000.
Electroless Pd and Pt catalytic addition of SnO_2 nanopowders	Raül Díaz, Fausto Sanz, Albert Cirera, Albert Cornet, Joan R. Morante	Material Research Society Fall Meeting 2000.

Table 1.5. Papers in journals and communications in congress and workshops.

Therefore, this thesis contents two different parts. While the first two chapters mainly describe the state of the art of SGS, the following chapters are devoted to the scientific finding and technological developments commented above.

As seen, in this chapter we have introduced the semiconductor gas sensors. Their main problems as well as the usual research to improve them are considered. Finally the work of the thesis is outlined.

In second chapter we intend to give a wide overview of Semiconductor Gas Sensors. General aspects concerning its description and normative they should be compliant are jotted down. We review the use of sensing materials in SGS as well as the

main characteristics of SnO_2. The main applications of SGS are revised as well as the architectures for their implementations in these fields. A brief view of the commercial devices is done. Finally we analyse the models of sensitivity in order to explain the function of SGS.

The third chapter tries to present the experimental details of the different studies, except those related with material procedures described in next chapters. Different technological designs developed in this thesis are described in detail.

The material procedure for SnO_2 powder production (liquid pyrolysis and Microwave processing) is presented in chapter fourth. Hence we consider the main technological aspects as well the scientific findings related with the study of the material developed by this procedure. Electrical results show the feasibility of sensors made by this technology.

In chapter six the studies of sputtered SnO_2 thin film samples are presented, mainly those about microstructure thermal evolution and the characterisation applied to the study of different catalysing strategies. For such study, the knowledge on the microstructure developed in the former chapter is applied and data are compared.

General conclusion and critical review are given in the last chapter.

References

In chronological order

[Oeheme,87] F. Oeme, W. Göpel, "Chemische FeldeffektSensoren, Hard and Soft, Fachbeilage Mikroperiherik" Düsseldorf: VDI-Verlag, 1987.

[Schröder,88] N. Schröder, A. Zecrenssen, "Sensortechnik 2000" Prognos Weltrepart, "Technologieanalyse und prognose der Sensoren bis zum Jahr 2000" Basel, Switzerland, Prognos 1988.

[Azad,92] A.M. Azad, S.A. Akbar, S.G. Mhaisalkar, L.D. Birkerfeld and K.S. Goto "Solid-state gas sensors: a review" J. Electrocem. Soc, Vol 139, No 12, (1992), 3690-3704.

[Feng,94] C.D. Feng, Y. Shimizu, M. Egashira, "Effect of gas diffusion process on sensing properties of SnO_2 thin film sensors in a SiO_2/SnO_2 layer built structure fabricated by sol-gel process", J. Electrochem. Soc., 141 1 (1994) 220-225.

[Schweizer-Berberich,96] M. Schweizer-Berberich, J.G. Zheng, U. Weimar, W. Göpel, N. Bârsan, E. Pentia and A. Tomescu, "The effect of Pt and Pd surface doping on the response of nanocrystalline tin dioxide gas sensors to CO", Sensors and Actuators B, 31 (1996) 71-75.

[Göpel,97] "Chemical Sensors Based on Catalytic Reactions", W. Göpel and K. D. Schierbaum, in: W. Knözinger (Ed.), "Handbook of Heterogeneous Catalysis", Vol. 3, VCH, Weinheim (FRG) 1997, pp. 1283-1310, ISBN 3-527-29212-8.

[Flingelli,97] G. Flingelli, M. Fleisher, H. Meixner, "Selective detection of methane in domestic environments using a catalyst sensor system based on Ga_2O_3", proceedings of Eurosensors XI, Warsaw (1997) 1173-1176.

[Marco,98] S. Marco, A. Cornet, J.R. Morante, E. Castaño, R. Jané, S. Jiménez, A. Pardo, A. Ortega, A. Cirera, "Smart multisensor integrating methane and carbon monoxide gas detection with improved selectivity by signal processing" proceedings of IGRC'98. San Diego (1998).

[Šundić,98] T. Šundić, Algoritmos cuantitativos de procesado de señal para los detectores de gas de bajo coste, Research thesis, University of Barcelona, 1998.

[Williams,98] D.E. Williams, "Semiconducting Oxide Gas Sensors: Past and Future", invited conference at EurosensorsXII, Southampton (1998). The digest of the conference is found in: D.E. Williams, "Semiconducting oxides as gas-sensitive resistors", Sensors and Actuators B 57 (1999) 1-16.

[Morooka,99] S. Morooka, K. Kusakabe, "Microporous Inorganic Membranes for Gas Separation", MRS bulletin, March (1999) 25-29

[Shimizu,99] Y. Shimizu, M. Egashira, "Basic Aspects and Challenges of semiconductor gas sensors", MRS bulletin, 24 6 (1999) 18-24.

[Schweizer-Berberich,99] M. Schweizer-Berberich, S. Strathmann, U. Weimar, R. Sharma, A. Seube, A. Peyre-Lavigne, W. Göpel, "Strategies to avoid VOC cross-sensitivity of SnO_2-based CO sensors ", Sensors and Actuators B, 58 (1999) 318-324.

[Capteurs,00] Capteur gas sensor company, Gas Sensor catalogue and technical information (Capteur Sensors Ltd). Information available in http://www.capteur.co.uk/.

[Figaro,00] Figaro gas sensor company, Gas Sensor catalogue and technical information (Figaro and Figaro USA Inc). Information available at www.figarosensor.com

[Fis,00] Fis gas sensor company, Gas Sensor catalogue and technical information (Fis Inc.). Information available at www.fisinc.co.jp

[Mics,00] Mics gas sensor company, Gas Sensor catalogue and technical information (MicroChemical Systems SA). Information available at www.microchemical.com

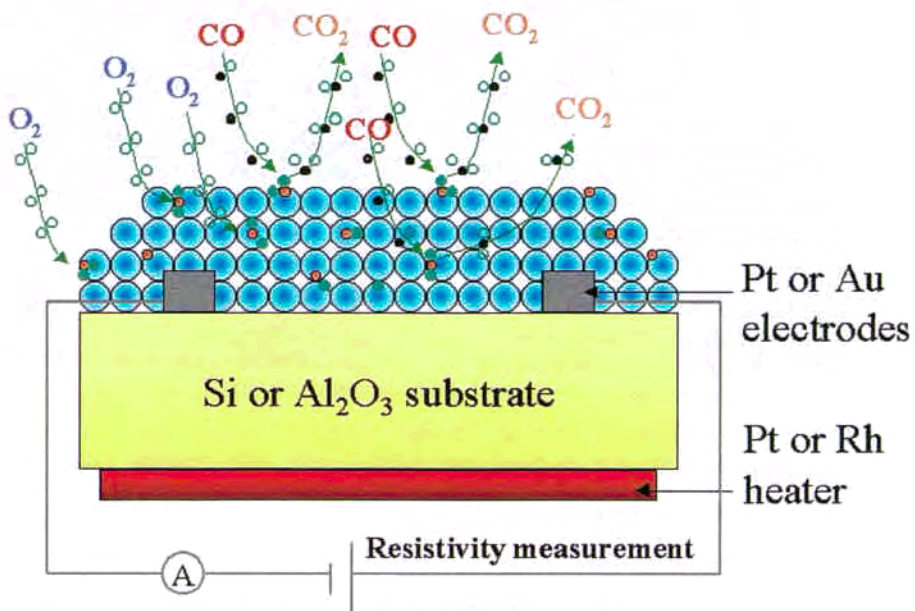# 2. η-SnO$_2$ based Semiconductor Gas Sensors, an overview

2.1 General aspects

Semiconductor Gas Sensors are based on the change of resistivity of a sensing material after gas exposure with respect the resistance measured in air.

Figure 2.1. Structure of SGS.

The enhancement of such sensors involves both heating sensing material and the use of sensing material in nanophase, usually nanocrystalline tin oxide (η-SnO$_2$). A sketch is drawn in figure 2.1. Substrates of SGS are usually made by alumina or micromachined

silicon, although other materials have been tested in different laboratories. Heater and electrodes are both printed or sputtered on substrate using platinum. In some cases special electrodes of gold can be used to improve the sensitivity or selectivity. Sensing material is implemented by a high number of different technologies [Sberveglieri,92].

Sensing material production	Implementation on sensors
Sol-Gel [Kappler,97]	Sintering [Williams,95]
Microwave processing [Cirera,00]	Printing [Harris,97]
Liquid pyrolysis [Cirera,99]	Spin Coating [Atashbar,98]
Hydrothermal [Yu,97]	Spray Coating [Jiménez,00]
Laser pyrolysis [Musci,92]	Droping [Llobet,00]
Laser ablation [Williams, 99]	Dipping [Lee,89]
Sensing material production and deposition	
Chemical techniques	Physical techniques
Spray pyrolysis [Gordillo,94]	Sputtering/RGTO [Sberveglieri,95]
Liquid pyrolysis [Cirera,99]	PVD [Schweizer-Berberich,96]

Table 2.1. Technologies of SnO_2 production, deposition and implementation.

As seen in table 2.1, technologies related with SGS sensing material arise from integrated silicon technologies –as sputtering or CVD- standard chemical procedures – Sol-Gel or hydrothermal- or ceramic-like procedures –sintering, spin coating, printing-. The advantage of silicon technology procedures is the accurate parameter control as well as low cost for mass implementation in integrated devices. Cost improvement of medium-series or non-integrated sensors requires chemical methods and sometimes further ceramic-like procedures of sensor material implementation.

Both kinds of technologies ensure very good pricing of SGS compared with the other kinds of solid-state gas sensors. This is the main reason of its development, as consequence of an industrialised society that demands the control of toxic emissions.

In this way, some countries have established laws or regulations on the requirements of gas detectors in domestic environments that intend to ensure the quality of such devices. Examples are the US [Ul,92], the UK [BS,96], Italy [Ital,93], and the European Union [Cenelec,97a][Cenelec,97b] regulations.

COHb in blood (%)	Damage
<10	No damage
15	Light headache
20	Headache
25	Headache and nauseous
30	Sleepiness
40	Regurgitation
45	Coma, irreparable brain damage
50	Irreparable brain damage, death

Table 2.2. Usual effects of the presence of COHb in blood.

As example of a hazardous gas, CO is a very toxic gas, and can not be detected by human nose. Its toxicity is based on the fact that CO fixes to the haemoglobin (Hb), forming carboxy-haemoglobin (COHb), that is no more enabled for oxygen transport. Since CO fixes irreversibly the COHb, the toxicity is not dependent on the gas concentration only, but also on the exposure time. In table 2.2 are summarised the effects of concentration of COHb in blood.

For this reason, different national as well international institutions give guidelines for air quality levels, considering no only the maximum gas concentration allowed for humans but how to measure it, as shown in table 2.3.

UK National Air Quality Strategy (Department of Environment, Transport & Regions) [UK,00]

Gases	Concentration	Exposure Measured as
CO	10 ppm	Running 8 hour mean
NO2	150 ppb	1 hour mean
O3	50 ppb	Running 8 hour mean
SO2	100 ppb	15 minute mean

OSHA (Occupational Safety & Health Administration) USA. [OSHA,00]

Gases	Concentration	Exposure Measured as
CO	50 ppm	Running 8 hour mean
NO2	1 ppm	15 minute mean
O3	100 ppb	Running 8 hour mean
SO2	500 ppb	Running 10 hour mean

WHO (World Health Organisation) [WHO,00]

Gases	Concentration	Exposure Measured as
CO	50 ppm	Running 8 hour mean

NO2	100 ppm	1 hour mean
O3	60 ppb	Running 8 hour mean
SO2	185 ppb	10 minute mean
NIOSH (National Institute for Occupational Safety & Health) [NIOSH,00]		
Gases		Immediately Dangerous to Life & Health
CO		1200 ppm
NO2		20 ppm
O3		5 ppm
SO2		100 ppm

Table 2.3. Air quality standards for different international institutions.

In this framework, SGS seem to be the kind of devices that fulfils the requirements of the different standards, but keeping low-cost enough to reach mass implementation in domestic, industrial and automotive applications. Because of its lower price in front of the other devices, it is currently the most widely used gas sensor for the identification of gases.

In fact, Brattain and Barden showed in the 50's [Brattain,53] that the gas adsorption at Ge surface lead to a variation of the conductance. Since then, the first built structure to be used as gas sensor has been attributed to Seiyama et al [Seiyama,62] who developed a semiconductor gas sensor based on ZnO. Few later Taguchi patented the first SGS [Taguchi,62].

The first SGS based on SnO_2 was developed in 1970 by Taguchi [Taguchi,70] and was commercialised by Figaro. Since that moment SnO_2 has become the most investigated material for semiconductor gas sensors.

2.2 Sensing Materials

2.2.1 Sensing Materials in Semiconductor Gas Sensors

In the most cases, the change of resistivity of a sensing material after gas exposure is related with the binding or recombination of atmospheric oxygen atoms with sites or oxygen vacancies in sensing material. This reaction changes the potential barrier between grains (surface trapped oxygen) or modulates the bulk conductivity of sample (recombination with vacancies). In both cases changes on resistivity are produced under gas exposure due to the variations of above reactions.

When sensing material binds atmospheric oxygen on its surface, this oxygen becomes ionised negatively and a potential barrier arises –named Schottky barrier-. When exposed to gas (i.e. CO), this gas dynamically reacts with ionised surface-trapped oxygen ($CO+O^{2-} \rightarrow CO_2+2e^-$) leading to changes in Schottky barrier.

As usually defined in the field of SGS, the sign of response (resistance increase or decrease) leads to a simple classification: gases can be classified as oxidising or reducing then materials classified as p or n-type according to the sign of response. p-type materials show a resistance raise in the presence of traces of reducing gases, and resistance decreases to oxidising gases, n-type materials show opposite behaviour.

The classification n and p is used to describe the sensing materials because it is believed that this reflects the charge type of the majority carriers in the two cases, but this is not necessary true.

As exposed above, such kinds of reaction are based on bounded atmospheric oxygen at sensing surface. This is the reason why a systematic study of a large range of oxides showed that sensitivity of conductivity to the presence of traces of reactive gases

in air was a phenomenon common to oxides and not specific to few special cases, as cited in [Williams,98a].

Different studies showed how most part of oxides could be used as gas sensors. After these studies and the great scientific work done, numerous publications reviewed the sensing properties in tables or lists that usually contains sensing materials, doping, working temperature, and detected gases. In order to do not repeat this work, we report not a list of sensing materials but the reference of these tables as well as sensing materials, target gases and other parameters given in the references (table 2.3). Although this wide variety of sensing materials, the most part of commercial sensors for domestic applications are made by SnO_2 doped/modified with palladium. Some of them are made by In_2O_3, WO_3 and $CrTiO_3$.
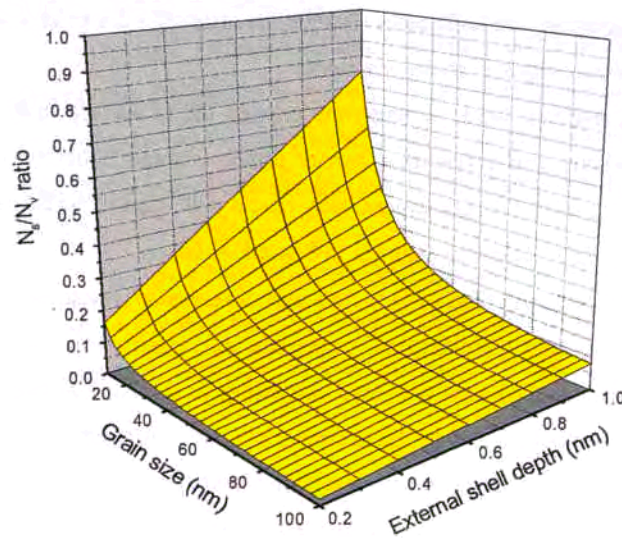

Figure 2.2. Grain boundary with respect bulk as function of grain size for spherical-shaped particles.

Where materials differ from one to another (apart from important issues of feasibility of production and stability of microstructure) is, to some degree, in the response magnitude, response time and relative response to different gases. Such differences can be rationalised as due to variations in the rate constants of oxygen and different gases reactions with sensing material surface.

Besides the properties of sensing materials, another characteristic that it is usually to improve the sensor response is the use of sensing material in nanoparticles phase.

As described in previous chapter, one of the most desired characteristics of such materials is nanometric size due to the increase of surface area. In fact, we can evaluate the amount of surface atoms (N_S) over bulk atoms (N_V) as

$$\frac{N_S}{N_V} = \frac{4(D/2)^2}{r^2}\frac{r^3}{\left(\frac{1}{2}D\right)^3} = \frac{8r}{D} = \frac{0.8}{D}\,nm \tag{2.1}$$

where D is the grain size and r the depth of external shell of atoms (assumed 1Å) [Abello,98]. We can see in figure 2.2 how in low grain size most part of grain atoms are in the surface and hence exposed to gas.

Reference	page	Sensing Materials	Target Gases	Parameters
[Göpel,97]	1297	SnO$_2$	AsH$_3$,H$_2$S,NO$_2$,H$_2$, NH$_3$,SO$_2$,NO$_x$,CO, CH$_3$COOH,CCl$_4$, C$_2$H$_2$O$_4$,CH$_4$,CO$_2$	Temperature, technology, doping
[Göpel,96]	105	SnO$_2$,Fe$_2$O$_3$,La$_2$CuO$_3$, Ga$_2$O$_3$,ZnO,In$_2$O$_3$,V$_2$O$_5$,B i$_2$Sn$_2$O$_7$,GaAs,Bi$_2$Sr$_2$, CuO$_6$,Co$_3$O$_4$,WO$_3$,Cr$_2$O$_3$, Bi$_4$Fe$_2$O$_9$	CO,CH$_4$,NO$_x$,H$_2$, C$_2$H$_2$,C$_6$H$_6$	Sample form, temperature, doping
[Sberveglieri,92]	240	SnO$_2$	NO$_2$,CO,NO$_x$,CH$_4$, O$_2$,ethanol,phenylarsi ne,CH$_6$,ether,H$_2$S,H$_2$, ammonia,iso-C$_4$H$_{10}$	Technology, annealing after growth
[Göpel,95]	7	SnO$_2$	H$_2$,NH$_3$,SO$_2$,CH$_3$CO OH,C$_2$H$_5$OH,CH$_4$,As H$_3$,H$_2$S,NO$_2$,NO$_x$,CCl $_4$,CO$_2$	Temperature, technology, doping
[Moseley,92]	154	ZnO,WO$_3$,TiO$_2$,Fe$_2$O$_3$, CdIn$_2$O$_4$,NiTa$_2$O$_6$,CoTa$_2$ O$_6$,CuTa$_2$O$_6$,BaTiO$_3$(Ag), SrFeO$_3$,Zn$_x$GeO$_y$N$_z$, Cr$_2$O$_3$,In$_2$O$_3$,BaSnO$_3$,Bi$_2$S n$_2$O$_7$, Bi$_6$Fe$_4$Nb$_6$O$_{60}$	H$_2$,CCl$_2$F$_2$,CHClF$_2$,C O,NH$_3$,H$_2$,CH$_4$,C$_4$H$_{10}$,N$_2$H$_4$,H$_2$S,SO$_2$,(CH$_3$) $_3$N,C$_3$H$_8$,C$_2$H$_5$OH,C$_3$ H$_8$,Cl$_2$,NO$_2$	n or p-type, temperature, doping

[Sberveglieri,95]	104	SnO_2,ZnO,Cu_2O,Nb_2O_5	O_2	Temperature, doping
[Sberveglieri,95]	105	SnO_2	H_2,H_2S,NO,NO_x, C_2H_5OH,C_3H_6,ethylet her,halotone,H_2NH_3, NO_2,C_3H_8,Hydrocarb ons,H_2Cl_2,CH_2,Cl_2, $CHCl_3$,CCl_4,AsH_3,C_4 H_{10}, n-C_4H_{10}	Doping
[Sberveglieri,95]	105	$YBa_2Lu_3O_{7-\delta}$,In_2O_3, $LnCoO_{3-x}$,Sm,Eu,La, $Bi_xMo_yO_z$,$Cr_{0.8}Ti_{0.2}O_3$,Zn O,ITO,$CdIn_2O_4$,In_2O_3, $Sn_{1-x}Fe_xO_y$	NO,O_3,CO,alcohols,k etones,NH_3,H_2,CH_4,C $_4H_{10}$,C_2H_5OH,NO_2,et hanol	Doping
[Schimizu,99]	23	SnO_2(Pd),Ag/SnO_2,SnO_2(Ag),SnO_2(ZrO_2),SnO_2 (Al_2O_3),SnO_2(CuO), SnO_2(Pt),WO_3(Au), $Ti_{0.9}Cr_{0.1}O_2$,$IrTiO_2$/In_2O_3(MgO),Pt/In_2O_3(MgO), Ru/TiO_2,In/TiO_2,ZnO (Al_2O_3),SnO_2(La_2O_3), Er_2O_3/ZnO,Rh/WO_3	H_2S,CH_3SH,NH_3, Dimethylamine, Trimethylamine, capronaldehyde, 2- methylpyrazine	Gas concentration, sensitivity, operating temperature.

Table 2.4. Report of different tables available at the literature containing sensing materials, target gases and other properties.

2.2.2 Properties of SnO_2

The properties of sensing material hardly influence the behaviour of sensing device. Two approaches can be made to these properties. In one way, the bulk properties define the material structure and are mainly responsible for the device stability. But surface properties (or properties derived from the low dimensionality of sensing material) should be taken into account for the description of the device response.

From a structural point of view, we can assume that the structure of nanocrystals is the same as single crystals [Gordillo,94][Dieguez,96], only taking into account the induced variations due to grain size. Yet interesting works
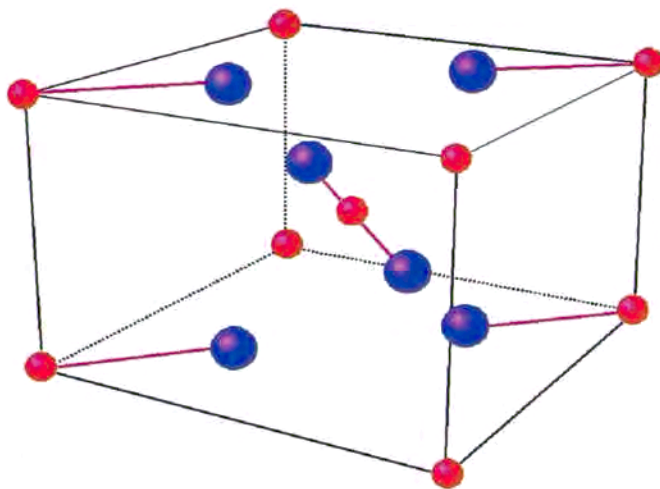
[Eastman,94][Yu,97] have shown the existence of lattice defects associated to grain nanophase. These properties will be discussed with detail when analysing liquid pyrolysis and sputtered samples in chapter 4 and 6.

The data given in this brief rapport are enough for the development of this thesis, nevertheless further properties are given in the works [Schmitte,80][Jarzebski,76] [Fonstad,71].

2.2.2.1 Symmetry and crystal structure

Starting with bulk properties, tin (IV) oxide (II) has only a stable phase (and no metastable ones) in a tetragonal arrangement of the atoms known as rutile or cassiterite. It contains metal atoms in octahedral co-ordination and oxygen in planar three-co-ordination (see figure 2.3).

Figure 2.3. Rutile structure of SnO₂. Bigger atoms represent oxygen. The position of atoms is in scale but not their diameter.

Lattice parameters are a=4.737 Å (both horizontal parameters) and c=3.186 Å. The atomic position at 300K in the unit cell is (0,0,0) and ½(1,1,1) for

the metal and ±(u,u,0) and (½+u, ½-u,½) being u=0.307 for the oxygen. The rest of the atoms can be obtained applying the rutile symmetry D^{14}_{4h} (C_{2v}, $P4_2/mnm$ point group or tP6 Pearson Symbol)[Munnix,83][Gervais,83] [Rantala,94]. From this structure can be derived the Brillouin zone as presented in figure 2.4.
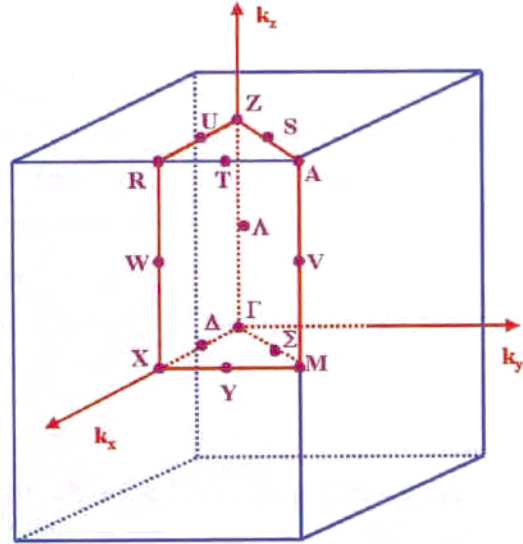

Figure 2.4. Brillouin zone for the rutile structure. Data from [Arlinghams,74]
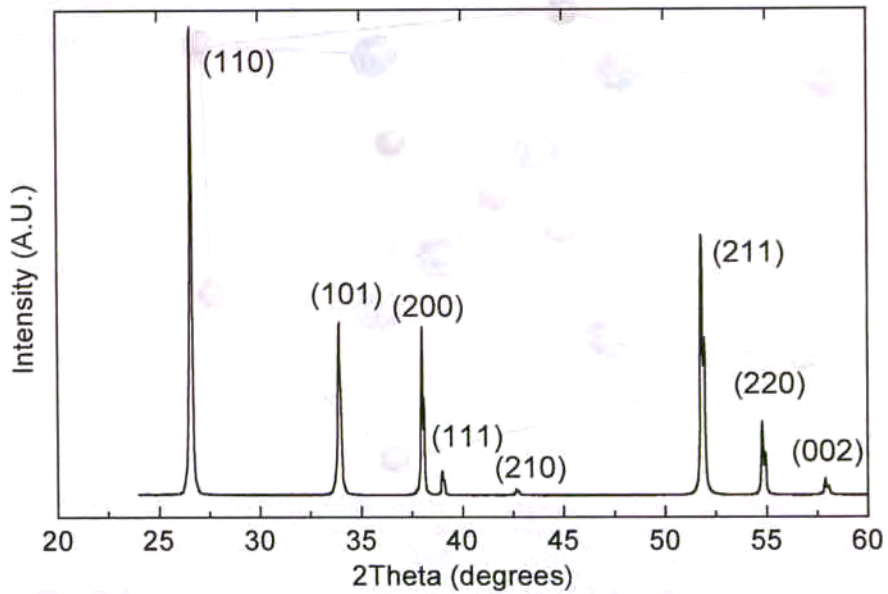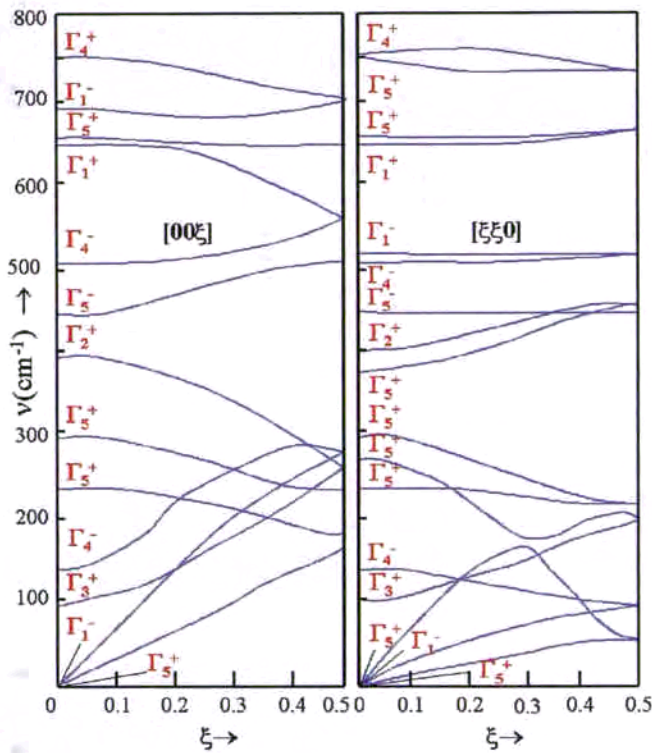

Figure 2.5. XRD pattern of common polycrystalline sample (see JCPDS 21-1250)

According with the above mentioned symmetry as well atomic lattice position, the common X-Ray Diffraction (XRD) pattern is given in figure 2.5.

2.2.2.2 Lattice dynamics

From the point of view of lattice dynamics, the presence of six atoms in the unit causes the existence of 18 branches of vibration modes. Different authors [Katiyar,71] [Gervais,85] have calculated the correspondent dispersion relations, as seen in figure 2.6.

Figure 2.6. Dispersion relations for phonons propagating along [0,0,ξ] and [ξ,ξ,0] directions [Katiyar,71]. These directions can be related with the Brillouin zone in figure 2.4.

Mathematically, the irreducible representation of phonon modes becomes

$$\Gamma = \Gamma_1^+ \oplus \Gamma_2^+ \oplus \Gamma_3^+ \oplus \Gamma_4^+ \oplus \Gamma_1^- \oplus \Gamma_4^- \oplus \Gamma_5^- \qquad (2.2)$$
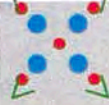
Mode	Koster not.	Deg.	Branch	Type	Calc. freq. in Γ point (cm^{-1})	Meas. freq. (cm^{-1})	Active	Vibration scheme in [001] direction
Γ_1^+	A_{1g}	1	1	Optical	646	634	Raman	
Γ_2^+	A_{2g}	1	1	Optical	398			
Γ_3^+	B_{1g}	1	1	Optical	100	184	Raman	
Γ_4^+	B_{2g}	1	1	Optical	752	779	Raman	
Γ_5^+	E_u	3	7	1TA +3TO +3LO	$\nu_1^{TO}=$ 236 $\nu_2^{TO}=$ 297 $\nu_3^{TO}=$ 651 $\nu_1^{LO}=$ 268 $\nu_2^{LO}=$ 377 $\nu_3^{LO}=$ 750	243 273 605 273 368 757	IR	
Γ_1^-	A_{2u}	1	3	1LA +1TO +1LO	$\nu^{LO}=$ 687 $\nu^{TO}=$ 512	704 465	IR	
Γ_4^-	B_{1u}	1	2	Optical	140 505			
Γ_5^-	E_g	2	1	Optical	441	476	Raman	

Table 2.5. Phonon modes reported in literature [Katilyar,71][Schmitte,80][Merle,80] [Gervais,83]. Some discrepancies arise from different calculated and measured frequencies. In the case of Raman-active measured modes these discrepancies are within ±6 cm⁻¹. Measurements are carried out at 300K.
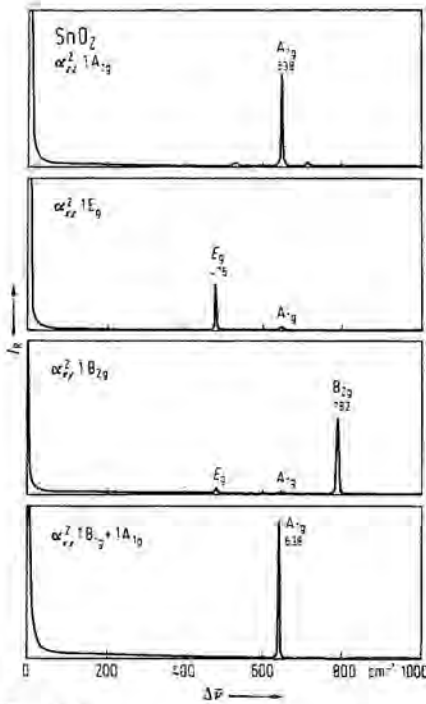
Figure 2.7. Raman spectra of SnO₂. Polarised light on nanocrystalline sample have been used to discriminate single vibration modes.

Table 2.5 summarises the properties of these modes. It is worth to observe how in Raman active modes Sn atoms keep its position while oxygen atoms are vibrating. The observation by Raman spectroscopy of these phononic modes leads to spectra like those in figure 2.7, where polarised light experiments have been performed.

2.2.2.3 Electronic properties

As shown in figure 2.3 tin atom is surrounded by a distorted octahedron of six oxygen atoms and each oxygen atom has three tin nearest neighbours at the corners of an almost equilateral triangle.

Following the well-known formalism LCAO (linear combination of atomic orbitals), we can describe the bulk Bloch wave functions $\Psi_{n,\vec{k}}(\vec{r})$ as linear combination of atomic orbitals $\varphi_\alpha(\vec{r})$ according to

$$\Psi_{n,\vec{k}}(\vec{r}) = \sum_{\alpha,\nu} c_{\alpha\nu}^n(\vec{K}) \chi_R^{\alpha\nu}(\vec{r})$$

(2.3)

where by Bloch theorem the wavefunctions $\chi_R^{\alpha\nu}(\vec{r})$ have the periodicity of the lattice:

$$\chi_R^{av}(\vec{r}) = \frac{1}{\sqrt{N_3}} \sum_j \exp\left[i\vec{K} \cdot (\vec{R}_j - \vec{\tau}_v)\right] \varphi_\alpha(\vec{r} - \vec{R}_j - \vec{\tau}_v) \qquad (2.4)$$

In these expressions, $\vec{R}_j$ is a Bravais lattice vector and $\vec{\tau}_v$ specifies the positions of the atoms in the unit cell. As j runs over the atomic positions, N_3 is the number of lattice points in the normalisation volume of the Bravais lattice.

The common tight-binding scheme has been already developed [Robertson,79]. In this work it has been proposed that the linear combination of orbitals should be –that is α runs over- the 2s and 2p orbitals for oxygen and 5s and 5p orbitals for Sn, taking into account that chemical bonding is mainly governed by these orbitals. Including interactions until second-nearest neighbours we obtain a 24x24 Hamiltonian matrix, whose diagonalisation yields the energy dispersion relations $E_n(\vec{K})$ as well the wave functions $\Psi_{n,\vec{k}}(\vec{r})$. A schematic draft of the results is shown in figure 2.8.

Figure 2.8. Schematic draft of valence and conduction bands of SnO_2. The top of the valence band is a 0 eV. The dominant orbital is indicated as follows: Sn s (|||), Sn p (///), O s (|||), O bonding p (///), O *lone-pair* (\\\). Data from [Munnix,83].
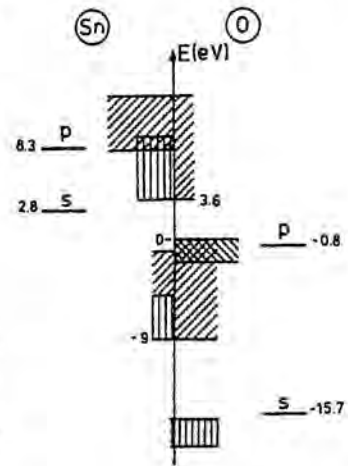
The works [Fonstad,71][Schmitte,80][Robertson,84][Erickson,87][Cox,88][Cox,89] [Kövér,95] and the references therein show experimentally or validate by means of further developments of the mathematical model that the above description is mainly correct when describing the SnO_2 electronic structure.
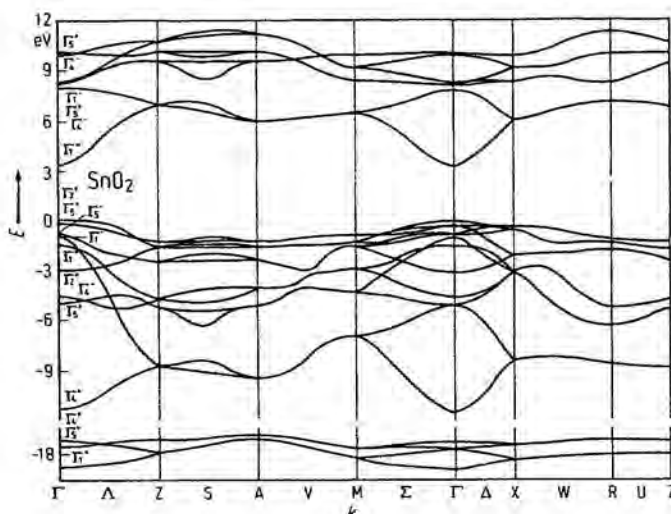
Figure 2.9. SnO₂ calculated band structure [Robertson,79].

As shown, the band located around -17 eV originates essentially from oxygen s states, with a very small fraction of Sn s and Sn p. As it is separated by a gap of 7 eV from the upper valence band, these states are only weak coupled to higher bands.

The main valence band is 9 eV wide, and may be divided in three parts of different orbital composition. The region between -9 and -5 eV results from a coupling of Sn s orbitals to O p orbitals (with bonding p character). The strong s-p interaction produces high dispersion of these bands. The bands in the region between -5 and -12 eV consist of oxygen bonding p orbitals mixed with

Figure 2.10. XPS valence band in comparison with theoretical spectrum calculated by (DVMO) model [Kövér,95].
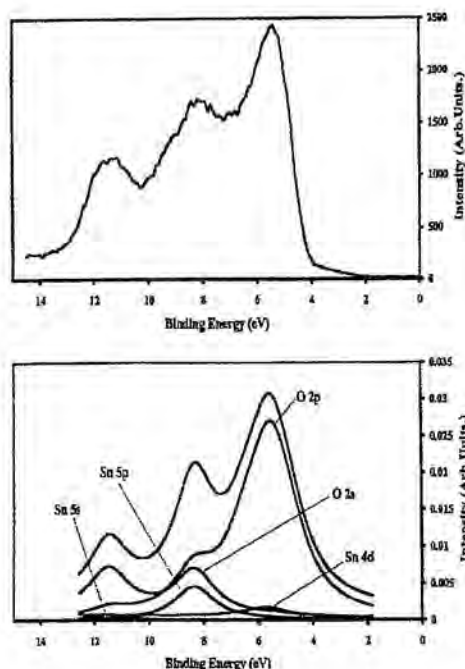
a smaller fraction of Sn p orbitals. The region between   −2 eV and the valence-band edge (0 eV) consists mainly of 0 p *lone-pair* orbitals.

Whole calculations are given for every point of Brillouin zone in figure 2.9. As seen, top of the valence band is a state of Γ^+_3 symmetry as well as bottom of conduction band is Γ^+_1. Therefore the gap is $E(\Gamma^+_3-\Gamma^+_1)$=3.6 eV and lays in Γ point as direct gap.

These calculations as well as further refined discreet variational molecular orbital (DVMO) method [Kövér,95] showed how in valence band spectrum the O 2p and 2s orbitals give dominant contribution. These results are shown in figure 2.10.

2.2.2.4 Oxygen vacancy structure and surface related properties

Besides, the chemical reaction that involves gas sensitivity occurs at sensor material surface. Therefore the properties of surface becomes very influencing. Nevertheless, the currently status of physics and chemical properties are not well developed enough to know clearly the effects of surface properties on gas sensitivity.

As shown, the role of atmospheric oxygen in gas sensitivity seems indicate that the presence of oxygen vacancies in gas sensing metal oxides is very influencing. However, the whole knowledge of the influence of vacancies is difficult not only due to the nature of the study but considering the applied study on nanoparticles exposed to gas.

Consequently both characteristics, oxygen vacancy structure and surface related properties, should be taken into account for the whole comprehension of the sensing phenomena. Thus, let me give few words about these topics.

It is widely accepted that usual non-stoichiometry in SnO_2 induces n-type semiconductor characteristic due to the presence of oxygen vacancies [Robertson,84][Erickson,87]. It has been shown how the different states of oxygen
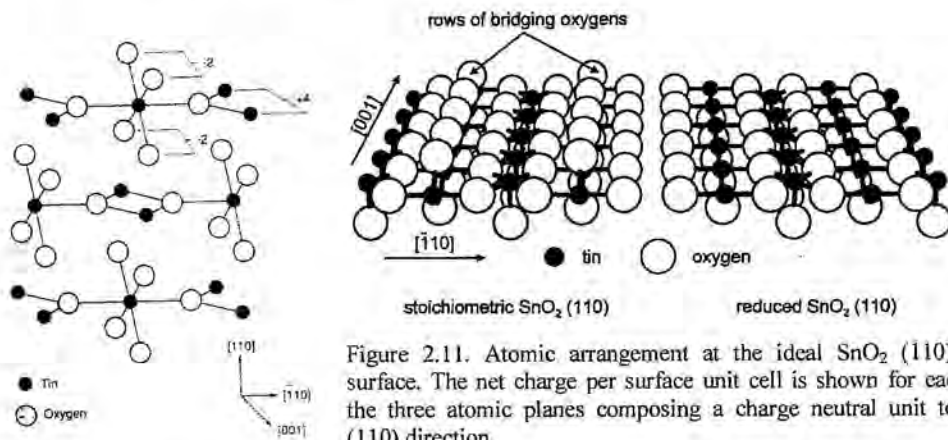
vacancies lay around the conduction band minimum. While unrelaxed vacancies $[V_o]$[1] are above (within the conduction band) [Robertson,84], they become shallow donor centres in the band-gap at about 30 and 150 meV when are single ionised $[\overset{\cdot}{V}_O]$ or

double ionised $[\overset{\cdot\cdot}{V}_O]$ [Fonstad,71].

But the study of defects becomes especially important in surface because different thermal treatments lead to different vacancy scenarios. When studying SnO_2 surfaces, most part of the works are focussed on (110) terminating surface due to thermodynamic arguments that consider this surface as the most energetically stable [Theil,76][Semancik,90][Goniakowski,96] and therefore the predominant crystal face in polycrystalline samples [Jarzebski,76]. In fact when viewed along the [110] direction, the crystal is seen to be compensated of charge-neutrals units, each containing three atomic planes –see figure 2.3-. A charge-neutral unit terminates an ideal stoichiometric (110) surface, and because this unit has not dipole moment in the [110] direction, the (110) is nonpolar, terminating the (110) surface with a complete, nonpolar, charged number of cation-anion bonds relative to the bulk structure [Cox,88]. This ideal (110) surface is terminated with an outermost plane of oxygen atoms which appear as rows in the [001] direction and occupy bridging position between the second-layer sixfold-coordinated tin atoms (see figure 2.11). It has been shown experimentally [Cox,88] how these outermost oxygen atoms –so-called *bridging* oxygen- are substituted by vacancies after UHV annealing at temperatures less than 800 K. For annealing above 800K, a second and deeper layer of oxygen atoms in the same plane than tin atoms –named *in plane* oxygen- are removed. Surface sheet conductance measurements have shown how oxygen vacancies in (110) surfaces can increase the surface conductivity by more than

---

[1] Kroner-Vink notation will be used in text. A prime denotes one negative charge with respect to the lattice, · denotes a positive charge and x denotes neutrality. Subscripts denote the atom that would normally occupy this site; V represents a vacancy and n denotes a conduction electron.

two orders of magnitude with respect to the bulk conductivity [Erickson,87]. As stated, oxygen vacancies in the bulk act as n-type donors, and the previous cited works demonstrate a similar behaviour for surface oxygen vacancies.

However, in process of UHV anneals and posterior re-oxidation, different (110) surface reconstruction may arise. While oxidised (nearly perfect) surface maintains a (1x1) periodicity –see figure 2.11- over the entire composition range, the ion bombarded surfaces undergoes a different reconstruction (c(2x2) and (4x1)) before assuming (1x1) periodicity [Cox,89]. Both mechanisms to obtain 1x1 reconstruction, UHV annealing of bombarded (110) surfaces as well as oxidation processes suggest that 1x1 is thermodynamically stable and should be taken into account for further description of gas sensitivity.

Figure 2.11. Atomic arrangement at the ideal SnO₂ (110)-1x1 surface. The net charge per surface unit cell is shown for each of the three atomic planes composing a charge neutral unit to the (110) direction.

Further interrelation of (110) surface and bulk electronic structure taking into account the influence of surface vacancies has been performed by Munnix and Schmeits [Munnix,83][Munnix,86], by means of computations in Scattering-Theoretical Method (STM). For this, the authors have considered the Green's function G^b associated with the bulk Hamiltonian H^b of the crystal. G^b is defined as,

$$G^b(E) = \lim_{\varepsilon \to 0_+} (E + i\varepsilon - H)^{-1} = \sum_{n,\vec{K}} \frac{|n,\vec{K}\rangle\langle n,\vec{K}|}{E^+ - E_n(\vec{K})} \qquad (2.5)$$

where $|n,\vec{K}\rangle$ and $E_n(\vec{K})$ are the eigenvectors and eigenvalues of H^b and where E^+ stands for $E+i\varepsilon$, with $\varepsilon \to 0_+$. Because of the surface parallel two-dimensional transitional symmetry, the authors expressed the wave functions as Bloch sums of layer orbitals,

$$\langle \vec{r} | m,\alpha,\mu; \vec{q} \rangle = \frac{1}{\sqrt{N_2}} \sum_j \exp\{i\vec{q}\cdot(\vec{\rho}_j + \vec{\lambda}_\mu^m)\}\varphi_\alpha(\vec{r} - \vec{\rho}_j - \vec{\lambda}_\mu^m) \qquad (2.6)$$

being $\vec{q}$ a two-dimensional wave vector, $\vec{\rho}_j$ a lattice vector of the two-dimensional Bravais lattice and $\vec{\lambda}_\mu^m$ the position in the unit cell of the atom μ located in the mth layer. N_2 is the number of lattice points contained in the normalisation area. $\varphi_\alpha(\vec{r})$ is an atomic orbital of type α centred on $\vec{r} = 0$. The development and resolution of

$$D(\vec{q},E) \equiv \det\left|-G_{ij}^b(\vec{q},E)\right| = 0 \qquad (2.7)$$

gives the density of states (DOS) of the surfaces studied.

In the case of (110) surface, the results allow to demonstrate that the gap is nearly free of surface states, nevertheless two s states appear in the lower conduction-band region being the Sn s orbital the most important contribution [Munnix,83]. See figure 2.12.
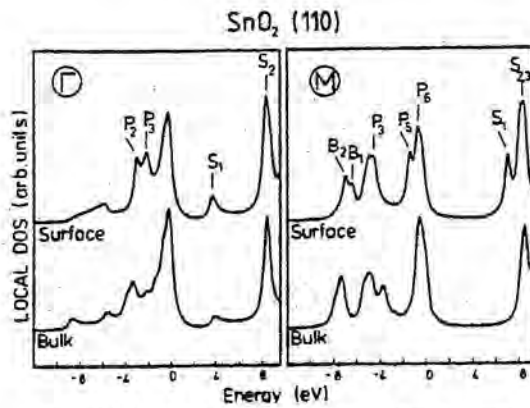
Figure 2.12. DOS (densitiy of states) for the surface layer of ideal SnO₂ (110) in comparison with the DOS of the corresponding bulk layer for the symmetry points Γ and M [Munnix,83].

This light differences in surface DOS' are due to the strongly ionic character of SnO_2, that leads to surface electronic charge distributions which are relatively stable. On the Phillips ionicity scale, the ionicity has been estimated to 0.78, as compared to 0.32 for GaAs or 0.65 for ZnO.

But perhaps the most interesting property that arises from high ionicity is the no influence of surface vacancies on the bulk band gap states.

In the works [Munnix,86][Munnix,87], various vacancy configurations (not only oxygen but tin too) on (110) surfaces have been investigated by means of the above mentioned STM formalism. The main conclusion is that none of the vacancy systems considered gives rise to a bound defect state in the gap. This experimental result is supported by UPS and some conductance measurements (as stated in [Rantala,94]), and also by some conductance measurements after exposure to methane [Kohl,92]. Nevertheless, Cox *et al* [Cox,88] have found experimentally that in (110) surfaces bridging oxygen vacancies lead to defects states in the band gap near the VBM and in-plane oxygen
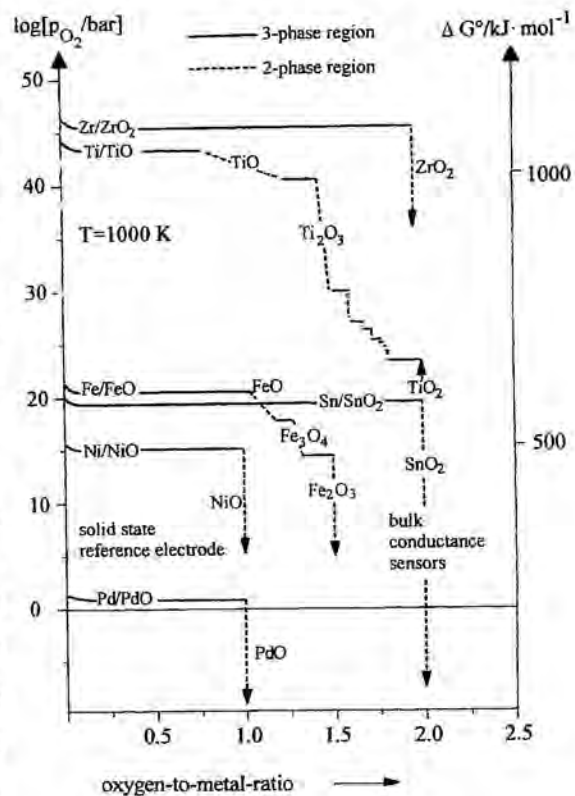

Figure 2.13. The stability ranges of different binary oxides at 1000K as function of the oxygen partial pressure P_{O2} or free enthalpy of formation ΔG_o characterised by the oxygen –to-metal ratio.

vacancies lead to states higher in the gap.

A different behaviour, however, is observed in TiO_2. In such material it has been found experimentally that defects on (110) surface produce defect states at 0.7 eV below the conduction band edge. The different crystal and electronic properties related with high ionicity, makes SnO_2 the most interesting material –from the point of view of surface and bulk stability- in front other gas sensor materials [Göpel,85] [Schierbaum,95].

Besides, the oxygen bulk vacancy stability in SnO_2 has been shown experimentally [Göpel,96]. As shown in figure 2.13, constant free enthalpies of formation (ΔG°) in some metal oxides (such as TiO_2 and Fe_3O_4) are a function of partial oxygen pressure (P_{O2}) within the two-phase regions. Therefore P_{O2} determines their non-stoichiometry. In contrast, ΔG° is constant in other metal oxides, such as SnO_2.

These results lead to a material with stability enough for applications, such as SGS, where working temperatures and atmospheres can induce different kinds of defects and instabilities.

2.2.3 Standard technological procedures for η-SnO₂ production

Besides the usual techniques for metal oxide electronic material production, new or adapted technologies for η-SnO₂ arise from the necessity of nanocrystalline material stable at high working temperature.

As stated previously, we can distinguish between chemical and physical procedure. Usually what decides if a method is chemical or physical is the instrumentation involved in this one.

It is worth to distinguish between methods that produce a sensor material layer over a substrate –that is, they allow produce material while depositing- from other methods where powder is obtained for posterior implementation on sensors –see table 2.1-.

There is two facts influencing on the development and study of these new technologies, the procedure facility for obtaining SnO_2 and stabilisation thermal treatment. First, it is easy to obtain nanocrystals (~100 nm). In fact it is very difficult to growth single crystals for surface studies and hence it is easy reach nanophase in almost all technologies. Nevertheless, there are a large number of technological critic parameters that affect the material properties even as sensor. Some of these parameter influences are known, and the rest should be studied for every specific application.

Another important point in the nanocrystals production is the thermal stabilisation to avoid drifts at high working temperatures. But this annealing is not only due to the necessity of erasing thermal memory. Some technologies like (Sol·Gel) do not give directly the sensing material, but a kind of precursor that needs calcination for the chemical transformation in tin oxide. In other cases, the obtained material is SnO_x with a very low stoichiometry. In these cases thermal assisted oxidation is needed.

Moreover, in processes where time drifts are observed, it is usual to apply thermal treatments of cure on the sensors after stabilisation. Usually these effects are attributed to residual concentration of wet chemical route products, like in spray pyrolysis. In other cases the effects are due to grain growth or recrystallisation.

Let me give a brief description of the most common technological procedures in gas sensors. We will present the most important characteristics of the main methods used for the production of the sensor material as well as the technological steps or variations allowing to introduce the catalytic additives in each case. Further information

about it can be obtained in the references therein as well in specialised papers such as [Sberveglieri,92][Göpel,95][Göpel,96]

2.2.3.1 Sol·Gel

The procedure called Sol·Gel consists in a complex and long chemical process where, starting from a tin chloride, tin hydroxide is formed by precipitation. The result of this precipitation is called Sol. This *Sol* usually contains rests of chlorides and ammonia ions (Cl⁻, NH$_4^+$). A drying at low temperatures (60°C) is needed to obtain the Xerogel, although it is also possible to obtain it by water washing to clean these impurities. Once washed, two alternative ways are followed. It is possible to dip the substrate in the *Sol* and after anneal it (>400°C). This variant is the "dip-coating" process. It is also possible freezing the Sol at 60°C until obtain the *Gel* what finally is needed to anneal. Further details of this technique and their variation are found in [Orel,94],[Schmidt,98].

In spite of its chemical complexity, this procedure has been very successful not only in SnO$_2$, but in a multitude of metal oxides.

For the fabrication of nanocrystalline tin oxide powders for gas sensors applications, some university laboratories [Kappler,97] propose a simplified version of the procedure consisting in a first reaction:

$$SnCl_4 + 4NH_4OH \rightarrow Sn(OH)_4 + 4NH_4Cl \qquad (2.8)$$
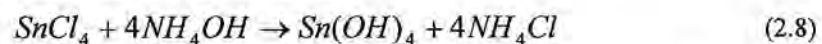
At low temperature (~0°C) the hydroxide –the Sol- precipitate. We can then obtain the SnO$_2$ powders by means of thermal annealing, as schematised in figure 2.14.
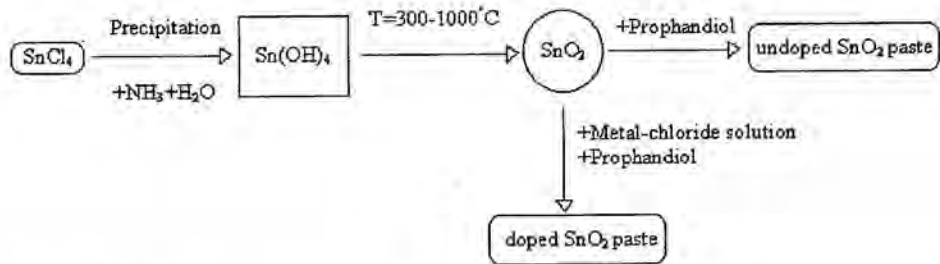
Figure 2.14 The Sol·Gel route for catalytic modified nanocrystalline SnO_2 as proposed in [Kappler,97]. Variations in the catalytic introduction step are considered in [Cabot,00].

The material catalisation is usually done by impregnation when tin oxide has been produced [Diéguez,99], but it is possible to introduce it with good results when Sol is obtained [Cabot,00].

Summarising, the Sol·Gel procedure has became one of the most important technologies in the research on SGS, as well in other fields. Although long and complex chemical process, the above simplification allows to obtain high amount of tin oxide powders –catalysed if needed- with high repeatability.

2.2.3.2 Spray Pyrolysis

In the process of spray pyrolysis a tin chloride solution is pulverised (sprayed) on a heated substrate. As consequence, on this substrate nanocrystalline SnO_2 is produced by means of pyrolytic reaction. The usual chemical reactions are:

$$SnCl_4 + 2H_2O \rightarrow SnO_2 + 4HCl$$
$$SnCl_4 \cdot 5(H_2O) \rightarrow SnO_2 + 4HCl + 3H_2O$$

(2.9)
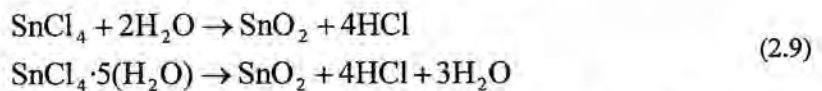
Nevertheless a variety of chemical precursors are used and organic-metallic ones are being used nowadays. A complete description of this technique is found in [Zhang,92],[Correa-Lozano,96].

In spite of the apparent simplicity of this technology, two main problems arise. In one side, the presence of chlorides at high temperature –see eq. 2.9- as a reaction product induce oxidation, contamination and degradation of the experimental set-up as consequence of such harsh environment. To avoid these problems, complicated designs able to isolate the reaction place are needed. Anyway, due to the fact that reaction takes place on the substrate, it is impossible to isolate it from the chloride and this makes this technology incompatible with silicon microelectronics and micromechanics technology.

In other side, different technological parameters becomes strongly influencing on the layer structural characteristics and, therefore, on sensing device:

✓   kind of substrate [Agashe,93]
✓   substrate temperature [Foglietti,96]
✓   sprayed solution [Smith,95]
✓   solution concentration [Gordillo,94]
✓   sprayed flow [Gordillo,94]
✓   reaction atmosphere [Ocampo,95]

Due to these difficulties, and to the fact that chlorides usually remain in the deposited layer, this technology did not get the success obtained by other techniques in gas sensors. Nevertheless, in other fields, such as the deposition of tin oxide or ITO transparent electrodes for solar cells, the spray pyrolysis lays as a constant subject of scientific and technologic research.

2.2.3.3 Sputtering

Nowadays, the cathodic pulverisation (or most commonly sputtering) is one of the most developed techniques for SGS applications. It is worth to say that some companies such as Microsens, Motorola and Mics introduce their sensing material by this technique.

The long and wide use of this technique in microelectronics has become probably the most important factor for a fast and generalised implementation in the field of η-SnO_2 based SGS.

As known, the technique is based on the pulverisation with an ion flow from a target that contains the material to be deposited. An electrical field guides this pulverisation towards the substrate. As usual in microelectronic, a thin film is obtained, which has been reported positive for gas sensing application due to the enhancement of sensitivity caused by this thickness reduction [Sberveglieri,92].

From a technical point of view, it is possible to use a Sn or a SnO_2 target but none of these possibilities ensure the deposition a stochiometryc layer of tin oxide. In fact, oxygen reactive atmospheres are required to improve the stoichiometry of the sputtered layers that anyway needs to be improved after thermal oxidation. Besides this factor the control of the substrate temperature (between 100 and 400°C) becomes important. Voshchilova et al [Voshchilova,95] have demonstrate that the control of this last parameters can lead to layers near to SnO_2 the stoichimetry.

Concerning the effects of temperature, an important approach to the deposition of nanocrystals has been made by Sberveglieri *et al* under the name of RGTO (Rheotaxial Growth and Thermal Oxidation) [Sberveglieri,92]. This variation is based on the deposition of a tin oxide thin layer by physical vapour deposition (sputtering or other) over substrates heated over the melting point of tin. In this way, the metal keep in this temperature without sublimation, but forming microdrops due to surface tension. A raise of this temperature would induce the coalescence of these drops. The second step in the process RGTO consists on the thermal oxidation of the deposited material (i.e. 400°C for 8h in synthetic air) Aste *et al* [Aste,94] have shown that by combining thermal treatment with the proper O_2 partial pressure during oxidation, it is possible to control some microestructural parameters and therefore to modulate the sensing properties of the layer.

Besides the expensive production process that can be improved by mass implementation on silicon microsensors wafers, one of the main critiques made against

RGTO and sputtering in general is the presence of a non-oxide state inside the solidified and oxidised nanocrystal, that can induce important time drifts [Nelli,98]. In general, this is related with the fact that tin oxide is being synthesised at the same time as deposition occurs. So, stabilisation techniques should be done on the layer deposited on the holding substrate. As one of the major features of the use of sputtering techniques is to relate this deposition technique with microelectronic-micromechanised substrate, these further stabilisation anneals should keep CMOS compatibility, leading to a limitation on the maximum temperature to be used.

Moreover, at the present status of the technology, two other problems have to be solved. The first is concerning with the porosity of the obtained layers and the second with the catalysing distribution.

Most part of works related with sputtered SnO₂ gas sensors give reports of very good sensitivity to H₂ [Sberveglieri,92] while it does not seem to report well known sensitivities for CO [Schweizer-Berverich,96]. In fact the formation of a spongy porous agglomerate is crucial to obtain electrically connected sensors [Aste,94]. This fact has been discussed for thick film gas sensors [Shimizu,98] where higher H₂ sensitivity observed for the interior region of the sensors compared with the surface region has proved to be attributed to lower diffusivity of higher molecules. This argument can be extended for thin film gas sensors where the low porosity disables the bigger molecule diffusivity and therefore its sensitivity.

Concerning the introduction of catalytics, an homogeneous distribution of these additives is required to improve the sensor performances. This homogeneous distribution is very difficult to obtain with the sputtering and usually the catalytic is deposited on the top of the layer. Although this catalytic configuration give good results in some gases [Semancik,91][Miszei,93] their results are not comparable with those obtained with thick film gas sensors. To avoid this problem, novel strategies are being tested, as multilayer structures where sandwiches consisting of several layers based on ultra-thin catalytic metals have shown an enhancement of the selectivity [Galdikas,97].

2.3 Sensor designs and configurations

One of the most important goals making SGS is to achieve a reliable sensor design. In spite of the simplicity of sensor parameters involved on the measurement (working temperature and resistance) the requirements are conditioned by physics related on gas sensing mechanism.

Concerning substrate election, it should be taken into account that high temperature is required (usually until $500^{\circ}C$) and low power consumption is desired. Besides, substrate should be electrical insulator, good thermal conductor and non-catalytic active in front of neither gases nor sensing material. These requirements lead to the ceramic substrates. Although different kinds of ceramic can be used (steatite, cordierite, zirconia) the alumina is appreciated due to its stability. Moreover, in some research applications, quartz has been used. In some cases, low thermal inertia is also required to perform non-isothermal measurements. In this case micromechanised and passivated silicon or silicon carbide are used.

In the case of heater, the design becomes critical due to thermal requirements and low power consumption necessities. While in the case of alumina substrates, heat transfer from heater to sensing material through substrate is usually roughly estimated, numerical simulation can be done in micromechanised silicon structures. Some results show how in spite of the low thickness of the sensing layer, it can be exposed to a high gradient of temperature from centre to borders [Briand,99].

Regarding the electrodes, its design is very important to measure the great variations that gas exposures and temperature can produce on sensing layer resistivity. These can increase or decrease resistivity by more than three orders of magnitude. But in some investigation it turned out that other parameters like electrical measuring condition, sensing layer and electrode geometry and the electrode material can also have a significant influence [Jain,90][Lantto,91][Fukui,93][Ylinampa,93][Ionescu,95]

[Ionescu,96][Bauer,97]. In some cases the electrode/material sensing interface resulted in Schottky union, and their consequences should be take into account for further electrical measurements.

Besides the individual influence of each one of these factors, the whole design can introduce cross effects. One of the most important is related to the gas diffusivity and the relative placement of the electrodes, that has been already widely studied [Vilanova,98a][Vilanova,98b]. In fact these effects can be used to achieve improved structures with electrodes at different heights with respect the active layer able to improve selectively [Shimizu,93][Hausner,97].

In the next sections, the most common sensor designs that have been developed until now, will be revised.

2.3.1 Taguchi-design sensors

After the first semiconductor gas sensor developed by Seiyama *et al* in 62' [Seiyama,62], N. Taguchi patented different configurations and embodiments of this device [Taguchi,62][Taguchi,70].
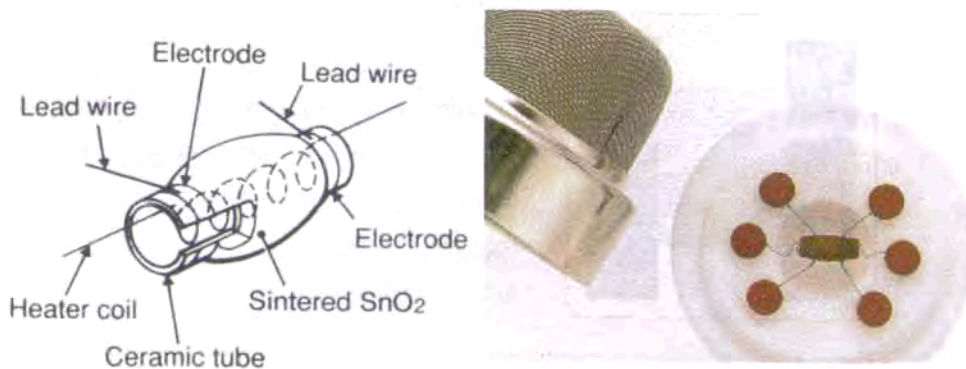

Figure 2.15. Taguchi-design sensor. Left, scheme view. Right, encapsulation in TO6 socket.

The embodiment consists in an empty ceramic tube –preferred in alumina- that contains inside a heater coil (see figure 2.15). Electrodes, generally printed in platinum and/or gold, are placed outside of the ceramic tube, and the sensing layer between them. This sensor can be mounted in a TO-like socket, thus final embodiment can contain a filter.

This sensor was used as commercial sensor by the company Figaro and was in market until few years, being used at the IPC institute of the University Tübingen for scientific porpoise.

Two main problems arise from this design. The first is the high power consumption of the heater, due to the fact that this heater is not in full contact with the ceramic tube. There is a loss of power due to the heating of the air chamber. Another problem is the geometry of the device. A cylindrical geometry is always difficult to industrialise for mass production due to obvious difficulties in printing/sintering technologies. Both problems lead to the next generation of sensors.
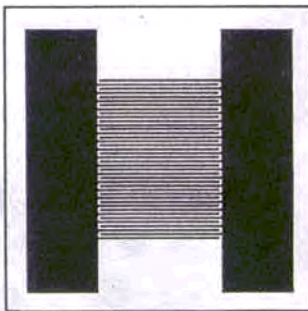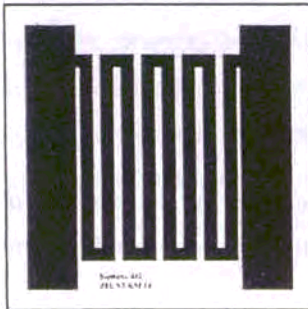
2.3.2. 2d-design sensors

In order to improve problems with industrialisation and heat transfer, planar-substrate sensors were developed. On these sensors (fig. 2.16), the heater is located in one side and the electrodes for measurement in the other side.

Figure 2.16. 2d-design sensor developed in Siemens AG. Up, heater at bottom side of substrate. Down, interdigitate electrodes at the topside. Further information about the design can be found in [Feischer,97]

Although the most common substrates are made by alumina (96 or 98%) there are also substrates on quartz [Sulz,93] or silicon [Llobet,00]. The thickness and shape of the substrate can differ from one to other design. In the case of thickness, it usually ranges from 200 to 600 μm.

Concerning the shape, different approaches have been considered. In most common domestic applications square shaped substrate –like in figure 2.16- are used. This kind of substrates allows TO mounting.

Other applications, such harsh or vibrating environments, need more resistant encapsulations. For this use elongated sensors has been developed, which are able to be encapsulated in rigid sockets [Fleischer,97][Ingrisch,95], as shown in figure 2.17.
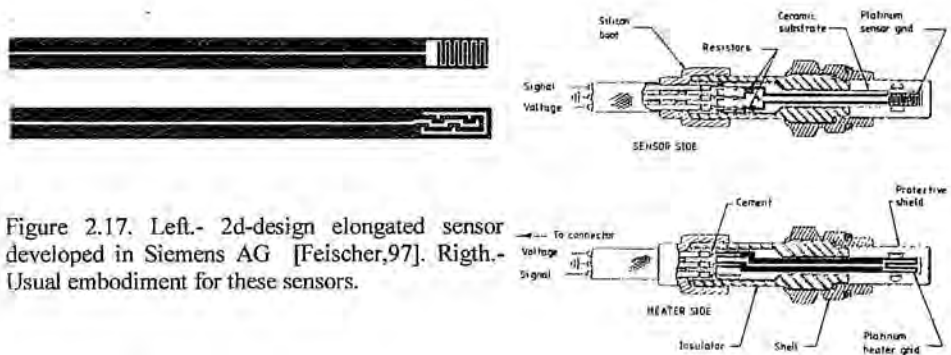

Figure 2.17. Left.- 2d-design elongated sensor developed in Siemens AG [Feischer,97]. Rigth.- Usual embodiment for these sensors.

This kind of sensors is being used by the most part of research laboratories at university level (as example [Bârsan,99]). At industrial level it is being used by Siemens AG [Feischer,97] and Bosch Gmbh [Ingrisch,95] for automotive applications, not only with SnO₂ but also with other kind of semiconductor sensor materials, such as TiO₂.

For home applications, different companies like Figaro [Figaro,00], Fis [Fis,00] and Capteur [Capteur,00] produce sensors with this design. In figure 2.18 sensors from these companies are presented.
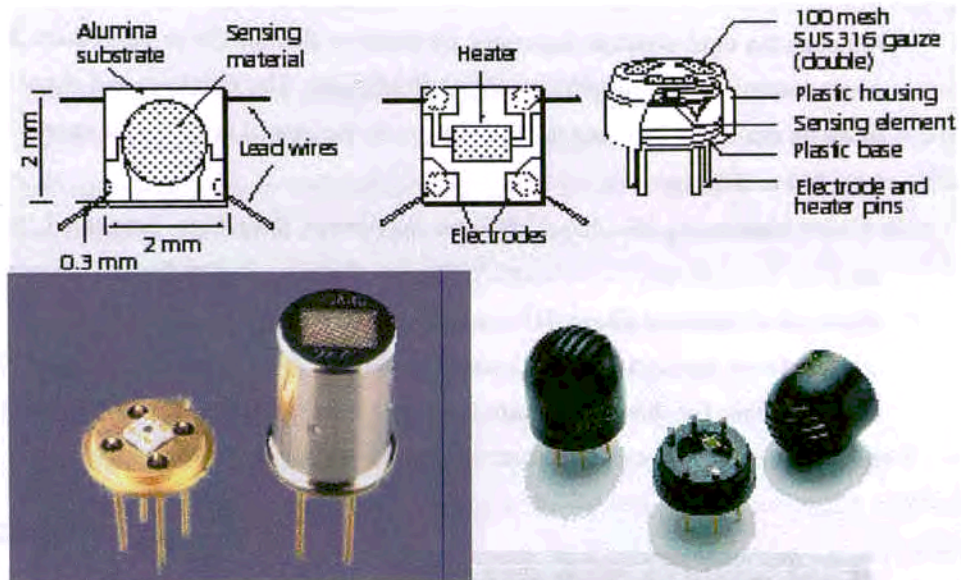
Figure 2.18. Sensors from up, Fis, down left,Figaro, and down right, Capteurs.

These companies offer a wide variety of gas sensors depending on the gas to be detected. Although CO and CH_4 can be well detected with properly catalysed SnO_2, other gases are better sensed with other sensing materials like In_2O_3, WO_3, $CrTiO_3$ ... In general, these sensors are relative small (about 3x3 mm^2) and the power required to get the working temperatures ranges from 300 to 600 mW, instead the several watts that can consume the elongated gas sensors presented previously. The thermal stabilisation time can take from several seconds until still one minute.

Although usually electrodes and heater are printed or sputtered by platinum, heaters of gold or palladium/silver and heater of RuO_2 can be also found [Tomchenko,98].

From a point of view of mass production, the main characteristic of these sensors is that electrodes, heater and sensing material can be deposited with printing technology, a well known–as I will expose in the next chapter- cheap and fast technique.

2.3.3 1d-design sensors

An improvement of the previous sensor design consists in the use of the same face of the ceramic substrate to place the heater, the electrodes and the sensing layer. See figure 2.19.
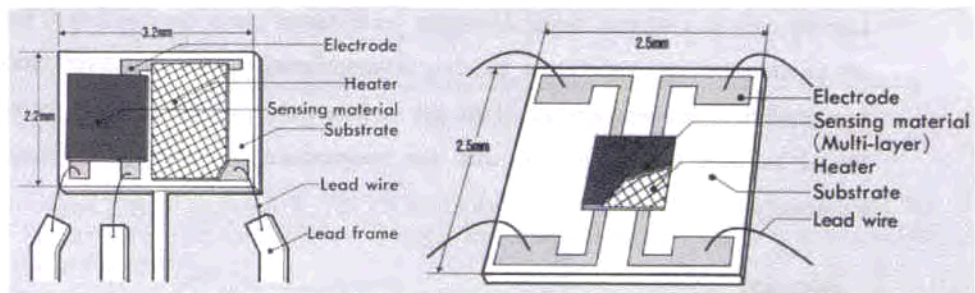
Figure 2.19. 1d-design sensors. Left, sensor with sensing layer by heater. Right, sensor with material sensor over the heater.

Obviously the problem arise when electric contact exists between the heater and the sensing layer. In the case that the sensing layer is placed on the heater, a passivating layer (i.e. Al$_2$O$_3$) between is required.

Figure 2.20. SEM image of an 1-d design sensor for automotive applications from NTK. Left, cross section. Right, detail of the cross section. Blackest is alumina, lightest are electrodes and heater (at the same level, 1-d) and granulated material is TiO$_2$.

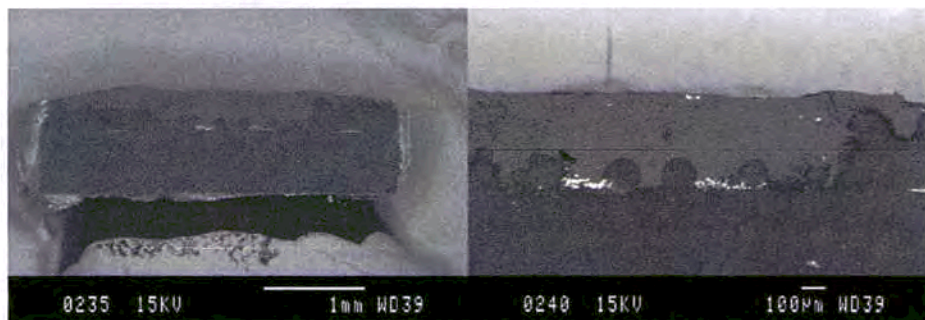In spite of the problem related with insulation, the production rate is strongly increased. Due to this reason, companies devoted to automotive products, like NTK-NGK, have developed sensors in 1-d design, as shown in figure 2.20 [Westbrook,94].

2.3.4 Bead-design sensors

In spite of the high performances that can achieve the sensors above exposed, they can operate only in isotherm mode. However, as different gases have different maximum sensitivity working temperature, building a sensor array requires that every specialised sensor work at one temperature. If the gas sensors were low- thermal inert enough they would be able to change fast with the temperature and measure different gases selectively.
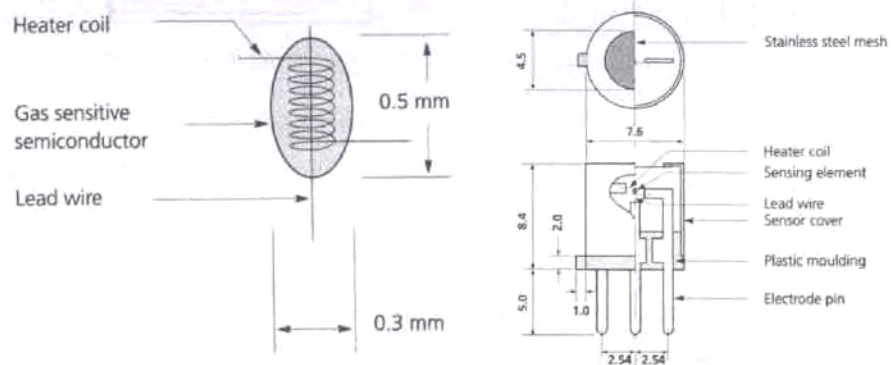

Figure 2.21. Left, bead designed sensor and embodiment. The heater coil is embedded in the sintered sensing material. This design only has 1 electrode. Right, equivalent circuit. V_C is circuit voltage, V_H is the heater voltage, R_L is the load resistance, R_H is the heater resistance and V_{RL} is the voltage across the load resistance. See more information in [Fis,00].
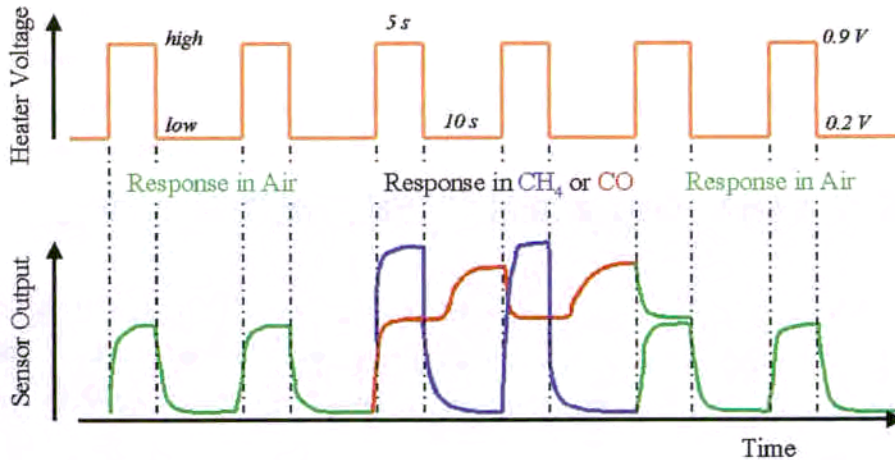
Figure 2.22. Pulsed mode in FIS SB sensor for CO/CH₄ monitoring. The sensor spent few seconds in every temperature and is more selective for CO at low temperature and for CH₄ at high temperature.

This problem is solved by a nice and simple idea consisting in a bead (drop) of sintered sensing material enveloping the heating wire and also locating a measuring wire. See figure 2.21. As there is no substrate, the thermal inertia decreases dramatically.

This kind of sensors has been developed by Fis [Fis,00] and the nominal maximum power consumption is less than 120 mW. This data indicates the low-thermal inertia as consequence of the low quantity of heated mass. This fact allows using this sensor in pulsed mode, producing a continuous variation of the temperature to obtain better sensitivity to different gases. In figure 2.22 there is an example of pulsed mode.

As shown in the figure, when the sensor is operated with high/low periodic operation, sensor signal changes according to the temperature dependency characteristics. By detecting the sensor signal at sufficient timings (at high temperature

for methane and low temperature for CO), selective detection of both methane and CO is achieved.

2.3.5 Silicon micromechanised sensors

As indicated previously, it is possible to use silicon for 2-d and 1-d design as well as microelectronic technology for depositing the electrodes and heater. Nevertheless it becomes a very expensive technology compared with alumina substrates and printing techniques.
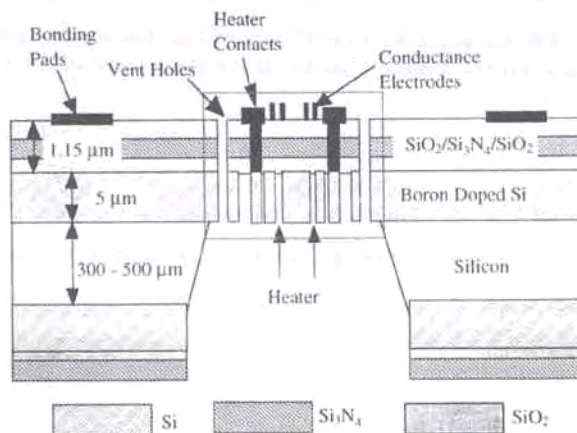
Figure 2.23. Standard layers in micromechanised silicon sensor.

Therefore the main reason to use silicon substrates is the integration of sensors to obtain very small sensors or arrays of sensors in a compatible CMOS technology with active circuitry. But the feasibility of micromachining in silicon makes this material the most indicated to achieve ultra thin heating membranes with very low thermal inertia and very low consumption [Wu,93]. As shown in figure 2.23, there is different technological steps (passivation, metalisation, masking, attack, bonding...) that makes this design only economical viable for mass production.

Two companies (Motorola and Microsens) have started the production of micromechanised substrates with sputtered active layer. A couple of years ago they ceased their activity in sensors to start a joined venture (Mics, [Mics,00]). Sensors of Motorola and Mics are showed in figure 2.24
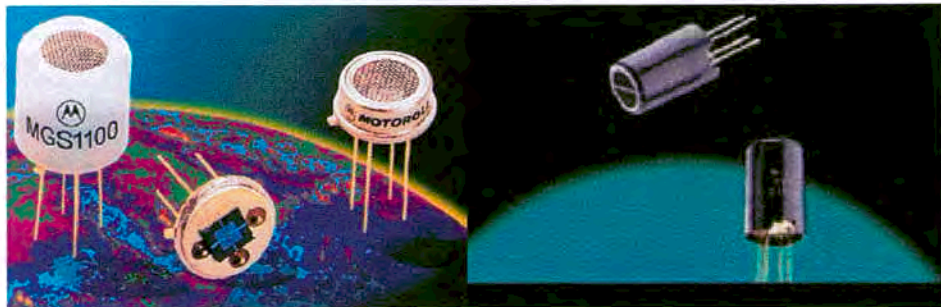
Figure 2.24. Silicon micromachined sensors from Motorola (left) and Mics (right).

One of the major efforts done by these companies was to improve the heat transfer. Finite element simulation [Briand,99], allowed to design sensors able to work only with 20-30 mW [Sheng,98][Mics,00], what is considered the lowest consumption achieved until now in SGS. A scheme of the improved Mics micromachined membrane is showed in figure 2.25.

At academic level, different research laboratories have developed micromechanised sensors with the SnO$_2$ deposited by sputtering or RGTO [Gutierrez,98] [Sberveglieri,95]. But to keep within the limits of CMOS technology, further stabilisation annealing of the structure can not exceed 400°C. Besides, the control of the deposited material becomes more much
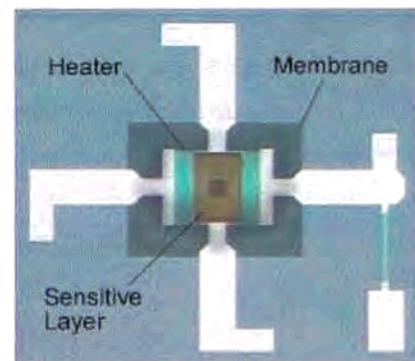
Figure 2.25. Scheme of the Mics sensor membrane.

difficult than in other techniques where sensing material powder is produced and then implemented on sensors.

To overcome these difficulties, a new technique named microprinting or microdroping or drop coating has been developed [Briand,99]. This technique consists in depositing a microdrop of a solution containing the sensing material fully stabilised on a sensor membrane –see figure 2.26-. After low heating the solvent is removed and the sensors is ready for use. A complete description of such technique will be given in the next chapter.
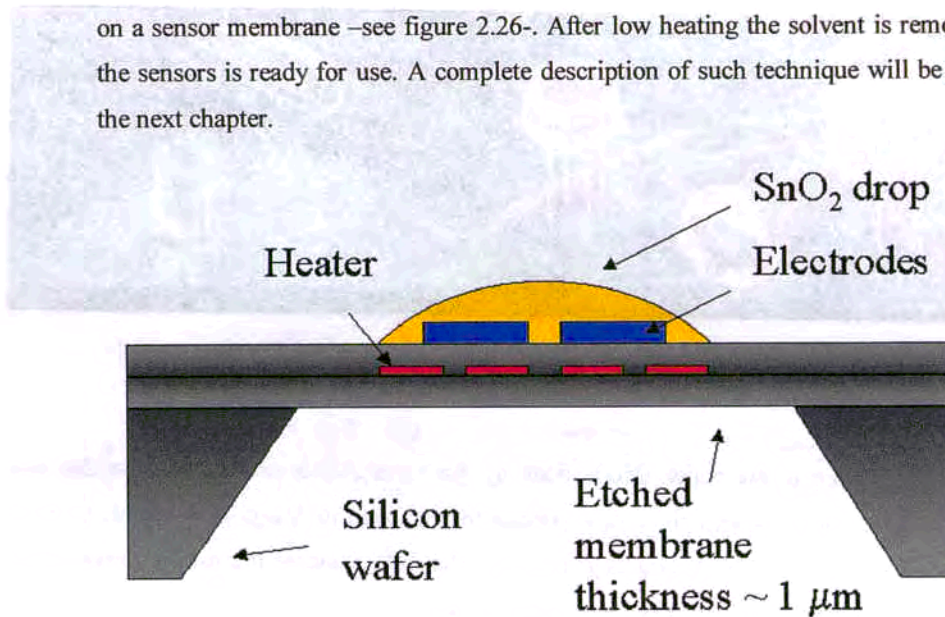
Figure 2.26. Scheme of the microprinted sensor.

2.4 Comprehensive description of sensitivity models

Although a great effort has been done to develop comprehensive models for semiconductor gas sensors, we are far away to know how work these devices in detail. Nowadays we can give some qualitative (or semiquantitative) descriptions about the physic-chemical phenomena that take place, but instead to other semiconductor devices, we can not give general mathematical expressions able to be implemented in a parametrical model, such a SPICE.

In fact, a great number of experiments on sensing surfaces are being done today in order to achieve deeper knowledge. These experiments are usually based on surface quantitative techniques that allow to know the chemical species involved in reaction under pseudo-working conditions, such as Infrared Spectroscopy, Thermal Programmed Desorption, Mass Spectrocopy, and X-Ray Photoelectron Spectroscopy.

In the following pages, we will give some of the keys about sensing phenomena such as the interaction between gas and sensing surface, the effects of former phenomenon on sensing material, the role of additives used in SGS and finally the role of water vapour. For simplicity we will focus on SnO₂ as sensing material and in CO as sensed gas, nevertheless the most part of equations can be extended to other reducing gases. In the case of oxidising gases, only qualitative description is given.

Although the diffusivity of gases in the sensing material becomes a fundamental subject for the whole understanding of the sensitivity in SGS, I will give no information. Good description of adsorption-diffusion-reaction models, which are note the subject of this work, are given in [Vilanova,98a][Vilanova,98b][Llobet,97] [Llobet,98][Williams,95][Williams,98b] and the references therein.

2.4.1 Intuitive description of phenomena

We start from the fact that the atmospheric oxygen interacts with the SnO_2 surface reacting with available sites, the origin and nature of which will be considered later. If we expose the sensor to a reducing atmosphere (CO, CH_4, H_2), the resistivity of the sensor decrease, while the resistivity increase if it is exposed to oxidising gas (NO_2, CO_2). The variation of this resistivity is called sensitivity –as defined in equations 1.1 and 1.2-.

The maximum sensitivity temperature depends mainly on the gas and on the presence of additives (catalytic and doping). For CO and CH_4 maximum sensitivity temperature is about $425°C$ for non-modified tin oxide and between 200 and 300 for Pd or Pt modified material [Schweizer-Berberich,96], for NO_2 this temperature is about $225°C$ [Göpel,95] –see figure 2.27-.
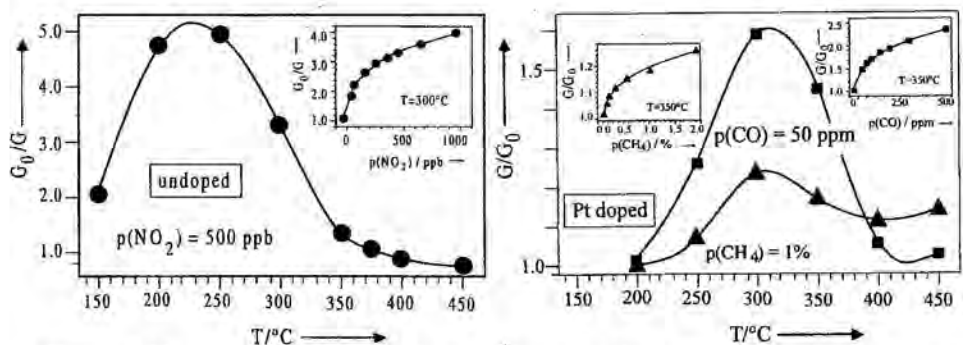

Figure 2.27. Typical examples of the resistance behaviour with temperature and concentration. R is the sensor resistance with gas and R_o in air. a) pure SnO_2 sensor exposed to NO_2. b) Pt-modified SnO_2 exposed to CO and CH_4 [Göpel,94].

The response of the sensors to gas concentration (P_{gas}) can be fitted by expressions such as [Williams,98b]

$$\frac{R_{o,d}}{R_{g,d}} = 1 + A_g \left(\frac{P_{gas}}{P_{air}} \right)^{1/n} \tag{2.10}$$

where $R_{o,d}$ denotes the baseline resistance in dry air (P_{air}) of the conditioned sensor and $R_{g,d}$ the resistance in dry gas of concentration P_{gas}. A_g denotes the sensitivity in dry gas at that particularly level of conditioning (the subscripts g and d refer to "gas" and "dry" -We will give further comments about the effects of water vapour in section 2.4.5-). The exponent n depends on the gas, sensing material and catalysation. Thus for pure SnO₂ sensing CO and CH₄ coefficient takes value 2. Other sensing materials, sensing other gases and modified with different catalytic exhibit different exponent, as reviewed in the table 2.4 references.

The understanding of this behaviour requires the answer to a variety of related questions:

✓ About the capture of gaseous species at sensing material surface, how are they fixed and which are the physic and chemistry involved.

✓ Concerning the kinetics of surface reactions, at which rate the molecules are adsorbed or desorbed of surface, and which are the rate of the surface reactions.

✓ Regarding the conductance level, how the presence of gas influences the driving mechanisms of the electrons through the sensing material.

✓ At electronic level, which are the consequences of such reactions, and how redistributes the energy electronic bands.

The first two questions are the subject of *2.4.2 Gas/surface interactions* section, while *2.4.3 Effects on sensing material* is devoted to the last two. But before to start these points, let me give an intuitive description of the phenomena that is mainly accepted by most of the authors [Schierbaum,91][Azzad,92][Göpel,96][Kappler,97] [Williams,98a].

If we keep the sensor at the proper temperature in a clean atmosphere (in absence of interfering or detectable gases), on the polycrystalline tin oxide surface the reaction

$$O_2 + 2e^- \longrightarrow 2O_s^-$$
(2.11)

takes place. In this reaction, the atom of oxygen captures one electron when it is adsorbed (indicated by s). Thus, the sensor material localises an electron on its surface. In the presence of a reducing gas (R), this gas will be oxidised with the adsorbed oxygen, leaving free the trapped electron. The new molecule keeps free,

$$R + O_s^- \longrightarrow RO + e^-$$
(2.12)

In the scheme described by equation (2.11), we have a surface charge density that is the origin of a potential barrier known as Schottky barrier. This barrier is obviously much less energetic when the reaction (2.12) occurs, due to the diminution of surface charge.
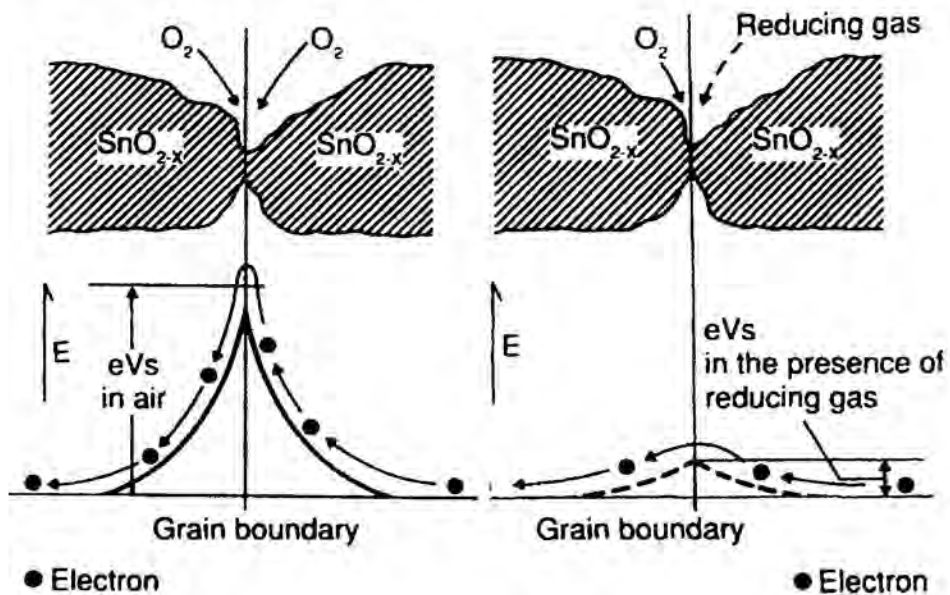

Figure 2.28. Schottky barrier between two nanocrystalls. Left, the presence of oxygen at surface increases the height of the barrier. Right, the number of such oxygen atoms diminishes due to reducing gas oxidation reaction.

See figure 2.28. In this way, after reducing gas exposure, there will be a smaller barrier on the polycrystalline surface and the electronic conduction between grains will be easier. Macroscopically, this implies a diminution of the resistivity in presence of reducing gases.

In the case of oxidising gases, such as NO_2, an increase of Schottky barrier is expected due to the fixation of more molecules on surface. The ionic charge of such molecules becomes higher than that of the oxygen and, therefore, the resistivity increases.

2.4.2 Gas/surface interactions

2.4.2.1 Topological description of the sensing layer

Although nanocrystalline materials are desired for sensor technology, other topologies such as epitaxial layers or different stages of sintered materials also exhibit variation of conductivity under gas exposure.

In fact, due to the annealing treatments required for the stabilisation of material before sensing, the powders can lead to different massive porous stages. Therefore the grains can be connected by neck that can act or not as electrical wire –see figure 2.29-.

Three general cases can be considered and in each of them the depletion layer represents a substantial fraction of the material comprising the intergrain contact. In the case a) –denoting a well sintered case with a fully open neck between adjacent grains- the surface states cause a depletion zone extending to a depth marked by the dashed line on both sides of the neck. In this case the conductivity would be mainly determined by

activation of electron from donor states in the bulk (*bulk-trap-limited* regime) and would be affected by the gaseous atmosphere through changes in the effective channel width only.

The situation exhibited in b) shows the case of a closed neck where the overlapping of the depletion zones of each surface provides a higher-resistance ohmic path through the centre. This geometry could arise because less-complete sintering leaves a narrower neck or it could arise from an open neck being constricted by alteration in the composition of the atmosphere causing a change in the depletion layer thickness. In this case the conductance in the neck would be determined by activation of electrons from surfaces states into the conduction band (*surface-trap-limited regime*) and would be directly affected by the influence of the gaseous atmospheres on the occupancy of the surface states.

The scheme c) is the situation where material is completely porous. Whereas inside the two grains there is ohmic behaviour, at the point of contact, a Schottky barrier appears, arising out of charge trapped in the surface states. In this case, conductivity would be

Figure 2.29. Three model for conductance limited by intergrain constriction. a) open neck, b) closed neck, c) Schottky barrier. Dashed line represents the depletion charge region limit.

limited by charge transport across the barrier and, as we will see in the point *2.4.3.1* the conductivity takes forms such as $\sigma \propto \exp(eV_s/KT)$, being V_s the height of the

Schottky barrier. This situation occurs as a limiting case as the necks are, in principle, distinctly different from the two other cases.

Although in the past different authors assumed different schemes for the same kind of sintered pellets [McAleer,87], the present technology involving low sintering stages and grinding process ensures that the scheme of Schottky barrier is the most appropriate for the description of the sensing phenomena in η-SnO₂. Nevertheless the other schemes should be taken into account in order to explain sintered or very compacted layers.

Figure 2.30. Characteristic solid-gas interaction steps pictured by the dependence of the potential energy on distance from the surface with several relative minima. The examples characterise O_2 interaction steps with the prototype surface TiO_2 (110) and ZnO (10-10). [Göpel,83].

2.4.2.2 Oxygen and CO interaction schemes

There is a wide range of different reaction that can lead to bounded oxygen in tin oxide. As shown generically in figure 2.30 for metal oxides, t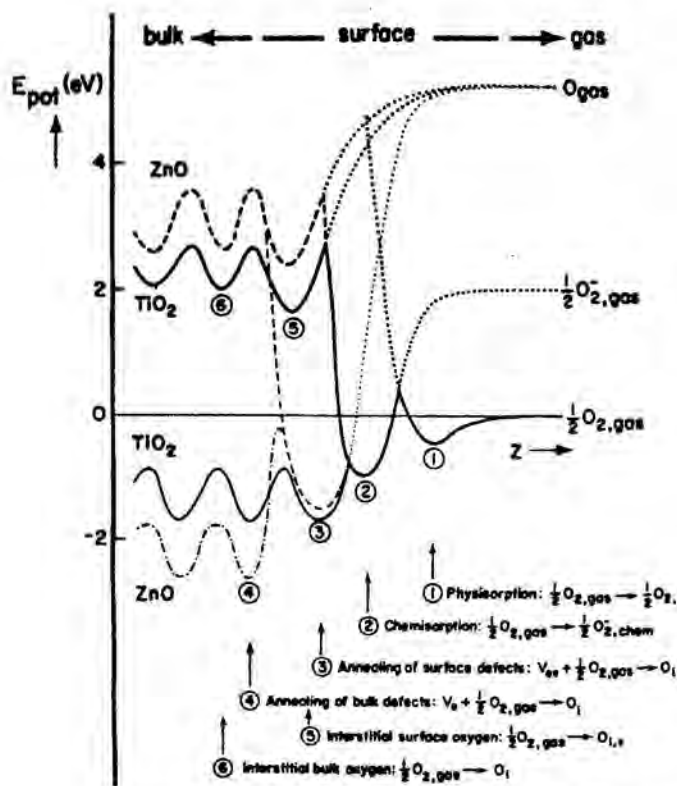he reaction of oxygen with sensing surface can be related with different phenomena that exhibit relative energy minima as function of molecule/surface distance.

While at lower temperature only physisorption and some chemisorption reactions are possible, the recombination with bulk oxygen vacancies seems to be energetically possible at higher temperature.

These reactions can be studied by different spectroscopic techniques such as FTIR, TPD, TDS or EPR and are able in some cases to show the desorbed ionic species or

Figure 2.31. Characteristic thermal desorption spectra (TDS) of molecular oxygen in metal oxides surfaces [Göpel,91]

the origin of this one –see figure 2.31-. We give in table 2.6 a brief summary of the main reaction involving oxygen and water in SnO$_2$.

Temperature (°C)	Physical Change	Reference
80	Desorption of physisorbed O$_2$	[Yamazoe,79]
150	Desorption of O$^-_2$	[Yamazoe,79]
160	O$^-_2$ – O$^-$ transformation	[McAleer,87]
280	Water loss begins	[McAleer,87]
400	Desorption of water from OH$^-$	[McAleer,87]
520	Desorption of O$^-$ or O^{2-}	[Yamazoe,79]

Table 2.6. Temperatures of physical changes in SnO$_2$.

As shown in the table, only O$^-$ and O^{2-} can be related with the chemical reactions that are involved in the sensitivity mechanism because they are found in the

range of SGS working temperatures. Other chemical species such as O_2 or O_2^- are desorbed or transformed according the following reaction path:

$$
\begin{array}{ccccccccc}
\text{Gas} & & \text{Physisorption} & & \text{Chemisorp.} \rightarrow & & & & \\
\tfrac{1}{2}O_2 & \leftrightarrow & O_s & \leftrightarrow & O_2^- & \leftrightarrow & O^- & \leftrightarrow & O^{2-} \\
1 & & 2 & & 3 & & 4 & & 5
\end{array}
$$

(2.13 a)

$$
\tfrac{1}{2}O_2 \leftrightarrow O_s \leftrightarrow O_2^- \leftrightarrow
\begin{array}{c}
2OH^- \\
\updownarrow H_2O + e^- \\
O^- \\
\downarrow \\
RO
\end{array}
\leftrightarrow O^{2-}
$$

(2.13 b)
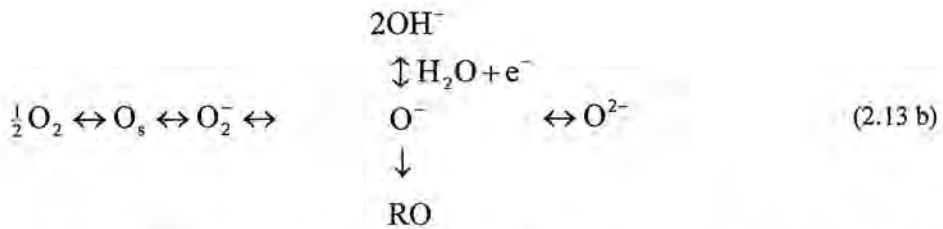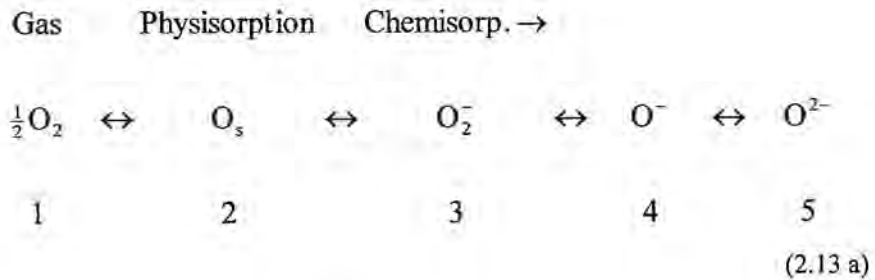
The oxygen molecule is first physisorbed by oxide surface due to electrostatic attraction. This corresponds to the first energy minimum of the system (fig 2.30). As it can be observed in this figure, to go further in the interaction scheme, it is necessary an interchange of electronic charge as indicated in the step 2-3 of the reaction 2.13 a.

In the model proposed by [McAleer,87], the ionic form involved in the reaction with reducing gas or humidity is O^-, as shown in the reaction 2.13 b.

However other authors do not agree with this and they propose that O^{2-} is the ionic form involved in the reaction. As this ionic species is considered not stable as chemisorbed ionic form in tin oxide surface they assume that should react immediately with CO [Bârsan,93][Bârsan,94]. Likewise, it has been proposed that the analysis of the conductance variation with gas concentration implies that the active oxygen species is best formulated by O^{2-} [Williams,95][Williams,98a] and that the correct formulation of

the O^{2-} state coming from an oxygen molecule adsorbed in or on an oxygen vacancy can be formulated as an elementary reaction between oxygen and a surface defect complex [Williams,98b]:

$$\left[Sn_{Sn}^{''} \cdot V_o^{''} \right] + O_2 \rightarrow \left[Sn_{Sn}^{''} \cdot O_o \right] - O \xrightarrow{2n'} \left[Sn_{Sn}^{''} \cdot O_o \right] - O^{2-} \qquad (2.14)$$
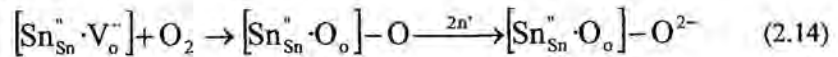
where $V_o^{''}$ denotes an oxygen vacancy with charge 2+ with respect to the lattice and $Sn_{Sn}^{'}$ denotes a double ionised tin atom on a tin site with charge 2- with respect to the lattice. The neutral species (Sn^{4+}) on Sn site are denoted by Sn_{Sn}. As we shown in the point 2.2.2.4, spectroscopic results have demonstrated the oxygen defective nature of the tin oxide surface.

At electronic level, the O^{2-} represents a shallow trap state while O^- induces a deep state, therefore the influence on conductivity is dominated by O^{2-}. However as the coverage of this species is the minor contribution, the fraction of the reaction proceeding the O^{2-} species may be considered small [Williams,95].

Although the doubts of what ionic species of oxygen reacts with CO, there is no doubt that this reaction occurs because CO_2 has been found experimentally, mainly by FTIR [Lenaerts,94].

2.4.2.3 Kinetic models for steady state analysis

We present here the two models usually accepted by the scientific community to describe the reactivity involved in sensing phenomena.

Single reaction model

In the first one by developing (2.11) and (2.12), the reactions that oxygen atoms and reducing gases undergoes at sensing material surface becomes

$$\frac{m}{2}O_2^{(g)} + Ie^- + S \underset{k_{-1}}{\overset{k_1}{\rightleftharpoons}} O_{ms}^{I-}$$

(2.15)

$$mCO^{(g)} + O_{ms}^{I-} \overset{k_2}{\to} mCO_2^{(g)} + Ie^- + S$$
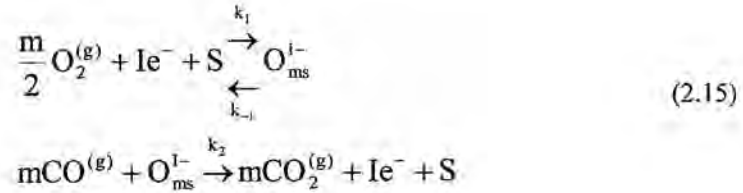
where the ionic states are denoted by:

$$O^- : \qquad m=1 \qquad I=1$$

$$O_2^- : \qquad m=2 \qquad I=1 \qquad\qquad (2.16)$$

$$O^{2-} : \qquad m=1 \qquad I=2$$

In these equations S denotes the sites of reaction at surface where oxygen can be fixed and, as exposed in the former point, this is equivalent to an oxygen vacancy. We can introduce the concept of coverage, as the ratio of occupied vacancies by an oxygen atom,
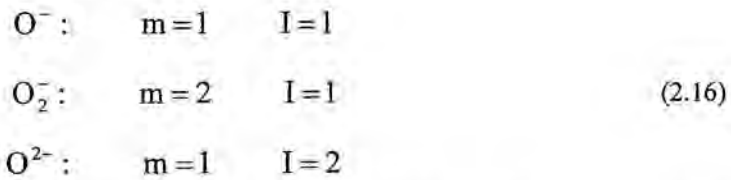
$$\theta = \frac{\left[O_{ms}^{I-}\right]}{\left[S_T\right]}$$

(2.17)

where S_T is the total density of vacancies per surface unit.

Some authors ([McAleer,87][Bârsan,93]) propose kinetic steady states for the formalism (2.15) by taking $\frac{\partial}{\partial t}\left[O_{ms}^{I-}\right] = 0$ and arriving to expressions such as

$$k_1[S]n_s^I P_{O_2}^{m/2} = (k_{-1} + k_2 P_{CO}^m)\left[O_{ms}^{I-}\right]$$

(2.18)

where k_x denotes the reaction constants introduced in (2.15) and n_s the electrons energetically *able* to react at surface. Substituting (2.18) in (2.17) we obtain,

$$\theta = \frac{k_1 n_s^I P_{O_2}^{m/2}}{k_{-1} + k_2 P_{CO}^m + k_1 n_s^I P_{O_2}^{m/2}}$$

(2.19)

In the work [McAleer,87] two further conditions to take into account the effect of the partial pressure of the reducing gas are introduced,

$$k_{-1} \ll k_2 P_{CO}^m \quad \text{and} \quad k_1 n_s^I P_{O_2}^{m/2} \gg k_2 P_{CO}^m \tag{2.20}$$

The result (2.19) defines a range of coverage between 0 and ~1. As it can be seen the coverage increases when raising the partial pressure of oxygen and decreases when raising the partial pressure of reducing gas. This result is similar to Freunlich adsorption isotherm, derived from thermodynamic arguments and expressed as:

$$\theta(P) \approx P^\alpha \tag{2.21}$$

where $\alpha = T / T_C$ is the critic exponent of the reaction and T_C is a parameter that describes the width of the site energy distribution.

Step reaction model

Besides, another interesting approach has been done considering a possible double step reaction but only an energetically possible ionic state of oxygen [Kappler,97]:

$$O_2^{(g)} + e^- \underset{k_{-1}}{\overset{k_1}{\rightleftarrows}} O_2^- \tag{2.22}$$

$$e^- + O_2^- \overset{k_2}{\rightarrow} 2O^-$$

Thus the scheme (2.13) is followed according the different steps of charge of the ionic oxygen. But this implies that the reaction of the reducing gas with bounded ionic oxygen can be with both ionic species:

$$CO^{(g)} + O_2^- \overset{k_3}{\rightarrow} CO_-^{(g)} \cdot O_2 + e^-$$
$$CO^{(g)} + O^- \overset{k_4}{\rightarrow} CO_2^{(g)} + e^- \tag{2.23}$$
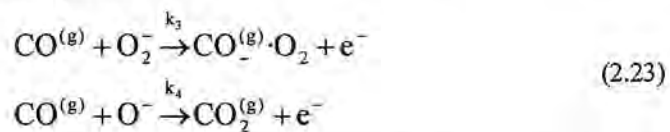
However, only the later reaction is energetically possible.   If we consider the kinetic steady state we obtain:

$$\frac{\partial}{\partial t}\left[O_2^-\right] = k_1 n_s \left[O_2\right] - k_{-1}\left[O_2^-\right] - k_2 n_s \left[O_2^-\right] = 0 \tag{2.24}$$

that we can rewrite as

$$\left[O_2^-\right] = \frac{k_1 n_s \left[O_2\right]}{k_{-1} + k_2 n_s} \tag{2.25}$$

We can obtain similar expression for steady state of O^-:

$$\left[O^-\right] = \frac{2 n_s^2 k_1 k_2 \left[O_2\right]}{\left(k_{-1} + k_2 n_s\right) k_4 \left[CO\right]} \tag{2.26}$$

But with two ionic species of oxygen chemisorbed at surface it is necessary rewrite the coverage as

$$\theta\left[S_T\right] = \left[O_2^-\right] + \left[O^-\right] \tag{2.27}$$

Thus, combining (2.27),(2.26) and (2.25) we obtain an alternative expression for the coverage found in (2.19),

$$\theta = \frac{\dfrac{2 n_s^2 k_1 k_2 \left[O_2\right]}{k_4 \left[CO\right]} + k_1 n_s \left[O_2\right]}{k_{-1} + k_2 n_s} \tag{2.28}$$

As it can be seen, a raise in the CO concentration with respect the oxygen concentration does not ensure a decrease of the coverage near to zero. Therefore, the CO can only react with one of the two ionic states of the oxygen (with O^-), while the other one (O_2^-) can occupy the sites without reaction with CO.

As introduced, the difference between both models mainly consists on that whereas in the first the coverage can tend to zero because the reaction with CO is assumed to take place with the only one oxygen ionic state participating in the reaction, in the second, the coverage can't never be zero because CO can only react with one of the two possible oxygen ionic species. Consequently, some sites will be always occupied by the non-reacting species.

2.4.2.4 Dynamic model for transient analysis

Besides the previous models that describes the steady state of the chemical reactions that happens at sensing surface, there are simple models that explain the transient response of the sensor. As we will show, these models are based on the analysis of differential equations of reaction/reflection of the molecules on sensing material surface, but the rate of the reactions are not described with more detail. Therefore, these models can be applied to other kinds of solid state gas sensors where the differential equation could be assumed. The most interesting work about these models has been done by I. Lundström [Lundström,96], although other interesting approaches about rate reactions were done in the past by Windischmann *et al* [Windischmann,79] Sometimes these models are called *kinetic models*; let us change this name by *Dynamic models* to distinguish clearly this model from the models exposed in the former point where the *kinetic* of reaction was analysed.
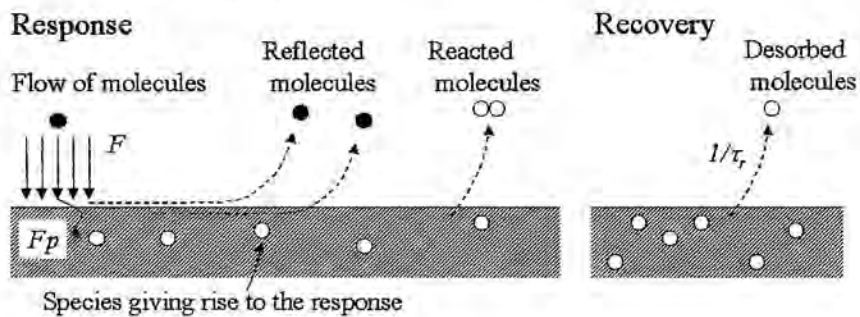

Figure 2.32. Schematic illustration of the chemical reactions occurring during the response and recovery of a gas sensor.

Since the detection of the species depends on phenomena like adsorption/desorption and/or chemical reactions on the surface or within the sensing

material, the response cannot be faster than these phenomena. Any physical process necessary for the detection to occur will slow down the detection if this process has similar or larger time constants than the chemical phenomena. In figure 2.32 it is illustrated the main processes for response –reaction and reflection of molecules- and for recovery –desorption and back reaction-.

We will assume that the chemical reactions are determined by first order reactions:

$$\frac{\partial}{\partial t}\theta = \frac{Fp}{S}(1-\theta) - r\theta \qquad (2.29)$$

where F is the flow of molecules detected by the sensor and p the reaction response probability occupying a site of reaction S. The relation between the coverage, surface sites and bounded species at surface (2.17) is still valid but in a general sense, because now the reacting molecules are CO and the sites should be oxygen atoms bound at surface. In the first term of the differential equation, the probability of reaction –namely the increase of the coverage- is proportional to the amount of molecular flow, the probability (p) and the free sites ($=(1-\theta)/S$). The possibility of molecular reflection is considered to be proportional to a factor r by the coverage.

Usual expressions for the molecular flow as function of thermal speed give:

$$F = n\sqrt{4\pi kT/m} \qquad (2.30)$$

where n is the density of detected molecules at sensor surface and m the mass of the molecule.

Two time constants can be introduced for the description of the forward (reaction) or reverse (reflection) processes,

$$\tau_f = \frac{S}{Fp} \quad \text{and} \quad \tau_r = \frac{1}{r} \qquad (2.31)$$

Therefore the response of the sensor can be written as[2]

$$\theta = \frac{\tau_r}{\tau_r + \tau_f}\left\{1 - \exp\left[-\left(\frac{1}{\tau_f} + \frac{1}{\tau_r}\right)t\right]\right\} \qquad (2.32)$$

being the steady state is given by

$$\theta_s = \frac{\tau_r}{\tau_r + \tau_f} \qquad (2.33)$$

When the detected species are removed from the ambient of the sensor the coverage during the recovery process can be written by

$$\theta = \frac{\tau_r}{\tau_r + \tau_f}\exp\left(-\frac{t}{\tau_r}\right) \qquad (2.34)$$
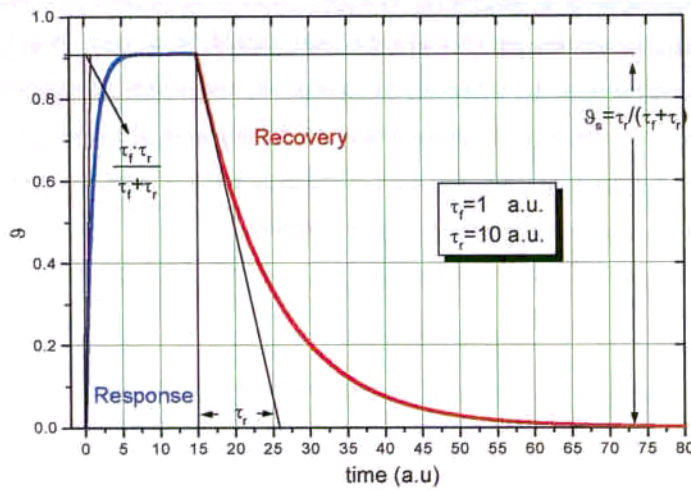
Figure 2.33. Simulation of the response/recovery states. τ_f takes value 1 and τ_r takes 10 in arbitrary units.

In figure 2.33 it is presented a figure with the simulation of the response/recovery states, with the constant of reaction τ_f taking value 1 and the constant τ_r taking value 10 in arbitrary units.

---

[2] We would like to note the mistake on the sign of the corresponding equation in Lündstrom paper [Lundström,96].

We have to note that the initial rate of change of the sensor signal is proportional to $(1/\tau_f+1/\tau_r)$ and for the recovery $1/\tau_r$.

It is worth to observe how for first order process, the response is faster than the recovery. This implies that larger responses will produce slow recoveries. As it is shown in figure 2.34, the response increases when the reverse rate does.

Even if we neglect time constants due to physical phenomena in the sensor (diffusion, heat production, charge transfer), there are possibilities that the chemistry itself will lead to a time dependence much different than that suggested by (2.29). It is clear that we have assumed that the sites of the reaction in this equation were the oxygen fixed at surface which have been considered varying only with CO

Figure 2.34. Simulation of coverage in the response scheme as function of the time and reverse rate τ_r, considering τ_f of 1 au.

concentration, however as the sites evolution have their own kinetics, the differential equation concerning the evolution rate of oxygen sites should be also taken into account.

Second order reactions can be considered for further description of phenomena taking into account these chemical processes, especially when two species are present. These second order models have been successfully applied [Lundström,76].
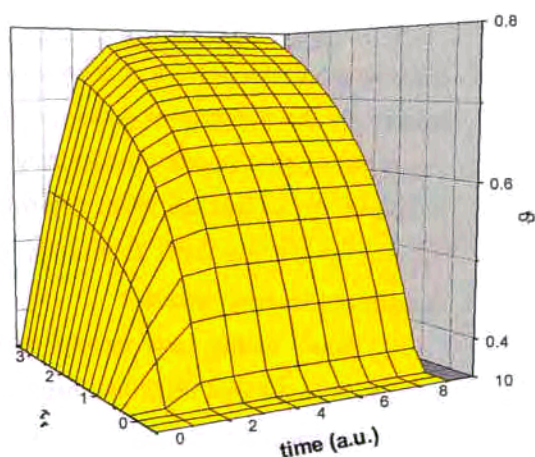
2.4.3 Effects on sensing material

2.4.3.1 Schottky barrier and conductivity between grains

The transducer function in a SGS consists in to measure the resistivity variations induced by the presence of gases. As stated previously, in the case of independent nanoparticles, the Schottky barrier determines the variation of conductivity after gas exposures. As we will see, we can calculate this barrier from the integration of Poisson equation of the electronic charges at surface. Therefore the result depends on the geometry of sensing material.

Some studies have focused on the shape of these nanocrystals. After some theoretical discussions about the shape of these nanocrystals due to thermal growth, N. Bârsan proposed the study of cylindrical nanocrystals [Bârsan,94]. This geometry was previously studied by Romppainen *et al* [Romppainen,88] as well as the one-dimensional case and the overall conductance of a random barrier network. Other authors [Seto,75a][Tarng,78] studied the conduction in polysilicon grains assuming spherical geometry. After the TEM study done in all this work, we will consider this geometry the most adequate for the description of the Schottky barrier, although not always is possible to integrate the equations in this geometry.

Let us assume that we have a set of spherical nanocrystals of diameter L and only one atomic species (the oxygen atoms) fixed and distributed uniformly on their surface (O_{ms}^{1-}). We consider the existence of S_T sites for oxygen bonding. These sites, which we will related with oxygen vacancies in previous points, will fix oxygen atoms that will produce a spatial charge region (or depletion region) when ionised. This spatial

charge region is depleted of conduction electrons until a certain depth (between ½L and *l*). Therefore only ionised impurities lay as charged species in the depletion region.

Taking into account the high density of oxygen vacancies present in the material [Fonstad,71][Jarzebsky,76] and the fact that this vacancies are the main impurity contribution, we can assume that the conduction electron density will approximately equal to oxygen vacancy density.

The Poisson equation in one dimension for simplicity leads,

$$\frac{\partial^2}{\partial x^2}V = \frac{-en_b}{\varepsilon\varepsilon_0} \qquad \text{between } l<|x|<\text{½L} \qquad (2.35)$$

where (½L − *l*) denotes the external depleted shell of the grain. Integrating twice this equation and applying the continuity condition in the potential $(V(0){=}V_0)$ and in the field $(\partial V/\partial x\big|_{x=l} = 0)$ we obtain

$$V(x) = \frac{-en_b}{2\varepsilon\varepsilon_0}(x-l)^2 + V_0 \qquad \text{between } l<|x|<\text{½L} \qquad (2.36)$$

And we can compute the height of the Schottky equation,

$$V_s = V(\tfrac{1}{2}L) - V(l) = \frac{-en_b}{8\varepsilon\varepsilon_0}L^2 \qquad (2.37)$$

in the case of a fully depleted grain, or

$$V_s = V(\tfrac{1}{2}L) - V(l) = \frac{-el\left[O_{ms}^{l-}\right]^2}{8\varepsilon\varepsilon_0 n_b} \qquad (2.38)$$

in the case of partial depleted grain[3]

---

[3] A complete discussion about the meaning of complete (or not) depletion is given in [Seto,95]. As summary, in a depleted grain we have $Ln_b<l[O_{ms}^{l-}]$. L (the depletion region) is related with $[O_{ms}^{l-}]$ and n_b and is usually misunderstood with the Debye length L_D by most of authors, as very well described in [Diéguez,99].

But, as pointed out in the work [Diéguez,99], the expression (2.38) is only valid when the oxygen is fixed with a state below the Fermi level. In general, N_s surface charged states lying in E_s energy bands is distributed by a Fermi-Dirac statistics. This gives the following expression for the Schottky barrier:

$$V_s = \frac{-eN_s^2}{2\varepsilon\varepsilon_0 N_D}\left[1+\exp\left(\frac{E_s - E_F}{KT}\right)\right]^{-2}$$

(2.39)

In the case of oxygen, as this atom fixes electrons at surface, it can be considered as creating acceptor levels and its energy state should be below the Fermi level. This fact has been experimentally shown for (110) TiO_2 surfaces [Göpel,83] and by LCAO cluster model in (110) SnO_2 surfaces [Rantala,95].

Following the expressions found by Bethe ([Seto,75b] is possible to calculate the density of current by thermoionic emission between grains as,

$$J_T = -en_b\left(\frac{KT}{2m^*\pi}\right)^{1/2}\exp\left(\frac{eV_s}{KT}\right)\left[\exp\left(\frac{-eV_a}{KT}\right)-1\right]$$

(2.40)

Where V_a is the biasing potential seen by the nanocrystals, therefore if there are G resistors –nanograins– , the actual potential seen by a grain is $V = V_a/G$. Thus, when

$$\frac{eV_a}{G} \ll KT$$

(2.41)

we can approximate,

$$J_T \approx e^2 n_b\left(\frac{1}{2m^*\pi KT}\right)^{1/2}\exp\left(\frac{eV_s}{KT}\right)V_a$$

(2.42)

and deriving we obtain the conductivity as

$$\sigma = e^2 n_b\left(\frac{1}{2m^*\pi KT}\right)^{1/2}\exp\left(\frac{eV_s}{KT}\right)$$

(2.43)

Substituting the expression for the Schottky barrier (2.38) in this equation and with the definition of coverage (2.17), the conductivity leads to

$$\sigma = e^2 n_b \left(\frac{1}{2m^* \pi KT} \right)^{\frac{1}{2}} \exp\left\{ \frac{-e^2 IS^2 \theta^2}{8 \varepsilon \varepsilon_0 n_b KT} \right\} \tag{2.43}$$

This equation gives a useful expression of the conductivity as function of the former coverage expressions found for the different models.

2.4.3.2 Effects on the electronic bands

It is expected that oxidising molecules (O_2, NO_2 and CO_2) create acceptor levels because they capture electrons at the surface from the bulk, while reducing ones (H_2, CO, CH_4) introduce donor levels because they give electrons to the SnO_2 through the creation of an oxygen vacancy. Consequently the surface charge per unit area Q trapped during the chemisorption of n_s^{ad} particles per unit area can be expressed as

$$Q = e\left[\int_{-\infty}^{\infty} D_D(e)f(E_F - E)dE - \int_{\infty}^{-\infty} D_A(E)f(E - E_F)dE \right] \tag{2.44}$$

with $D_D(E)$ and $D_A(E)$ the donor and acceptor densities of surfaces per unit area. This scheme is showed in figure 2.35.
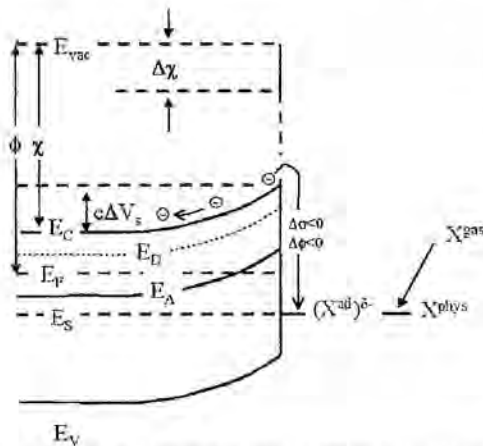
When the molecule is chemisorbed as $(X^{ad})^{\delta-}$ the band bends a value ΔV_s. This bending can be evaluated by using a *Kelvin probe* that measures the changes in the work function $\Delta\phi$ [Schierbaum,91]. The

Figure 2.35. Schematic presentation of chemisorption and charge transfer at a semiconductor surface in the electronic band scheme of the surface. The gas phase molecule X^{gas} forms the precursor physisorption state [Göpel,94].

variations in the work function can be related with changes in Schottky barrier as,

$$\Delta\phi = -e\Delta V_s + \Delta\chi + \Delta(E_C - E_F)_b \qquad (2.45)$$

although the variations in the bulk Fermi level position can be neglected if bulk diffusion of atoms or ions can do [Göpel,97]. In this point, although Romppainen *et al* [Romppainen,88] have considered the possibility of oxygen vacancies mobility when the temperature is high enough, in the work [Blaustein,99] it is shown experimentally how the oxygen vacancies distributions seems to be frozen at normal working temperatures (<300°C).

In the case of variations due to changes in electron affinity, its origin consists in an induced dipole moment attributed to the adsorption complexes:

$$\mu^{ad} = \varepsilon_s\varepsilon_o\Delta\chi \Big/ n_s^{ad} \qquad (2.46)$$

This term was first introduced by Göpel *et al* [Göpel,83] in equation (2.45) to explain the differences between the changes in work function and Schottky barrier.

The equation (2.45) allows relating the phenomena of chemisorption (fig. 2.35) with the evolution of electronic bands and gives a useful expression to evaluate this effect by means of Kelvin probe measurements.

2.4.4 Promoting effects of additives

Usually, the addition of some metals increases the sensitivity and lowers the maximum sensitivity temperature. Some of them –Pt, Pd, Au, Al and others found in the references of table 2.4- increase the device sensitivity much more to a gas than the others. Therefore the selectivity is strongly enhanced [Shimizu,99]. Nevertheless, their activity depends not only on the way of addition of the metals –such as impregnation, electroless or in-situ doping- but to a wide variety of considerations such as their

distribution, the metallic or oxide state of the additive or the grain size of the sensing material.

In the case of CO detection, it has been shown that the addition of Pd decreases the maximum sensitivity temperature of SnO$_2$ from 450 to 250°C, together with an enhancement of sensitivity about 20 times better. In the case of Pt, whereas the maximum sensitivity temperature is still lower (200°C), the sensitivity is only enhanced about 10 times [Schweizer-Berberich,96].

The mechanisms by which the metal additives have been shown or postulated to modify the properties and behaviour of tin oxide gas sensors can be separated in different effects as [Henshaw,96]: catalytic oxidation of gases at lower temperatures, spill over of chemisorbed reactant gases from the metal to the oxide, distortion of the SnO$_2$ lattice structure at the metal/oxide interface, electronic effects as pinning of the oxide Fermi level to that of the additive, intergranular Schottky barrier formation determined by the contact potential formed at the metal/oxide interface … In fact, a wide variety of effects can be related with the addition of metals in tin oxide and, probably, the effects of the metal addition on sensitivity are a mix of most part of them. Let me give a brief explanation of these effects.

Catalytic sensitisation

A first approximation consists on the catalytic effect of the metals. Some observations have shown how Pd and Pt form clusters on SnO$_2$ surfaces [Matsushima,89] [Labeau,93a][Labeau,93b]. These clusters enable catalytic processes on the semiconductor surfaces. The metallic clusters present a higher sticking coefficient to gases than the semiconductor –as exposed in [Semancik,90] and on the cluster nearly all the gas molecules are dissociated, the products being *spilt-over* the semiconductor surface [Matsushima,88].

Spill-over

It is reported that platinum additive produces hydrogen dissociation *spill-over* [Kappler,97],

$$2Pt\cdot+H_2 \rightarrow 2Pt:H$$
$$2Pt\cdot+O_2 \rightarrow 2Pt-O$$

(2.47)

after oxygen exposure, the reaction becomes

$$O+e^- \rightarrow O^-$$
$$2H\cdot+O^- \rightarrow H_2O+e^-$$

(2.48)

Moreover, Henshaw *et al* [Henshaw,96] showed how Pt^o and $Pt(OH)_2$ species are able to catalyse CO combustion at room temperature and PtO_2 below $100^{\circ}C$, while tin dioxide surface promotes combustion at $200^{\circ}C$. Multiple Pt species can promote CO combustion at higher temperatures. In the case of Pd, it is proposed that the electronic interaction between PdO and SnO_2 should be assisted by adsorbed oxygen. Oxygen should be adsorbed at the interface between PdO and SnO_2 when the system exposed to air. These oxygen adsorbates can accept electrons by themselves, but the more important aspect is that they act as a bridge between SnO_2 and PdO to form an electronic junction such as a p-n (or more exactly MIS) junction [Xu,96].

Electronic sensitisation

Another approximation is the electronic sensitisation. While additives at the surface of the semiconductor act as receptors, the semiconductor acts as a transducer of the changes taking place at the surface under gas adsorption. This type of sensitisation has so far been observed in SnO_2 elements impregnated with Ag and Pd [Diéguez,99], which form stable metal oxides when exposed to air. When they are exposed to reducing gas, their chemical state change, inducing the corresponding change in the electronic state of the semiconductor. In the case of H_2, the large decrease in electrical

resistance for the Pd-loaded element in contact with H$_2$-containing air so far has been considered to result from the reduction of PdO into Pd, as cited in [Xu,96].

In other cases, it is considered that the effect on Schottky barrier is increased by the addition of noble metals [Vlachos,96], what is confirmed experimentally by higher resistances with the addition of Pd and Pt [Schweizer-Berberich,96]. This implies that the metal particles acted as electron sinks [Henshaw,96]. Experimentally, XPS measurements disclosed evidence of electronic interaction between SnO$_2$ and Pd or Ag particles dispersed on sensing material surface [Matsushima,88]. The shifts induced disappear on exposure to H$_2$ and are recovered on exposure to O$_2$. These results strongly suggest that the Fermi level of SnO$_2$ shifts in response to a change in oxidation states of the metal additives.

As shown, the exposed models can explain the modification of sensitivity by noble metal addition and the three are probably involved in the actual enhancement of sensitivity.

2.4.5 The role of water vapour

SGS are sensitive to water vapour, and their response to combustible gases is affected by the ambient humidity [McAleer,87]. As the adsorption and desorption of water and hydroxyl groups results in a sigmoid conductance-temperature relationship, they can give important drifts. Moreover, it should be taken into account that hydroxyl group has been experimentally observed at SnO$_2$ surfaces until 400°C –table 2.6-. Besides, ageing phenomena reported for tin oxide may be attributed to changes in water adsorption.

In fact, it is established that H_2O is adsorbed on the tin oxide surface in both molecular and hydroxyl forms [Thornton,75][Egashira,81][Pijolat,88]. In addition, Boyle *et al* [Boyle,77] demonstrates that water exhibit donor properties at adsorption in the molecular form while the hydroxyl exhibits acceptor properties.

In general, it is accepted that the humidity raises the conductivity of the tin oxide [Clifford,82][Mukode,89][Reti,95] and interferes with other gases [Martinelli,93] [Vlachos,95].

Experimentally, it is found an increase of the conductivity for CO and CH_4 after water vapour exposure [Schierbaum,91]. The sensitivities can be expressed as,

$$S = \left(\frac{p_{CO}}{p_{CO,0}} \right)^{n_{CO}} \left(\frac{p_{H_2O}}{p_{H_2O,0}} \right)^{n_{H_2O}} \tag{2.49}$$

above a partial pressure of water over 15000 ppm (what is the 50% of relative humidity in air in normal conditions) the characteristic parameter n_{CO} is constant and independent of the partial pressure of water.

The corresponding results of work functions for different partial pressures of H_2O are

$$10^{\Delta\phi/\Delta\phi_0} = 10 \left(\frac{p_{CO}}{p_{CO,0}} \right)^{n_{CO}} \left(\frac{p_{H_2O}}{p_{H_2O,0}} \right)^{n_{H_2O}} \tag{2.50}$$

in this case, the parameter n_{CO} depends on the water partial pressure for all values of it.

It is known that the surface of SnO_2 adsorbs greater quantities of water than oxygen. To explain it, some authors discussed it in terms of the displacement of chemisorbed oxygen by H_2O and OH^-, but it seems more clear a scheme as introduced by equation (2.13) [McAleer,87], where water interacts with O^-. Besides, carbon monoxide may react both with the oxygen surface state and with the state associate to hydroxyl groups. Therefore the full scheme of interaction becomes as the exposed by figure 2.36.
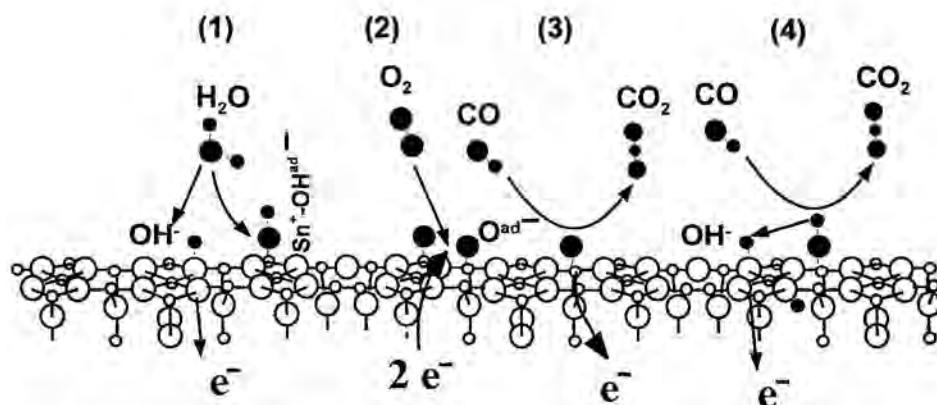
Figure 2.36. Reaction scheme in (110) SnO₂ surfaces. 1.- Dissociative reaction of water leading two hydroxyl groups. 2.- Chemisorption of oxygen as O⁻ ion. 3. Combustion of CO with this ion. 4.Combustion of CO with hydroxyl group.

It is widely accepted that molecular water will generally bond to most oxide surfaces through the attraction of its electric dipole to the ionic charges. The adsorption in nearly perfect TiO_2 (110) surfaces occurs by molecular adsorption of H_2O at five-fold co-ordinated cation sites, followed by dissociation to give OH⁻ attached by its oxygen end to the cation, and H⁺ bonded to lattice oxygen to form a second type of hydroxyl group. These results seem to be similar for SnO_2, although the experimental evidence is less extensive [Goniakowski,96] according to

$$H_2O + Sn_{lat} + O_{lat} \rightarrow (HO - Sn_{lat}) + O_{lat}H + e^-$$ (2.51)
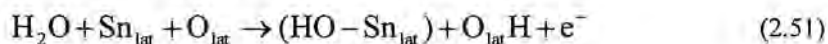
It has been shown that the dissociative reaction is the most stable, although both reactions are possible [Goniakowskik,95]. Besides, investigation of a possible reaction path for the surface dissociation of water shows the absence of any energy barrier and it was found the existence of an effective repulsive interaction between adsorbed species.

Some dynamic simulations have shows water dissociating on the TiO_2 (110) surface. The simulation ran for 1.6 ps at a temperature of 500 K for a molecule initially 3 Angstroms above the surface [Lindan,98]. In the case of tin oxide, the same author has performed some preliminary simulations where the water molecule is given a thermal (450 K) velocity directing it towards the 5-fold Sn site, and the time evolution of the system is calculated. After less than a picosecond the dissociation is complete, with two hydroxyls attached to the surface. These calculations were experimentally confirmed after the interpretation of conductive measurements in poisoned tin oxide [Williams,98b]. It was found an electrically charged oxygen site able to dissociate the water in hydroxyl group and proton and a site for molecular chemisorption of water.

Dynamic equilibrium reactions temperatures involving water can be used to avoid its related problems by means of temperature-pulsed modes of operation [Romppainen,90][Geloven,91].

From a sensor user point of view, Korotchenkov *et al* [Korotchenkov,99] have shown how the humidity can induce some maximums and complicated form hysteresis in the temperature dependency of the sensor resistance. This hysteresis is strongly reduced when heating sensors over $400^{\circ}C$; at this temperature the desorption of OH leads to higher stability.

References

By chronological order

[Brattain,53] W.H. Brattain, J. Bardeen, Bell Systems Tech. J. 32 1 (1953).

[Seiyama,62] T. Seiyama, A. Kato, K. Fujisishi, M. Nagatoni, "A new detector for gaseous components using semiconductive thin film", Anal. Chem., 34 (1962) 1052-1953.

[Taguchi,62] N. Taguchi, Japanese Patent 45-38200 (1962)

[Taguchi,70] N. Taguchi, UK patent 1280809 (1970) and US patent 3631436 (1970)

[Fonstad,71] C.G. Fonstad, R.H. Rediker, "Electrical propierties of high-quality stannic oxide crystals" , J. Appl. Phys, 42 7 (1971) 2911-2918.

[Katiyar,71] R.S. Katiyar, P. Dawson, M.M. Hargreave, G.R. Wilkinson, "Dynamics of the rutile structure III. Lattice dynamics, infrared and Raman spectra of SnO₂", J. Phys. C. 4 (1971) 2421-2431.

[Arlinghans,74] F.J. Arlinghans, J. Phys. Chem. Solids 32 (1974) 931

[Seto,75a] J.Y.W. Seto, "The electrical properties of polycristalline silicon films", J. Appl. Phys., 46 12 (1975) 5247-5254.

[Seto,75b] Reference 8 in [Seto,75a]

[Thornton,75] E. Thornton, P. Harrison, "Tin oxides: Part I, surface hydroxyl groups and the chemisorption of carbon dioxide and carbon monoxide on tin (IV) oxide", J. Chem. Soc. Faraday Trans. 71 (1975) 461-470.

[Jarzebsky,76] Z.M. Jarzebski, J.P. Marton, "Physical properties of SnO₂ materials (I,II i III)", J. Electrochem. Soc. (1976) 199C.

[Lundström,76] I. Lundström, T. Di Stefano, "Hydrogen induced interfacial polarization at Pd-SiO₂ interfaces", Surf. Sci., 59 (1976) 23-32.

[Theil,76] B. Theil, R. Heilbig, "Growth of SnO₂ single crystals by a vapour phase reaction method" J. Cryst. Growth 32 (1976) 259-264.

[Boile,77] J.F. Boyle, K.A. Jones, "The effects of water vapor and surface temperature on the conductivity of SnO₂ gas sensor", J. Electron. Mater. 6 (1977) 717-733.

[Tarng,78] M.L. Tarng, "Carrier transport in oxygen-rich polycrystalline-silicon films", J. Appl. Phys. 49 7 (1978) 4069-4079.

[Robertson,79] J. Roberston, "Electronic structure of SnO₂, GeO₂, PbO₂, TeO₂ and MgF₂", J. Phys. C: Solid State Phys., 12 (1974) 4767-4776.

[Windischmann,79] H. Windischmann, P.Mark, "A model for the operation of thin-film SnOₓ conductance modulation carbon monoxide gas sensor", J. Electrochem. Soc.: Solid-State Science and Technology 126, 4 (1979) 627-633.

[Yamazoe,79] N. Yamazoe, J. Fuchigami, M. Kishikawa, T. Seiyama, "Interactions of tin oxide surface with O₂, H₂O and H₂", Surf. Sci., 86 (1979) 335-344.

[Merle,80] P. Merle, J. Pascual, J. Camassel, H. Mathieu, "Uniaxial-stress dependence of first-order Raman spectrum of rutile: I. experiments" Physical Review B 21 4 (1980) 1617-1626.

[Schmitte,80] M. Schmitte, *Properties of SnO₂* in "Numerical data and functional relationships in science and technology". New Series III/17f. Landolt-Börnstein.

[Egashira,81] M. Egashira, M. Nakashima, S. Kawasumi, "Temperature programmed desorption study of water adsorbed on metal oxides. 2, tin oxide surfaces", J. Phys. Chem. 85 (1981) 4125-4130.

[Clifford,82] P.K. Clifford, D.T. Tuma, "Characteristics of semiconductor gas sensors I. Steady state gas response", Sensors and Actuators 3 (1982) 233-254.

[Gervais,83] F. Gervais, W. Kress, "Lattice dynamics of incipient ferroelectric rutile TiO₂", Physical Review B, 28 6 (1983) 2962-2969.

[Göpel,83] W. Göpel, G. Rocker, R. Feierabend, "Intrinsec defects of TiO₂ (110): Interaction with chemisorbed O₂, H₂, CO, and CO₂", Physical Review B, 28 6 (1983) 3427-3438.

[Munnix,83] S. Munnix, M. Schmeits, "Electronic structure of tin dioxide surfaces", Physical Review B, 27 12 (1983) 7624-7635.

[Robertson,84] J. Robertson, "Defect levels of SnO$_2$" Physical Review B, 30 6 (1984) 3520-3522.

[Gervais,85] F. Gervais, W. Kress, "Lattice dynamics of oxides with rutile structure and instabilities at metal-semiconductor phase transitions of NbO$_2$ and VO$_2$", Physical Review B, 31 8 (1985) 4809-4814.

[Göpel,85] W. Göpel, "Chemisorption and charge-transfer at ionic semiconductor surfaces: implication in designing gas sensors" Prog. Surf. Sci. 20 (1985) 9-103.

[Munnix,86] S. Munnix, M. Schmeits, "Electronic structure of point defects on oxide surfaces", Phys. Rev. B 33, 6, (1986) 4126-4144.

[Erickson,87] J. W. Erickson, S. Semancik, "Surface conductivity changes in SnO$_2$ (110): Effects of oxygen", Surface Science 187 (1987) L658-L668.

[McAleer,87] J.F. McAleer, P.T. Moseley, J.O.W. Norris, D.E. Williams, "Tin dioxide gas sensors", J.Chem.Soc., Faraday Trans. 1 (1987) 87 1323-1346.

[Munnix,87] S. Munnix, M. Schmeits, "Electronic structure of oxygen vacancies on TiO$_2$ (110) and SnO$_2$ (110) surfaces", J. Vac. Sci. Technol. A, 5 (1987) 910-913.

[Cox,88] D.F. Cox, T.B. Fryberger, S. Semancik, "Oxygen vacancies and defect electronic states on the SnO$_2$ (110)-1x1 surface", Phys. Rev. B 38 3 (1988) 2072-2083.

[Pijolat,88] C. Pijolat, R. Lalauze, "Influence of adsorbed hydroxyl species on the electrical conductance of SnO$_2$", Sensors and Actuators, 14 (1988) 27-33.

[Maier,88] J. Maier, W. Göpel, "Investigations of the bulk defect chemistry of polycrystalline tin (IV) oxide", Journal of Solid State Chemistry 72 (1988) 293-302.

[Matsushima,88] S. Matsushima, Y. Teraoka, N. Miura, N. Yamazoe, "Electronic interaction between metal additives and tin dioxide-based gas sensors", Japanese Journal of Applied Physics, 27 10 (1988) 1798-1802.

[Romppainen,88] P. Romppainen, V. Lantto, "The effect of microstructure on the height of potential energy barriers in porous tin dioxide gas sensors", J. Appl. Phys. 63 10 (1988) 5159-5165.

[Fryberger,89] T.B. Fryberger, J.W. Erickson, S. Semancik, "Chemical and electronic properties of Pd/SnO_2 (110) model gas sensors", Surface and interface analysis, 14 (1989) 83-89.

[Cox,89] D.F. Cox, T.B. Fryberger, S. Semancik, "Surface reconstructions of oxygen deficient SnO_2 (110)", Surface Science 224 (1989) 121-142.

[Lee,89] D.D. Lee, W.Y. Chung, "Gas-sensing characteristics of SnO_{2-x} thin films with added Pt fabricated by the dipping method", Sensors and Actuators, 20 (1989) 301-305.

[Matsushima,89] S. Matsushima, J. Tamaki, N. Miura, N. Yamazoe, "TEM observation of the dispersion state of Pd on SnO_2", Chem. Lett. (1989) 1651-1654.

[Mukode,89] S. Mukode, H. Futata, "A semiconductor humidity sensor", Sensors and Actuators, 16 (1989) 1-11.

[Jain,90] V. Jain, A. H. Harker, A. M. Stoneham, D.E. Williams, "Effect of the electrode geometry on sensor response", Sensors and actuators B, 2 (1990) 111-114.

[Kohl,90] D. Kohl, "The role of noble metals in the chemistry of solid-state gas sensors", Sensors and actuators B, 1 (1990) 158-165.

[Romppainen,90] P. Romppainen, V. Lantto, S. Leppävuori, "Effects of water vapour on the CO response behaviour of tin dioxide sensors in constant temperature and temperature –pulsed modes of operation", Sensors and Actuators B, 1 (1990) 73-78.

[Semancik,90] S. Semancik, F.B. Fryberger, "Model studies of SnO_2 based gas sensors: vacancy deffects and Pd additive effects", Sensors and actuators B, 1 (1990) 97-102.

[Geloven,91] P. Van Geloven, M. Honore, J. Roggen, S. Leppävuori, T. Rantala, "The influence of relative humidity on the response of tin oxide gas sensors to carbon monoxide", Sensors and Actuators B, 4 (1991) 185-188.

[Göpel,91] W. Göpel "Chemical sensor technologies: empirical art and systematic research", in *Sensors: A comprehensive survey* vol.2: "Chemical and Biochemical Sensors", VCH, Weinheim FRG (1991), pg 114.

[Lantto,91] V. Lantto, T. S. Rantala "Equilibrium and non-equilibrium conductance response of sintered SnO₂ samples to CO" Sensors and actuators B, 5 (1991) 103-108.

[Schierbaum,91] K.D. Schierbaum, U. Weimar, W. Göpel, R. Kowalkowski, "Conductance, work function and catalytic activity of SnO₂-based gas sensors", Sensors and Actuators B, 3 (1991) 205-214.

[Semancik,91] S. Semancik, R.E. Cavicchi, "The growth of thin, epitaxial SnO₂ films for gas sensing applications", thin solid films, 206 (1991) 81-87.

[Xu,91] Ch. Xu, J. Tamaki, N. Miura,N. Yamazoe, "Grain size effects on gas sentitivity of porous SnO₂-based elements", Sensors and Actuators B, 3 (1991) 147-155.

[Azad,92] A.M. Azad, S.A. Akbar, S.G. Mhaisalkar, L.D. Birkerfeld, K.S. Goto, "Solid-state gas sensors: a review", J. Electrocem. Soc, Vol 139, No 12, (1992), 3690-3704.

[Kohl,92] D. Kohl, "Oxidic semiconductor gas sensors", in *Gas Sensors*, G. Sberveglieri (ed.), Kluwer, Dordrecht, 1992.

[Moseley,92] P.T. Moseley, "Materials selection for semiconductor gas sensors", Sensors and Actuators B, 6 (1992) 149-156.

[Musci,92] M. Musci, M. Notaro, F. Curcio, M.C. Casale, G. De Michele, "Laser synthesis of vanadium-titanium oxide catalysts", J.Mater. Res. 7 (1992) 2846-2852.

[Sberveglieri,92] G. Sberveglieri, "Classical and novel techniques for the preparation of SnO₂ thin-film gas sensors", Sensors and Actuators B, 6 (1992) 239-247.

[Ul,92] Underwriters Laboratories Inc, "Simple and multiple station carbon monoxide detectors", US (1992).

[Zhang,92] S. Zhang, Y.F. Zhu, D.E. Brodie, "Photoconducting TiO_2 prepared by spray pyrolysis using $TiCl_4$", Thin Solid Films, 213 (1992) 265-270.

[Bârsan,93] S. Zhang, Y.F. Zhu, D.E. Brodie, "The mechanism of the interaction between CO and CH_4 in SnO_2 surface: the role of water vapour", Sensors and Actuators B, 12 (1993) 71-75.

[Labeau,93a] M. Labeau, B. Gautheron, F. Cellier, M. Vallet-Regi, E. García, J.M. González-Calbet, "Pt nanoparticles dispersed on SnO_2 thin films: a microstructural study", J. Sol. Stat. Chem., 102 (1993) 434-439.

[Labeau,93b] M. Labeau, B. Gautheron, G. Delabouglise, J. Peña, V. Ragel, A. Varela, J. Román, J. Martinez, J.M. González-Calbet, M. Vallet-Regi, "Synthesis, structure and gas sensitivity properties of pure and doped SnO_2", Sensors and Actuators B, 15-16 (1983) 379-383

[Fukui,93] K. Fukui, M. Nakane, "Effects of tin oxide semiconductor-electrode interface on gas sensitivity characteristics", Sensors and Actuators B, 13-14 (1993) 589-590.

[Martinelli,93] G. Martinelli, M.C. Carotta, "Influence of additives on the sensing properties of screen-printed SnO_2 gas sensors", Sensors and Actuators B, 3 (1991) 205-214.

[Mizsei,93] J. Miszei, "Activating technology of SnO_2 layers by metal particles from ultrathin metal ions", Sensors and actuators B, 15-16 (1993) 328-333.

[Ital,93] Normativa Italiana, "Requisiti generali per i revelatori di gas d'uso domestico o similare", (1993).

[Shimizu,93] Y. Shimizu, Y. Nakamura, M. Egashira, "Effects of diffussivity of hidrogen and oxygen through pores of thick film SnO_2-based sensor on their sensing properties", Sensor and Actuators B, 13-14 (1993) 128-131.

[Sulz,93] G. Sulz, G. Külner, H. Reiter, G. Uptmoor, W. Schweizer, H. Löw, M. Lacher, K. Steiner, "Ni, In and Sb implanted Pt and V catalysed thin-film SnO$_2$ gas sensors", Sensors and Actuators B, 15-16 (1993) 390-395.

[Wu,93] Q. Wu, K.M. Lee, C.C. Liu, "Development of chemical sensors using microfabrication and micromachining techniques", Sensors and Actuators B, 13-14 (1993) 1-6.

[Ylinampa,93] A. Ylinampa, V. Lantto, S. Leppävuori, "Some differences between Au and Pt electrodes in SnO$_2$ thick-film gas sensors", Sensors and Actuators B, 13-14 (1993) 602-604.

[Aste,94] T. Aste, D. Berutto, R. Botler, L. Ciccarelli, M. Giordani, P. Pozzolini, "Microstructural development during the oxidation process in SnO$_2$ thin films for gas sensors", Sensors and Actuators B, 18-19 (1994) 637-641.

[Bârsan,94] N. Bârsan, "Conduction models in gas-sensing SnO$_2$ layers: grain size effects and ambient atmosphere influence", Sensors and Actuators B, 17 (1994) 241-246.

[Göpel,94] W. Göpel, "New materials and transducers for chemical sensors", Sensors and Actuators B, 18-19 (1994) 1-21.

[Gordillo,94] C. Gordillo, L.C. Moreno, W. de la Cruz, P. Teheran, "Preparation and characterization of SnO$_2$ thin films deposited by spray pyrolysis from SnCl$_2$ and SnCl$_4$ precursors", Thin Solid Films 252 (1994) 61-66.

[Lenaerts,94] S. Lenaerts, J. Roggen, G. Maes, "FT-IR charactererisation of tin dioxide gas sensors materials under working conditions", Spectrochimica Acta, 51 (1994) 883-893.

[Matsuhata,94] H. Matsuhata, J. Ej¢nne, J. Taft¢, "A study of the structure factors in rutil-type SnO$_2$ by high-energy electron diffraction", Acta Cryst. A50 (1994) 115-123.

[Orel,94] B. Orel, U. Laurenčič-Štangar, Z. Crnjak-Orel, P. Bukovec, M.Kosec, "Structural and FTIR spectroscopic studies of gel-xerogel-oxide transitions of

SnO$_2$ and SnO$_2$:Sb powders and dip-coated films prepared via inorganic sol-gel route", J. of non-crystalline solids 167 (1994) 272-288.

[Rantala,94] T.S. Rantala, V. Lantto, T.T. Rantala, "A cluster approach for the SnO$_2$ (110) face", Sensors and Actuators B, 18-19 (1994) 716-719.

[Westbrook,94] M.H. westbrook, J.D. Turner, "Automotive Sensors", Institute of Physics Publishing, Bristol and Filadelfia, 1994.

[Chen,95] Q. Chen, Y. Qian, Z. Chen, G. Zhou, Y. Zhang, "Fabrication of ultrafine SnO$_2$ thin films by the hydrothermal method", Thin solid films 264 (1995) 25-27.

[Göpel,95] W. Göpel, K.D. Schierbaum, "SnO$_2$ sensors: curent status and future prospects", Sensors and Actuators B 26-27 (1995) 1-12.

[Ingrisch,95] K. Ingrisch et al. "Chemical sensors for CO/NO detection in automotive climate control systems" SAE technical paper series, 960692 (1995)

[Ionescu,95] R. Ionescu, A. Vancu, "Polarization effects in SnO$_2$ thick-film sintered sensors", Phys. Stat. Sol. A, 151 (1995) 135-142.

[Kövér,95] L. Kövér, G. Moretti, Zs. Kovács, R. Sanjinés, I. Cserny, G. Margaritondo, J. Pálinkás, H. Adachi, "High resolution photoemission and Auger parameter studies of electronic structures of tin oxides", J. Vac. Sci. Technol. A, 13 3 (1995) 1382-1388.

[Ocampo,95] E. Ocampo, R. Arce, R. Koropeski, R. Buitrago, "Effects of the carrier gas on properties of SnO$_2$ deposited by pyrolysis", Solar Energy Materials and Solar Cells 36 (1995) 327-337.

[Papadopoulos,95] C.A. Papadopoulos, J.N. Avaritsiotis, "A model for the gas sensing properties of tin oxide thin films with surface catalysts", Sensors and actuators B, 28 (1995) 201-210.

[Rantala,95] T.S. Rantala, V. Golovanov, V. Lantto, "A cluster approach for the adsorption of oxygen and carbon monoxide on SnO$_2$ and CdS surface", Sensors and Actuators B, 24-25 (1995) 532-536.

[Reti,95] F. Reti, E. B. Varhegyi, I. V. Perczel, J. Giber, M. Fleischer, J. Gerblinger, U. Lampe, H. Meixner, "Comparison of the water effect on the resistence of different semiconducting metal oxides", Sensors and Actuators B, 26-27 (1995) 103-107.

[Schierbaum,95] K.D. Schierbaum, "Engineering of oxide surfaces and metal/oxide interfaces for chemical sensors: recent trends", Sensors and actuators 24-25 (1995) 239-247.

[Smith,95] A. Smith, J.M. Laurent, D.S. Smith, J.P. Bonnet, R. Clemente, "Relation between solution chemistry and morphology of SnO$_2$ based thin films deposited by a pyrosol process", Thin Solid Films 266 (1995) 20-30.

[Sberveglieri,95] G. Sberveglieri, "Recent developments in semiconducting thin-film gas sensors", Sensors and Actuators B 23 (1995) 103-109.

[Vlachos,95] D.S. Vlachos, P.D. Skafidas, J.N. Avaritsiotis, "The effect of humidity on tin oxide thick-film gas sensors in the presence of reducing and combustible gases", Sensors and Actuators B, 24-25 (1995) 491-494.

[Voshchilova,95] R. Voshchilova, D. Dimitrov, N. Dolotov, A. Kuz'min, A. Makhin, V. Moshnikov, Y. Tairov, "Forming the structure of gas sensitive layers of tin dioxide produced by reactive magnetron sputtering", Semiconductors 29 11 (1995) 1036-1039.

[Williams,95] D.E. Williams, G.S. Henshaw, K.F.E. Pratt, R. Peat, "Reaction-diffusion effects and systematic design of gas-sensitive resistors based on semiconductor oxides", J. Chem. Soc. Faraday Trans. 91 23 (1995) 4299-4307.

[BS,96] Technical Commitee EEL/31 "Specification for carbon monoxide detectors (electrical) for domestic use2, BS 7860:1996, British Standard (1996).

[Correa-Lonzano,96] B. Correa-Lozano, Ch. Comninellis,A. De Battisti, "Physicochemical properties of SnO$_2$-Sb$_2$O$_5$ films prepared by the spray pyrolysis technique", J. Electrochem. Soc. Vol 143 1 (1996) 203-209.

[Diéguez,96] A. Diéguez, A. Romano-Rodríguez, J.R. Morante, U. Weimar, M.Schweizer-Berberich, W.Göpel, "Morphological analysis of nanocrystalline SnO$_2$ for gas sensors", Sensors and Actuators B 31 (1996) 1-8.

[Foglietti,96] V. Foglietti, A. Galbato, A. Beazotti, A. Galloppa, D. Maltese, "Improved spray-pyrolysis deposition system for polycrystalline conductive SnO$_2$ thin films", M R S Symposium Proceedings 403 (1996) 435-440.

[Goniakowski,96] J. Goniakowski, M.J. Gillan, "The adsorption of H$_2$O on TiO$_2$ and SnO$_2$ (110) studied by first-principles calculations", Surface Science 350 (1996) 145-158.

[Göpel,96] W. Göpel,G. Reinhardt, "Metal oxide sensors: New devices through tailoring interfaces on the atomic scale", from Sensors Update vol. 1, H. Baltes, W. Göpel, J. Hesse (Eds), Weinheim, 1996.

[Henshaw,96] G.S. Henshaw, R. Ridley, D.E. Williams, "Room-temperature response of platinised tin dioxide gas-sensitive resistors", J. Chem. Soc., Faraday Trans. 92 18 (1996) 3411-3417.

[Ionescu,96] R. Ionescu, "Diode like SnO$_2$ gas detection devices", Proceedings of Eurosensors X, Leuven (1996).

[Lundström,96] I. Lundström, "Approaches and mechanisms to solid state based sensing", Sensors and Actuators B 35-36 (1996) 11-19.

[Schweizer-Berberich,96] M. Schweizer-Berberich, J.G. Zheng, U. Weimar, W. Göpel, N. Bârsan, E. Pentia and A. Tomescu, "The effect of Pt and Pd surface doping on the response of nanocrystalline tin dioxide gas sensors to CO", Sensors and Actuators B, 31 (1996) 71-75.

[Vlachos,96] D.S. Vlachos, C.A. Papadopoulos, J.N. Avaritsiotis, "On he electronic interaction between additives and semiconducting oxide gas sensors", Appl. Phys. Lett. 69 5 (1996) 650-652.

[Xu,96] C.N. Xu, J. Tamaki, N. Miura, N. Yamazoe, "Nature of sensitivity promotion in Pd-loaded SnO$_2$ gas sensors", J. Electrochem. Soc, 143 7 (1996) L148-L150.

[Bauer,97] M. Bauer, N. Bârsan, K. Ingrisch, A. Zeppenfeld, I. Denk, B. Schuman, U. Weimar, W. Göpel, "Influence of measuring voltage, geometry and electrodes on the characteristics of thick film SnO₂ gas sensors" Proceedings of 11th European Microelectronics Conference (1997) 37-44.

[Cenelec,97a] Comision Europeenne pour la Normalisation Electrique, Technical Commitee TC 116, "Electrical apparatus for the detection of combustible gases in domestic premises", pr50194, final draft, European Standard (1997)

[Cenelec,97b] Comision Europeenne pour la Normalisation Electrique, Technical Commitee TC 116, "Electrical apparatus for the detection of carbon monoxide in domestic premises", pr50291, final draft, European Standard (1997)

[Fleischer,97] M. Fleischer, H. Meixner, "Fast gas sensors based on metal oxides which are stable at high temperatures", Sensors and actuators B, 43 (1997) 1-10.

[Galdikas,97] A. Galdikas, S. Ka☐iulis, a. Mironos, A. Šetkus, "Gas induced resistance response in ultra-thin metal films covered with non-conductive layers", Sensors and Actuators B, 43 (1997) 186-192.

[Göpel,97] W. Göpel, K.D. Schierbaum, "Chemical Sensor based on catalytic reactions" in *Handbook of heterogeneous catalysis* E. Ertl, H. Knözinger, J. Weitkamp (Eds.), VCH, Weinheim, (1997) pgs 1283-1310.

[Harris,97] N. Harris, M. Koch, S. Beeby, N. White, A. Evans, "Thick-film printing of PZT onto silicon for micromechanical applications", Mat Lett, 31 (1997) 109-112.

[Hausner,97] M. Hausner, C. Hillebrecht, H. Karagözoglu, J. Zacheja, J. Binder, "On-chip redundant measurement principles realized by a silicon sensor substrate", J. Micromech. Microeng. 7 (1997) 259-262.

[Kappler,97] J. Kappler, "Herstellung von Halbleitergassensoren durch Sol-Gel Technologie auf Dickschicht basis", Research Thesis (*Diplomarbeit*) at the University of Tübingen (1997).

[Llobet,97] E. Llobet, X. Vilanova, J. Brezmes, R. Alcubilla, J. Calderer, J.E. Sueiras, X. Correig, "Conductance transient analysis of thick-film tin oxide gas sensors under successive gas injection steps", Meas. Sci. Technol., 8 10 (1997) 1133-1138.

[Sangaletti,97] L. Sangaletti, L.E. Depero, A. Dieguez, G. Marca, J. R. Morante, A. Romano-Rodriguez, G. Sberveglieri, "Microstructure and morphology of tin dioxide multilayer thin film gas sensors", Sensors and Actuators B, 44 (1997) 268-274.

[Yu,97] K.N. Yu, Y.Xiong, Y. Liu, C.Xiong, "Microestructural change of nano-SnO₂ grain assemblages with the annealing temperature", Physical Review B, 55, 4 (1997) 2666-2671.

[Abello,98] L. Abello, B. Bochu, A. Gaskov, S. Koudryavtseva, G.Lucazeau, M. Roumyantseva, "Structural characterisation of nanocrystalline SnO₂ by X-ray and Raman spectroscopy", J. Solid State Chem., 135 (1998) 75-85.

[Atashbar,98] M.Z. Atashbar, H.T. Sun, B. Gong, W. Wlodarski, R. Lamb, "XPS study of Nb-doped oxygen sensing TiO₂ thin films prepared by sol-gel method", Thin Solid Films, 326 (1998) 238-244.

[Lindan,98] P. J. D.Lindan, N. M. Harrison, M. J. Gillan, "Mixed dissociative and molecular adsorption of water on the rutile (110) surface", Phys. Rev. Lett., 80 (1998) 762-765. Simulations about the dissociation of water in tin and titanium (110) surfaces are available as mpeg files at the site http://www.dl.ac.uk/TCSC/MatSci/Projects/Surface_Chemistry/tio2.html

[Llobet,98] E. Llobet, X. Vilanova, J. Brezmes, J.E. Sueiras, R. Alcubilla, X. Correig, "Model for the steady-state and transient behaviour of thick-film tin oxide gas sensors in the presence of gas mixtures", J. Electrochem. Soc., 145 5 (1998) 1772-1778.

[Nelli,98] P. Nelli, E. Cereda, G. Gabetta, A. Dieguez, A. Romano-Rodriguez, S. Groppelli, J.R. Morante, G. Sberveglieri, "Electrical and structural

characterization of long term ageing effect on SnO$_2$-Au thin films sensors", proceedings of Eurosensors XII (1998) 629-632.

[Ortega,98] A. Ortega, "Sistema de test para sensores de gas", Research thesis (*treball d'investigació de 3er cicle*) at the University of Barcelona (1998).

[Schmidt,98] "Sol-Gel production", Ed. H. Schmidt, Trans. Tech. Pub., Zurich 1998.

[Sheng,98] L.Y. Sheng, Z. Tang, J. Wu, P.C.H. Chan, J.K.O. Sin, "A low-power CMOS compatible integrated gas sensor using maskless tin oxide sputtering", Sensors and Actuators B 49 (1998) 81-87.

[Shimizu,98] Y. Shimizu, T. Maekawa, Y. Nakamura, M. Egashira, "Effects of diffusivity and reactivity on sensing properties of thick film SnO$_2$-based sensors", Sensors and Actuators B 46 (1998) 163-168.

[Tomchenko,98] A.A. Tomchenko, V.V. Khatko, I.L. Emelianov, "WO$_3$ thick-film gas sensors", Sensors and Actuators B, 46 (1998) 8-14.

[Vilanova,98a] X. Vilanova, E. Llobet, J. Brezmes, J. Calderer, X. Correig, "Numerical simulation of the electrode geometry and position effect on semiconductor gas sensor response" Sensors and Actuators B 48 1-3 (1998) 426-432.

[Vilanova,98b] J. Vilanova, "Estratègies per a l'increment de selectivitat dels sensors de gasos basats en òxids semiconductors. Caracterització dinàmica de la resposta d'estructures multielectròdiques", PhD thesis at the University Politècnica de Barcelona (2000).

[Williams,98a] D.E. Williams, "Semiconducting Oxide Gas Sensors: Past and Future", invited conference at EurosensorsXII, Southampton (1998). The digest of the conference is found in: D.E. Williams, "Semiconducting oxides as gas-sensitive resistors", Sensors and Actuators B 57 (1999) 1-16.

[Williams,98b] D.E. Williams, K. F. E. Pratt, "Classification of reactive sites on the surface of polycrystalline tin dioxide", J. Chem. Soc. Faraday Trans., 94 (1998) 3493-3500.

[Gutierrez,98] Influence of the thin film thickness on the methane gas sensor selectivity, A.M. Gutierrez, J.A. Díez de Ulzurrun, S. M. Olaizola, E. Terrón., G. García, E. Castaño, F. J.Gracia, Proceedings of Sensor 99, Nüremberg 1999.

[Bârsan,99] N. Bârsan, J.R. Stetter, M. Findlay, W. Göpel, "High-performance gas sensing of CO: comparative test for semiconducting (SnO_2-based) and for amperiometric gas sensors" Anal. Chem. 71 (1999) 2512-2517.

[Blaustein,99] G. Blaustein, M.S. Castro, C.M. Aldao, "Influence of frozen distributions of oxygen vacancies on tin oxide conductance", Sensors and Actuators B, 55 (1999) 33-37.

[Briand,99] D.Briand, B. Schodt, N.F. Rooij, A. Krauss, U. Weimar, N. Bârsan, W. Göpel, "High temperature microhotplates for drop coated gas sensors" Proceedings of Eurosensors XIII (1999) pg. 357-358.

[Cirera,99] A. Cirera, A. Diéguez, R. Diaz, A. Cornet, J.R. Morante, "New method to obtain stable small-sized SnO_2 powders for gas sensors", Sensors and Actuators B, 58 (1999) 360-364.

[Diéguez,99a] A. Diéguez, "Structural analysis for the improvement of SnO_2-based gas sensors", PhD thesis at the University of Barcelona (1999).

[Korotchenkov,99] G. Korotchenkov, V. Brynzari, S. Dmitriev, "Electrical behavior of SnO_2 thin films in humid atmosphere", Sensors and Actuators B 54 (1999) 197-201.

[Shimizu,99] Y. Shimizu, M. Egashira, "Basic Aspects and Challenges of semiconductor gas sensors", MRS bulletin, 24 6 (1999) 18-24.

[Williams,99] G. Williams, G.S. Coles, "The gas-sensing potential of nanocrystalline tin dioxide produced by a laser ablation technique", MRS Bulletin 26 4 (1999) 25-29.

[Cabot,00] A. Cabot, "Additive effects on tin oxide nanopowders for gas sensing applications", Research thesis (treball d'investigació de 3er cicle) at the University of Barcelona (2000).

[Cirera,00] A. Cirera, A. Diéguez, R. Diaz, A. Cornet, J.R. Morante, "Microwave processing for low cost and mass production of undoped and in-situ catalytic doped nanosized SnO$_2$ gas sensor powders", Sensors and Actuators B, 64 (2000) 65-69.

[Capteurs,00] Capteur gas sensor company, Gas Sensor catalogue and technical information (Capteur Sensors Ltd). Information available at http://www.capteur.co.uk/.

[Figaro,00] Figaro gas sensor company, Gas Sensor catalogue and technical information (Figaro and Figaro USA Inc). Information available at www.figarosensor.com

[Fis,00] Fis gas sensor company, Gas Sensor catalogue and technical information (Fis Inc.). Information available at www.fisinc.co.jp

[Jiménez,00] I. Jiménez, A. Cirera, O. López, A. Cornet, J.R. Morante, "Innovative method of pulverization coating of previously stabilised nanopowders for mass production of gas sensors", Proceedings of Eurosensors XIV (2000) 69-70

[Llobet,00] E. Llobet, G. Molas, P. Molinàs, J. Calderer, X. Vilanova, J. Brezmes, J.E. Sueiras, X. Correig, "Fabrication of highly selective tugsten oxide amonia sensors", J. of the electrochemical society 147 2 (2000) 776-779.

[Mics,00] Mics gas sensor company, Gas Sensor catalogue and technical information (MicroChemical Systems SA). Information available at www.microchemical.com

[NIOSH,00] US National Institute for Occupational Safety & Health. Information available in http://www.cdc.gov/niosh/81-123.html

[OSHA,00] US Department of Labour, Occupational Safety & Health Administration, information available in http://www.osha.gov/

[UK,00] UK National Air Quality Strategy Department of the Environment, Transport and the Regions. Information available in http://www.environment.detr.gov.uk/airq/aqinfo.htm

[WHO,00]   World   Health   Organisation.   Information   available   in http://www.who.int/peh/air/Airqualitygd.htm.

3. Technology and
test systems in SGS

The present chapter is devoted to the technological aspects of this thesis. As SGS become a relative new subject of research, technologies are not well established and have high influence on device response.

Therefore, this leak of technological background impelled our group to develop some new techniques or technologies, devoted either to the obtaining of basic material (such as liquid pyrolysis [Cirera,99] or microwave treatments [Cirera,00a]) either to the implementation of sensing layers on appropiate substrate (microprinting [Cerdà,00] and pulverisation coating [Jiménez,00]). As the obtaining of sensing material requires the optimisation of technological parameters by means of the analysis of the influence of these parameters on the structural properties, a detailed description of the obtaining technological steps as well the corresponding characterisation will be done in the next chapter.

Hence, we will introduce in this chapter the description of the novel and standard technologies for the development of gas sensors.

Once sensor devices are obtained, they have to be measured by means of gas test to show their reliability. Different test stations were made and its description is also given.

In the case of material characterisation, I will not give more information than the technical parameters of measurements that one can found in annex I. A full description of the characterisation techniques and the instruments can be found in [Diéguez,99].

3.1 Standard procedure for powder processing

As shown in the former chapter, when making a SGS, there are two approximations. It is possible to obtain the powders of the sensing material (in our case SnO_2) by means of a chemical wet route and implement it on a substrate with electrodes and heater. Other way consists in the deposition of the material directly on the substrate while this material is forming. In this case, sputter technology can be used.

The first approximation was developed in the group EME[1] and the second one in the group CEIT[2], in the context of a CICYT[3] project.

Although there is no established technology for powder procedure, it is commonly accepted that different treatments or steps should be applied on the powders to increase their sensitivity, selectivity and stability.

Once the sensing material powders are obtained, they can exhibit important structural shift under high working temperature, therefore a thermal stabilisation treatment is required to avoid these problems.

But this annealing leads to an agglomerated material with necks between grains –as those schematised in figure 2.29-. This low degree of porosity is bad for the necessary diffusion of gas molecules through the sensing layer. Consequently, a treatment able to increase the porosity of the layer, such as grinding, is appreciated.

---

[1] EME: Enginyeria i Materials Electronics –*Electronic Materials and Engineering*- research laboratory of the Departament d'Electrònica –*Electronics Department*- of the Universitat de Barcelona –*University of Barcelona*-.

[2] CEIT: Centro de Estudios e Investigaciones Técnicas de Guipuzcoa –*Centre for Technical Studies and Research of Guipuzcoa* in San Sebastian.

[3] Spanish CICYT project MAT96-1030-CO2-01.

Finally, the implementation of such powders on a substrate to get the final gas sensor is made by means of printing, because until now that is the easier but reproducible technique for sensing applications.

These three steps —thermal stabilisation, grinding and printing-, together with the obtaining method of the sensing powder, define the main process of the SGS production run.

In our case, the production run is schematised in figure 3.1. The steps are followed in the same order as presented above and were designed following the known art in the main European laboratories [Kappler,97]. The main characteristics of them are presented below.

✔ Obtaining of nanophase sensing material

⬇

✔ Thermal Stabilisation

⬇

✔ Grinding

⬇

✔ Paste preparation

⬇

✔ Implementation

⬇

✔ Firing

⬇

✔ Test

3.1.1 Thermal stabilisation
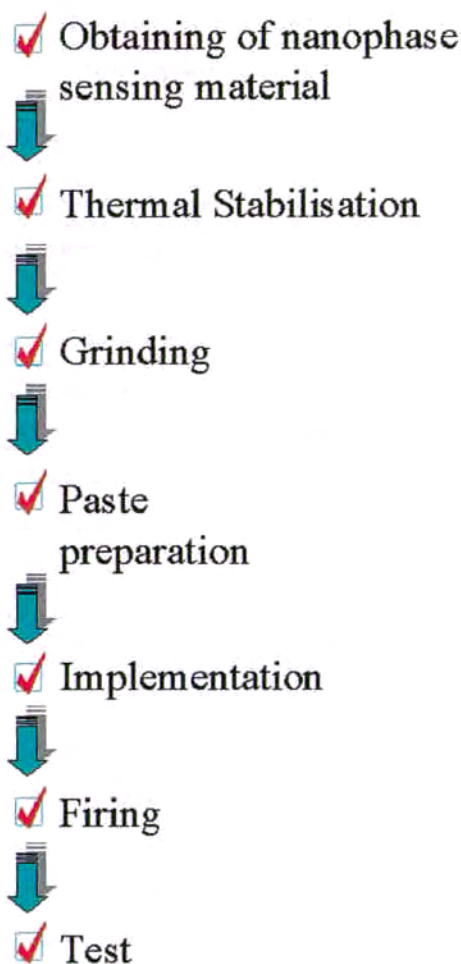
Figure 3.1. Standard procedure for powder processing in SGS

As it will be shown, from a point of view of material microstructure, the thermal stabilisation —also called calcination or annealing- becomes the most affecting process.

Usually, when the material is obtained, it exhibits a set of physic characteristics that are very far from the thermodynamic equilibrium. Besides, depending on the

obtaining procedure, the material also presents rests of chemical species, such as chlorides. But, together with the influence of these two factors, it should be considered that if the sensing material contains the metal additives, these would undergo the thermal effects.

In general, the usual recipe for stabilisation consists in applying thermal treatments over the working temperature that will be used in the sensor. Nevertheless let me give a few considerations about all the previous influencing factors applied to the case of tin oxide.

The main physical difference that can exhibit the material without annealing with respect a stabilised material consists in that the former can be not SnO_2, but a non-stoichimetric tin oxide, or even metallic tin or $Sn(OH)_4$. All these products are very unstable over $150°C$ and therefore oxidising annealing is required. Once reached the stoichiometry in tin oxide, surface and bulk properties as well as grain growth should be stabilised. To overcome this first problem, it should be taken into account that, despite results obtained from measurement with structural techniques (XRD, DTA) suggest a crystallisation temperature of about $400°C$ [Cao,96], there is no common acceptation of this value.

Bulk physical properties should be beard in mind. Experimental work has reported the existence of important lattice distortions in nanocrystalline tin oxide [Yu,97]. The origin of these distortions has been related to oxygen vacancies in the bulk, interface properties between grains or residual OH groups; I will focus in the next chapter about the actual origin of these distortions. For a practical use, the distortions vanish when higher treatments are applied. Therefore its existence can be in the origin of important drifts in the microstructure of the sensing material and, consequently, in device behaviour. We showed how the actual mechanism by which the distortions vanish not only depends on the temperature but also on the thermal energy that the sample undergo [Cirera,00b]. This implies that a thermal treatment of $700°C$ during half an hour can be equivalent to other $500°C$ during 10 hours.

Other physical effect consists in the expected growth of the nanoparticles during heating. Experimentally it has been found that the growth strongly increases at temperatures above 450°C during 8 hours and in the case of treatments about 1000°C the nanometric range is loss leading particles between 100 and 200 nm [Diéguez,96a] [Cabot,00]. Therefore 1000°C should be considered the maximum temperature that the nanocrystals should undergo in order to keep the nanometric range.

Since surface becomes the transducer of gas reactions for sensing mechanism, changes in the atomic arrangement, such as faceting or reconstruction during working life, should be avoided. In general this is the most difficult effect to control due to the intrinsic complexity of the physics involved on, and the scientist usually renounce to it.

But from a chemical point of view, the surface of tin oxide becomes a source of chemisorbed compounds due to its high reactivity. These compounds can be remaining molecules or ions from the chemical route for material obtaining, such as chlorides and ammonia. In the case of chlorides, it is known that treatments of more than 550°C during 8 hours are required for its evaporation, but even after this treatment, they could be found on the sensing surface.

Other related species like hydroxyl can be hardly bounded at surface. An evidence of this bonding strength is that while water stars desorption of tin oxide at 280°C, hydroxyl groups are observed on surface until 400°C [McAleer,87]. In fact hydroxyls are not considered as contamination, nevertheless they occupy sites for sensing reaction. Besides, the distribution of surface charges can be changed, thus the surface bending of electronic energy bands is influenced.

Moreover, the effects on the thermal treatment on the metal additives should be taken into account due to the sensitisation effects on the sensor as consequence of its introduction. First it should be considered in which process the additives are added to the sensing material. The main difference consists in if they are added before (*in-situ*) or after (*ex-situ*) the powder stabilisation. These differences have been studied for sol-gel

tin oxide production technology [Diéguez,99b][Cabot,00]. In our case I will focus on *in-situ* addition, as I will show in the next chapter. Of course, the precursor substance of the metal as well as the addition method becomes a technological parameter for the actual thermal effects on additives.

The additives, usually palladium and platinum, can exhibit a wide variety of thermal effects. But, considering its smaller size and concentration its study becomes more difficult than tin oxide thermal effects.

The first effect of the temperature on the additive consists on the chemical reaction that the precursor of the additive undergoes. If the precursor is a chloride of the metal, such as $PdCl_2$ or $(NH_4)_2PtCl_4$, the molecule should decompose. This leads to the production of chloride species that can be attached at the sensing surface, as exposed above. But it is known that the evaporation of chloride can drag metal atoms. This fact reduces the efficiency of metal addition.

At the beginning, the remaining additive is a non-metallic state. When temperature is applied, it is expected that the non-metallic state transforms into metallic state. The temperature at which metallic states are predominant depends on the element. In our case, Pd^{2+} is found from $400°C$ (forming PdO) whereas Pt^{4+} will keep until $800°C$.

During this process, other aspects (diffusivity, reactivity) have to be taken into account. In some cases, big clusters, showing low reactivity to the gas, can be formed. As example, a big Pt cluster formed on
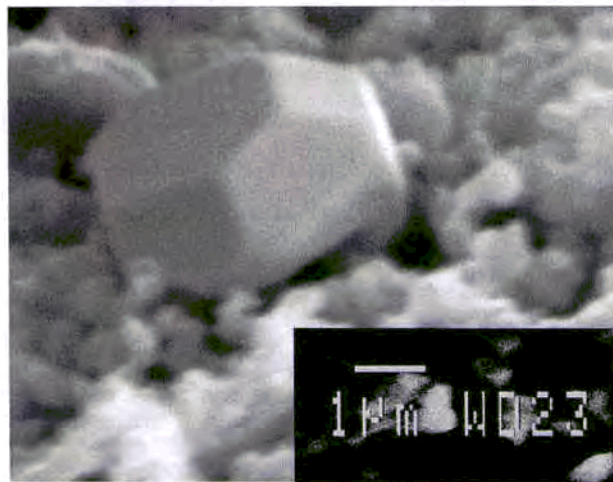
Figure 3.2. Platinum metallic cluster in cubododedrical structure.

metallic oxide is shown in figure 3.2.

Other cases, like palladium additive in tin oxide, the formation of such great clusters is not expected due to the stability of the PdO chemical state, nevertheless it can diffuse inside the tin oxide nanoparticle and change its microestructural properties.

As will be shown in the next chapter, temperatures over $450^{\circ}C$ are required to remove rests of chemical reactions and to stabilise the bulk properties. At these temperatures, the additives do not still transform the chemical state. This temperature should be kept during several hours to avoid the lattice distortions present in as-obtained material.

But higher temperatures than $800^{\circ}C$ become negative since larger grain size are produced. This coalescence can be induced in the additives too. Therefore this temperature constitute a limit for maximum temperature annealing.

For our applications in tin oxide stabilisation, the physic and chemistry of the above phenomena were considered, as shown in the next chapter. For the annealing, a muffle furnace Carbolite 1100 with Eurotherm PID temperature controller was used. Alumina crucibles with perforated lids (from Alfa Aesar) were used.

To avoid contamination, these crucibles were cleaned following steps of, first, washing with deionised water (Millipore Elix); second, ultrasounds cleaning in deionised water; three, washing with double deionised water (Millipore Simplicity); four, drying at $70^{\circ}C$ during several hours; five, cure annealing of the empty crucible at $1000^{\circ}C$ during 2 hours; five, washing with double deionised water; six, drying. Finally the crucibles are always kept in a desiccating box to avoid both contamination and the adsorption of water in the walls of crucibles.

3.1.2 Grinding

During the thermal stabilisation of the nanoparticles, the different growth mechanisms (nucleation, coalescence and Ostwald ripening) are thermally activated. As consequence, matter between adjacent grains should form necks. Besides, the compacticity of the powder will rise. Both effects are not desired.
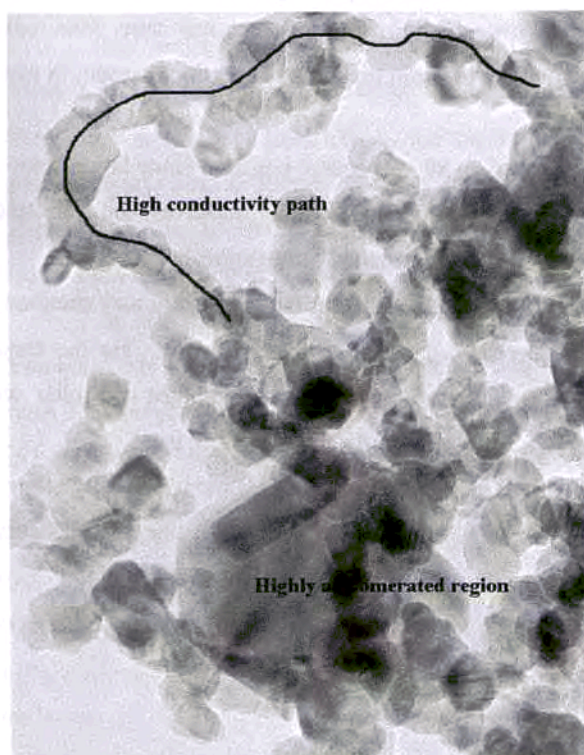
As seen in 2.4.2.1, the formation of necks between grains affects the mechanism of conduction. This effect should be added to the Schottky barrier control. Nevertheless, only Schottky barrier control ensures an improved response of the sensor to gas exposure –see section 2.4.3.1-. Therefore the grinding is desired to restore the Schottky barrier control.

It is worth to observe that, this mechanism leads always to more resistivity scenarios. As showed in the figure 3.3, as consequence of the grinding step, low resistivity paths will be broken.

Figure 3.3. TEM micrograph of a liquid pyrolysis sample annealed at 800°C without grinding. The mean grain size of these grains is 18±5 nm. In the upper left part there is a set of connected nanograins that forms a low resistivity electronic path. After grinding, this path will be broken and the mean resistivity will raise. In the lower right part, there is a region with highly agglomeration. The diffusivity of gas here is very limited by the compactness. After grinding, higher porosity will enable easier gas diffusion.

Moreover, the compactness of the powders will decrease after grinding process, which is appreciated to improve the gas diffusion through the sensing layer. As compacticity increases in material, the effects of high specific surface area are annihilated, the sensitivity of sensing layer is reduced only to the top part and the back-reaction after the exposure increases strongly the recovery time.

For all the exposed reasons, grinding treatments were applied on stabilised SnO_2 samples. A Fristch Pulverissette 7 machine was used. This machine is a planetary ball mill, where powder is introduced in a mug together with balls. A double rotation ensures the grinding of the samples. Due to the simultaneous rotation of the disc (onto which the milling mugs are located) and the milling mugs, the balls inside the mugs are accelerated towards the powder particles. See figure 3.4.
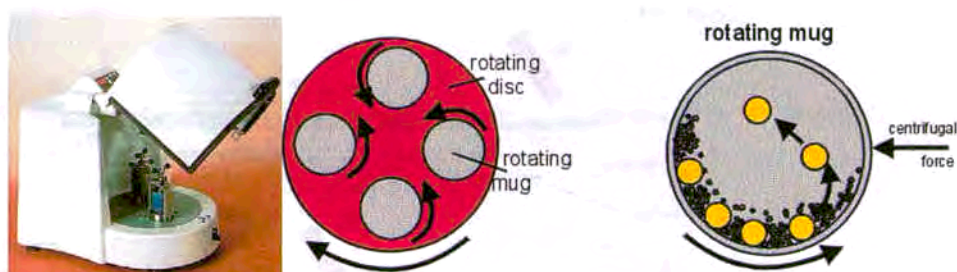
Figure 3.4. Left, Pulverissette 5 milling machine. Right, simultaneous rotation of the disc.

For the application on tin oxide, ZrO_2 mugs and balls were considered the most appropriated. Quantities above 2 grams of material are recommended to avoid zirconia contamination. Double deionised water was used as dispersing media.

3.1.3 Screen Printing

In the recent years, screen printing has become one of the most usual alternatives for the implementation of powders on substrates for gas sensing applications [Diéguez,99b] [Cabot,00]. High reliability and performances has been reported [Harris,97].

The process of screen printing is based in the known process of serigraphy developed in Japan several centuries ago. As seen in figure 3.5, a substrate, that contains electrodes and heater, is fixed on a nest. Over this substrate is placed a *screen* made by a mesh (in metal or plastic). This screen has been coated on the backside by a photosensitive emulsion. By means of photolithography the required design has been performed on the mesh.
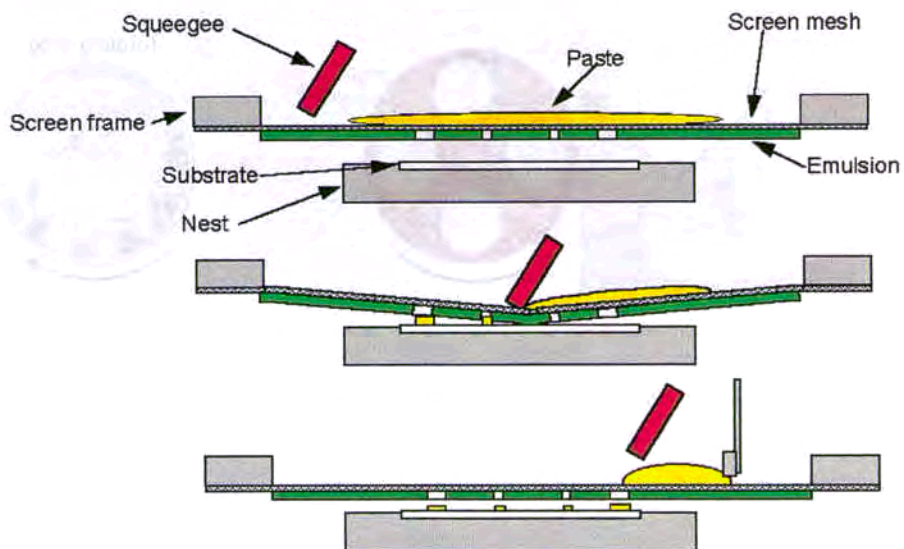
Figure 3.5. The basic screen printing process.

The top part of the screen is filled with a paste. In our case this paste contains the sensor material. A squeegee drags the paste while it makes pressure over the screen.

As in the dragging the paste fills the holes defined by photolithography, the paste is deposited on the substrate, drawing the desired pattern.

In spite of the simplicity of the process and the high degree of repeatability obtained, the high number of parameters in the process makes this technology quite complex when a specific design should be achieved. It is worth to take into account that the viscosity of the paste, the mesh, the gap between mesh and substrate, the thickness of the emulsion and the pressure of the squeegee are first order parameters that define the thickness and resolution of the printed layer. Other second order parameters are the temperature, the speed of squeegee drag, the angle of the squeegee with respect the screen, the roughness of the substrate, the thickness of the mesh ... A complete description of the printing process and parameters can be found in [Hobby,97]

As summary, screen printing becomes an easy technique and able for fast implementation, although the parametrical control results very complicate.

For the implementation of stabilised and grounded powders, we have implemented in the laboratory a DEK J1202 machine (see figure 3.6). In some sensors other printing machines have been used.

The production of the paste is performed by the addition to the stabilised and grounded powder of a quantity about 25% in weight of 1,2 propanediol. After several hours in a

Figure 3.6. DEK J1202 printing machine.

magnetic stirrer, viscosity ranges from 10 to 100 poise. When the paste is printed, the sensor should be dried in at $70°C$ during at least 2 hours.
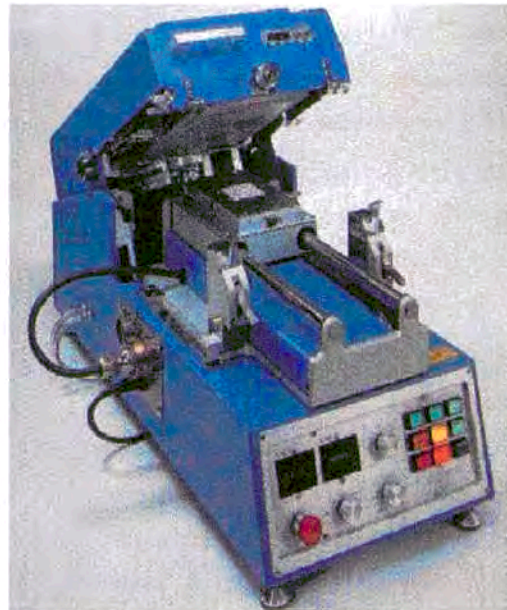
Despite the sensor can be used immediately, it could exhibit important drifts. Rests of volatile compounds can be responsible of it. For this it applied a last firing process. In some cases a reducing firing is applied to froze the oxygen vacancy distribution, which has been reported positive for sensing mechanisms [Blaustein,99].

3.2 Technology for sputter deposition

As commented above, the technology for sputter deposition concerned in the project has been developed at the technological centre CEIT in San Sebastián. A complete description of this technology has been reported elsewhere [Olaizola,99a] [Olaizola,99b][Gutierrez,99], nevertheless let me give a brief description for the better understanding of this work.

The deposition of tin oxide was performed on silicon wafers with intedigited electrodes and heater, in the process described as follows.

The silicon wafers were oxidised in different steps of dry, wet and dry full oxygen atmosphere during 21, 4.5 and 4 hours at $1100^{\circ}C$ to obtain $1\mu m$ of SiO_2. Then a 100nm-thick heater of chrome and platinum is deposited by sputtering. The microheater is patterned by means of photolithography process. Platinum is removed in a wet

Figure 3.7. CEIT Silicon substrate.

etching solution of $1HNO_3$:8HCl aged 1 hour at $70^{\circ}C$ for 7 minutes. Chrome is etched by plasma dry etching method. The heater is covered by a $2\mu m$-thick SiO_2 dielectric layer in order to avoid electrical shortcuts between the microheater and the sensing layer. Cr/Pt interdigited electrodes with a thickness of 200 nm were deposited on the SiO_2. The distance between electrodes is 50 μm. The aspect of the substrate at this point is shown in figure 3.7
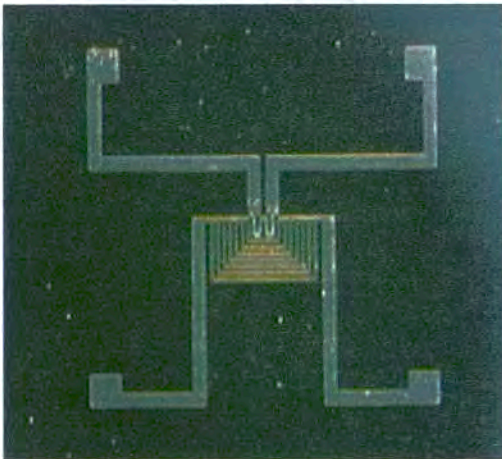
Once ready the substrate, the tin oxide can be deposited. For this process different approaches are followed, as we will present and discuss widely in the fifth chapter. Tin and tin oxide targets are used for reactive D.C. magnetron sputtering in different atmospheres from 60 to 100% of oxygen and argon. The thickness of the tin oxide ranges from 450 to 700 nm.

After deposition of tin, catalytic improvement of the sensing layer is followed by the addition of palladium by D.C magnetron sputtering. Three strategies are followed for the catalisation: the addition of a superficial layer of Pd, a buried layer of Pd in the tin oxide near the electrodes and a multilayer structure consisting in 8 layers of catalyst between tin oxide. The film is stabilised at temperatures that range from 400 to 900°C for 10 hours in synthetic air.

In order to achieve a micromechanised device the wafers are anysotropically etched using KOH at 80°C. The etching is stopped by using the electrochemical etch stop method in an epitaxial layer with a membrane thickness of 10μm. A scheme of the final micromechanised device is shown in figure 3.8
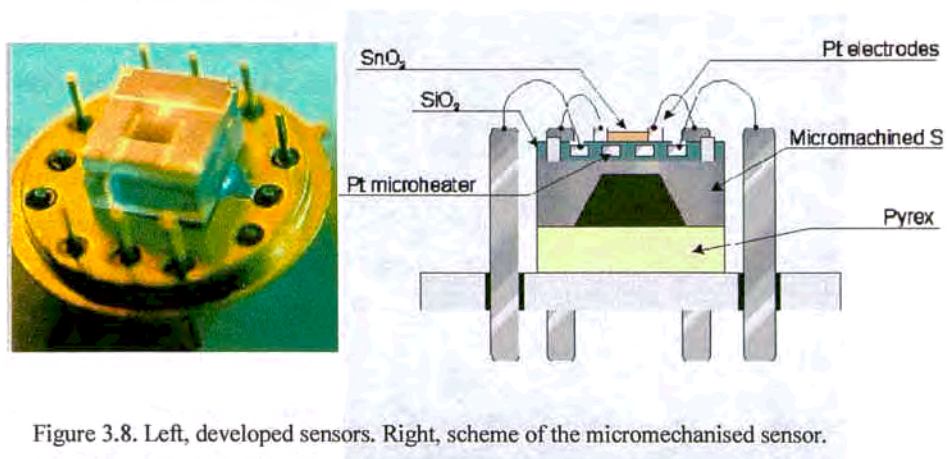
Figure 3.8. Left, developed sensors. Right, scheme of the micromechanised sensor.

3.3 Substrate technology for powder implementation

Concomitantly to the design of the micromechanised silicon substrate developed at CEIT for sputtering deposition, we were in the necessity to use substrate for the test of the powders developed by different techniques, such as liquid pyrolysis and microwave treatments, implemented by classical and novel techniques (printing, microprinting, and pulverisation coating). This scope impelled us to the development of new substrates based on alumina and silicon. These last were developed in collaboration with CNM[4].

As we shown in the chapter 2 -2.3 *Sensor design and configuration*- the design of the sensors is not obvious due to the variety of parameters that should be taken into account. In the next two points, I will give the design of the sensors as well as the main considerations for its design and use.

3.3.1 Alumina substrates

Three different kinds of substrates based on alumina have been developed. The use of alumina instead other ceramics, such as zirconia, steatite or cordierite is due to the high thermal conductivity and extremely low electric conductivity. Moreover, the strength of the bound between aluminium and oxygen makes Al_2O_3 one of the most stable and inert

---

[4] CNM-CSIC: Centro Nacional de Microelectronica del Consejo Superior de Investigaciones Científicas –*National Centre for Microelectronics of the Scientific Research Council*-.

materials for harsh environment applications. Besides, the commercial availability of alumina that can be supplied in different forms and shapes is appreciated.

The first prototype only contains electrodes for measurement but not heater, therefore an external source of heat should be used.

The design of the substrate consists on two interdigitated electrodes –see figure 3.9-. The distance between electrodes is 1.9 mm, and they were deposited by sputtering on an alumina substrate (Coors ceramic, 99.6% purity, thickness 0.6 mm and 8.5x8.5 mm^2). The composition of electrode is platinum with a thickness of 150 nm and the connection pad is gold (0.4μm).

The second design was developed considering the advantages of the previous design but overcoming three major problems that are the high resistance of the sensing layer the leak of selfheating and the connectivity. The material
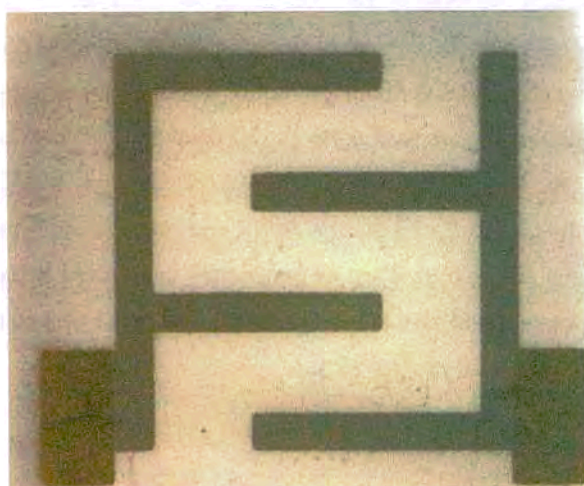
Figure 3.9. Design 1 of alumina based substrate for SGS test.

for the electrodes and heater is platinum. The substrate was acquired from Ceramtek.

As seen in figure 3.10, the interdigitated electrode design is similar to fig. 3.9, but reducing the distance between fingers. This design reduces value of sensing layer resistance and consequently the measurement becomes easier. While the resistance with the previous design can reach easily to 10 MΩ, in this design the resistance is reduced by a factor approximately four due to the half distance between fingers. In spite of the decrease of the measured resistance with this substrate design, the sensor substrate is

not very good for the measurement of oxidising gases, which rises the resistance of the sensor with respect the air.
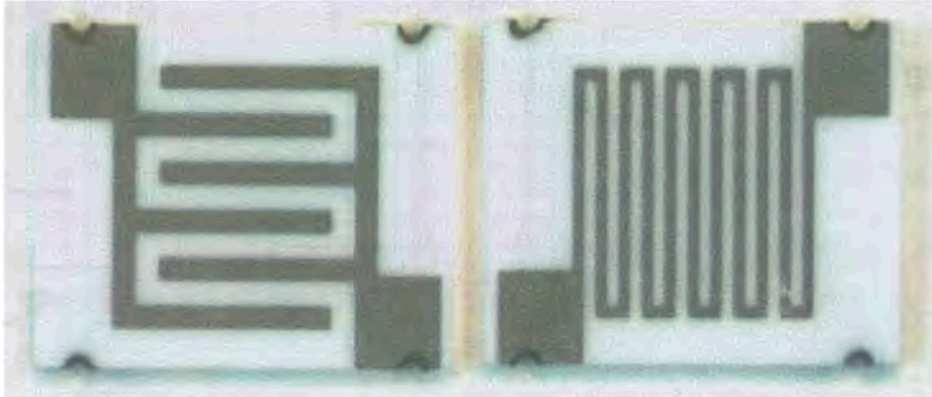

Figure 3.10. Design 2 of alumina based substrate for SGS test.

The selfheating was obtained by the addition of a meander-shaped heating resistance in the back face of the alumina. Although the heater allows reaching temperatures higher of those required for SnO_2-based sensing applications by applying several watts, the design was not optimised taking into account the electrical consumption. Only laboratory test considerations of sensor process feasibility were taken into account.

But the most innovative idea consists in the design for test encapsulation that includes platinum coated holes that make sensor substrate able to be mounted on a TO socket. The holes coincide with the pins of the TO and therefore the sensor substrate is wired for electrical feed of the heater and measurement of the resistance. These holes increase approximately the cost of the substrate by a factor two. Nevertheless the extracost should be reduced as the scale of fabrication increases.

Although no specialised research was done, we did not detect problems or incompatibilities due to the roughness of the surface. In the both former designs the nominal roughness of the surface was less than 1 µm.
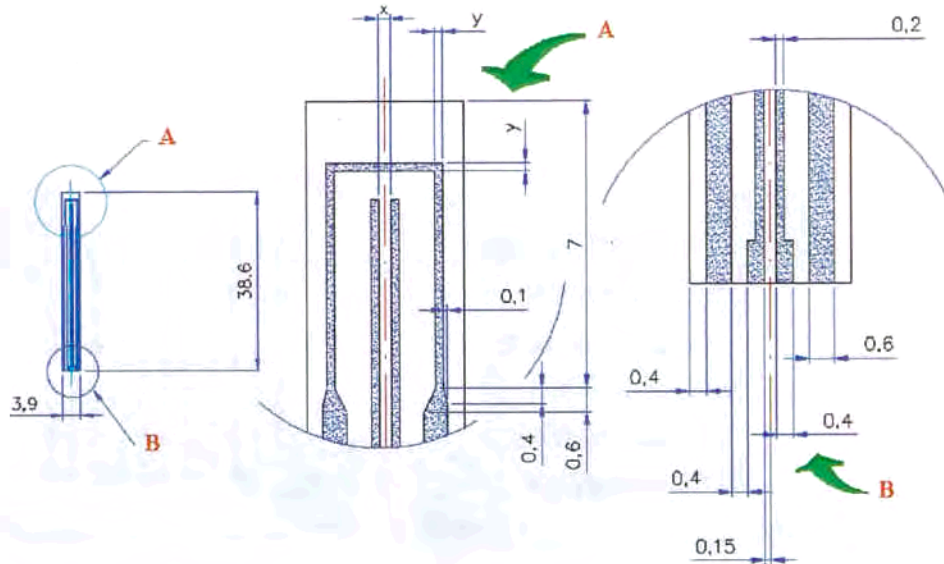
Figure 3.11. Design 3 of alumina based substrate with electrodes and heater. Left, elongated alumina substrate. Right, details of the up and bottom part.

The last design of alumina based was developed for harsh environment applications, such as automotive or boilers exhaust gas [Westbrook,94]. Besides, this substrate design can be applied for domestic gas monitor. The sensor consists on an elongated square-shaped alumina piece over which electrodes and heater are printed both in platinum. The paste for printing was acquired to Englehard-Clal (model A-3443). A final cure process for platinum printing is performed at 1200°C.

To study power dissipation and the conductivity of the sensing layer, different thickness of the heater (y, ranged 200 to 300 μm) and distance between electrodes (x, ranged 300 to 500 μm) were considered, as seen in figure 3.11.

In some cases the exposition of these electrodes at high temperatures and harsh environments could damage it. Passivating layer is required to avoid these problems. Alumina was considered the proper material to use as passivating due to its thermal conductivity, null electric conductivity and the low mismatch with substrate. See design in figure 3.12.
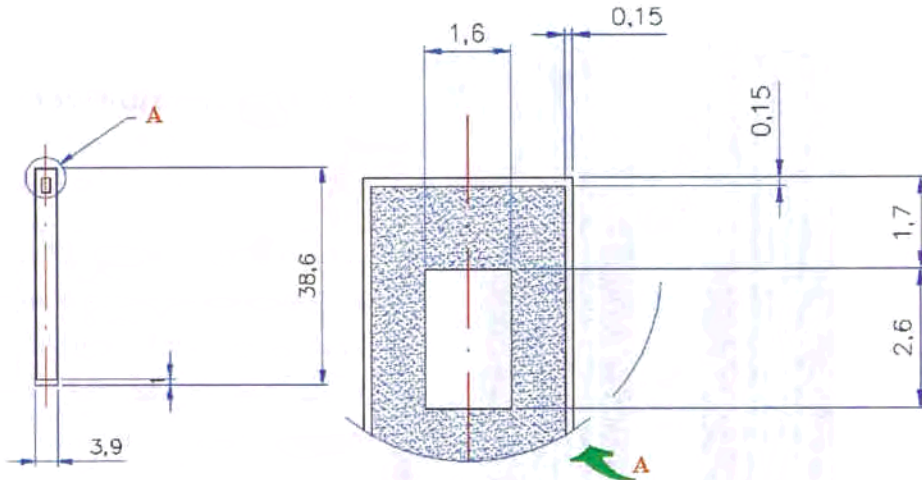
Figure 3.12. Alumina passivating layer to avoid electrode and heater degradation in harsh environments.

The passivating layer was implemented by printing. For this use a paste with the alumina powder (Guzman, mean size 50 μm) should be prepared. 1,2 propanediol was used together with a small quantity of *glass frit*. Final annealing at 1100°C during 2 hours is applied to reach the full consistency of passivating layer.

The actual look of these sensors at different steps of fabrication is shown in figure 3.13. It is worth to note that the total cost per sensor is less than 1€ when low or medium scales of production are considered.
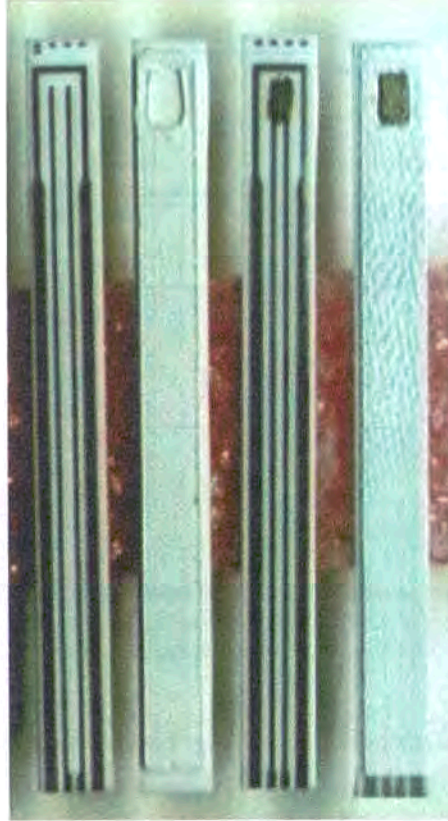
Figure 3.13. Sensor substrate at different steps of fabrication. From left to right: 1. alumina substrate with heater and electrodes, 2. alumina substrate with alumina passivation layer, 3. alumina substrate with heater, electrodes and sensing layer, 4. whole sensor with electrodes, heater, alumina passivation layer and sensing layer.

3.3.2 Silicon substrates

As introduced in section 2.3.5, the use of micromachined substrates is appreciated in order to reduce the consumption of these sensors and to keep the advantages of microelectronics integration [Wu,93]. Nowadays, they become the most advanced and promising substrates for SGS. Therefore, micromachined substrates were developed.

The design of these micromechanised substrates was developed together with CNM. The clean room process was done in CNM and the simulation, sensing material implementation and gas electrical test at EME laboratories.

For a deep study of the dissipation in micromachined membranes different geometries were considered. As seen in figure 3.14, an array of 4 micromachined substrates composes the chip. Two of these (S1 and S2) have a membrane of 1000x1000 μm^2 and a heater of 400x400 μm^2. The membrane of the other two (S3 and S4) is 1500x1500 μm^2, with a heated area of 900x900 μm^2. The thickness of the micromachined membrane is 0.3 μm.

Nevertheless, not only the size of the membrane was varied but also the heater. While in S1 and S4 the heater, made of polysilicon 0.48 μm height, the thickness is 65 μm and the separation is 15 μm, in S2
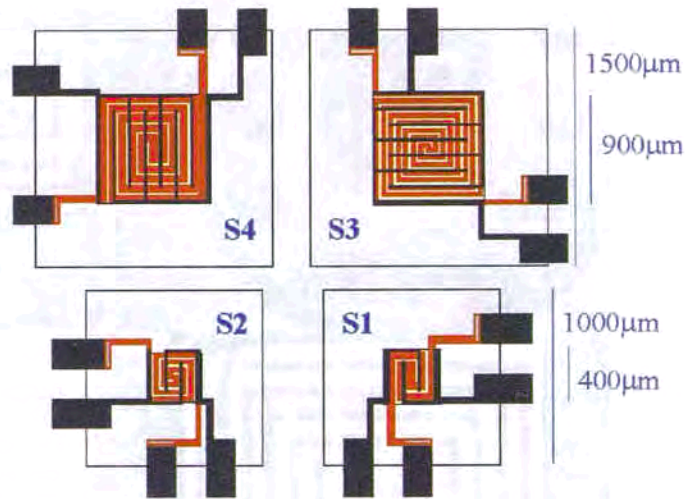

Figure 3.14. Scheme of the micromachined substrates.

and S3 the size is 40 and 20 μm respectively.

Over the heater, the electrodes for resistance measurements are patterned. These are made of platinum 0.33 μm height in an interdigitated geometry with a length between fingers of 100 μm. To avoid electric short-circuit, a passivating layer of SiO_2 of 0.3 μm thick was deposited between the electrodes and the heater.

The final chip is mounted in TO12 socket by usual encapsulation techniques, as shown if figure 3.15. Simulation data indicates that the consumption of these substrates is very optimised, reaching 480°C the model S1 when supplied 40 mW and the same temperature for model S3 when supplied 120 mW. Dynamic response of the sensors is in less than 40 ms to heat when 150°C are needed [Vilà,00]. Similar simulations developed for other micromachined sensors indicated that the temperatures ranges linearly with the power [Sheng,98].
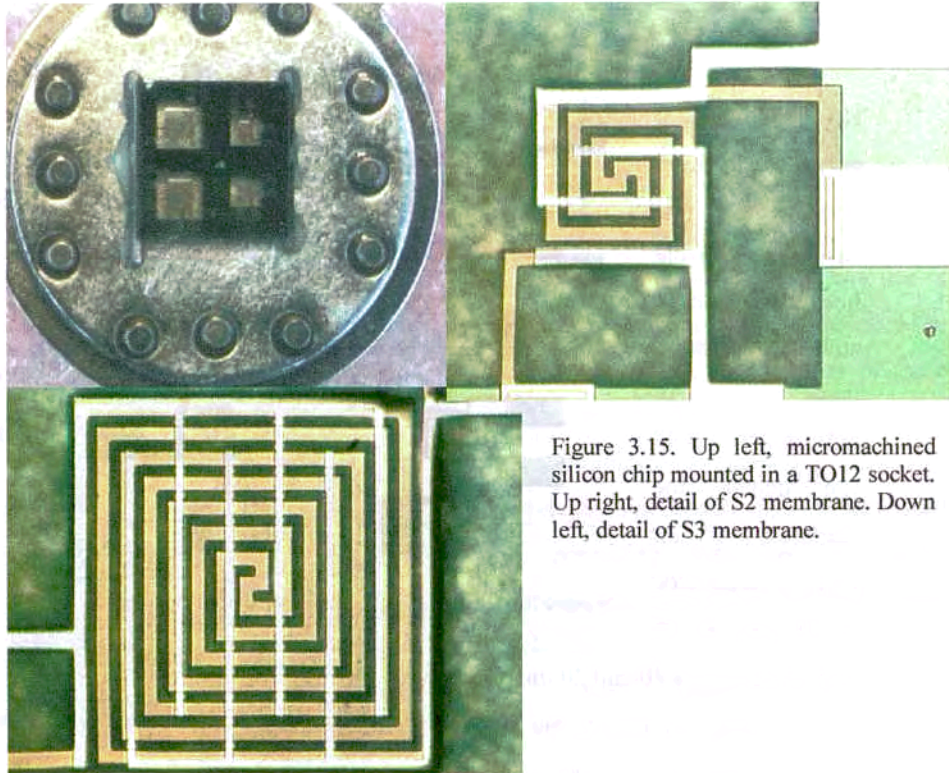
Figure 3.15. Up left, micromachined silicon chip mounted in a TO12 socket. Up right, detail of S2 membrane. Down left, detail of S3 membrane.

3.4 New implementation techniques of previously stabilised nanopowders

The use of sensing materials such as metal oxides is based on the property of these materials to change its conductivity under gas exposure. Usual chemical techniques – sol-gel, microwave processing– allows to obtain nanopowders of very good quality and extremely controlled properties [Cirera,00a]. They need to be implemented on substrates by thick film technologies such as printing or sinterisation of pellets. Besides, the use of integrated silicon technologies on chemical sensors influenced the use of sputtering (RGTO) and CVD techniques. They are able to have an accurate control over the thickness of films. However, postoxidation is a drawback for the properties of the material [Cirera,00b].

	Microprinting	Pulverisation Coating
Technology based on	Printing	Spray coating
Control over	Deposited volume	Deposited thickness
Leak of control	Deposited thickness	Deposited surface
Necessity of mask	No	Yes
Implementation step	Final encapsulated substrate	After masking, before etching
# sensors coated per process	1	Whole wafer
Posterior stabilisation process by	Self heating	Furnace or self heating
Compatibility with resin masking definition	Medium	High
Compatibility with physic mask	Null	Very high
Repeatability	High	Very high
Control difficulty	Medium	High
Applicability on silicon substrate	Yes	Yes
Applicability on alumina	No	Yes
Present automation	Low	High

Table 3.1. Technological comparative table between Microprinting and Pulverisation Coating.

In this section, we present two innovative ways to coat previously stabilised material. Therefore, the sensing material reliability and repeatability is assured while mechanical properties of the sensing layers are controlled by these methods. Moreover, advantages of common thin film techniques [Sberveglieri,92] such as mass production and use of silicon micromachined substrates can be supported by both methods.

While the microprinting is based on the controlled transport and deposition of a small quantity of paste, which contains the stabilised sensing powders, the pulverisation coating consists on a spray of the solution that contains sensing powders against the substrate. Therefore, both techniques are complementary and can be specially indicated for different applications. In table 3.1 I give a brief comparative study of both techniques; further details are given in the next two subsections.

3.4.1 Microprinting

The microprinting technology is based on the use of a paste prepared with nanopowders of different ceramic oxides, previously stabilised and having already added the catalytic element, if needed. Then, the paste is deposited on a membrane of a micromachined silicon substrate using a microdeposition drop technique. Finally, the deposited sensitive layer is fired in order to remove the organic solvent used in the paste preparation. The control of the paste parameters and deposition parameters have a strong influence on the properties of the deposited material such as size, porosity, thickness, adhesion, cracking, etc.

This procedure easily allows the fabrication of gas sensors. On one hand, microprinting takes advantage of micromachined silicon based sensors, i.e. low thermal inertia, low power consumption, optional pulsed operation mode, etc. On the other hand, it takes profit of thick film nanomaterial printable methods, i.e. use of wet chemical routes, easily stabilisation processes, high porous degree, etc. As well

chemical routes as stabilisation processes have been performed before the implementation, the only process that could damage micromachined substrate is the implementation (the microprinting). An accurate control of the implementation parameters minimises this risk, being nearly null.

3.4.1.1 Set-up and description

In the same way of conventional printing, first step in the process of microprinting consists in the preparation of the printable paste. In this case, solution should be less viscous. 1,2 propanediol was used as solvent for the preparation of paste. Different concentrations were evaluated and it was found that similar proportion in weight of solvent and sensing material produces a suitable paste for the process.

Once prepared this paste, it should be introduced in the microinjector. In our case, an IM16 microinjector from Narishigue was used together with TW-100 micropipettes. This step should be carefully controlled to avoid the introduction of air in the microinjector since it acts as compressible fluid resulting in a loss of control in the injection.
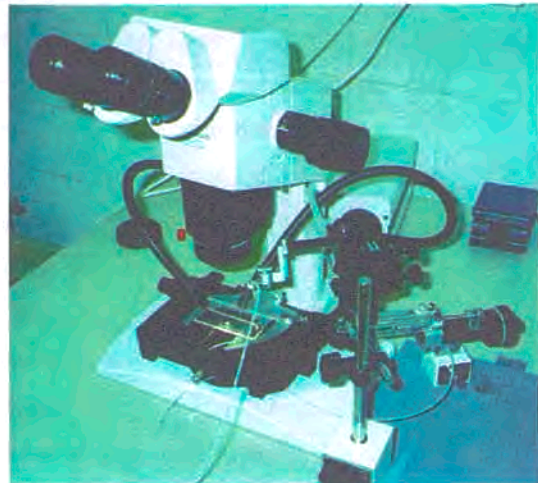

Figure 3.16. Photograph of the system for microprinting.

The micropipette full of paste is positioned over the sensor by means of micromanipulator, such as MN152. For better visualisation microscope (SZX9 from

Olimpus) is required. Cold light is appreciated to avoid the drying of the paste when illuminating the sensor and micropipette. For this, HL2100 cold illumination system from Olimpus is used. The complete system is shown in figure 3.16.

When vertical alignment of the micropipette full of paste and sensor as well as proper visualisation and illumination, is obtained the step of deposition starts. Some tests showed that although the control of the deposition by means of the amount of injected volume of paste is possible, better control is reached by means of the proper use of the paste surface tension. For this, an overpressure in the micropipette is obtained lightly turning the knob of the microinjector. As consequence, in the sharp point of the micropipette a meniscus of the paste is formed. Using the knob for vertical control of the micromanipulator, the point of the micropipette is moved until the meniscus hits the sensor. At this moment, a neck of paste evacuates the overpressure between the micropipette and the substrate. When overpressure is evacuating, sensing material paste goes from the micropipette to the substrate. The process can be stopped moving away the micropipette. Therefore, the amount of paste deposited is controlled by the time of micropipette/sensor contact through the neck of the paste.

Since both micropipette and sensor are never in full contact, the procedure ensures to avoid the break of the micromechanised membrane.

Following this procedure is possible to deposit drops with a diameter of 100 μm. As we will present in the next section, 200 μm or higher diameter drops are very well controlled. Nevertheless the control of the drop height is not possible at the present status of the experimental set-up. It was observed that the drops are quite flat, for example, a height of 25 μm is measured on a 200 μm diameter drop. This represents a system control for the deposition of less than 5 nanolitres.

After this deposition, a thermal process is required to evaporate the organic solvent and to improve the mechanical adhesion of the drop on the substrate. Although temperatures in the order of 700°C would be adequate for this process, one should keep the temperatures reached by the own heater of the sensor in the case that drop is deposited on a sensor substrate.

3.4.1.2 Reliability

Once proved the feasibility of the use of microprinting for sensing material implementation on silicon substrates, it is important to verify the reliability of this technique. Besides the proper function of the sensor, the most important points concerning reliability are the repeatability of the deposition, the compatibility with micromachined substrates, the compatibility with masking processes and the verification of the obtained thickness.
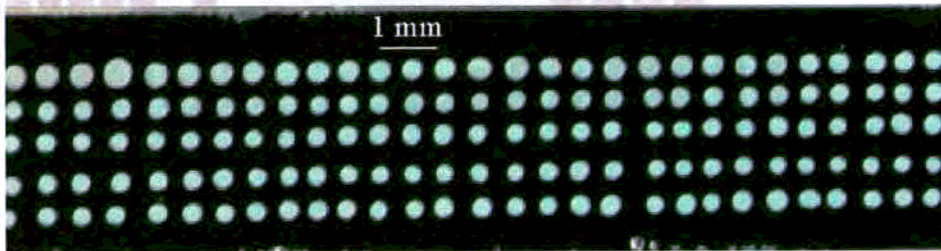

Figure 3.17. Set of microprinted drops.

To verify the repeatability of the deposition process, a repetitive deposition experiment was designed. This consisted on the deposition of four sets of drops, as those shown in figure 3.17. For every set a different micropipette was used. As the deposition was done on a clean silicon dice without alignment marks nor wires, only deposition time allows the control of the deposited paste, as stated above. The control of the process was
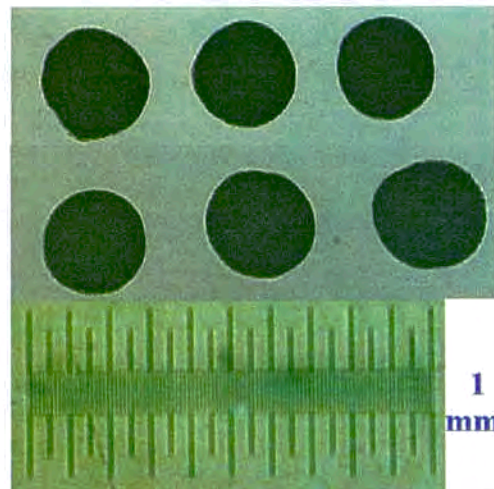

Figure 3.18. Optical inspection of the drops size. See the repeatability of the process. Bottom, 1 mm rule supplied by Afora.
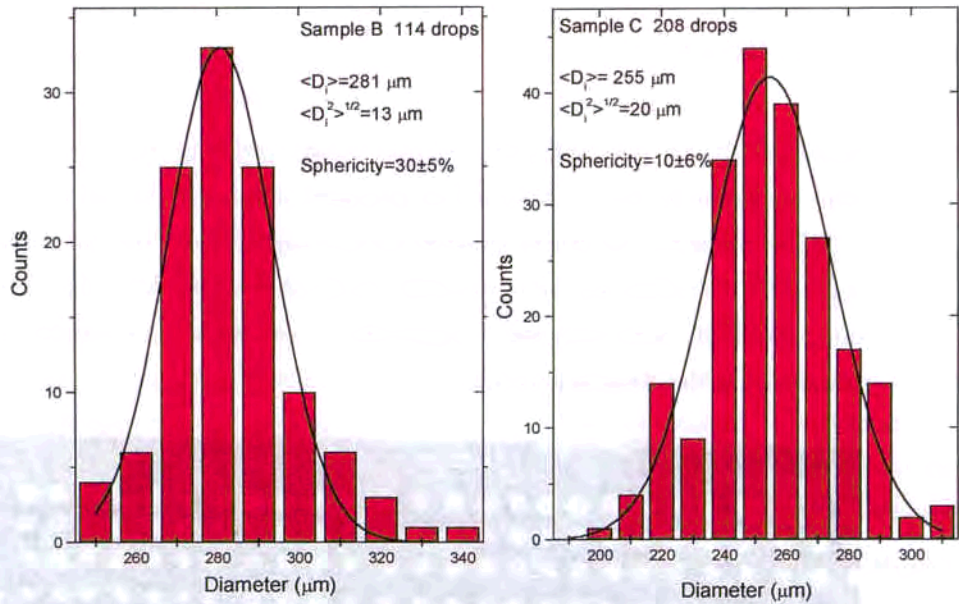
Figure 3.19. Histograms of drop diameters. Left, set B. Right, set C. The data were fitted after a rejection ≤ 2% of the total number of drops.

completely manual, therefore it is considered that the automation of the process will give better performances.

After deposition, about 500 drops of the different groups were measured by optic microscope, see figure 3.18. The radius of the drops ranged from 200 to 300 μm and in some of the sets of drops, these were found more elliptic than spherical. The distribution of drop diameters can be fitted by Gaussian function, considering the *high number* theorem and random distribution, two examples are shown in figure 3.19.

As seen, the results can be well fitted by Gaussian distribution. Therefore we can only give the mean and standard distribution as main parameters. These data and the percentage of sphericity, defined as the major radius less minor radius divided by the major radius, are given in table 3.2.

Set	Measured drops	Mean diameter (μm)	Standard deviation (μm)	Sphericity
A	60	238	25	12±7%
B	114	281	13	30±5%
C	208	255	20	10±6%
D	111	295	18	23±6%

Table 3.2. Statistical data of the drop sets deposited on silicon. See how standard deviation is between 5 and 10% of the mean diameter.

These statistical data become very important since they shown clearly that the degree of control and repeatability even in the case of manual control is very high. For example considering set B, a yield of 95% will be reached if drops of 280 μm with a tolerance of ±20 μm (7% of tolerance) are required.
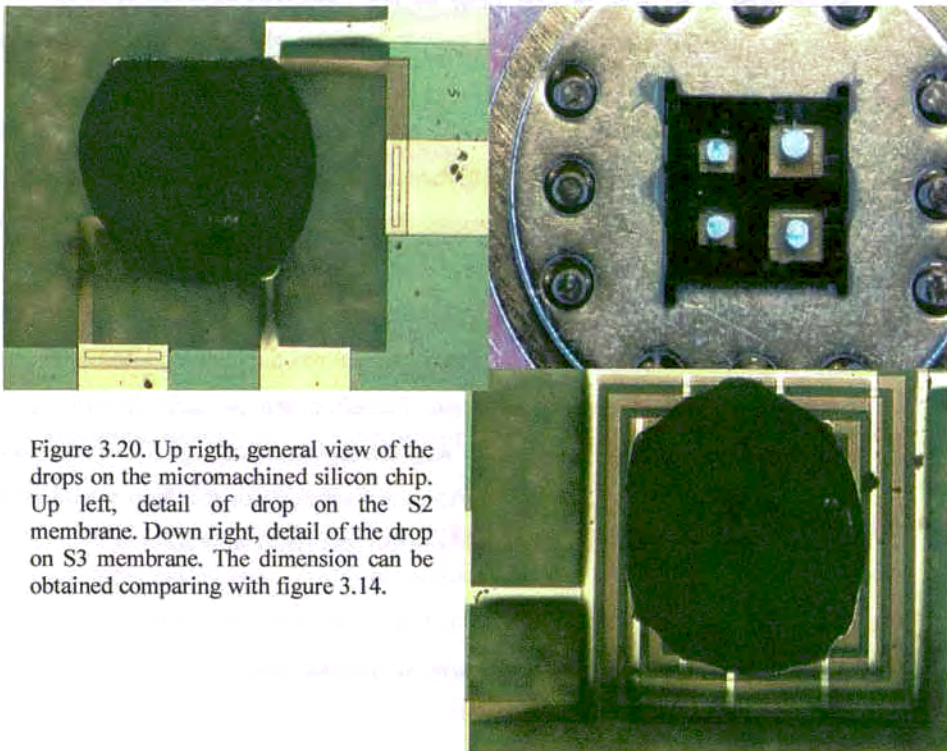

Figure 3.20. Up rigth, general view of the drops on the micromachined silicon chip. Up left, detail of drop on the S2 membrane. Down right, detail of the drop on S3 membrane. The dimension can be obtained comparing with figure 3.14.

About the sphericity, it should be deduced that it depends mainly on the micropipette and its relative orientation with respect the substrate.

After the statistical verification of the procedure, a test of the feasibility of microdeposition on silicon micromachined substrates was performed. Previously presented micromachined substrates -figure 3.15- were used. As seen in figure 3.20, the deposition is successful, although several aspects should be taken into account.

The implementation of the drop should be done over the heated area. As it has been shown, the deposition of drops between 200 and 300 μm diameter becomes very controllable. In the case of small membranes, such as S3 and S4 with a heated area of 400×400 μm^2, it is not difficult to coat the whole heated area. But in the case of bigger areas, such as S1 and S2 with 900×900 μm^2, the control becomes more difficult. As seen in figure 3.19, whereas it was easy to coat the whole surface of S3 membrane, S2 is not completely coated.

It is worth to observe how the thickness of the electrodes can affect the shape of the drops. As seen in figure 3.20, the top part of the drop is flattened when it arrives to the outermost part of the electrodes. Therefore these can redistribute the paste and modify the shape of the drop.

With respect to the compatibility with masking process, some proves showed how the adhesion of the drop is not enough to avoid the disintegration of drop when the ultrasound is used to remove the resin. Therefore, this process should be applied only using the organic solvent (acetone) and soft manual shaking. If thermal cure process were induced before removing the resin, the adhesion of the drop would be improved but the degradation of the resin could difficult the removal process.

3.4.1.3 Critic review and future improvement

The reached compatibility guarantees this procedure as an alternative in front of other physical methods such as sputtering for which each new condition (the use of new

ceramic oxide or new catalytic additive) needs a lot of time for the optimisation of the sputtering conditions. Moreover, the sputtered material needs to be stabilised at high temperature for a long time, which could be difficult to make compatible with other required processes. In summary, this microprinting alternative method becomes an easy and fast technique to perform sensitive layers for gas sensors.

Although the present status of the experimental set-up ensures the repeatability in the implementation process, the industrialisation should consider the automation of micropipette and sensor movement as well as the automatic optic recognition.

Both aspects would make this technique suitable for mass implementation, nevertheless the exposed leak of compatibility with the masking process is still a point that should be enhanced. This compatibility is important due to the economic impact that it could induce. As at the present status microprinting implementation is done on the encapsulated sensor, rejected drops represents higher cost than in the case of deposited before substrate micromachining.

3.4.2 Pulverisation coating

Pulverisation coating is a complementary technique for the implementation of previously stabilised sensing material. This approach differs from the former in the fact that solution, which contains sensing material, is not driven over a patterned way until the substrate, but dispersed by pulverisation on it.

Therefore, this technique requires a fine process of masking but, at the contrary of the former technique, can be applied to as many sensors can be in a wafer. Moreover, this implementation technique allows a fine control of the thickness, ranged from 0.2 μm up to more than 10 μm.

For the pulverisation, previously stabilised nanopowders are diluted in organic solvent at different concentrations and, then the deposition is performed by means of a carrier gas, which is controlled by a mass-flow controller. Computer controls temperature of the substrate, duration of pulverisation and flow of gases. These parameters have important influence on the physical properties of the obtained layers so computer control gives a very high repeatability.

3.4.2.1 Description and set-up

The first step in the process of pulverisation coating consists in the preparation of the solution to be pulverised. For this process both 1,2 propanediol and methanol were tested in concentrations 40 times higher than the weight of sensing powders. Both organic solvents exhibit good properties for this use, but methanol seems to need lower substrate temperature for a good coating. Nevertheless its use requires long time of stirring, even several days, to have an homogeneous solution.

Then the solution is introduced in a bottle with nitrogen inlet and solution outlet –see scheme in figure 3.21-. The amount of solution that goes out of the bottle is controlled by the amount of driver nitrogen that comes in. The proper control of the flow of driver nitrogen allows the control of solution pulverisation. This control is performed by means of Brooks mass flow controller (MFC) in the range from 10 to 500 ml/min. The MFC allows the control of the fluid with an accuracy of 2% of full scale.
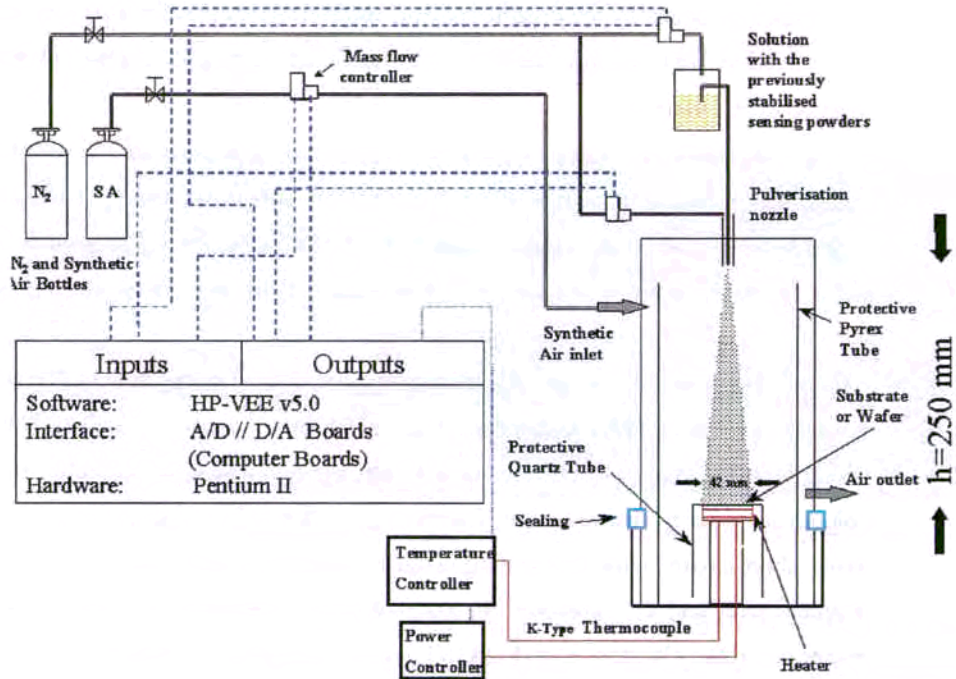
Figure 3.21. Scheme of the pulverisation coating set-up.

This MFC is governed by analogue A/D (16 bits) and D/A (12 bits) PC-boards (from Computer Boards). HP-VEE 5.0 (from Hewlett-Packard) was used for the software interface design between the PC and the PC-boards as well as graphic user interface.

In order to produce the pulverisation, together with the solution liquid, a high flow of carrier nitrogen is introduced in the external shell of the pulverisation nozzle. This nozzle consists in two concentric tubs. In the inner tub flows the solution liquid while in the outer one the carrier nitrogen flows. The actual flow of carrier nitrogen is controlled two by using a MFC of similar characteristics to previous one but in the range from 0.6 to 30 l/min. Good pulverisation coatings are produced when the flow of carrier nitrogen is about 25 l/min and the driver nitrogen about 15 ml/min.

Due to the high quantity of nitrogen that comes into the pulverisation area and the vapours produced by the organic solvent, controlled synthetic air inlet and outlet are appreciated. A MFC controls the flow of synthetic air coming in this area in the range from 10 to 500 ml/min.

The wafer or substrate to be coated is placed at a distance of 250 mm from the nozzle. But to ensure a good coating, this substrate should be heated at temperatures higher than 80°C when methanol is used as solvent or 200°C for 1,2 propanediol. If the wafer is heated at lower temperatures than required the pulverised sensing material becomes liquid and slides on the wafer surface.

The proper temperature is reached by means of a heating system composed by a heater, a thermocouple, a temperature controller and a power controller. The heater (Watlow model MB1A1JN1) is placed in the column where the substrate lies. This column is made by stainless steel, therefore good thermal conduction is supposed. To avoid short-circuit when pulverising, a quartz protective tube is placed between the stainless steel and the substrate. An external power controller feeds the heater. This power controller (Watlow model DA1V) is able to regulate the amount of given power after an input signal that contains information about the quantity of power required. A temperature controller (Watlow model 988A-12FA) gives this signal. This instrument computes the amount of power required by PID algorithms considering the actual temperature of the heated system measured by a thermocouple. In our case, the thermocouple (type K, imbedded in an elongated kanthal case) is placed in the centre of the heated tube, and hits the quartz protective tube.

3.4.2.2 Reliability

The reliability of the process in mainly ensured by the computer control of the main deposition parameters; namely, the deposition timing, the flow of carrier and driver nitrogen, and the temperature of the process.

In fact the parametric control allows a fine-tuning of the thickness of the layer from 0.2 to 5 μm –as shown in the figure 3.22-. Besides the obtained material exhibits a proper porosity for gas sensing applications.
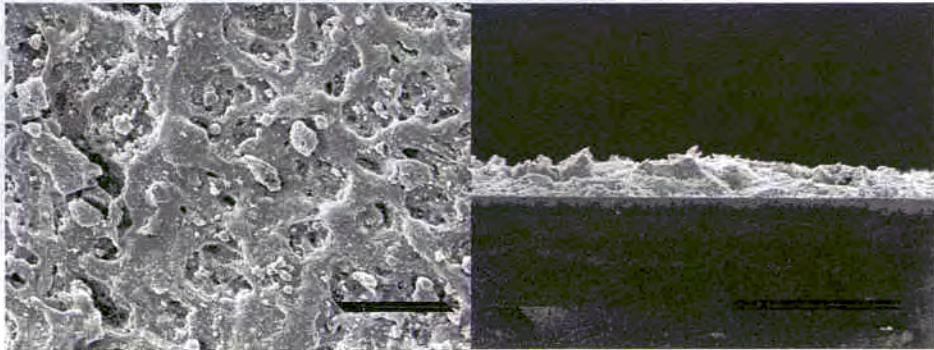

Figure 3.22. SEM micrographs of the layers. Left, surface definition. Right, thickness of the layer. In both cases the bars are equivalent to 20 μm.

However, as we have previously described and schematised in table 3.1, the lateral resolution of this technique, like sputtering, is lost since it is a non-directional technique. Thus the lateral resolution should be externally implemented by using physical or resin-based masks. Only this masking process can ensure the compatibility with CMOS and micromachining process.

The physical masks, defined on thin film epoxy, were satisfactory used. But although physical mask can be easily implemented due to the non-destructive coating process, its resolution hardly covers the micrometric range desired for the microelectronic applications.

Thus common microelectronic resin-based masks deposited on silicon were tested and the coating perfectly adapts to the definition of this mask. The only problem arises when temperature is needed for the coating. Resin can undergo 90°C during few minutes (enough for the deposition), but it becomes harder and much more difficult to remove. Posterior acetone bath is not enough to remove the resin and ultrasound cleaning is necessary. Nevertheless, as the coating is not thermally stabilised, its

adherence is still weak and the ultrasound energy can disintegrate the layer if the

process spends more than three minutes.

At the present status, although the resin-based masking process is not easy due to the exposed problems, the difficulties have

Figure 3.23. SEM micrograph of the resin-mask improved resolution.

been overcame and it has been possible to remove the resin by means of a close control of the process. See figure 3.23 as an example of resin-based mask resolution.

3.4.2.3 Critic review and future improvement

In summary, this method to perform both thin and thick layers of gas sensitive nanoparticles points out a good control over the properties of the layer such as thickness and porosity. Likewise, it seems to be completely suitable to obtain gas sensitive layers based on different kind of metal oxide nanopowders. For these reasons, the future improvements of this method should improve the deposition conditions, especially those derived from the relationship between the pulverisation and the substrate. A better control of the solid angle, the planarity of substrate with respect the nozzle, and the temperature of deposition –which highly depends on the geometry of the substrate- would be appreciated.

Moreover, the masking process –based on physical masks or based on resins– should be improved to get better performances for the whole compatibility of this method with CMOS and micromachined silicon.

For the future development of this technique, the electrically assisted deposition should be considered. In this way, plasma assisted has been already developed [Segall,98] for the application in the field of tribology. Besides, further study considering the morphology of the coated layer, in the way of [Sobolev,98], would be also interesting.

3.5 Device gas test systems

3.5.1 A portable test station for in-situ characterisation

This simple system was designed as controllable atmosphere supplier, able to introduce moderate quantities of CO and NO_2 as well as humidity in a synthetic air carrier. The system is portable because was mounted in a small trolley, but robust enough for secure transport. Thus, the system has been designed to be compatible with the carrying out of measurements with characterisation techniques such FTIR, STM, STS and AFM [Arbiol,00a][Arbiol,00b]. The production of a controllable atmosphere in the sample holder also allows simple test of gas sensor devices [Cirera,98].

The control of gases is done by rotameters that allows to set manually the concentrations. Let me suppose we needed a concentration x_T in ppm of gas 1 in a carrier gas 2, and we have a bottle of with a concentration of x ppm of the gas 1 in the gas 2. Then the relation between the needed concentration x_T and the flow required from the bottle ϕ_B is

$$x_T = \frac{\phi_1}{\phi_1 + \phi_2} = \frac{x\phi_B}{\phi_B + \phi_2} \qquad (3.1)$$

where ϕ_1 is the actual flow of gas 1, and ϕ_2 is the actual flow of gas 2. For instance, if we need 100 ppm of CO in synthetic air (x_T) in a total flow of 200 ml/min ($\phi_B+\phi_2$) and we have two bottles, first 1000 ppm CO solved in synthetic air (x) and second of pure synthetic air (ϕ_2), the flow ϕ_B should be 20 ml/min and ϕ_2 180 ml/min.

This station allows the production of flows of 100 ml/min with concentrations up to 1000 ppm of CO, and 5 ppm of NO_2. It allows too the control of relative humidity by means of the air bubbling in water.

In the figure 3.24 we can observe the station in detail. The mobile part of the station consists in a trolley 515x415 mm^2 surface. An external synthetic air connection is needed when this compound acts as carrier gas.
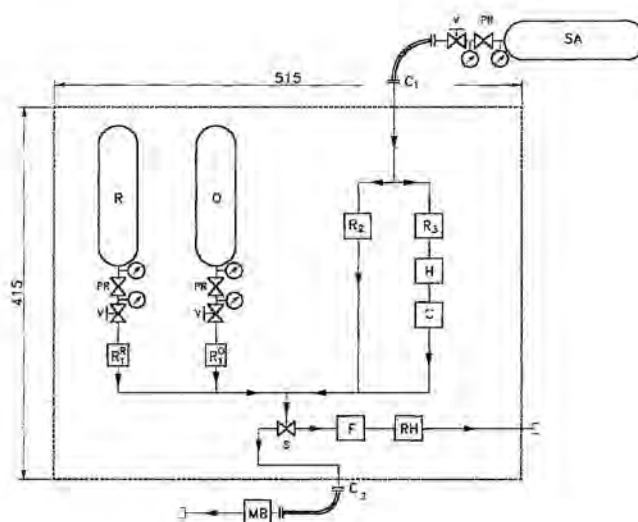

Figure 3.24. The portable test station for in-situ characterisation. Left, scheme of test station. Right, the actual system mounted for in-situ STM measurements, such in [Arbiol,00b]

The main parts of the former scheme are described. SA is the synthetic air bottle (Abelló Linde). R is the reducing gas mini-bottle, in our case 102 ppm of CO solved in synthetic air (Abelló Linde). O is the oxidising gas mini-bottle, in our case 10.5 ppm of NO_2 solved in synthetic air (Abelló Linde). R_1^r is the rotameter for the reducing gas (Key Instruments), which measures in the range $2 \div 100$ ml/min ($\pm 5\%$ FS). R_1^o is the rotameter for the oxidising gas, with the same performances than the former one. R_2 is the rotameter for the dry synthetic air (Key Instruments), $5 \div 300$ ml/min ($\pm 5\%$ FS). R_3 is the rotameter for the humidified synthetic air (Key Instruments), $4 \div 160$ ml/min ($\pm 5\%$ FS). H is the humidifier, this consists in a bottle full of double distilled water where the air is conduced to the bottom of the bottle and when bubbles rise, they dilute water inside. But together with solved water some water drops are carried with the humidified air. To avoid the undesired

effects of these drops a second bottle (C) is plenty of ice, which acts as condenser trap, this system has been previously tested [Hierlemann,95][Endress,95][Ortega,98] with satisfactory results. The generation and control of gases is completed with a digital flow meter (noted as F in the scheme and acquired to Key-Instruments) that allow a better control of the gas flow and measures in the range $5 \div 500$ ml/min ($\pm 2\%$ FS). RH is a thermohygrometer (Schlee) for the measurement of the temperature $0 \div 50$ °C ($\pm 0.5\%$ FS) and the humidity $2 \div 98$ %RH ($\pm 5\%$ FS). Swagelock fittings and racords were used, together with 6x4 mm stainless steel and Teflon pipeline.

Some gas test electrical measurements of sensors were done with this station, such as those done in the work [Cirera,98]. For this, the outline of the station was coupled to an environmental chamber (Linkam, model 600) that allows heat until 600°C while doing electrical measurements. This chamber contains an optical window for the experimental use on characterisation techniques, such as Raman spectroscopy.

3.5.2 Test station for high-temperature exhaust gas sensors

Exhaust gas monitoring is one of the most important fields of application of SGS. The main difference in the design of SGS for such application consists in the harsh environment that sensors undergo. This environment, like the induced in a boiler or car outlet, usually contains high proportions of oxidising and reducing gases, such CO, NO_x, CO_2, hydrocarbons ... Besides, high temperature is produced since this gases are the product of a fuel combustion.

To reproduce and control such exhaust atmosphere, the possibilities of use of a real combustion engine was considered, nevertheless the control over atmosphere parameters, mainly gas concentration and temperature, would become very difficult. For this reason, a test station able to generate these atmospheres from the control of gas

flowing from bottles was designed. Other parameters, such as temperature, were properly controlled, as we will show in the next sections. Further details of such test station can be found in [Folch,00].


Figure 3.25. Photograph of the test station.

3.5.2.1 Objective and general conception

Once considered the different approaches for the generation of exhaust gas atmospheres - the collection of engine exhaust gases, the combustion of synthetic fuel, and the synthetic generation [Bozek,92][Kohli,99] - this last possibility was found the most appropriate for a whole control of the atmosphere parameters.

One of the main points related with the election of this alternative was the reported knowledge about the chemistry of the combustion processes, as I briefly describe below.

In a combustion, a flammable gas burns in a reaction such as [Tien,75],

$$CH_x + yO_2 + 3.76yN_2 \rightarrow CO_2 + \frac{x}{2}H_2O + 3.76yN_2 \qquad (3.2)$$
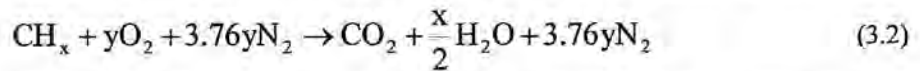
In this reaction it is supposed that hydrocarbon reacts with air, therefore nitrogen is indicated in the chemical equation although it does not react.

But in an engine the actual reaction is not always stoichiometric. In fact, it is much more usual a rich combustion (more fuel than required for stochiometric combustion) or lean combustion (less fuel than required). Since several years, it has been used the lambda parameter as a merit figure of such relation [Lampe,94b]

$$\lambda = \frac{\left(m_{air} / m_{fuel} \right)_{reaction}}{\left(m_{air} / m_{fuel} \right)_{stoich}} \qquad (3.3)$$

where m_{air} is the mass of air and m_{fuel} the mass of fuel. The subscript *reaction* refers to the actual burning concentrations while *stoich* refers to those concentrations in a stoichimetric reaction such as 3.2. Therefore, when $\lambda < 1$ the combustion is rich and when $\lambda > 1$ the combustion is lean.

Brettschneider developed a model of combustion that analyses the different contribution of exhaust gas to the λ parameter [Brettschneider,79]:

$$\lambda = \frac{21}{21 + 50\mu x \dfrac{[CO][CO_2]}{k + [CO]/[CO_2]}} \times$$

$$\times \frac{[CO]/_2 + [CO_2] + [O_2] + \left\{ \dfrac{H_{cv}K}{4(K + [CO]/[CO_2])} \right\} \left([CO] + [NO]/_2 + [CO_2] \right)}{\left(1 + H_{cv}/_4 - O_{cv}/_2 \right) ([HC] + [CO] + [CO_2])}$$

$$- \frac{W_{cv}/_2 \dfrac{[CO]/[CO_2]}{k + [CO]/[CO_2]} ([HC] + [CO] + [CO_2])}{\left(1 + H_{cv}/_4 - O_{cv}/_2 \right) ([HC] + [CO] + [CO_2])}$$

$$(3.4)$$

where x is the humidity in grams of water vapour in grams of dry air, [XX] is the concentration of a gas in vol %, μ is the relation of molecular mass of air over water (1.608), K is the equilibrium constant of gaseous water (3.5), H_{CV} is atomic ratio of hydrogen in hydrocarbon (in CH_4, H_{CV}=4), O_{CV} is atomic ratio of oxygen in hydrocarbon, W_{CV} is atomic ratio of water in hydrocarbon.

In the combustion of dry methane we can chose x=0, H_{CV}=4, O_{CV}=0 and W_{CV} =0, leading to a simplified form,

$$\lambda = \frac{[CO_2] + [CO]/2 + [O_2] + \left\{ \dfrac{3.5}{3.5 + [CO]/[CO_2]} \right\} ([CO_2] + [CO] + [NO]/2)}{2([CO_2] + [CO] + [CH_4])}$$

$$(3.5)$$

Some measurement without water [Lampe,94a] showed small shifts of the characteristic response for gallium oxides SGS. Nevertheless it is possible to overcome this difference by the addition of few percentage of solved water (about 5%) in the carrier gas.

Therefore, the conception of this test system is the generation of synthetic mixtures following the Brettschneider simplified relation 3.5 to simulate exhaust atmospheres. A scheme of the test station is shown in figure 3.26.
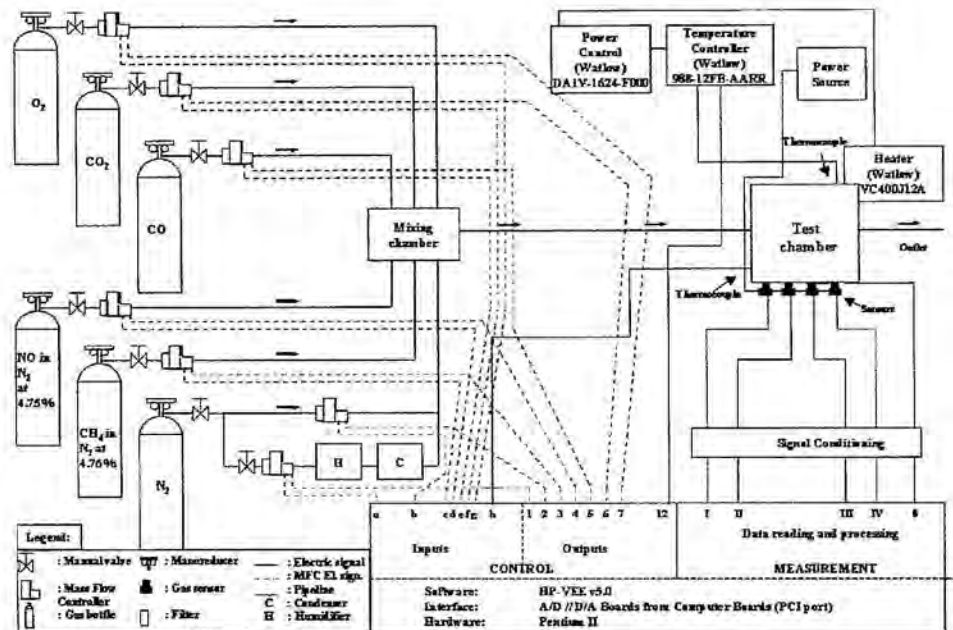

Figure 3.26. Scheme of the test station.

3.5.2.2 Gas generation

By using equation 3.5, Lampe *et al* [Lampe,94a] proposed the use of the set of gases exposed in table 3.3 to reproduce exhaust atmospheres in a wide range of λ.

λ	O_2 (vol. %)	CO_2 (vol. %)	CO (vol. %)	NO (ppm)	CH_4 (ppm)
1.334	7.28	10.9	0	460	0
1.221	5.45	10.9	0.45	910	450
1.176	4.55	10.9	0.45	910	910
1.116	3.64	10.9	0.91	1800	1100
1.071	3.64	11.8	1.82	2700	1600
1.052	3.19	12.7	1.82	3600	1800
1.034	2.73	12.7	1.82	3600	2000
1.017	2.27	12.7	1.82	3600	2300
1.004	1.82	12.7	2.27	3600	2300
1.001	1.82	12.7	1.82	3600	2500
0.997	1.82	12.7	1.9	3200	2500
0.994	1.82	12.7	2.0	2700	2500
0.992	1.82	12.7	2.1	2700	2500
0.989	1.82	12.7	2.2	2700	2500
0.986	1.82	12.7	2.3	2700	2500
0.984	1.82	12.7	2.3	2300	2700
0.982	1.82	12.7	2.3	2300	3000
0.981	1.82	12.7	2.3	1800	3200
0.978	1.82	12.7	2.4	1800	3200
0.976	1.82	12.7	2.5	1800	3200
0.974	1.82	12.7	2.6	1800	3200
0.971	1.82	12.7	2.6	1400	3400
0.966	1.82	12.7	2.7	900	3400
0.962	1.82	11.8	2.8	900	3600
0.947	1.6	11.8	3.0	900	3700
0.941	1.5	11.8	3.1	900	3700
0.921	1.37	11.8	3.6	900	4100
0.885	0.9	11.8	4.5	900	4500
0.859	0.9	10.9	5.5	900	4500
0.801	0	10.9	7.3	460	4600

Table 3.3. Set of gas concentrations to reproduce exhaust atmospheres in a lambda range from 0.801 to 1.334. The carrier gas is nitrogen. All of these concentrations verify the equation 3.5. From [Lampe,94a]

To implement these gases in our system, pure bottles (from Abelló-Linde) of O_2 (purity 5.0), CO_2 (4.0), CO (4.7) and N_2 (5.3) were used. Diluted bottles of NO and CH_4, both solved in N_2 at 4.75 and 4.76% respectively are used to.

The control of these gases is done by using *Mass Flow Controllers* (MFC, see [Ortega,98] for a complete description of such instruments) supplied by Bronkhorst. These instruments have an accuracy of ± 0.2% of full scale, the error in the repeatability of reading is <0.2% of the reading and the response is less than 2 seconds. Although a special instrument can govern these MFC's, I preferred the control from PC together with the rest of controllable instruments. For this application, analogue 0÷5V signal is used both for the commanded flow and for the measurement of it.

Considering the minimum controllable flow of these instruments (that is the 2% FS) and the total flow (usually below 2 l/min), the range of measurement selected for every MFC is shown in table 3.4

Controlled gas	Flow Range (ml/min)
O_2	2-100
CO_2	3-150
CO	2-100
NO in N_2 at 4.75%	2-100
CH4 in N_2 at 4.76%	2-100
N_2	80-4000

Table 3.4. MFC range of measurement

Once selected the proper flow for every gas, they collect in the mixing chamber –see figure 3.25-. Since stationary flows were considered not possible, this chamber does not contain any special geometry for turbulent flow generation.

Although the system was designed to control the humidity, obtained in a similar way than the former test station, no measurements with humidity were done yet due to satisfactory results of dry gas measurements.

3.5.2.3 Test chamber, the problem of temperature

In spite of the simple sensor sockets, which are encapsulated in a 50 mm-length hexagonal embodiment with a M18 x 1.5 thread, some requirements with the measurement temperature make difficult the design of the test chamber design.

The simulation of exhaust temperatures requires the heating of the simulation gases of at least 500-600°C. The low thermal capacity of gases, especially N_2, seems to indicate that it is easy. Nevertheless, two factors play against this heating. The first is that the speed of the gases in the pipeline is very high, therefore although the molecules could *see* a high thermal radiation, the average thermal equilibrium between the radiation and the gas is not reached. The second factor is that as soon the low thermal capacity makes easy to heat a gas, it makes easy the cooling. Consequently, a high volume of mass, such the measuring chamber or the pipeline, reduces dramatically the temperature of gases. Both reasons indicate that the heating process should be done in
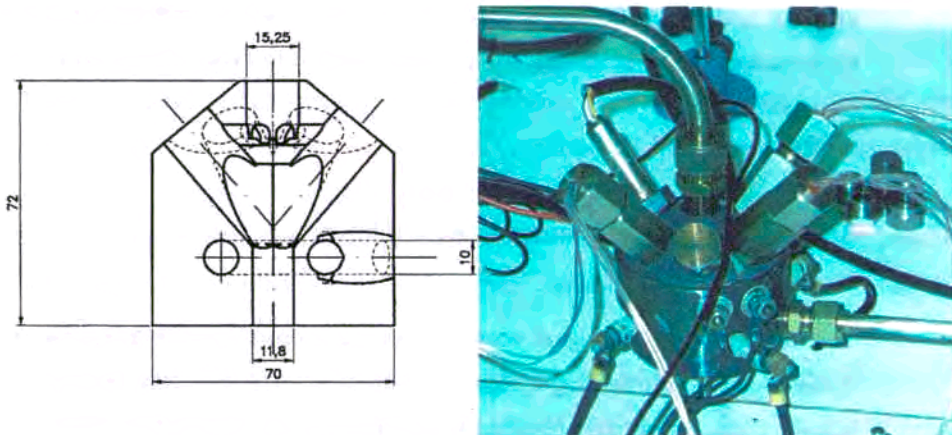
Figure 3.27. Measuring chamber. Left, scheme. Right, photograph. This test chamber allows measuring 6 sensors, two heating systems and thermocouple reading as well gas inlet and outlet.

the measuring chamber and considering maximum thermal exchange efficiency solutions.

These considerations were implemented in a design of test chamber that holds two different kinds of heating systems. The first consists in a set of four heaters for diesel combustion. These heaters are specially designed for the heating process of gases for the diesel engine, therefore it was expected that the thermal exchange efficiency were high enough. These heaters were fed by DC power supply.

A second step of heating consists in a heating brace around the chamber (as indicated in figure 3.27). This heater allows to heat the whole chamber, therefore we can overcome thermal loses in the measuring chamber. A computer controlled this heater in a similar way than the system shown in the pulverisation coating (section 3.4.2.1). Moreover, with this last heater the system becomes fully controllable by computer since the first *diesel* heaters acts as a first stage of heating and the temperature is fine tuned by this last PC-controllable system.

These solutions become fully satisfactory. After the implementation of both kinds of heaters, temperatures above 550 °C were reached. Although probably higher temperatures can be produced, we have not tested it to avoid damage in the measuring chamber.

3.5.2.4 Acquisition, control and software

The acquisition of the signal coming from the sensors as well as the control of the system –MFC and heating system- was implemented by using analogue computer boards. These boards were installed in a PC (Pentium II, 120 MHz).

For the outputs –see scheme in figure 3.27-, ISA-bus D/A board CIO DAC-16 from Computer Boards was used. This board has 16 channels, in single mode use (common hearth), with independent D/A convert per channel. The resolution of this board is 16 bits. An interesting characteristic of this board is that it can work at

different ranges: ±10V, ±5V, 0-10V, and 0-5V. In this application the card was configured for 7 outputs in the range 0-5V to consign the 7 MFC (in the figure 3.26 they are noted by the letters *a* to *g*). Another output 0-5V consigns the temperature to the temperature controller (noted as *h*).

The input were performed by ISA-bus A/D board CIO-DAS1602/16 from Computer Boards. This board has 16 single-ended channels for read and additional 2 analogue output channels. Its resolution is 16 bits, and nominal sampling rate is 100KHz/channel. The available ranges are: ±10V, ±5V, ±2.5V, ±1.25V 0-10V, 0-5V, 0-2.5V, and 0-1.25V. For our application, the range was selected ±5V in all the channels. The implemented channels were 7 inputs for the measurement of the MFC flow (in the scheme noted with numbers from *1* to *7*), 1 input for the thermocouple -in this case Dataforth signal conditioner was needed for the adaptation of thermocouple 0-50mV to 0-5V- (noted with number *12*), 6 input correspond to the signal of the 6 sensors of the measuring test (noted as *I, II, …*). In the scheme of figure 3.25, *0* is the common hearth for input and output.

Hewlett Packard visual language of programming (HP-VEE 5.0) was used for the control of such boards as well for the in-situ visualisation of the obtained results, actual concentrations of gas and further analysis of the results.

The program first distinguishes the necessities of the user for the routine addressing. Therefore the core of the program contains three parts (parameterisation, test and analysis of data).

In the first part, the program allow the introduction of sequences of measurements controlling not only the lambda parameter, but the temperature, humidity, timings, purge if needed or the actual concentration of gases in the case of lambda parameter is not desired. The information can be saved and/or executed for the next routine.

The test can be done after the introduction of the former parameters or by reading a set of parameters previously saved. A complete panel allows the visualisation of the whole set of parameters, inputs and outputs for the in-situ verification of function. Once finalised the test, the results are saved in both HP-VEE and ASCII formats.

Finally the use of data analysis routine allows the statistical computation of the data. It is possible to reduce the transients after the introduction of the proper temporisation. The results are showed in the screen and can be printed. These results can be computed with the data once measured or with data previously saved.

3.5.3 Test station for domestic application sensors

Besides the former station, able to measure sensors of exhausts gases, a third test station was designed and constructed. This station should be able to measures sensors for domestic application.

The necessities in this station differ from previous one in two facts. First the gases that should be generated are based on common atmospheres but with small addition of some hazardous or explosive gases, such CO, CH_4 and NO_2. Therefore the control of atmosphere will not based on lambda parameter but in the *ppm*'s of the toxic gas in the atmosphere. A second difference consists in that high temperatures are not needed, but a close control of the humidity and lower temperatures (in the range from 20 to 50°C) are needed since their influence of the gas sensors response, as shown in the previous chapter (section 2.4).

As the design and construction of this test station was posterior to the previous one, most of the original ideas and designs developed previously were implemented again. The use of similar instruments when possible makes this implementation much more easy and we can consider it as a goal in the flexible but proper functionality of the former test station design.

3.5.3.1 Gas generation

The main necessities in the gas generation were that the toxic gases should be measurable in two different chambers, when every chamber measure independent gases or exactly the same composition. In example one chamber should be able to reproduce synthetic air-based atmosphere plus 10 ppm of NO_2 at 80% of relative humidity and the other S.A.-based atmosphere plus 100 ppm of CO and 1000 ppm of CH_4 at 50% of RH.

Requirements on gas ranges were considered taking into account both regulations and scientific test interest. Thus, it was considered necessary to measure until 400 ppm of CO, 1000 ppm of CH_4 and 5 ppm of NO_2 at relative humidity of 80% .

The alternative of injection in a chamber [Yea,97][Llobet,97], was rejected
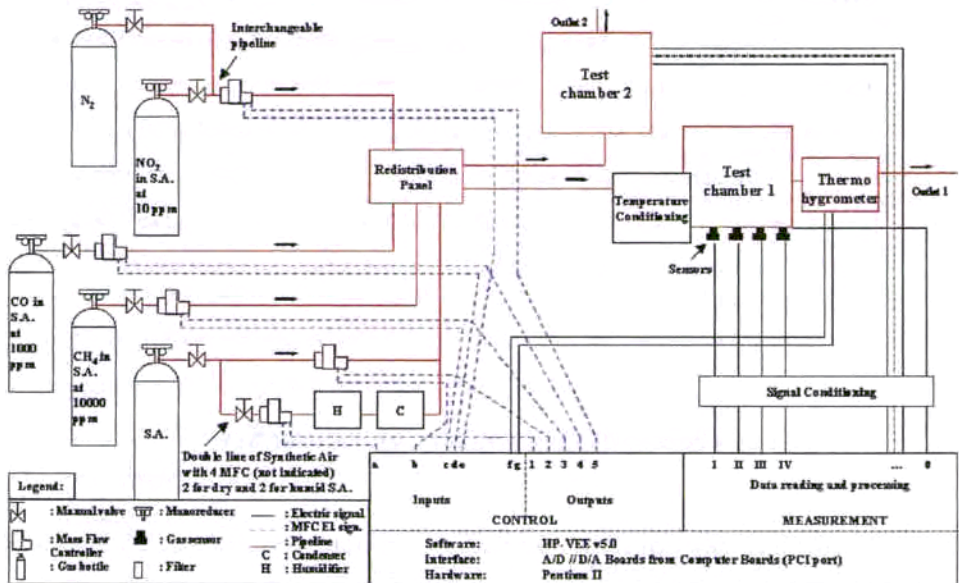
Figure 3.28. Scheme of the test station for domestic sensors. For better visualisation, the double synthetic air pipeline was reduced, only one is shown. Nevertheless, in the actual station, 4 S.A. MFC are implemented, two for the dry S.A. and two for the humidified S.A.

after the satisfactory experience of the construction of the former test station and other similar experiences [Endres,95][Hierlemann,95]

As shown in figure 3.28, similar design in the gas generation to previous test station was followed. Nevertheless, in this case all the MFC were selected in the same range (from 4 to 200 ml/min, the same characteristics to previous station). To obtain the required range, gas bottles contain the toxic gases diluted in S.A. Thus, the bottle of CO contains 1000 ppm of this gas, 10000 ppm for the CH_4 and 10 ppm for the NO_2. This alternative is very interesting when the ranges of measurement are not so well defined than in the previous station. In fact different bottles of the same gases but with different concentrations can be stored in the laboratory for future uses as the gases are a consumable product, nevertheless the use of different range MFC becomes very expensive. Another problem arises when pure bottles are used. As the concentrations required for this kind of sensors are very small, the required flows are very small to, therefore the cost of the MFC unit rise together with its fragility.

As seen in the figure 3.28, the double chamber gas generation was simple obtained with a simple redistribution chamber, that acts as mixing chamber, with different flow keys that allow the pass of the gas by one or another chamber pipeline.

Although the system has been designed to held a carrier gas (synthetic air –SA-) and three toxic gases (CO, CH_4 and NO_2), more gases can be added easily. As probe, N_2 gas line is usually interchanged by NO_2 to perform some experiences.

3.5.3.2 The control of temperature and humidity

For the humidity generation, air bubbling in water [Hierlemann,95][Endress,95] was considered the best solution, instead the direct water evaporation [Vilanova,98] [Llobet,97]. Therefore, when the gas is mixed in the gas distributor it has been already humidified, then it gets into the measuring chamber.
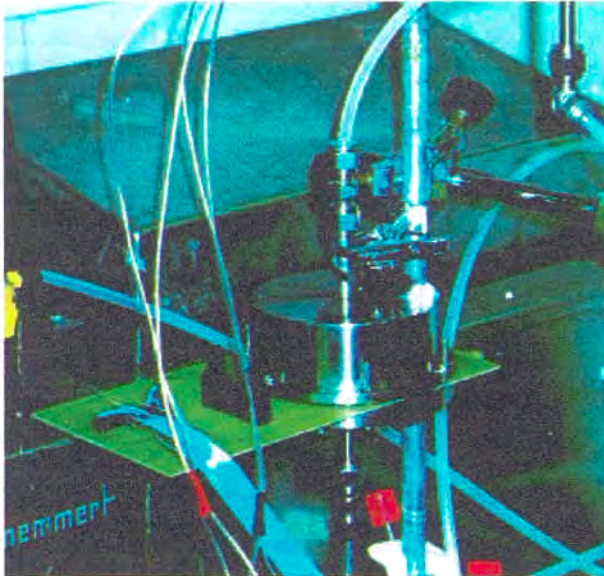
Figure 3.30. Photograph of the measuring chamber.

The design of the measuring chamber minimises its volume (figure 3.30), which is about 200 ml. The group of Dr. Marco has done the original design of this chamber, which was satisfactorily implemented. Since most part of sensors is encapsulated in TO sockets, the chamber contains a PCB board ready to hold these sockets.

After the measuring chamber, the gases collect in a posterior chamber for the measurement of the humidity and temperature. This measured relative humidity becomes a parameter that does not reflect the actual paper of the water in the sensors. The relative humidity is defined as the ratio of the actual vapour pressure in the mixture to the saturation vapour pressure, with respect to the water at the prevailing dry bulb temperature. Although the synthetic generation of relative humidity parameter becomes easy by the direct mix of dry air (0% RH) and air bubbled in water (~100% RH), its actual meaning does not have relation with the actual partial pressure of water, considering the Dalton law.

Therefore a relation that express the absolute humidity (or concentration of water in g/m^3) as function of the relative humidity and temperature is required. For this, it should be considered that the absolute humidity could be expressed as

$$AH = \frac{m_v}{V} = \frac{804e}{P_o} \frac{T_o}{T} \qquad (3.6)$$

where e is the water pressure, T_o=273.15K, and P_o is the atmospheric pressure and T is the absolute temperature. Therefore, the relationship between relative (RH) and absolute humidity (AH) becomes,

$$\%RH = 100 \frac{e}{e_s} = 100 \frac{AH}{AH_S} \qquad (3.7)$$

where the suffix s indicates the saturation in the water pressure and in the saturated absolute humidity. But the saturated water vapour is related with temperature by means of the Antoine equation:

$$\log e_s = A - \frac{B}{C+T} \qquad (3.8)$$

where A, B and C are parameters that depends on the gas. Therefore, a functional expression for the absolute humidity is obtained,

$$AH(g/m^3) = 18000 \frac{\%RH}{100*760} \exp\left\{ A - \frac{B}{C+T} \right\} \frac{1}{0.08205(273.15+T)} \qquad (3.9)$$

Fitting of the parameters A, B and C for the case of water gives values listed in the table 3.5.

Temp. (°C)	Relative humidity (%)										
	20	30	40	50	60	65	70	80	90	95	100
-10	0.47	0.71	0.94	1.18	1.53	1.41	1.65	1.88	2.12	2.23	2.35
0	0.97	1.45	1.94	2.42	2.90	3.15	3.39	3.87	4.36	4.60	4.84
10	1.88	2.82	3.75	4.69	5.63	6.10	6.57	7.51	8.45	8.92	9.39
20	3.45	5.18	6.91	8.63	10.36	11.22	12.09	13.81	15.54	16.40	17.27
30	6.06	9.09	12.12	15.15	18.18	19.70	21.21	24.24	27.27	28.79	30.31
40	10.20	15.30	20.40	25.50	30.60	33.15	35.70	40.81	45.91	48.46	51.01
50	16.53	24.08	33.07	41.33	49.60	53.73	57.87	66.13	74.40	78.53	82.67

Table 3.5. Relationship between temperature (in °C), relative humidity (%RH) and absolute humidity (g/m³). From [Fis,00].

External temperature control should be already improved by the whole climatisation of the chamber [Harvey,89][Hierlemann,95] or by using an inner system of heater and/or cooler –such as Peltier cells- [Auge,95]. The present system that heats the about 20 metres of pipeline before the test chamber present thermal losses, as described in the previous test station.

3.5.3.3 Acquisition, control and software

We used the same kind of A/D and D/A boards than in the former test station, after considering the option of multiplexation [Marco,98]. Specific instrumentation (such as voltmeters or ohmmeters) [Wilson,97][Amrani,96] were disparaged because a new card were needed (GPIB or similar) if PC control would be desired.

The software has been designed in a very similar way than previous station, but the parameterisation does not concern the lambda values but the desired concentration of the gases, a routine for the calculation and verification of the relative humidity values has been added together with an output channel for pulse mode operation of micromechanised sensors.

References

In chronological order

[Tien,75] T.Y. Tien, H.L. Stadler, E.F. Gibbons, P.J. Zackmanidis, "TiO$_2$ as air-to-fuel ration sensor for automobile exhausts" Ceramic Bulletin, 54 3 (1975) 280-285.

[Brettschneider,79] J. Brettschneider, "Berechnung des Luftverhältnisser λ von Luft-Kraftstoffgemischen und des Ein flusser von Messdaten auf λ", Bosch Tech. Berichte, 6 (1979) 4-12.

[McAleer,87] J.F. McAleer, P.T. Moseley, J.O.W. Norris, D.E. Williams, "Tin dioxide gas sensors", J.Chem.Soc., Faraday Trans. 1 (1987) 87 1323-1346.

[Harvey,89] I. Harvey, G. Coles, J. Watson, "The development of an environmental chamber for the characterization of gas sensors", Sensors and Actuators, 19 (1989) 393-405.

[Bozek,92] J. Bozek, "Operating characteristics of zirconia galvanic cells (lambda sensors) in automotive closed-loop control systems" SAE technical paper 920289 (1992).

[Sberveglieri,92] G. Sberveglieri, "Classical and novel techniques for the preparation of SnO$_2$ thin-film gas sensors", Sensors and Actuators B, 6 (1992) 239-247.

[Wu,93] Q. Wu, K.M. Lee, C.C. Liu, "Development of chemical sensors using microfabrication and micromachining techniques", Sensors and Actuators B, 13-14 (1993) 1-6.

[Lampe,94a] U. Lampe, M. Fleischer, H. Meixner, "Lambda measurement with Ga_2O_3", Sensors and actuators B, 17 (1994) 187-196.

[Lampe,94b] U. Lampe, J. Gerblinger, H. Meixner, "Lambda detection with thin-film metal oxides using synthetic exhaust gas mixtures", Sensors and actuators B, 18-19 (1994) 132-137.

[Westbrook,94] M.H. westbrook, J.D. Turner, "Automotive Sensors", Institute of Physics Publishing, Bristol and Filadelfia, 1994.

[Endres,95] H. E. Endres, H.D. Jander, W. Göttler, "A test system for gas sensors", Sensors and Actuators B, 23 (1995) 163-172.

[Hierlemann,95] A. Hierlemann, U. Weimar, G. Kraus, M. Schweizer-Berberich, W. Göpel, "Polymer based sensor arrays and multicomponent analysis for the detection of hazardous organic vapours in the environment", Sensors and Actuators B, 26-27 (1995) 126-134.

[Lavernia,95] E. J. Lavernia, Y. Wu, "Spray atomization and deposition", John Wiley & Sons, Chichester (1995).

[Amrani,96] M. E. Amrani, P. A. Payne, K. C. Persaud, "Multi-frequency measurements of organic conducting polymers for sensing of gases and vapours", Sensors and Actuators B, 33 (1996) 137-141.

[Diéguez,96] A. Diéguez, A. Romano-Rodríguez, J.R. Morante, U. Weimar, M.Schweizer-Berberich, W.Göpel, "Morphological analysis of nanocrystalline SnO_2 for gas sensors", Sensors and Actuators B 31 (1996) 1-8.

[Harris,97] N. Harris, M. Koch, S. Beeby, N. White, A. Evans, "Thick-film printing of PZT onto silicon for micromechanical applications", Mat Lett, 31 (1997) 109-112.

[Hobby,97] A. Hobby, "Printing thick film hybrids", from the DEK printing machines user manual. Similar information available at http://www.dek.com. Useful information is given too at http://www.4heraeus.com/tftech.html

[Kappler,97] J. Kappler, "Herstellung von Halbleitergassensoren durch Sol-Gel Technologie auf Dickschicht basis", Research Thesis (*Diplomarbeit*) at the University of Tübingen (1997).

[Llobet,97] E. Llobet, X. Vilanova, J. Brezmes, R. Alcubilla, J. Calderer, J.E. Sueiras, X. Correig, "Conductance transient analysis of thick-film tin oxide gas sensors under successive gas injection steps", Meas. Sci. Technol., 8 10 (1997) 1133-1138.

[Wilson,97] D.M. Wilson, S.P. DeWeerth, "Signal processing for improving gas sensors response time", Sensors and actuators B, 41 (1997) 63-70.

[Yea,97] B. Yea, T. Osaki, R. Konishi, "The concentration estimation of inflamable gases with semiconductor gas sensors utilizing neural networks and fuzzy inference", Sensors and actuators B, 41 (1997) 121-129.

[Yu,97] K.N. Yu, Y.Xiong, Y. Liu, C.Xiong, "Microestructural change of nano-SnO_2 grain assemblages with the annealing temperature", Physical Review B, 55, 4 (1997) 2666-2671.

[Cirera,98] A. Cirera, "Sensors de Gas Semiconductors: Nou mètode d'obtenció de SnO_2 nanocristal·lí", Research thesis (*treball d'investigació de 3er cicle*) at the University of Barcelona (1998).

[Marco,98] S. Marco, A. Cornet, J.R. Morante, E. Castaño, R. Jané, S. Jiménez, A. Pardo, A. Ortega, A. Cirera, "Smart multisensor integrating methane and carbon monoxide gas detection with improved selectivity by signal processing" proceedings of IGRC'98. San Diego (1998).

[Ortega,98] A. Ortega, "Sistema de test para sensores de gas" Research thesis (*treball d'investigació de 3er cicle*) at the University of Barcelona (1998).

[Segall,98] A. E. Segall, A.N. Papyrin, J.C. Conway, D. Shapiro, "A cold-gas spray coating process for enhancing titanium", JOM, September (1998) 52-54.

[Sheng,98] Lie-yi Sheng, Zhenan Tang, "A low power CMOS compatible integrated gas sensor using maskless tin oxide sputtering" Sensors and Actuators B, 49 (1998) 81-87.

[Sobolev,98] V.V. Sobolev, "Formation of splat morphology during thermal spraying", Material Letters 36 (1998) 123-127.

[Vilanova,98] J. Vilanova, "Estratègies per a l'increment de selectivitat dels sensors de gasos basats en òxids semiconductors. Caracterització dinàmica de la resposta d'estructures multielectròdiques", PhD thesis at the University Politècnica de Barcelona (2000).

[Blaustein,99] G. Blaustein, M.S. Castro, C.M. Aldao, "Influence of frozen distributions of oxygen vacancies on tin oxide conductance", Sensors and Actuators B, 55 (1999) 33-37.

[Cirera,99] A. Cirera, A. Diéguez, R. Diaz, A. Cornet, J.R. Morante, "New method to obtain stable small-sized SnO_2 powders for gas sensors", Sensors and Actuators B, 58 (1999) 360-364.

[Diéguez,99a] A. Diéguez, "Structural analysis for the improvement of SnO_2-based gas sensors", PhD thesis at the University of Barcelona (1999).

[Diéguez,99b] A. Diéguez, A. Vilà, A. Cabot, A. Romano-Rodríguez, J.R. Morante, J. Kappler, N. Bârsan, U. Weimar, W. Göpel, "Influence on the gas sensor performances of the metal chemical states introduced by impregnation of calcinated SnO_2 sol-gel nanocrystals", proceedings of Eurosensors XIII (1999). Accepted for publication in Sensors and Actuators B.

[Gutierrez,99] A.M. Gutierrez, J.A. Díez, S.M. Olaizola, E. Terrón, G. García, E. Castaño, F.J. Gracia, "Influence of the thin film thickness on the methane gas sensor selectivity", proceedings of Sensor'99 (1999) 171-175.

[Olaizola,99a] S.M. Olaizola, "Crecimiento de películas delgadas de SnO_2 mediante pulverización catódica para el desarrollo de microsensores de gas metano", PhD thesis at the University of Navarra (1999).

[Olaizola,99b] S.M. Olaizola, A. Cirera, G. García, A. Cornet, J.R. Morante, E. Castaño, F.J. Gracia, "Fabrication process of methane selective gas sensors", proceedings of CDE'99 (1999) 79-82.

[Kohli,99] J. Kohli, "Niobium pentoxide as a lean-range oxygen sensor", Sensors and Actuators B, 56 (1999) 121-128.

[Arbiol,00a] J. Arbiol, P. Gorostiza, A. Cirera, A. Cornet and J.R. Morante, "In-situ analysis of the conductance of SnO$_2$ crystalline nanoparticles in the presence of oxidizing or reducing atmosphere by scanning tunneling microscopy", Eurosensors XIV (2000).

[Arbiol,00b] J. Arbiol, P. Gorostiza, A. Cirera, A. Cornet and J. R. Morante, "In-situ analysis of the conductance of SnO2 crystalline nanoparticles in the presence of oxidizing or reducing atmosphere by scanning tunneling microscopy", Second International Conference on Scanning Probe Spectroscopy (SPS), (2000).

[Cabot,00] A. Cabot, J. Arbiol, J. R. Morante, U. Weimar, N. Bârsan, W. Göpel, "Analysis of the noble metal catalytic additives introduced by impregnation of as obtained SnO$_2$ sol-gel nanocrystals for gas sensors", Sensors and Actuators B, accepted for publication.

[Cerdà,00] J. Cerdà, A. Cirera, A. Vilà, A. Cornet and J.R. Morante, "Deposition on micromachined silicon substrates of gas sensitive layers obtained by wet chemical route" Proceedings of SGS seminar (2000).

[Cirera,00a] A. Cirera, A. Diéguez, R. Diaz, A. Cornet, J.R. Morante, "Microwave processing for low cost and mass production of undoped and in-situ catalytic doped nanosized SnO$_2$ gas sensor powders", Sensors and Actuators B, 64 (2000) 65-69.

[Cirera,00b] A. Cirera, A. Cornet, J.R. Morante, S.M. Olaizola, E. Castaño, J. Gracia, "Comparative structural study between sputered and pyrolysis nanocristaline SnO$_2$ samples", Materials Science & Engineering B, 69-70 (2000) 406-410.

[Folch,00] J. Folch, "Desenvolupament d'una estació de test per a sensors de gas d'alta temperatura", Research thesis (*treball d'investigació de 3er cicle*) at the University of Barcelona (2000).

[Jiménez,00] I. Jiménez, A. Cirera, O. López, A. Cornet, J.R. Morante, "Innovative method of pulverization coating of previously stabilised nanopowders for mass production of gas sensors", Proceedings of Eurosensors XIV (2000)

[Figaro,00] Figaro gas sensor company, Gas Sensor catalogue and technical information (Figaro and Figaro USA Inc). Information available at www.figarosensor.com

[Fis,00] Fis gas sensor company, Gas Sensor catalogue and technical information (Fis Inc.). Information available at www.fisinc.co.jp

[Vilà,00] A. Vilà, J. Puigcorbé, I. Jiménez, J.R. Morante, "Simulació dinàmica del compartament tèrmic de sensors de gasos micromecanitzats", Trobada transfronterera de Sensors i Biosensors.

4. Nanocrystalline

powder based sensors

4.1 Introduction

Since several years, the scientific and technical community who works on semiconductor gas sensors has been split in those groups developing tin oxide powder for the implementation on alumina substrates (*thick film*) and those groups developing tin oxide layers (*thin film*) for its application on micromechanised and/or integrated sensors.

In the first case, obtained tin oxide can be properly treated and catalysed before implementation on the sensors. Usual technologies to develop tin oxide powders are sol-gel [Sweizer-Berberich,96] or hydrothermal method [Yu,97]. At the contrary, in the case of thin film, obtained in example by means of sputter [Sberveglieri,95], the material control becomes much more complex [Diéguez,96][Sangaletti,97].

Despite this leak of control on material structure properties, in the recent years some industrial initiatives preferred the tin film obtained by means of sputtering in order to take the advantages of low consumption and integration of the silicon substrate technology.

One of the goals of the present work consists into break the distinction between both thick and thin film technologies. As we have presented in the previous chapter, the use of the microprinting and pulverisation coating techniques allow the implementation of fully stabilised sensing material in a micromechanised silicon substrate. Therefore the advantages of powder material control and microelectronic integration are kept.

But for the implementation of sensors, sensing powders are necessary. A revision of the standard technologies suggests that sol-gel (perhaps the most used way to obtain nanosized tin oxide for sensing applications) becomes a long and complicate technology –see subsection 2.2.3.1 from the previous chapter-. Besides, the obtained grain sizes after annealing – about 100 nm after 1000°C 8h treatments [Diéguez,96]- are

higher than desired for sensing applications. It has been suggested grain sizes between 6 and 12 nm as the better grain size rang for sensing applications [Yamazoe,91]. Aside from the physical argument of such calculation, it is widely accepted that a decrease of the grain size improves the sensor performances as more sensing surface is exposed to gas.

In this context we will present two new techniques to obtain nanostructured tin oxide as well as their characterisation and the main characteristics of the sensors developed with these powders. Oxygen vacancies are shown to play an important role on the structural evolution of the powders during the annealing.

As technological summary, the reliability of the obtained powders is verified by means of the microprinting implementation on micromachined substrates. These sensors have shown good performances attending critical aspects of SGS –sensitivity, selectivity, stability and smart consumption-.

4.2 Two new procedures to obtain stable nanostructured SnO₂ powders

4.2.1 Liquid pyrolysis

As stated before, the obtained grain sizes for sol-gel technique are considerable big for its application to gas sensors. This does not imply that the correspondent sensors do not function, but they can probably be improved.

Considering the different technologies for the production of nanoparticles, our feeling was always that spray pyrolysis can produce very small nanosized particles, but two problems arise from technical point of view. The first is the obtained material is attached to the substrate, therefore further treatments should include this substrate. The second, and most important problem, comes from base of the spray pyrolysis technology: a reaction on the substrate that produces the sensing material. In most of cases this reaction produces chloride species. Obviously the production of chloride compounds while depositing implies that integration with silicon technology is forbidden.

To overcome these difficulties but keeping the desired material properties we reproduced pyrolytic reactions in small drops deposited on polished surfaces. By this way its is possible to produce the tin oxide and recover it for its posterior implementation by means of printing, microprinting or pulverisation coating, but without production of chloride compounds during this implementation, which has been evacuated during the material procedure.

Let us explain the details of this procedure in the next subsection.

4.2.1.1 Material procedure

The first step consists in the preparation of a $SnCl_4 \cdot 5(H_2O)$ solution in methanol. Solution concentration was studied in the range from 0.1 to 5 molar. For this process a stirring thermal bath is required.

With the objective to allow the atmospheric oxygen access to the sample and easy chloride evacuation, tensioned small drops of 300µl are deposited on a polished substrate (in our case, silicon wafer was used) by micropipeting this solution.

Then, a thermal treatment is applied on these drops using a muffle furnace. When the thermal treatment is applied, sample undergo the pyrolitic reaction

$$SnCl_4 \cdot 5(H_2O) \rightarrow SnO_2 + 4HCl + 3H_2O$$
$$(4.1)$$
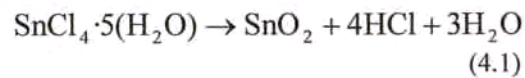
This treatment consists on 24 minutes of heating at the stabilisation temperature reached with a rate of $20Kmin^{-1}$. The stabilisation temperatures studied are in the range from 200 to 900°C.

After the thermal treatment, in the cooling process, it is better to recover the tin oxide at temperatures over $100^{\circ}C$ to avoid water condensation on the sample. An scheme of the process is shown in the figure 4.1.

Figure 4.1. Scheme of liquid pyrolysis process.

From a technical point of view, the use of microdrops seems to be valuable for the evaporation of the chloride from the muffle furnace, but the quantity of material obtained, even by deposition of several drops, does not reach 1g of tin oxide, when the initial solution is 5M (the quantity decreases if less molarity is used). As molarities above 5.5M precipitate, higher molarities cannot be used. So, for the mass production a belt furnace would be required. In order to simplify the procedure, an intermediate step is considering producing material at $300^{\circ}C$ and storing it for further treatments.

The in-situ catalysation of the material has been also considered. For this process solution of $(NH_4)_2PtCl_2$ or $PdCl_2$ in the order of 0.02M are added to the initial solution.

In order to verify the necessity of use of small drops (300µl) in the initial solution, higher volume (20 ml) was alternatively tested. In the following these samples will be labelled *mass production*. The results of the obtained material are shown in the next subsection.

4.2.1.2 Characterisation

Characterisation study allows to known the main features of the tin oxide obtained by liquid pyrolysis. As it can be seen in fig. 4.2, TEM micrographs show the nanometric range of the produced samples. The histograms of the grain sizes –fig. 4.3.- indicate the good sizes (11 and 18 nm) and acceptable dispersions (less than 5 nm).

As shown in figure 4.4, there is a unique crystalline phase (cassiterite –rutile- SnO_2 [JCPDS,97]), which appears above $400^{\circ}C$. The crystallinity of the samples increases when the annealing temperature do, as expected. This is an evidence of the

higher crystalline symmetry as consequence of both a diminution of crystalline defect density and higher grain sizes.
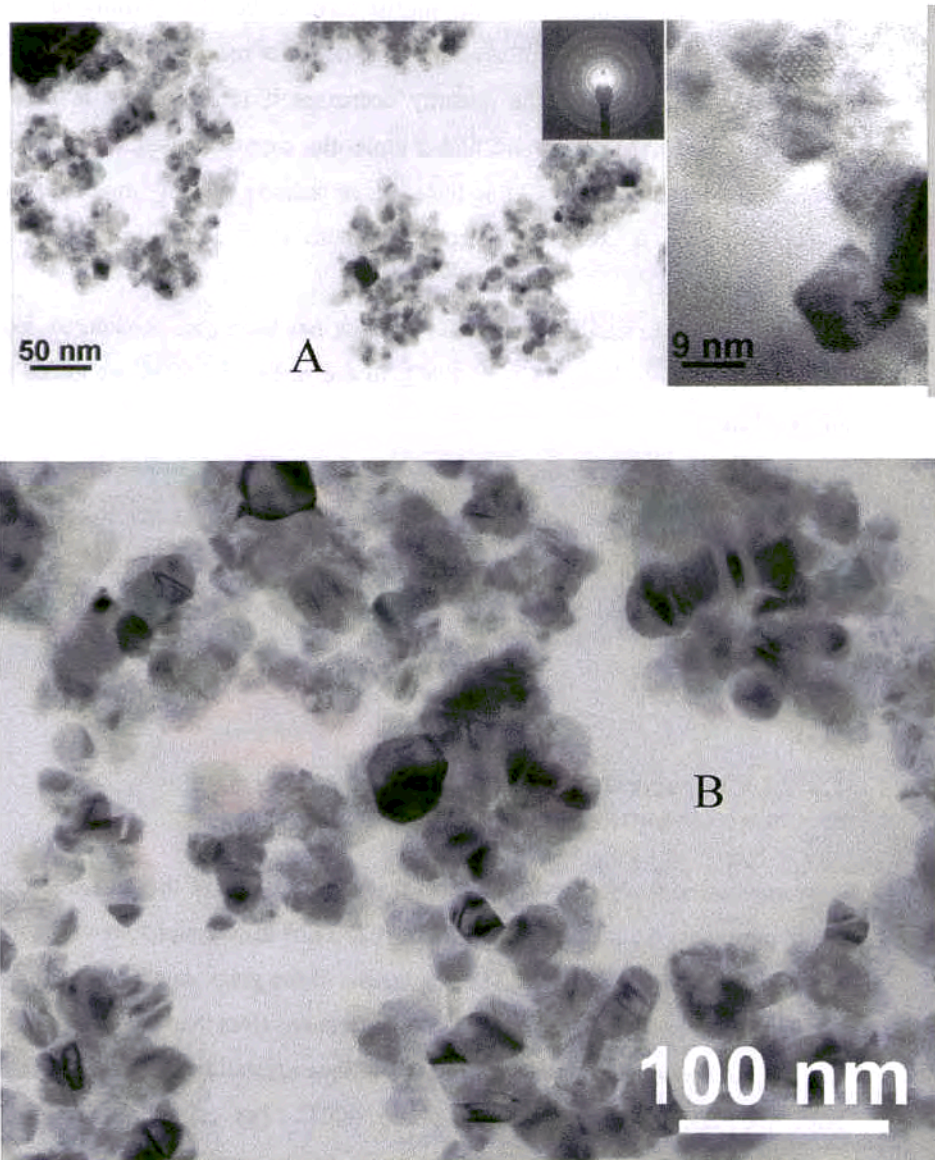
Figure 4.2. Transmission Electron Micrographs of the obtained tin oxide powders. A.- 600°C annealed sample. B.- 800°C annealed sample.
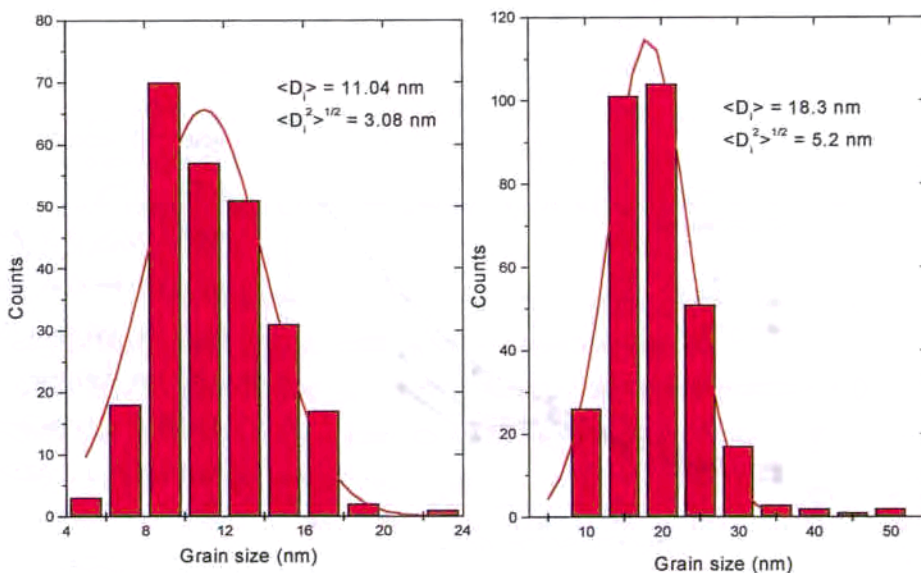
Figure 4.3. Grain size histogram of the $600°C$ (left) and $800°C$ (right) annealed samples.
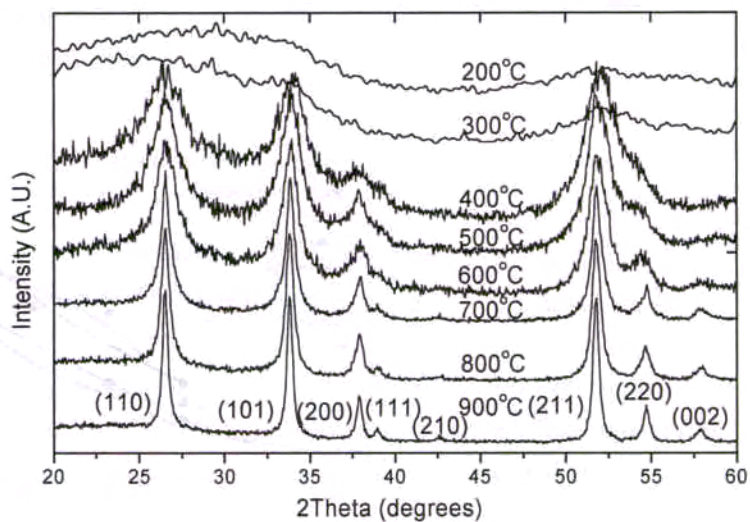

Figure 4.4. X-ray diffractograms of the 5M samples annealed from 200 to $900°C$.

This effect allows computing the grain size by means of the well known Scherrer formula [Bartram,67]:

$$D = \frac{\lambda}{\beta \cos \theta}$$ (4.2)

where D denotes the mean grain size, λ is the wavelength, θ is the angle of the reflection, and β is the ratio between the area and the intensity of the analysed reflection. In figure 4.5, the mean grain size considering different atomic planes is given. Differences between the calculations with different atomic planes are given later. Besides, there is an
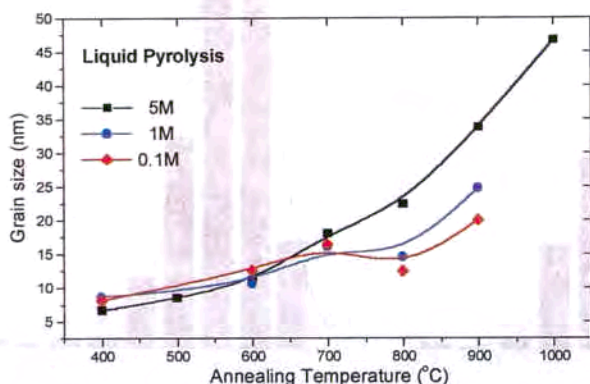
Figure 4.5. Grain size calculated by means of the Scherrer formula versus the annealing temperature for the different studied initial solution concentrations.

Figure 4.6. Grain size calculated by means of the Scherrer formula versus the annealing temperature for the samples obtained by the described process and by means of mass production process.
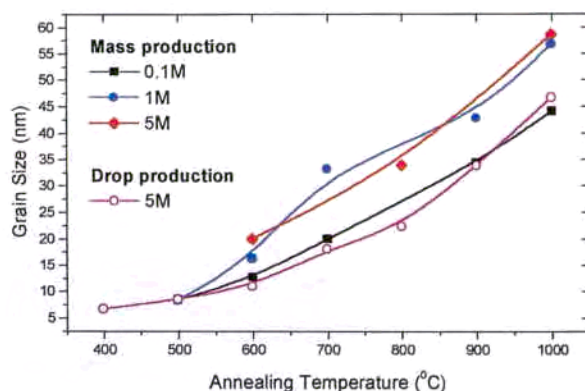
acceptable agreement with the TEM measurements.

The different initial solution concentrations lead to similar grain sizes until 700°C, at this temperature the lower concentrations produces lower grain sizes. This result could be understood as a hindering of the grain size due to the lower tin concentration in the initial solution. A similar result was obtained by Yoo *et al* [Yoo,95]. In that work, grain size decreases when the thickness of the coated sensing layer does.

The chemical composition is inspected by means of XPS. Aside of the tin and oxygen signal, carbon and chlorine signals are also observed –see figure 4.7-. Carbon is common in measurements of most part of pure materials and its presence is due to the surface chemisorption of molecules, being no dependence on temperature. As seen in figure 4.8, its concentration decreases when Ar$^+$ ion gun is applied.
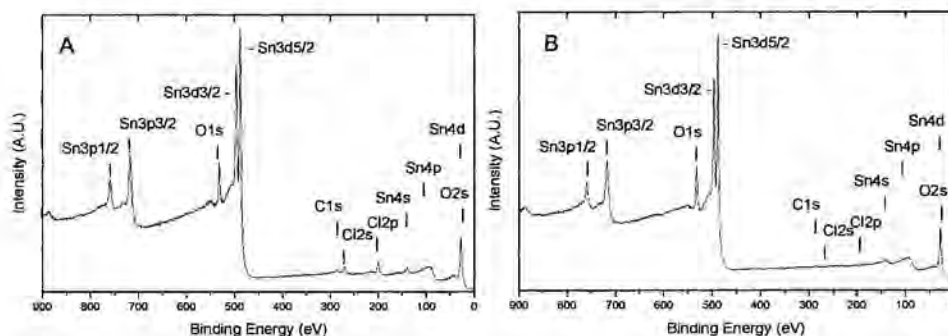
Figure 4.7. X-Ray Photoelectron spectra of 5M liquid pyrolysis samples processed at 200 and 800°C, labelled as A and B respectively..

Chlorine is a rest of the initial solution and its concentration decreases as annealing temperature increases. Above 700°C, its concentration lies within the detection limit of XPS (~0.1%). It is found that its concentration decreases when the ion gun is applied. Again, this fact indicates that these chloride compounds are mainly placed at surface. It

is worth to note how even at lower annealing temperature, the chlorine concentration is less than a 5%.

Despite of the difficulties for measuring the stoichiometry of tin oxide due to chemisorbed specimens, data indicate coherent values with that presented by the SnO_2 reference powders (Degusa 99.999% SnO_2 powders).
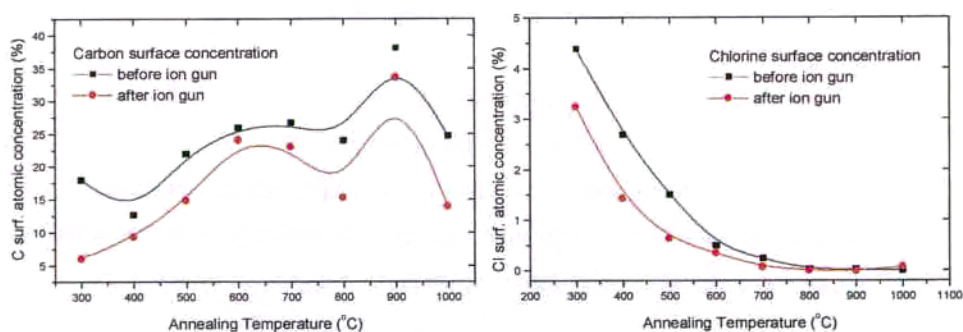

Figure 4.8. Surface atomic concentration measured by XPS as function the annealing temperature. Left, carbon. Right, chlor.

Under our view, the nanometric range of the obtained powders –shown by either TEM and XRD-, the proper crystallinity –shown by XRD-, and these XPS results about the chemical composition denotes the reliability of the present technique.

Annealing Temperature (^{0}C)	Grain Size (nm)	Grain Size (nm) after posterior annealing 450^{0}C 8h	Grain Size (nm) after posterior annealing 1000^{0}C 8h
400	7.0		
500	8.4	9.3	51.8
600	10.8		
700	16.9	16.3	53.8
800	22.9		
900	33.0	31.9	52.8
1000	46.7		

Table 4.1. Grain size calculated by Scherrer formula [Bartram,76] of the liquid pyrolysis samples obtained at different temperatures and post-annealed at 450 and 1000°C during 8h.

Nevertheless, the use of such material for sensing applications requires the verification of further aspects, such as the stability with further annealing treatments and the compatibility with catalysation procedures.

For the first analysis, selected samples were exposed to further annealing at 450 and 1000°C during 8h. The analyses indicate that in the case of 450°C annealing the effects on microstructure are negligible. Grain size, as exponent of the nanocrystallinity, keeps similar values –within the error of the Scherrer formula, that is believed to be about 2 nm-. In the case of 1000°C, higher grin size is obtained when the second treatment is applied –see table 4.1-.

After catalysation, microstructural properties do not seem to be highly affected and the surface concentration is inspected by means of XPS. Figure 4.9 shows how the concentration palladium increases with the annealing temperature and platinum decreases. Two mechanisms can be considered when catalysing nanoparticles with a noble metal.

By one side, the grain growths and, therefore, the specific surface decreases. If the additive is homogeneously distributed on the surface, the thickness of such coating should increase when grain size does. A surface technique, such a XPS with an excitation depth of 10-20 Å depending on material, reads more concentration when the thickness of the coating increases.

An additional involved phenomenon consists on the energetically favourable formation of metallic clusters –even until the micron size-. In this case, the coating is reduced as most part of the material lies in the cluster and, therefore, XPS gives less atomic concentration.

While in the case of palladium the first mechanism seems to be more important, some SEM observations –such as that in figure 3.2- indicates that platinum easily forms clusters in cuboctahedrical crystals.
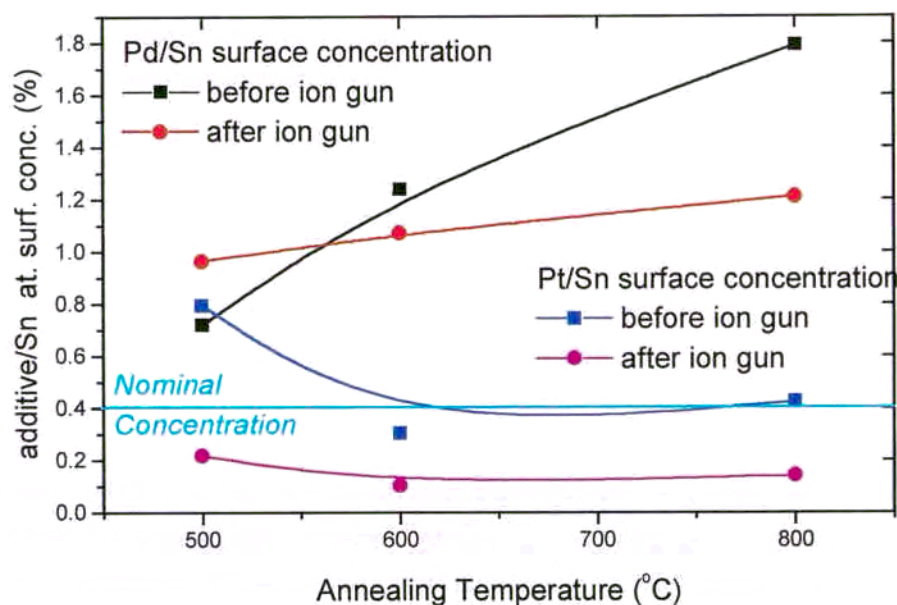
Figure 4.9. Catalyst concentration for samples annealed at 500, 600 and 800°C.

Different chemical contributions to palladium XPS signal can be considered. In fact, palladium comes from $PdCl_2$, but other oxidised states (PdO and PdO_2) together with metallic states could be also found.

Chemical compound	Pd metallic	PdO	PdO_2	$PdCl_2$
State	Pd^o	Pd^{2+}	Pd^{4+}	Pd^{4+}
Binding energy (eV)	334.9-335.4	336.1-336.5	337.7-338.2	338.1-338.6
Concentration in Liquid Pyrolysis samples				
500°C	very low	~29%	very low	~70%
600°C	very low	~30%	~38%	~30%
800°C	~15%	~32%	~34%	~15%

Table 4.2. Chemical states identification in liquid pyrolysis Pd-catalysed samples. Binding energy data from [Wagner,78].

In spite of the difficulties to fit 4 contributions in a peak, we have found some results that seem to keep logical sense and are in agreement with previous results [Cabot,00]. As seen in table 4.2, the $PdCl_2$ diminishes with the annealing temperature.

The apparition of oxidised forms seems to indicate that chloride compound decomposes into ionic states and then oxidises. The concentrations shown in table 4.2 suggest that $PdCl_2$ first transforms in PdO. Then, at higher temperature, a part of the PdO is oxidised into PdO_2. At $800°C$, the remaining PdO transforms both in Pd and PdO_2. An investigation of the XRD data does not suggest the apparition of none of these compounds in measurable quantity.

This behaviour of Pd, transforming first from chloride to oxide ($Pd^{4+} \rightarrow Pd^{2+}$) and then from this state into both double oxidised and metallic ($Pd^{2+} \rightarrow Pd^{4+}$ and $Pd^{2+} \rightarrow Pd^0$), becomes strange. Nevertheless, some thermodynamic data [Bard,76][Lide,97], indicate that the Gibbs free energy for the PdO_2 is too high compared with PdO. In fact, using water as reducing-oxidising vehicle, we found the following chemical potentials:

$$
\begin{aligned}
Pd^{2+} + 2e^- &\rightarrow Pd & \mu &= 0.951 \text{ V} \\
O_2 + 4H^+ + 4e^- &\rightarrow 2H_2O & \mu &= 1.229 \text{ V} \\
PdO + 2H^+ + 2e^- &\rightarrow Pd + H_2O & \mu &= 0.79 \text{ V} \\
PdO_2 + 2H^+ + 2e^- &\rightarrow PdO + H_2O & \mu &= 1.263 \text{ V} \\
PdO_2 + 4H^+ + 2e^- &\rightarrow Pd^{2+} + 2H_2O & \mu &= 1.194 \text{ V}
\end{aligned}
\tag{4.3}
$$
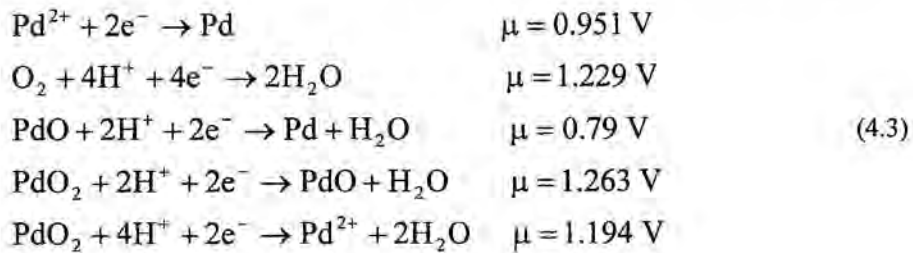
This data indicates a certain stability of the form PdO. The energy to transform Pd into PdO_2 is very high, therefore the only way of transformation could be from Pd^{2+} to PdO_2, as stated above.

Despite the easier chemical state identification for platinum, its signal is lower than palladium and quantification of compounds is more difficult. Nevertheless, some trends

are clearly observed in the spectra. While at lower temperature (500 and 600°C) the dominant orbital is Pt^{2+}, at higher temperature Pt^{4+} becomes still the only one contribution. In the case of higher temperature the identification of the orbital seems to coincide with PtO_2. For lower temperature there is uncertainty between PtO and the $(NH_4)_2PtCl_2$ catalysing compound. Nevertheless XRD data indicates the presence of metallic platinum at the three temperatures. This data suggest that low temperature XPS data (500°C) could show the oxidised external shell of a metallic particle or well there would be an instrumental shift of the data.

Another interesting topic to study is the electronic interaction between tin oxide and catalyst. Valence band measurements from XPS allows us to verify the states lying between the Fermi level and the top of the tin oxide valence band. The addition of such noble metals introduces states in the forbidden
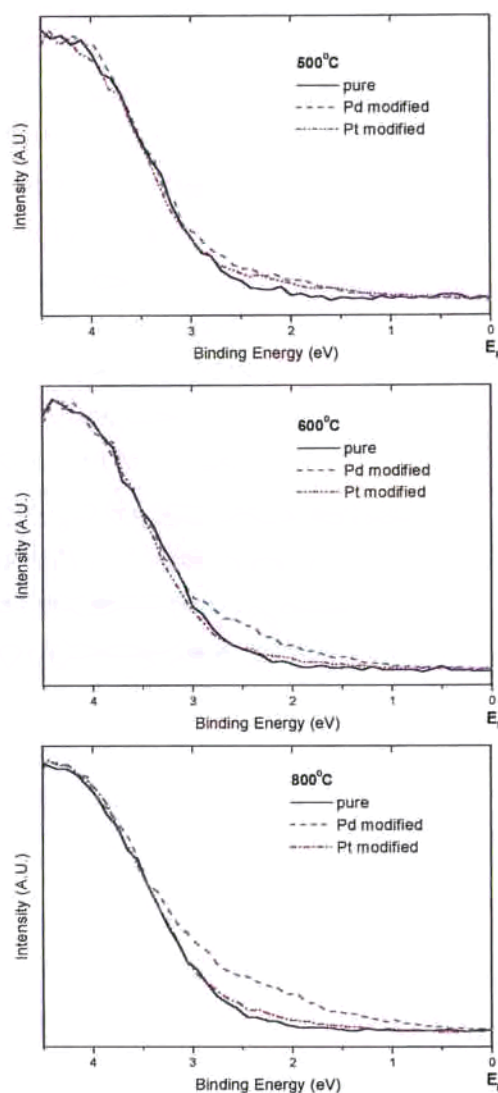
Figure 4.10. Detail of the valence band maximum for the catalysed samples at 500, 600 and 800°C. Pure tin oxide sample is plotted as reference. The samples have been sifted to reach all the similar VBM in order to observe better the states in the band gap. The origin of these shifts will be discussed in section 4.3.

bands, with respect liquid pyrolysis SnO_2 pure powders. As it can be seen in figure 4.10, both Pd and Pt modified SnO_2 exhibit states between 1 and 2 eV below the Fermi level. When increasing the temperature the relative density of such states becomes higher for Pd, whereas they almost vanish for Pt-modified SnO_2.

This data could corroborate the different interaction with SnO_2 that the two studied catalyst undergo. While Pd seems to be more related with SnO_2 structure, even coating the metal oxide, Pt seems to form metallic clusters.

To verify the feasibility of the use of such nanoparticles for gas sensor applications, some sensors were coated by printing on alumina substrates. Test, performed with CO, CH_4 and NO_2, reveals good sensor performances.
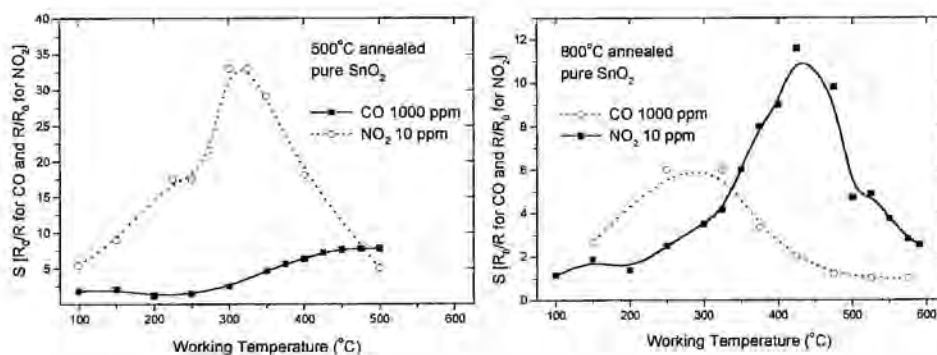
Figure 4.11. Response of liquid pyrolysis pure tin oxide sensor to CO and NO_2 as function of the sensor working temperature. Left, sensor coated with $500°C$ annealed powder. Right, with $800°C$.

Pure tin oxide exhibit usual sensitivity with the working temperature –see figure 4.11-. Whereas tin oxide powders obtained at $800°C$ are more sensitive to CO (working at $425°C$), those obtained at $500°C$ are more sensitive to NO_2.
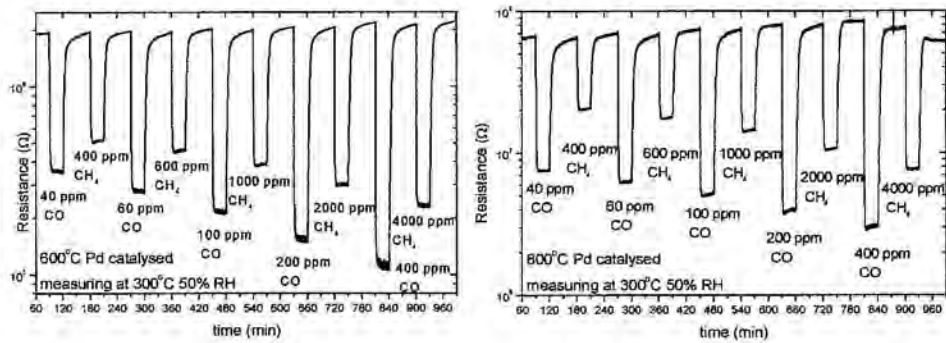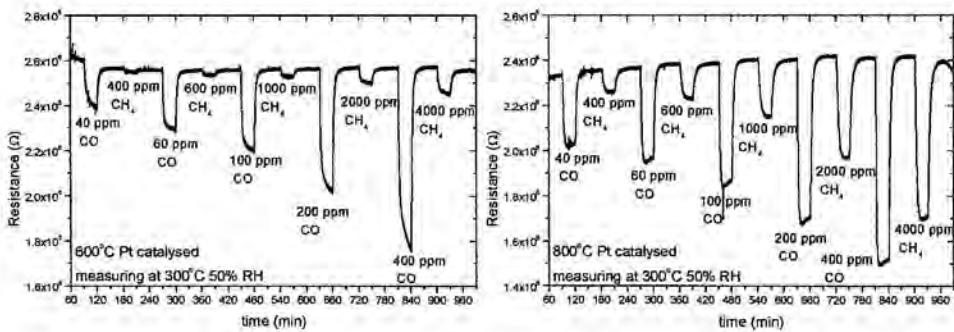
Figure 4.12. Response Pd catalysed liquid pyrolysis tin oxide sensors obtained at 600 (left) and 800°C (right) as function of the gas concentration –CO and CH$_4$-. Working temperature is 300°C in both cases.

To evaluate the performances of the catalysation, catalysed powders previously introduced were tested. As seen in figure 4.12, sensors based on Pd catalysed tin oxide exhibits good sensing properties to CO and CH$_4$ even at relative low temperatures (300°C). When powders have been annealed at higher temperature, higher resistance

Figure 4.13. Response Pt catalysed liquid pyrolysis tin oxide sensors obtained at 600 (left) and 800°C (right) as function of the gas concentration –CO and CH$_4$-. Working temperature is 300°C in both cases.

appears. In fact, these results could be related with the higher forbidden state density obtained shown in figure 4.10. In fact, higher density of acceptor states should be charge compensated with a higher surface bending, leading to higher Schottky barrier and resistivity of the material.

Sensors become sensitive to both CO and CH_4, but the use of the sensor in other temperatures would break the symmetry in the response, leading to higher selectivity.

In the case of platinum, the response is much more selective. As shown in figure 4.13, the response of the sensors is higher for CO than for CH_4. This fact is specially observed with the $600^\circ C$ annealed powder sensor, however, this sensor exhibit some drift in the response to CO. Probably this drift is associated with the low annealing that this powders undergo. In the case of $800^\circ C$ annealed powders, the response is more stable.

Despite the gas concentration becomes perfectly measurable with these sensors, it is interesting to observe how the baseline resistance and the sensitivity have strongly reduced with respect palladium catalysed sensors. Although the mechanisms of gas sensitivity with catalysed sensors not yet well understood, this decrease of the sensor performances could be related with the Pt clustering that we have measured by XPS and XRD in these samples.

4.2.2 Microwave treatment

For several years, many research works and commercial products have sought to exploit the properties of nanocrystals as a constitutive material in the sensitive layer for gas sensors.

However, achieving smaller grain sizes also requires a close control over the other characteristics of nanocrystals. If such control is not maintained, then sensor properties such as stability, sensitivity and sensor response to different gases is not the same from batch to batch or from laboratory to laboratory [Göpel,95].

Moreover, some of these processes require high energetic budgets and are time consuming, aspects that make them unsuitable for the mass production of these gas sensors. In the case of liquid pyrolisis, in every batch we obtain less than 1 gram. Despite this quantity is enough to coat hundreds of micromachined sensors, some powder treatments requires higher quantities of sensing material. In example, grinding needs 2g at lest to avoid contamination coming from mug and balls.

To overcome these difficulties, alternative technological processes need to be developed to simplify existing ones or to improve on present methods. Thus, today, major efforts are being directed towards achieving a high level of performance of the applied technology even for the well-known SnO_2 sol-gel process. Steps such as precursor fabrication, addition of catalytic metals, and thermal treatment are time consuming and also require high energetic budgets when implemented industrially.

This section describes the use of microwave radiation to obtain SnO_2 nanocrystalline powders in a rapid manner while keeping costs as low as possible. Our aim is to reduce the processing time and, hence, the energetic budget, as demonstrated for other materials and applications [Sutton,89][Clark,96], without losing all the desired nanocrystal properties and the characteristics required for good-performance gas sensors such as grain size control, grain surface states and property modifications due to the catalytic metal addition, baseline resistance level in air, sensitivity and stability. Pure and in-situ platinum and palladium catalysed sensors were produced using this procedure based on microwave radiation treatment. Their response under gas is reported and discussed, confirming the suitability of this method.

4.2.2.1 Material procedure

Briefly, the microwave procedure consists on the irradiation with microwaves of a solution containing the tin chloride plus the chloride compounds of the catalytic additives. After this irradiation, pseudo-crystalline tin oxide is obtained and need to be stabilised.

The microwave radiation is applied to saturated tin chloride pentahydrate ($SnCl_4 \cdot 5(H_2O)$) solution in methanol (5.5 M) to obtain the tin oxide nanopowder precursors. In-situ catalysed powders were obtained by adding chloride compounds of Pt and Pd ($PdCl_2$ and $(NH_4)_2PtCl_4$) to the tin chloride solutions, in quantities that ranged from 0.2 to 10% of atoms, as the standard catalytic agent for CO and CH_4 sensing [Schweizer-Berberich,96].

For this process a specially modified microwave oven was used. One of the main technological limitations consists on the evacuation of chloride compounds, which need to be expulsed out of the microwave oven by means of capillary tubs[1]. The radiation applied had a wavelength of 2.45 GHz and a power up to 1KW for times below 10 minutes. This wavelength, tuned with the molecular vibration of water, is specially indicated for the use on $SnCl_4 \cdot 5(H_2O)$, and it is expected that water desorption gives energy enough to remove certain amount of chlorine.

Further stabilisation treatments on materials were developed applying conventional thermal annealing from 450 to 1000°C for 2 and 8 hours, as is usual in other technologies such as sol-gel [Diéguez,96].

---

[1] The corresponding holes on the microwave wall should have a diameter smaller than the wavelength of the microwaves. When higher diameters are performed on the oven, Faraday box is appreciated to avoid microwave emission.
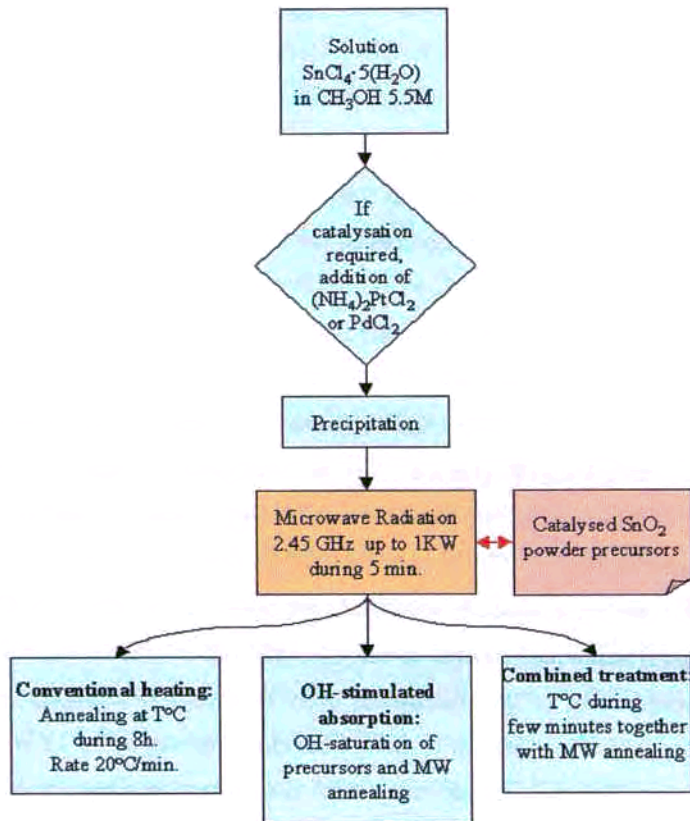
Figure 4.14. Scheme of microwave process.

Other microwave-based stabilisation treatments were considered in order to compare the reliability of new procedures: i.- OH-stimulated microwave absorption, and ii.- Combined microwave and usual thermal radiation (combined treatment). See in figure 4.14 a scheme of the microwave process.

In the first case (OH-stimulated), microwave absorption was stimulated by means of OH-group saturation of material. For this, equivalent quantities of bidistilled/deionised (Elix/Millipore) water and SnO_2 precursors are mixed. This process was repeated as many times as was necessary to stabilise the material.

In the second case, the combined process, microwave radiation was applied together with thermal radiation up to 700°C, the usual temperature for such materials [Martin,98]. A ceramic heater is mounted in the microwave oven in order to heat an alumina crucible exposed to the microwave irradiation.

4.2.2.2 Characterisation

For the precursor procedure, small-sized and unstable SnO_2 was obtained. As absorption of microwave energy varies with the composition and structure of material [Sutton,89], the process becomes self-limiting when no thermal treatment is applied simultaneously with microwaves. Whereas in other technologies there is a slow production rate, here the cost was kept low as the process is rapid.
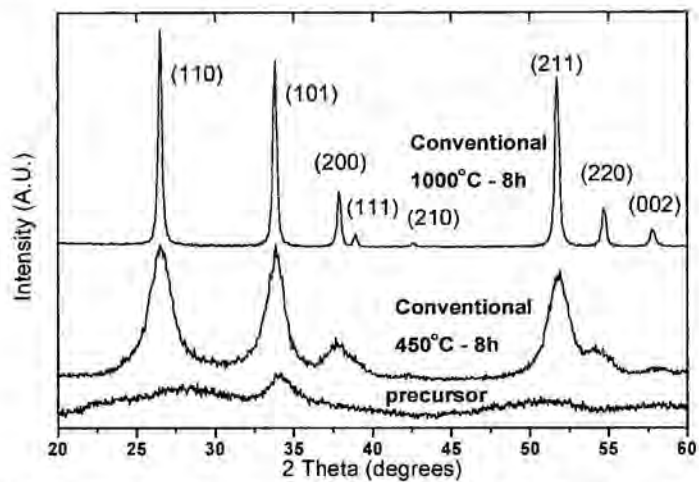
Figure 4.15. X-ray diffractograms of precursors and SnO_2 powders after conventional stabilisation.

After conventional thermal heating, the material exhibits the usual SnO_2 cassiterite diffraction pattern, as shown in figure 4.15. Usual X-ray intensities are found for all reflections [Cirera,99][Diéguez,96]. From the wide refraction peak of diffractograms, it can be deduced that lattice distortions are present in 450°C- treated material [Cirera,99]. The presence in the FTIR spectra -figure 4.16- of OH in a smaller concentration than SnO_2 signal suggests a good efficiency of the microwave process. Nevertheless some concentration remains at surface after the microwave treatment. In fact, one can expect the presence of water or surface hydroxyls even at 400-440°C [McAleer,87] [Korotchenkov,99]. Further conventional treatments are able to reduce such water content. Similar results were obtained with in-situ doped material.
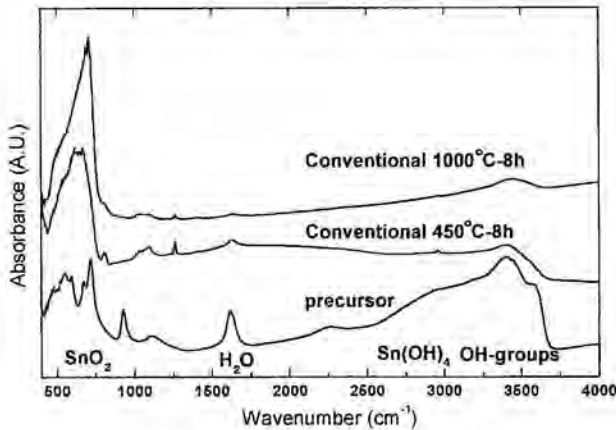
Figure 4.16. FTIR spectra of precursors and SnO_2 powders after conventional stabilisation.

TEM micrograph of 1000°C-treated pure material is shown in figure 4.17. As it can be seen, faceted surfaces are found in nanocrystalline grains indicating highly stabilised material. The presence of mainly planar defects (twins and stacking faults) indicates the coalescence of grains at this temperature. Despite this coalescence, the grain size is relatively small (about 60 nm), approximately half the value obtained using other techniques [Diéguez,96]. This result indicates that the growth of material keeps similar value to that obtained by liquid pyrolysis after annealing at 1000°C for 8h.
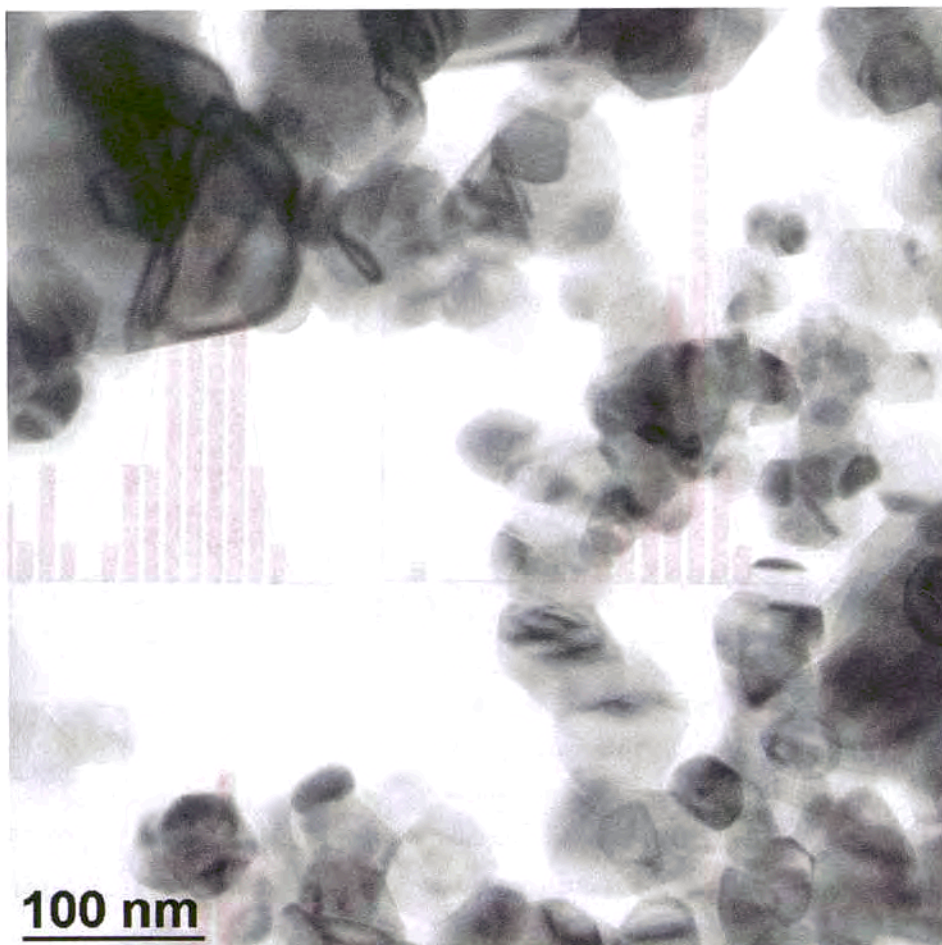
Figure 4.17. TEM microgaph of microwave pure tin oxide conventionally stabilised at 1000°C for 8 hours.

TEM micrographs allow us to compute the statistical grain sizes. The distribution was obtained, as we can see in figure 4.18, with a mean of 55 nm for pure powders. Similar values were obtained for 0.2% Pt in-situ catalysed tin oxide, but were slightly higher (66 nm) for palladium. In the later larger nanoparticles were observed. We also observed that in the case of catalysed samples there was an increase in the
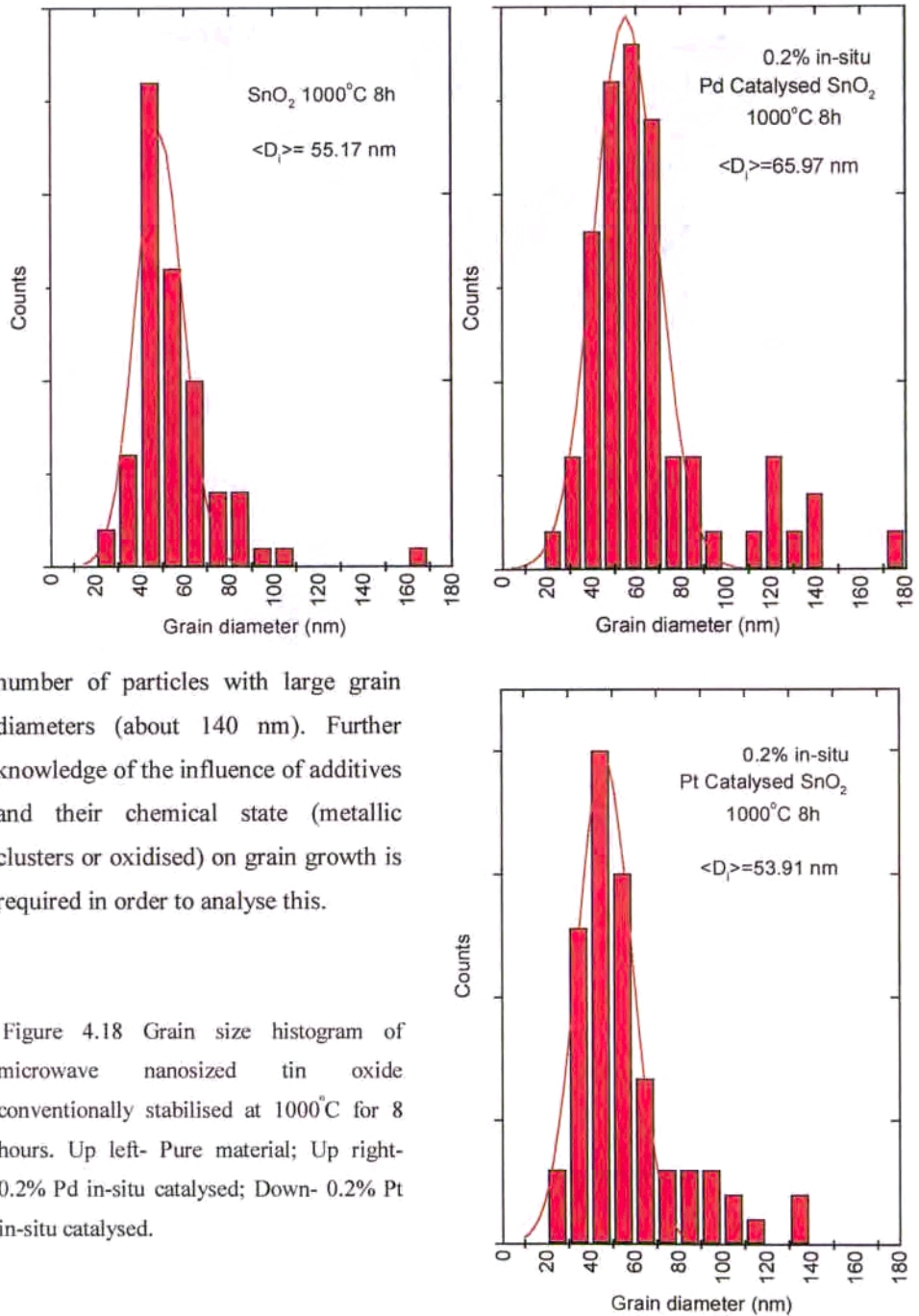
number of particles with large grain diameters (about 140 nm). Further knowledge of the influence of additives and their chemical state (metallic clusters or oxidised) on grain growth is required in order to analyse this.

Figure 4.18 Grain size histogram of microwave nanosized tin oxide conventionally stabilised at $1000°C$ for 8 hours. Up left- Pure material; Up right- 0.2% Pd in-situ catalysed; Down- 0.2% Pt in-situ catalysed.

Nevertheless, we expect that the sensitivity is not so much influenced by the new grain size distribution as by the catalytic effect related to the presence of additives.

Thus, the results indicate that in-situ catalysation interacts with the microstructure of the grain. As suggested by other autors [Matsushima,88], this interaction of catalytic agents at the grain surface induces a surface band bending of nanocrystal electronic levels towards higher energies. Therefore, this bending of electronic levels also gives rise to a higher Schottky barrier. Consequently, conductivity between grains, dominated by the Schottky barrier mechanism [Bârsan,94], falls and hence the resistivity of catalysed tin oxide is usually higher.
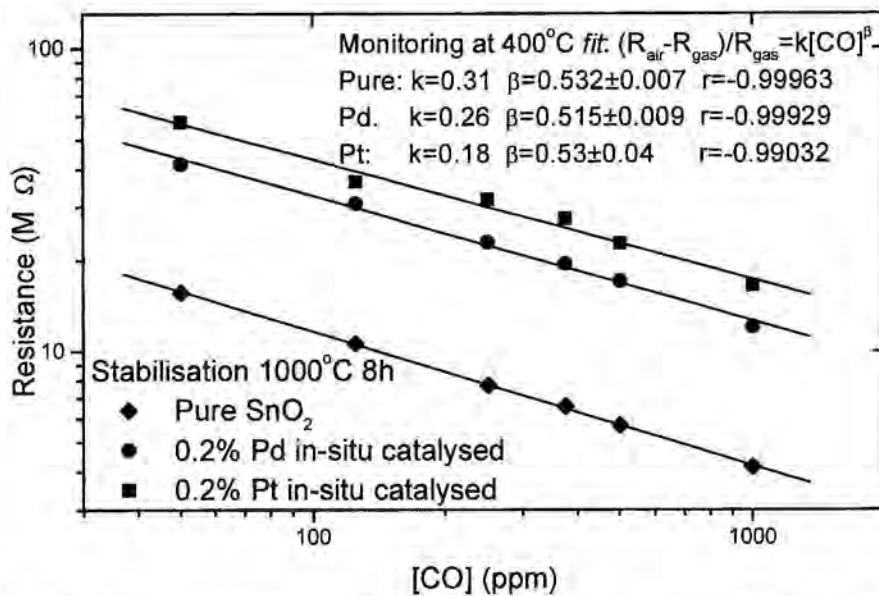
Figure 4.19. Resistance of pure, Pt and Pd in-situ catalysed sensors. Resistance dependence with CO concentration has been fitted according with equation (4.4).

Here, see figure 4.19, Pt and Pd catalysed material exhibited higher resistance (after dc resistance measurements) for a wide range of CO concentrations (from 0 to 1000 ppm

in synthetic air and without humidity) indicating interacting surface catalytic effects. We check the fit of these results to a previously reported model [Hensaw,96],

$$\frac{R_{air} - R_{gas}}{R_{gas}} = k[CO]^{\beta} \tag{4.4}$$

As seen in this figure, the slope of fit in graph (β) indicates the gas-material reaction model. Similar β values for sensors suggest non-effective catalysed sensitivity to gas. In fact, results of catalysed sensitivity can be found at lower temperature.

Figure 4.20. Sensitivity (resistance in air by resistance in gas) of pure tin oxide and in-situ palladium doped sensors after 500 ppm of CO.
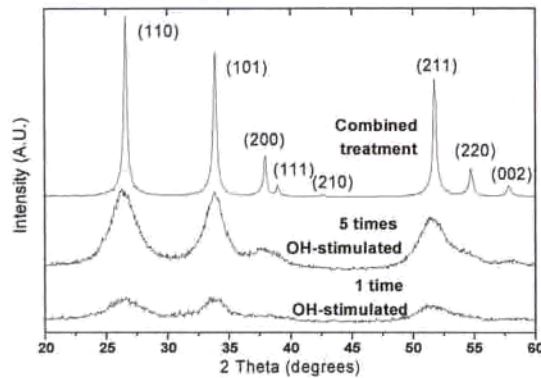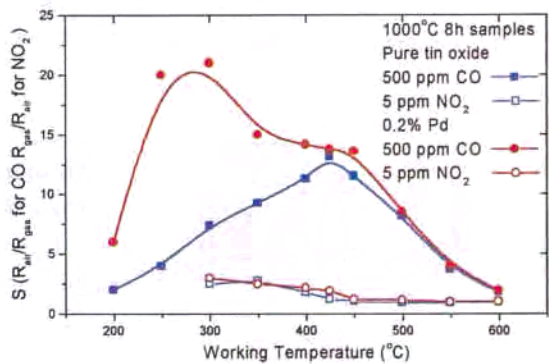
Figure 4.21. X-ray diffractograms of microwave SnO_2 nanopowders (OH-stimulated and combined stabilisation procedure).

As shown in figure 4.20, conventionally treated powders exhibit similar results of maximum sensitivity temperature to CO exposure to those found in the literature [Göpel,95]. Whereas good results were obtained in 1000°C treated powders for pure and palladium in-situ catalysed sensors, the sensitivity of Pt in-situ doped sensors shows unusual behaviour as their response was similar to not catalysed material. We also present in this figure the sensitivity to the

presence of NO_2 (5 ppm in synthetic air without humidity). These results show low cross sensitivity of this gas respect with CO.

Alternative stabilisation procedures were tested. OH-stimulated microwave absorption powders exhibited a cassiterite diffraction pattern (figure 4.21). In this case the 5-time repeated process increased crystallinity. This change in morphology is not continuous as the process is repeated. In comparison with other studies [Cirera,99] or conventionally annealed material (figure 4.15), this process would be equivalent to a 450/500°C conventional annealing procedure. This highlights the limitations for this stabilisation procedure as usual working temperatures are between 200 and 400°C.

Combined stabilisation treatments were much more effective. The diffraction pattern (figure 4.21) exhibited high crystalline structure, similar to samples stabilised conventionally at 1000°C for 8h (figure 4.17). Nevertheless, its control is quite difficult since experimental parameters, such as densification of powders and atmosphere, influence the process [Clark,96][Sutton,89]. In fact, microwave heating differs fundamentally from conventional heating in that microwaves penetrate the material being heated volumetrically. Stabilisation of the bulk temperature is reached during microwave processing since the energy is absorbed by the bulk and dissipated at the surface of the grain, the reverse of heat flow in conventional heating [Vriezinga,98][Tinga,98].

These results indicate the feasibility of microwave procedure to obtain catalysed tin oxide for sensing applications. The study of the stabilisation procedures suggests that whereas OH-stimulated stabilisation treatment does not stabilise material enough for SGS (equivalent reached temperature about 450°C), combined stabilisation treatment do. Nevertheless, the complex experimental set-up and the difficulty of the parameter control could lead in a leak of reliability. As consequence, further work with microwaves uses the conventional thermal annealing for the stabilisation of the microwave obtained material.

### 4.2.2.3 CO-CH$_4$ selectivity enhancement by in-situ Pd-catalysed microwave SnO$_2$

Regarding the structure and sensing models of tin oxide, the cross sensitivity between CO and CH$_4$ is one of the major problems of such oxide due to the same reducing character of both gases. This problem leads to a leak of selectivity.

Nowadays most research is devoted to the study of signal post processing to distinguish both gases using complicate arrays and/or signal treatments algorithms. Some of those treatments based on Principal Component Analysis or Pattern Recognition, uses until 8 sensors [Capone,00][Hahn,00].

Usually SnO$_2$ is modified with the addition of noble catalytic metals (Pd, Pt) in order to increase the CO sensitivity [Schweizer-Berberich,96]. This partial solution implies higher energetic budgets in the technological step procedures.

In the present section we show the use of microwave in-situ catalysation able to control the introduction of catalytic additives even at high levels needed for active filters.

Figure 4.22. Pure SnO$_2$ sensor response heated at 350°C.
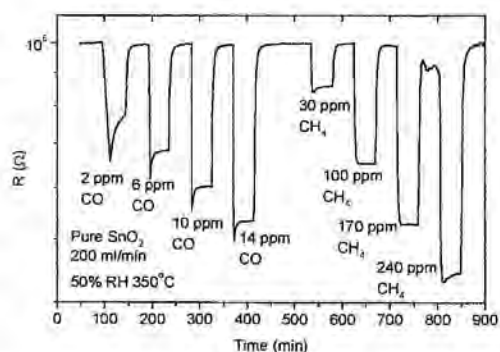
As reference, let us show the result of the electrical measurement for pure SnO$_2$, showing a good response even for low concentration of the target gases (CO and CH$_4$). In fact, tin oxide based gas sensors are appreciated instead other kinds of sensors –such amperometric- by their better analytical sensitivity

at lower concentrations due to their large signal for the initial exposure to gas mixtures [Bârsan,99].

As known, the addition of noble metals increases the sensitivity and selectivity at lower temperature. Although the sensing related phenomena are not well understood yet, it seems quite clear that CO combustion producing CO_2 is associated to these sensing phenomena [Lenaerts,94]. For the case of platinised tin oxide, Henshaw *et al* [Henshaw,96] showed by mass spectroscopy the oxidation of CO into CO_2, this combustion exhibits peaks between 250 and $350^\circ C$.
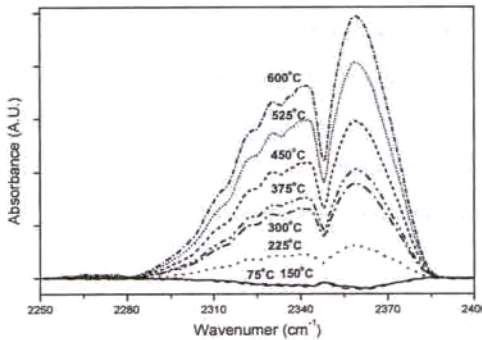
Figure 4.23. FTIR measurements on pure SnO_2 combustion gases at different material temperatures. Spectra are focussed on CO_2 molecular band region.

FTIR measurements allowed the monitorisation of CO_2 production in the CO combustion. For this, the sensing material is exposed to 1000 ppm of CO in synthetic dry air. Outlet gases are collected in an adapted test chamber for FTIR use and vibrational bands are measured in transmittance geometry. In these measurements –see figure 4.23- it can be seen how the CO_2 molecular vibration mode increases with temperature.

Figure 4.24. Normalised CO/CO_2 conversion efficiency as function of FTIR measurement temperatures.
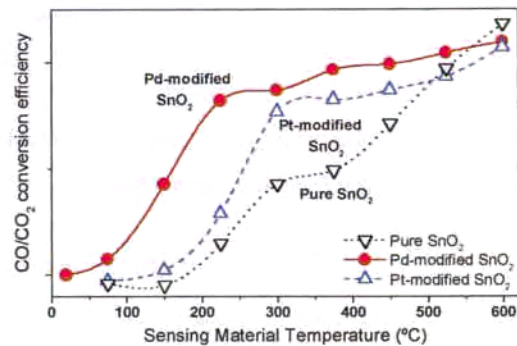
By the integration of the whole area of the CO and CO_2 peaks obtained from the different modified materials, we can calculate the relative CO/CO_2 conversion ratio, as shown in the figure 4.24.

The figure shows how the CO oxidation begins for microwave Pd modified sample at 100°C, while a thermal delay is observed for Pt modified or pure SnO_2. The analysis of such data seems to indicate that a high efficiency in CO/CO_2 conversion is obtained at 250°C (for Pd modified sample); higher temperatures increase this efficiency. It is considered that the incipient combustion that shows Pd-modified tin oxide could be correlated with better combustion performances since higher number of sites for CO combustion could be thermostatistically available.

The results of catalytic efficiency of the Pd catalysed tin oxide is in agreement with those results obtained by Khatko et al [Khatko,00] for sputtered films of palladium. Besides, Montméat et al [Montméat,00] shows similar results for platinum and indicates that the catalytic transformation from CH_4 to CO_2 is almost null for this material, as we show for Pd bellow considering electrical measurements.
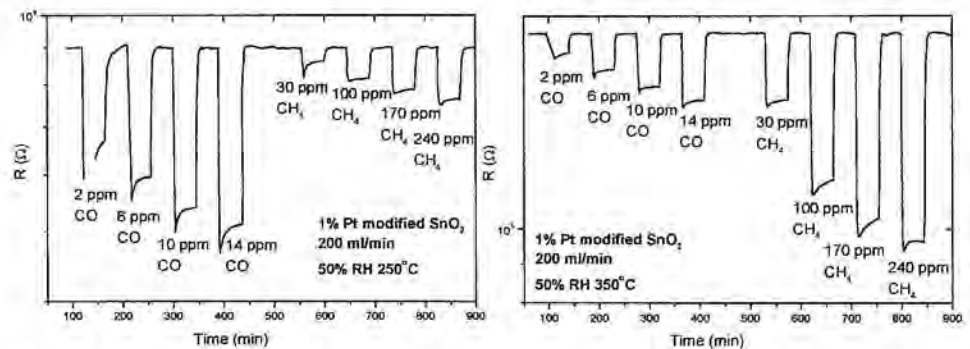

Figure 4.25. Response of the 1% Pt modified tin oxide sensor. Left, sensor operated at 250°C. Right, sensors working at 350°C.

The use of 1% Pt/Sn modified tin oxide lead to an increase of the selectivity for CO at low temperature (250°C), while the resistance variation with the CO exposure

remains approximately constant with respect the pure material. At a higher operating temperature the resistance variation induced by the introduction of low concentration of CH_4, being for this low concentrations larger than the variation to CO. This first approximation becomes a first approach to solve the problem of selectivity; in fact at $250°C$, the sensor is more selective to CO and for CH_4 at $350°C$.
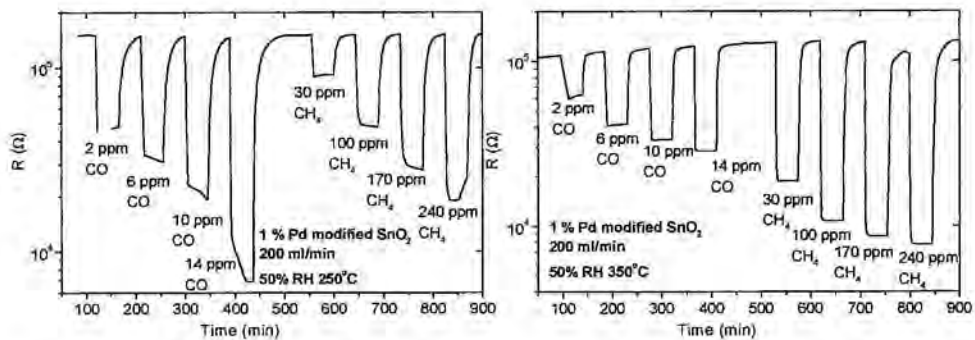

Figure 4.26. Response of the 1% Pd modified tin oxide sensor. Left, sensor operated at $250°C$. Right, sensors working at $350°C$.

In the case of the introduction of a 1% of Pd on the tin oxide base material, this leads to a clear increase of the sensitivity towards both gases, as shown in the figure 4.26. A large response of the sensors to the small CO gas concentrations introduced together with a small response towards CH_4 are observed for a temperature of $250°C$. When increasing the temperature until the $350°C$, the sensor shows a clear diminution of the CO sensitivity and a large increase of the CH_4.

The good response of this sensor, even for low the concentration of the target gases, can be compared with the response of other commercial sensor. This comparison seems indicate the reliability of such sensor for low concentration monitorisation –see figure 4.27-.
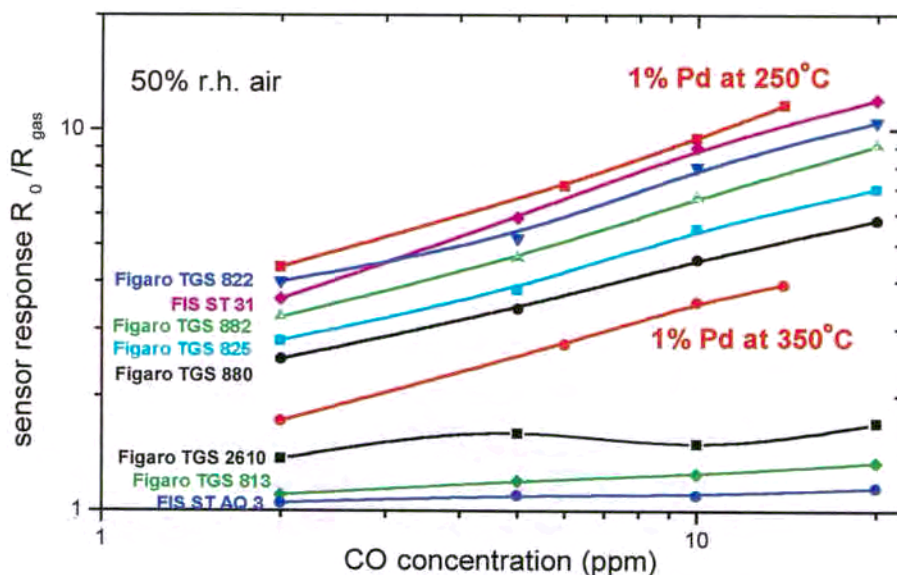
Figure 4.27. Comparative study of the sensor 1%Pd modified with respect other commercial sensors from Fis and Figaro.

In fact, the normalised response of the sensors can be drawn in a log-log plot in order to verify the actual sensor performances of such device –see figure 4.28-. In such figure we can observe the good sensing properties of 1%Pd catalysed sensor for CO working at $250°C$ and for CH_4 operated at $350°C$. This kind of temperature modulated selectivity is the basis for pulsed sensors [Lee,99]. But even in such operation of the 1%Pd catalysed sensor, that improves the selectivity of the SnO_2 pure sensor (fig. 4.22), a cross sensitivity between both gases appears.

It is observed that the increase of Pd until 10% distributed on all the sensing layer, which is not easy to perform using other techniques such as CVD or sputtering [Wöllenstein,99], produces a decrease of resistance due to the formation of a Pd net, with density enough to avoid resistance percolation effects. Therefore a Pd

homogeneous distribution is expected. This net represents a parallel resistance to the tin oxide contribution one.
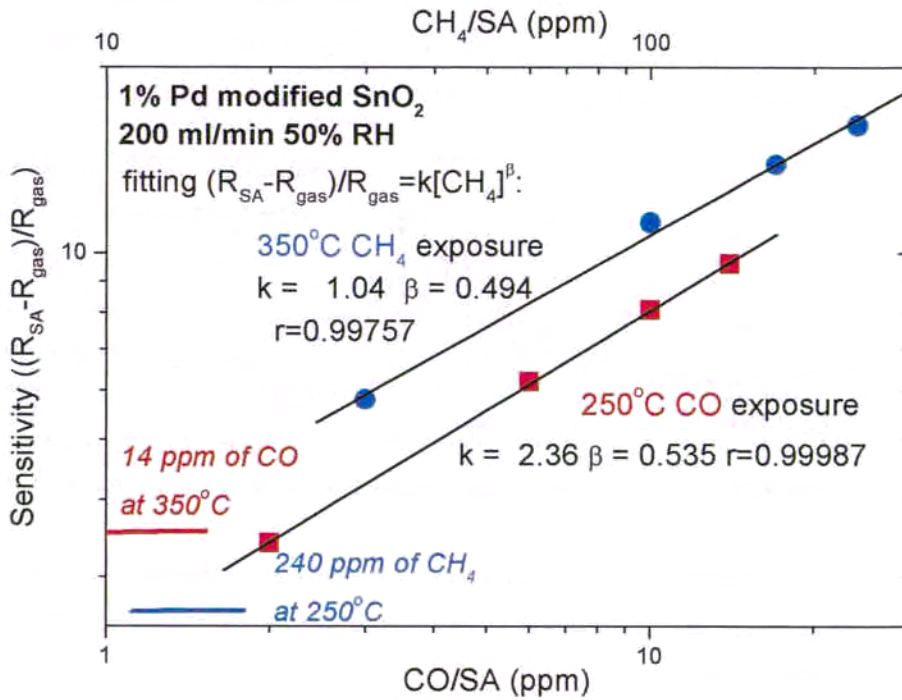

Figure 4.28. Normalised sensitivity of the 1% Pd catalysed sensor at 250 and 350°C. A fitting according equation 4.4 has been performed. The threshold of selectivity is plotted considering for CO detection at 250°C, the sensitivity of 240 ppm of interfering CH_4. In the case of CH_4 detection at 350°C, the interfering CO concentration is 14 ppm. The measurement is very selective under these thresholds.

At 250°C –figure 4.29a-, the CO sensitivity is comparable to CH_4 for the applied ranges. If compared with the figure 4.26, the selectivity for both gases is quite different. Moreover, the sensitivity ranges decreased for both gases.

However, much more interesting results are obtained when sensor is operated at $350°C$. In this case, no response for CO is found due to a whole and fast catalytic conversion such as it can observed in figure 4.29b. Despite in this case the sensitivity is low due to the decrease of resistivity, it is enough to distinguish few ppm of methane that is below the used range for CH_4 detectors.
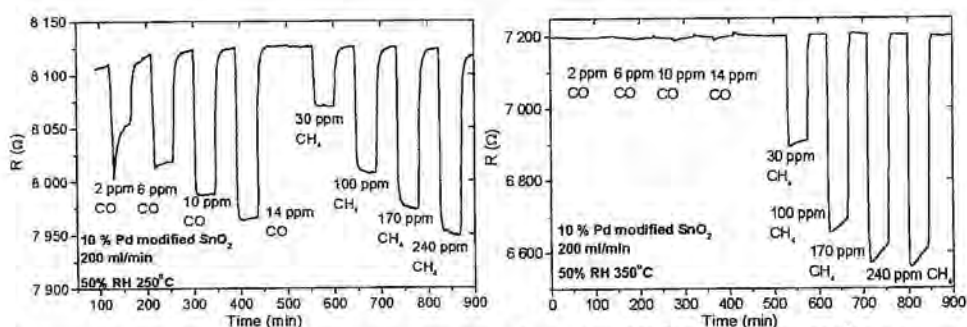

Figure 4.29. 10% Pd-catalysed sensor response heated at $250°C$ (a), and at $350°C$ (b).

In order to verify the reliability of such kind of catalysation, wider range of target gases has been tested. The results, summarised in figure 4.30 indicate that the use of such sensor can cover a very wide range, even for common industrial or safety applications.

Figure 4.30. 10% Pd-catalysed sensor response heated at $325°C$ under a wider range of target gases.
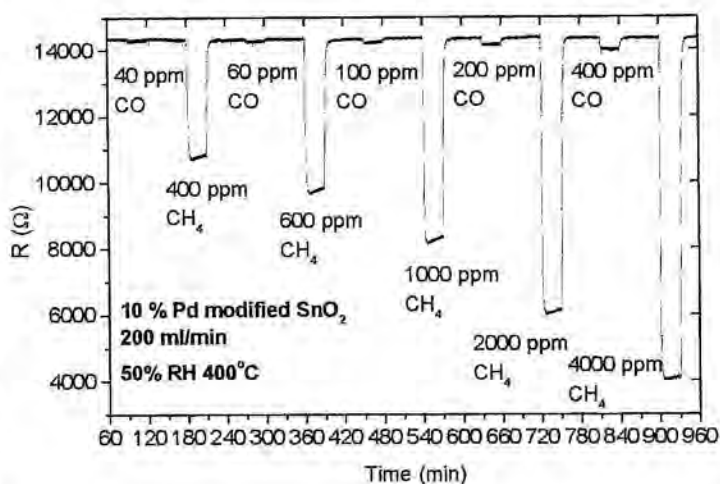
It is worth to observe how in the case of the 10% Pd catalysed sensor, the resistance decreases with the operating temperature. This fact indicates a semiconductor (SnO_2) predominant character in the samples. Therefore the introduction of the catalytic additive has reached concentration and distribution enough to get an optimised catalytic combustion, but keeping some of the main characteristics of the metal oxide.

A study of the structural differences between light and heavy catalysed materials shows how the introduction of palladium in higher quantities introduce a higher density of states between the Fermi level and the valence band, as seen in the figure 4.31
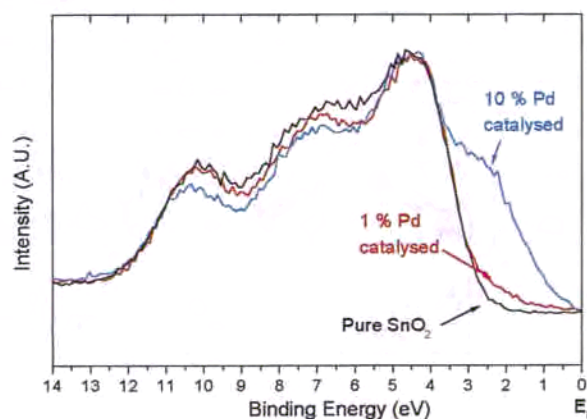

Figure 4.31. Valence band of Pd catalysed tin oxides with respect the pure sensing material.

Chemical comp.		Pd metallic	PdO	PdO$_2$	PdCl$_2$	Pd/ Sn
Pd/Sn nominal	Before/ After Ar$^+$ ion gun	Pd^o	Pd^{2+}	Pd^{4+}	Pd^{4+}	
1%	Before	Low	~15 %	~38 %	~37%	0.7%
	After	Very low	~31 %	~52 %	Low	1.1%
10%	Before	Very low	~23 %	~6%	~23%	9.2%

	After	Very low	~86 %	~8%	Low	11.9 %

Table 4.3. Concentration of the palladium states referred to the total palladium concentration. Last column indicates the measured concentration of palladium with respect tin.

The study of the states of the Pd doublet 3d are schematised in table 4.3 (peaks reference are the same as in table 4.2).
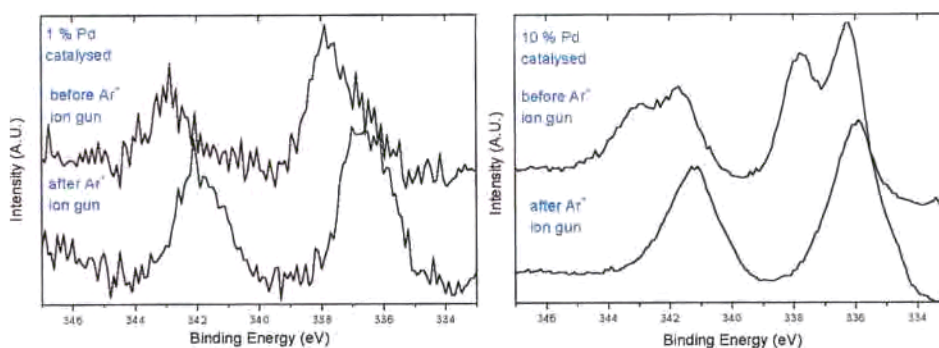

Figure 4.32. XPS spectra of the palladium 3d doublet region before and after ion gun for samples 1 (left) and 10% Pd/Sn catalysed (rigth).

The first consideration is about the remaining chloride compounds. As we have shown for the results of liquid pyrolysis, treatments of about 600°C are required to evacuate chlorine atoms (figure 4.8b). However, its strong reduction after ion gun suggests that this atom is placed at surface and it can removed by proper ageing of the sensor.

The second consideration comes from the good results about the efficiency that arise from the measurement of the Pd/Sn concentration. Despite the similar value to the nominal concentration, these data are indicating a distribution of the palladium on the tin oxide nanoparticles surface. When nominal concentration reach 10%, the measured palladium concentration (about 12%) indicates an equivalent of a 1 monolayer of Pd

coating on tin oxide. This result would explain the strong reduction of resistance observed in the test measurements of the figure 4.29.

For a further interpretation of the data, it is worth to pay attention to the reduction of palladium when its concentration is increased. The data basically reveals a change from Pd^{+4} to Pd^{+2} when the palladium concentration is increased from 1 to 10%. Fryberger *et al* [Fryberger,89] have shown by XPS how the Pd deposited on SnO_2 (110) undergoes a reduction of chemical state when increasing the equivalent monolayers of Pd on tin oxide. However, in that case the suggested reduction is Pd^o to Pd^{2+}. Despite the difficulties for the assessment of the actual chemical state of palladium, some similarities could be observed in both works, and in a subsequent work of the same authors [Semancik,90], they showed how surface dispersed Pd in the range of several monolayers produce effective catalytic adsorption for O_2, which could be involved in the burning of CO.

4.2.3 Comparing both technologies

Once analysed the two technologies for powder production –liquid pyrolysis and microwave treatment-, it is clear that both could be used for further sensor developments. However, at this moment it is reasonable to give priority to one of them. Different points of view – *technological*, *scientific* and *industrial*- should be considered in order to give a comprehensive value.

Concerning the technological aspects, despite both technologies have been satisfactory implemented, microwave procedure becomes easier for sample obtaining. As commented, most of the technological problems arise form the chlorine evacuation. Even in the case that other tin compounds were used in the precursor solution (such as nitrides or metalorganic compounds), one would have to evacuate a gas product of the

reaction. As in the case of microwaves treatments, teflon and glass are transparent to the radiation, it is possible to implement a chlorine outlet out of the oven. This is impossible to do in a muffle furnace, and only tubular one could be designed for this porpoise. As muffle furnace was used, very small quantities of tin oxide were produced per batch (<1 g) to avoid the massive generation of HCl and a difficult evacuation.

Anyway, as the set-up of liquid pyrolysis involves microdrop deposition, the microwaves –involving only solution preparation- becomes an easier technique.

From a scientific point of view, the quality of the material has been shown to be good in both cases. The purity, nanocrystallinity and stability of the obtained material seem to indicate adequate characteristics for sensing applications.

Moreover, interesting sensing performances were found in microwave catalysed material. The introduction of both Pd and Pt increases the sensitivity and selectivity even at lower temperatures. Whereas the introduction of Pd increases the sensitivity and selectivity in both technologies, Pt shows similar performances for microwave treatments but not for liquid pyrolysis. However, the catalysation with a Pd concentration reaching the active filter properties leads to a null cross sensitivity to CO; therefore CH_4 can be selectively detected by means of catalysed microwave tin oxide. This feature has been not tested under liquid pyrolisis technique.

Regarding industrial criteria, the production of a relative high quantity of sensing material becomes appreciated. Besides the diminution of production costs, the mass production ensures higher repeatability and a minor influence of the post-treatment process performed on the material -such as grinding or reduction-.

Aspect	Liquid Pyrolysis	Microwave treatment
Grams obtained per batch	Less than 1	3-4
Whole time per batch	4 hours	1 hour
Control of the microstructure	Excellent	Good
Grain size after annealing 450°C 8h.	10 nm	13 nm
Grain size after annealing 1000°C 8h.	53 nm	55 nm
Catalysation efficiency	Good	Good
Palladium catalysation performances	Good	Excellent
Platinum catalysation performances	Low	Good
Catalytic combustion possibility	Unknown	Good
Estimation of whole set-up cost	10000 Euros	8000 Euros

Table 4.3. Comparative study between liquid pyrolysis and microwave treatment.

As summary, despite both technology could give similar sensor performances, the use of microwaves seems to be an easy way to overcome the low production rate of the liquid pyrolisis.

4.3 Nanostructural evolution of SnO₂ with the annealing temperature

As exposed, gas monitoring is a surface phenomenon, therefore the use of high specific surface area materials (usually in the nanometric domain) is specially indicated ([Xu,91],[Yamazoe,91],[Bârsan,94]). This characteristic, that involves low grain size, is normally obtained by a reduction of growth and/or annealing temperature ([Diéguez,96],[Yu,97]). Nevertheless a reduction in such important technological parameter usually induces reduction effects on stoichiometry and instabilities.

Moreover, the use of nanosized material under harsh environments (i.e. high working temperature and poisoning atmospheres) requires a stable material able to undergo sensing reactions without variation of the microstructure.

For this study liquid pyrolysis and microwave samples have been annealed at different temperatures ranged from 200 to 1000°C. These samples were analysed by means of XRD, XPS and Raman spectroscopy. The study was assisted by TEM microscopy. A deep analysis of results reveals some regular variation of some derived parameters (relative intensities, strains, distortions, grain sizes, binding energies, valence band states and Raman shifts). We intend to relate all these regular variations with a unique physic phenomenon, that is the reduction of the oxygen vacancies with the annealing temperature.

As a considerable effort has been done to understand the influence of the leak of stoichiometry (oxygen vacancies) in gas sensitivity [Windischman,79][Sanjines,90] [Blaustein,99], this section provides useful data for technological improvement of sensor devices as well as a model of the oxygen vacancy reduction for scientific understanding of the thermal evolution of the microstructure in nanostructured tin oxide.

4.3.1 XRD results

Let us pay attention to the qualitative evolution of the liquid pyrolysis X-ray diffractograms –figure 4.4-. The samples exhibit only cassiterite in polycrystalline form, increasing its crystallinity as the stabilisation thermal treatment is carried out at higher temperature. However, we can consider different temperature ranges in both sets of samples.

In the first range, corresponding at temperatures below 400°C, XRD diffractograms show more phases than the crystalline cassiterite. In 400 and 600°C powder samples broad and not-well defined peaks are distinguished; the diffractogram baseline reproduces main cassiterite peak features, suggesting very small crystallisation nucleus.

Second interval ranges from 400 to 700°C. It starts with crystallisation arrangement for temperature higher than 400°C, in agreement with other previous works [Cao,96][Dieguez,96]. From this temperature material becomes crystalline, but not-sharp shaped diffractograms indicate still the presence of important lattice imperfections. Third interval corresponds to higher temperature than 700°C. In this range high quality diffractograms with sharper reflection indicated better crystalline symmetry.

In the evolution of diffractograms with the annealing temperature, special attention can be paid for the (220) reflection that becomes much better defined at 700°C. This fact suggests computing relative intensities. As it can be seen in figure 4.33, the intensity of (220) and (110) reflections increase with respect (101) and (211) ones.

Figure 4.33. Relative intensities of the analysed reflections as function of the annealing temperature.
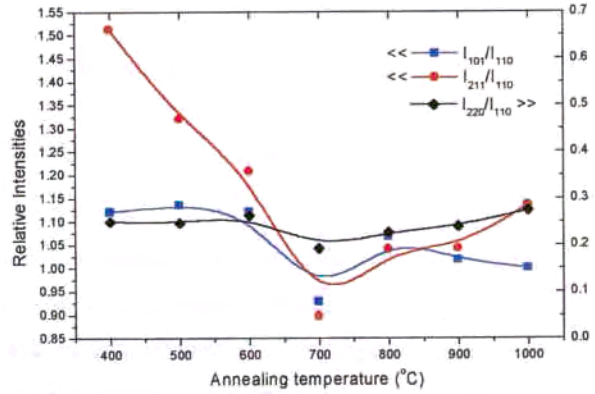
In a naive interpretation, tin oxide rutile structure (fig. 4.34) shows how (220) and (110) planes intercept high number of oxygen atoms, while the experimental sample procedure suggests thinking on a deficiency of oxygen in the lattice. Therefore the changes in the morphology of this planes can be related with the presence of oxygen vacancies.
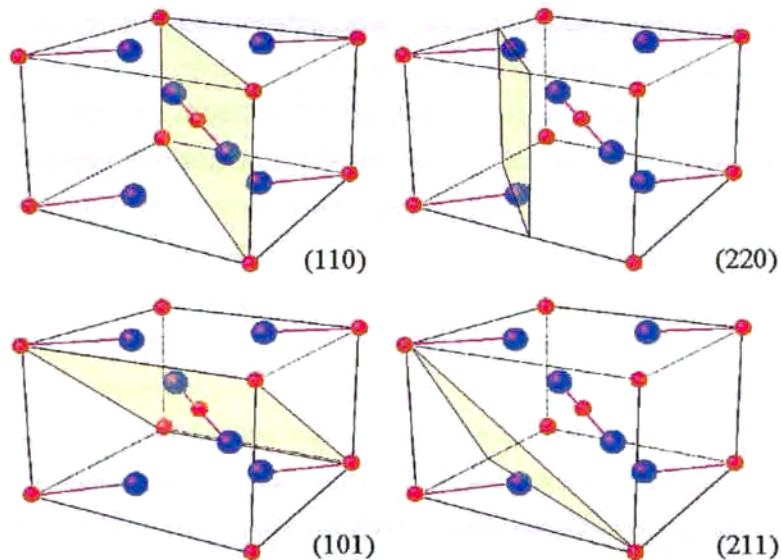

Figure 4.34. The different studied atomic planes in a rutile structure. Note how (110) and (220) intercept higher quantity of oxygen atoms –bigger atoms in blue- whereas (101) and (211).

In order to analyse properly the oxygen vacancy effects on XRD data, we can proceed calculating the structure factors of the material ([Snyder,92]),

$$F_{hkl} = \sum_{j}^{unit\ cell} f_j \exp\{2\pi i(hx_j + ky_j + lz_j)\} \qquad (4.4)$$

where x_j, y_j and z_j is the position of the j-th atom in the unit cell and f_j is the scattering factor, which could be decomposed in

$$f_j = f_{corr} \exp\left\{-\frac{B_j \sin\theta}{\lambda^2}\right\} \qquad (4.5)$$

The exponential term is the Debye-Waller temperature factor correction and f_{corr} is the correction due to anomalous scattering.

We define the occupation factor α, which keeps unit value when every oxygen position is occupied by an oxygen atom. If we consider oxygen vacancies uniformly distributed, we can write oxygen position scattering factor (f_O^T), in first approximation as,

$$f_O^T \approx \alpha\ f_O + (1-\alpha)f_{Vac} \qquad (4.6)$$

If there was null charge around a vacancy, we could take null value for vacancy scattering factor. These two approximations are more correct when the vacancy density is small ($\alpha \to 1$). As developed in [Matsuhata,94],

$$F_{hkl} = 2f_{Sn} + 4f_O \alpha \cos(2\pi hx)\cos(2\pi kx)$$
$$if \qquad h+k+l = even$$
$$F_{hkl} = -4f_O \alpha \sin(2\pi hx)\sin(2\pi kx) \qquad (4.7)$$
$$if \qquad h+k+l = odd$$

where the constant x takes value 0.304. Using (4.6) and (4.7), the analysed reflections give the following structure factors:

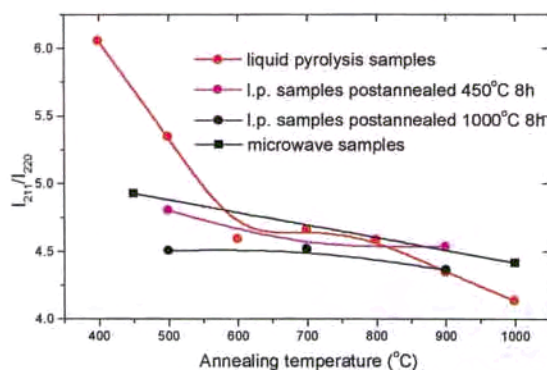$$F_{110} = 2f_{Sn} + 0.443f_O\alpha$$
$$F_{220} = 2f_{Sn} + 2.424f_O\alpha$$
$$F_{211} = 2f_{Sn} + 1.036f_O\alpha \qquad (7)$$
$$F_{101} = 2f_{Sn} - 1.331f_O\alpha$$

We can see that the effects of occupancy in (220) reflection are very important. The numerical difference between (220) and (110) is considered by Matsuhata *et al* [Matsuhata,94]. In this work, based on high-energy electron diffraction, is exposed that (110) reflection depends strongly on the ionicity degree of tin, while (220) reflection has a higher contribution from the oxygen.

Therefore, it seems much more indicated to evaluate vacancy effects using (220) reflection. Due to its proximity, which allows obviating the Debye-Waller temperature factor of equation (2.5), (211) reflection will be the reference of its evolution. Using f_j values found in the tables [Ibers,74], we compute the relative intensities as,

$$\frac{I_{211}}{I_{220}} = \frac{F_{211}^2}{F_{220}^2} \approx \frac{|71.36 + 4.48\alpha|^2}{|69.79 + 9.98\alpha|^2} \qquad (4.8)$$

This intensities ratio decreases when the occupancy growths (relaxation of vacancies), fact that is experimentally confirmed by figure 4.35. In this graph is shown how the effect of temperature is vanishing the oxygen vacancy density.

Figure 4.35. Relative intensity I_{211}/I_{220}.

The most immediate consequence of the existence of oxygen vacancies is the mechanical effects induced on the lattice. The first mechanical effect on the lattice is the induced strain. Such strain can be calculated with our data as the deviation of the atomic planes with respect its relaxed position,

$$\left\langle e^2 \right\rangle_{hkl}^{\frac{1}{2}} (T) \propto \frac{d_{hkl}^{relaxed} - d_{hkl}^{T}}{d_{hkl}^{relaxed}} \qquad (4.9)$$

where d_{hkl}^{T} represents the position of the plane with Miller indexes (hkl) of sample processed at a temperature T. This formula allows computing the mean strain of the atoms in plane (hkl) in the normal direction to this plane. The proportionality constant in equation 4.9 is taken100. The relaxed length is that indicated in references [JCPDS,97].

For the calculation of the distance between planes, we use the Bragg formula,

$$2d_{hkl}\sin\theta_{hkl} = n\lambda \qquad (4.10)$$

where d_{hkl} is the distance between planes with (hkl) Miller indexes, θ_{hkl} the angle of the reflection, n the order of the reflection and λ the wavelength of X-rays (see appendix 1).

Figure 4.36. Calculation of the mean deformation orthogonal to the plane (hkl) for liquid pyrolysis and microwave samples.
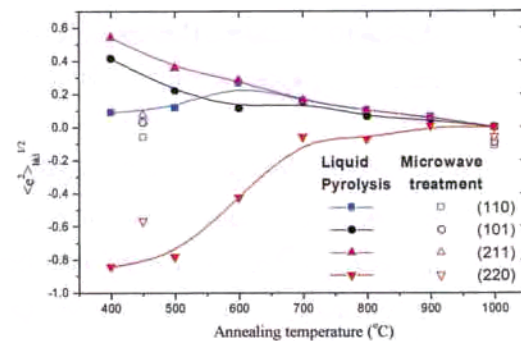
The result of the computation of the strain is shown in figure 4.36. As we can see, the strain in the plane (220) is tensile, whereas in other planes are compressive. This interesting result could be explained considering that O-Sn-O bonds are orthogonal to this atomic plane. When an oxygen atom vanishes, the resulting Sn-O bond relaxes,

217

increasing the distance between such atoms and moving away the (220) atomic planes, as schematised in figure 4.37. It is interesting to point out that the most reduction of strain takes place between 600 and 700°C.
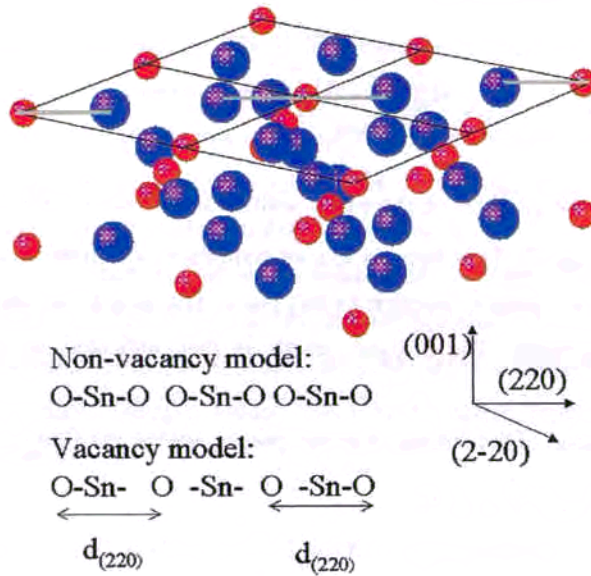

Figure 4.37. Scheme of the induced tensile strain for reduced (220) atomic planes.

Non-vacancy model:
O-Sn-O O-Sn-O O-Sn-O

Vacancy model:
O-Sn- O -Sn- O -Sn-O

$d_{(220)}$ $d_{(220)}$

Under the hypothesis of the incorporation of oxygen vacancies to the lattice, it is possible a deformation potential that mainly decomposes in (220) induced by a high density of such vacancies. As showed by F. Matossi [Mattossi,51] for TiO_2 in the same rutile lattice, the bond between metal and oxygen mainly decomposes in the direction (110) (the same direction to (220)).

At this point, it is worth to comment that despite (110)⊂(220), such mathematical relation is valid only in the case of a perfect structure. Thus, broken symmetries could induce differences between families of planes. In fact, the half of the (220) family is the (110) family. Such half will be the same even after broken symmetries, but not necessarily the other half (220) family.

Once analysed and discussed the measured differences between planes, and specially those referred to (220) and (110) planes, we would like to introduce a

computation of the distortions induced by vacancies on the lattice parameters. For this computation we should take into account the Laue condition,

$$\overline{G_o} = \left(\frac{2\pi}{d} \right) \tag{4.11}$$

so, we can write

$$\frac{1}{d^2} = \frac{G_o^2}{2\pi} = (hb_1 + kb_2 + lb_3)^2 \frac{1}{2\pi} \tag{4.12}$$

where b_i are the reciprocal vectors of the lattice and h,k and l the Miller indexes of every plane. As the rutile lattice is cubic, and both horizontal parameters are equal (**a**), we have,

$$b_1 = \frac{2\pi}{a} \qquad b_2 = \frac{2\pi}{a} \qquad b_3 = \frac{2\pi}{c} \tag{4.13}$$

and substituting (4.13) in (4.12), and using the Bragg relation (4.10), we have

$$\frac{4\sin^2\theta}{\lambda^2} = \frac{h^2 + k^2}{a^2} + \frac{l^2}{c^2} \tag{4.14}$$

This formula has been proposed by Yu *et al* [Yu,97]. For the present application, we propose computing $\Delta a = a_{220} - a_{110}$ and $\Delta c = c_{101-110} - c_{101-220}$. The obtained result is shown in figure 4.38.
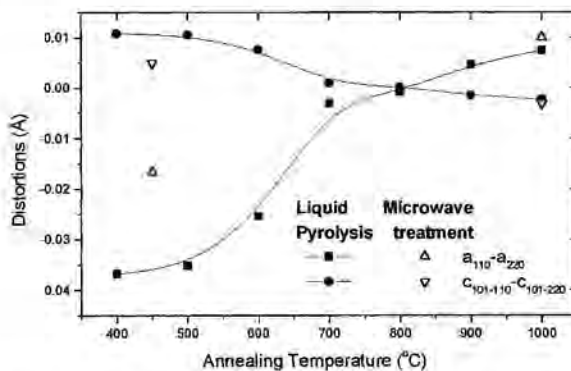

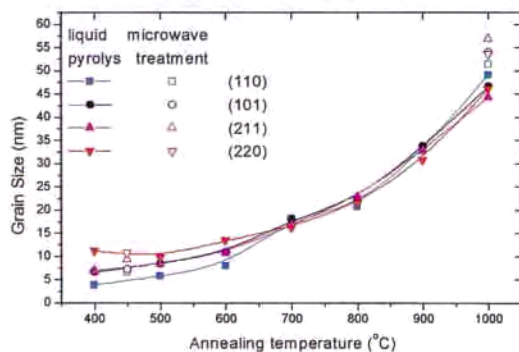Figure 4.38. Computation of the lattice parameters distortions.

The obtained data indicates that the effects of the oxygen vacancies mainly decomposes in the horizontal axis (the two **a**). The evolution with the temperature of the distortion also

suggest a strong diminution of the vacancies at temperatures between 600 and 700°C. However, the high reduction of the distortions vanishes when anneals at temperatures above 800°C are applied.

Despite the difficulties for the interpretation of the grain growth data – especially those data obtained by Scherrer formula (equation 4.2) applied to XRD-, some particularities should be noted in our samples. It is interesting to observe that until 700°C, the grain size evaluated by the different atomic planes gives light differences for the studied atomic planes. Thus, whereas (220) gives the higher grain size –revealing a wider reflection-, (110) is the smaller one, as consequence of a narrow FWHM in the correspondent reflection.

Different mechanisms can be considered for the growth of the nanocrystals: nucleation [Yu,97], Ostwald ripening [Lin,94] and coalescence [Family,88]. Their interrelation is not obvious and a detailed analysis of the data would require of a deep TEM/HREM work.

Figure 4.39. Grain size calculated by means of the Scherrer formula (equation 4.2).

Once exposed the XRD data, the hypothesis of oxygen vacancy diminution with the annealing temperature becomes reasonable. Before to start a deeper discussion about it, let me introduce the XPS and Raman spectroscopy data, which show a microstructural evolution that could be also related with such oxygen vacancy diminution.

4.3.2 XPS results

X-ray Photoelectron spectra, focused on O 1s and Sn 3d orbitals, are shown in figure 4.40. These data reveal a monotonous evolution of the binding energy of both oxygen and tin towards lower energies when temperatures are increased, as shown in figure 4.41. This evolution is inverted at 900°C and above, and shift turns towards higher energies.

Figure 4.40. X-ray Photoelectron spectra of the liquid pyrolysis samples. The observed regions are focussed on tin and oxygen main contributions.
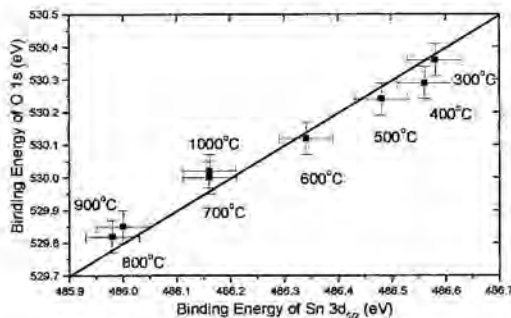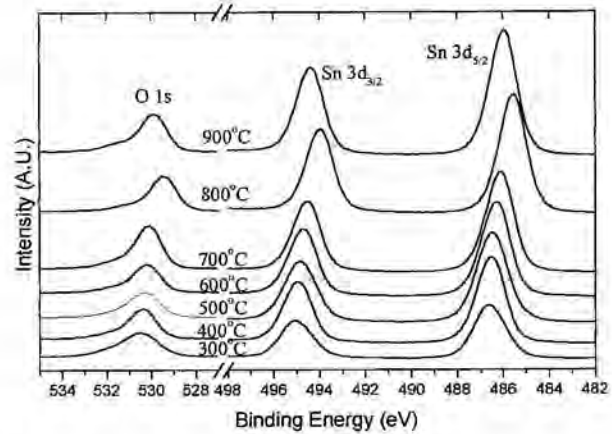
Figure 4.41. Binding energies of 1s oxygen orbital as function of Sn 3d 5/2 binding energy.

As these measurements of binding energies are relative to the Fermi level energy (E_F), a shift in the binding energy (ΔBE) can arise from the following contributions [Matsushima,88],

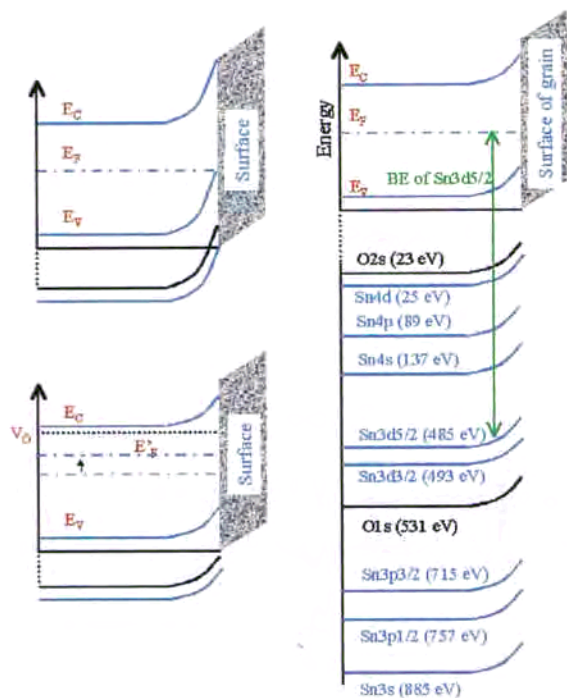$$\Delta BE = \Delta E - \Delta R + \Delta E_F \tag{4.15}$$

Figure 4.42. Scheme of the mechanisms able to induce shifts in the binding energies measured by XPS. Usual XPS measurement in common SnO_2 electronic structure. Up left, a change in the surface band bending induces the same change in the whole electronic structure –except in the Fermi level-, therefore the energy between Fermi level and bands varies, inducing a shift in the binding energy. Down left, the existence of oxygen vacancies donor levels changes the position of the Fermi level and, therefore , the binding energy.

where ΔE is the shift due to a change in the state charge distribution (such as a change in the oxidation state), ΔR is the shift due to a change in the relaxation process of screening of the hole resulting from photoionization and ΔE_F is the relative shift of the Fermi level. The sign (+ or -) indicates the direction of each shift.

With respect the state charge distribution (ΔE), we can consider similar charge distributions in all the samples as consequence of a common chemical structure ($Sn^{4+}O^{2-}$). Only in the case of 300°C, we have previously served (figure 4.4) how cassiterite structure is formed yet. Thus, other chemical species, such as $Sn^{2+}O^{2-}$, can be present in the samples.

In the case of screening (ΔR), the electrical contact between sample and earth by means of proper instrumentation allows us to ignore this

contribution.

Regarding the relative changes of the Fermi level with respect the electronic band structure, these can be attributed to a change in the Fermi level to valence band separation caused either by a shift in the Fermi level or band bending or both [Henshaw,96].

Previous works [Cox,88][Cox,89][Semancik,90] have shown that band bending shift exits due to the phase transformation-like reconstruction related to the oxygen vacancies. Whereas in that case, some structural parameters vary abruptly when changing reconstructions, in our XPS measurements the binding energies smoothly vary.

However, it is well known that oxygen vacancies induce shallow donor levels [Fonstad,71][Jarzebski,76]. These levels are able to move the Fermi levels towards the conduction band; thus E_F is moved away from the tin and oxygen orbitals levels.

Both mechanisms, surface band bending and Fermi level shift due to oxigen vacancies are schematised in figure 4.42.

Figure 4.43. Valence bands of the XPS spectra of the liquid pyrolysis samples. In order to be easily compared, all the spectra have been shifted to reach a common energy for the Valence Band Maximum.
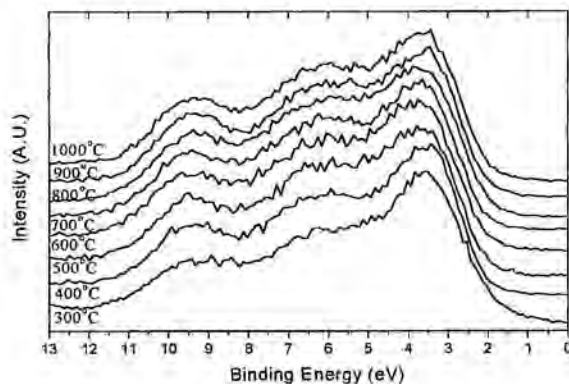
Besides the inspection of the tin and oxygen orbitals in the X-ray Photoelectron spectra, it is interesting to pay attention to the valence band region, shown in the figure 4.43. The obtained spectra for the valence band reveal an oxidised tin oxide (comparing with
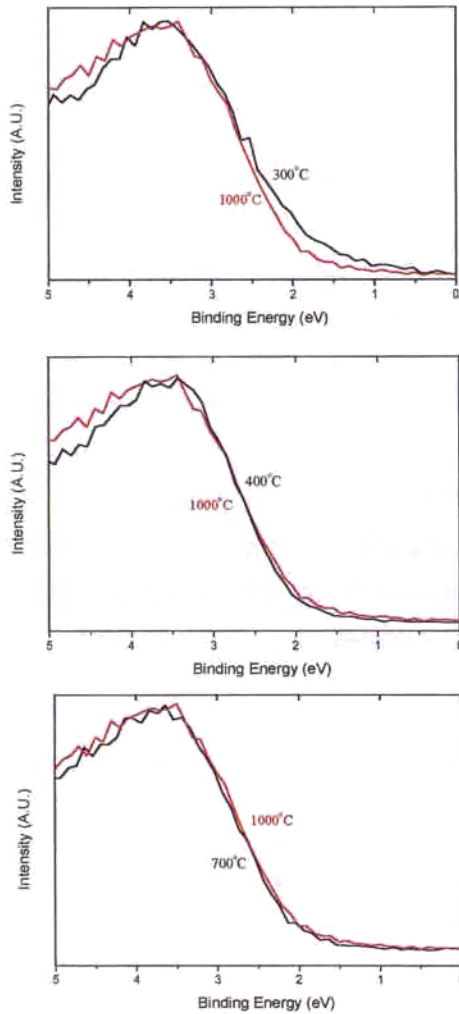
Figure 4.44. Detailed inspection of the forbidden band region between the Fermi level and the valence band maximum. As reference (in red) is plotted the 1000°C annealed sample. The rest of the samples present similar patterns to those of 400 and 700°C.

[Cox,88] data). Only the 300°C-annealed sample shows a spectrum which could be attributed to SnO [Kövér,95].

As we have shown previously, this is the only sample which diffractograms does not behave as cassiterite and the present data confirms a reduced structure (such as SnO). A detailed inspection of the forbidden band between the Fermi level (referred as 0 eV) and the Valence Band Maximum reveals some differences with the 1000°C-annealed sample (which is considered cassiterite representative). In fact, the actual meaning of those differences – states in the forbidden band or a structure corresponding to SnO_2- becomes a subject of complex assessment. However, for our study what is important is the non-existence of defects at annealing temperatures of 400°C and above, at least with reference to 1000°C annealed sample and within the detection limit of XPS.

This result could be associated with that obtained by Munnix *et* *al* [Munnix,86]

[Munnix,87], who found that different vacancy configurations on (110) surfaces –the most thermodynamically stable and, therefore, probable [Theil,76][Semancik,90][Goniakowski,96]- does not introduce a bound state in the gap. This finding has been experimentally supported [Kohl,92][Rantala,94].

4.3.3 Raman results

According the active Raman modes described in subsection 2.2.2 [Katiyar,71], we can observe (see figure 4.45) the modes el E_g (472cm^{-1}), B_{2g} (774cm^{-1}) i A_{1g} (630cm^{-1}). In agreement with the data exposed on the literature [Yu,97], these peaks becomes sharper from 400°C.

Figure 4.45. Raman spectra of the liquid pyrolysis samples annealed at different temperatures.
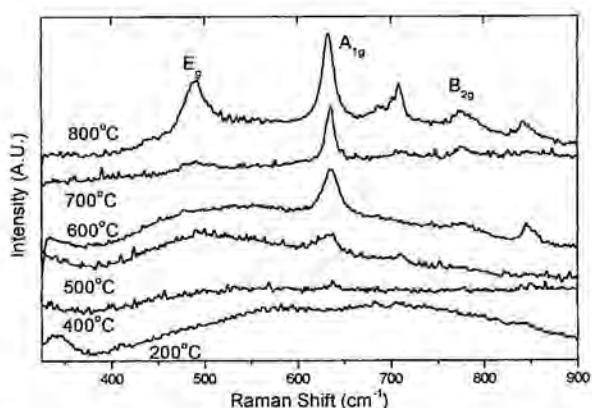
Aside the cited vibrations, new unknown vibrations appear, leading to complex explanations. These new peaks would be about 325, 550, 710 and 800 cm^{-1}. These three last vibrations would induce a unique wider peak when SnO_2 is low annealed (200°C). Besides, the relative intensity of the peaks centred at 325 and 550 cm^{-1} diminishes with the annealing temperature.

Abello *et al* [Abello,98] have suggested that the influence of the surface is much more important when measuring these nanoparticles and, therefore, different surface related modes could appear in the Raman spectra.
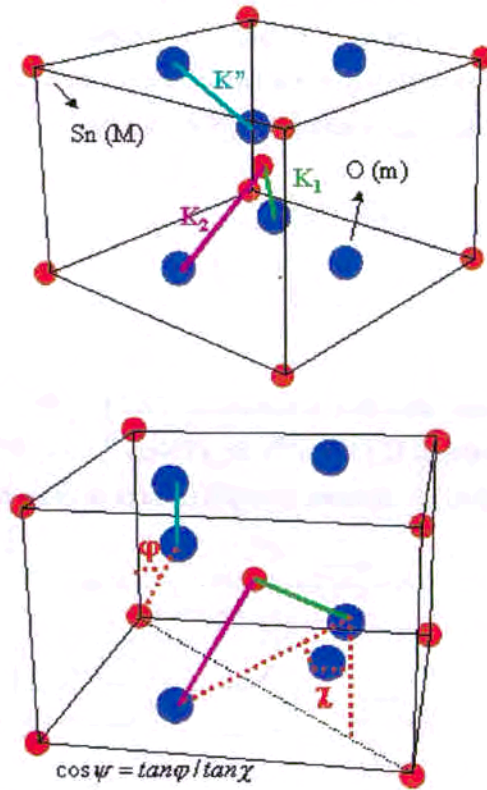
Figure 4.46. Scheme of the force constants and lattice parameters used by F. Matossi [Matossi,51] to describe the lattice dynamics of the rutile structure.

However, the explanation introduced by Yu *et al* [Yu,97] becomes more realistic. As this explanation is based on the lattice vibration model of F. Matossi [Matossi,51], let us briefly present this model.

The Raman spectrum, that is the result of the inelastic scattering of phonons and photons approximately gives the frequencies of the phonons at $\omega(k=0)$ [Grasselli,91]. In consequence, the use of classical and quantum description of phonons can be directly translated to Raman spectroscopy. In this way, the most simple approximation consist in the description of the phonons by means of a force constant model. The force constants as well as the lattice parameters in the calculation are introduced in the scheme of the figure 4.46.

Once developed a general model, only the parameters shown in the figure becomes necessary to give an expression for the most important vibrations:

$$A_{1g} : \omega^2 \approx \left[k_1 + 2k_2 \sin^2\varphi + 4k''(\cos\psi - \sin\psi)^2 \right]/m$$
$$A_{2g} : \omega^2 \approx \left[4k''(\cos\psi + \sin\psi)^2 \right]/m$$
$$B_{1g} : \omega^2 \approx \left[4k''(\cos\psi - \sin\psi)^2 \right]/m \qquad (4.16)$$
$$B_{2g} : \omega^2 \approx \left[k_1 + 2k_2 \sin^2\varphi + 4k''(\cos\psi + \sin\psi)^2 \right]/m$$
$$E_g : \omega^2 \approx \left[2k_2 \cos^2\varphi + 8k''\cos^2\chi \right]/m$$

As seen, A_{1g}, which is the main vibration and is quite close to the main vibration mode of the molecule, can be explained as the vibration of the molecule (k_1 constant, the main contribution) plus the second neighbour contributions.

Moreover, these frequencies verify the following relation[2],

$$w^2(A_{2g}) = w^2(B_{1g}) + w^2(B_{2g}) - w^2(A_{1g}) \qquad (4.17)$$

which is impossible to verify by Raman spectroscopy because A_{2g} is Raman inactive in perfect rutile.

However, Yu *et al* [Yu,97] have introduced the hypothesis that a high density of oxygen vacancies could shift the B_{1g} vibration frequency and transform A_{2g} into Raman active. In this case, the measured Raman frequencies should verify the composition rule (4.17).

In our case this implies that we should observe the inactive Raman mode at 555 cm^{-1}. As we have introduced at the beginning, this is one of the bands that appear in the spectra. However its poorly defined shape suggest us that a more accurately application of a oxygen vacancy distribution on more recent models developed on lattice dynamics of the rutile ([Katiyar,71][Gervais,83][Gervais,85]) would give more precise and credible results than those exposed previously.

---

[2] We would like to prevent to a sign error in the correspondent equation of [Yu,97]

Figure 4.47. Raman shift of the A_{1g} vibration as function of the annealing temperature. The grain size calculated by means of the model of quantum localisation of the phonon (see text) is indicated by the experimental points.

Aside of these new vibrations that appear in the Raman spectra, a more accurately inspection of the results reveals a displacement of the Raman shift frequency as function of the annealing temperature. In order to explain these results, a new effect, based on the localisation of the phonons in the nanocrystals [Grasselli,91] should be considered.
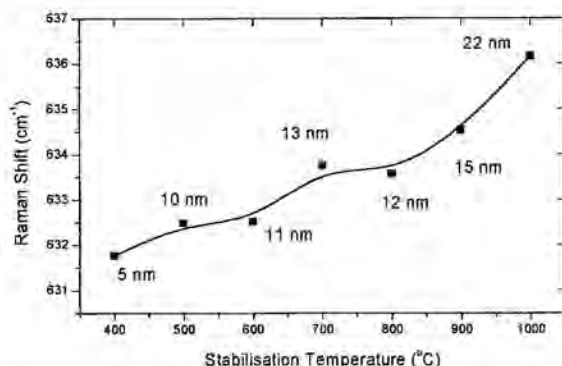
Figure 4.47. Raman shift of the A_{1g} vibration as function of the annealing temperature. The grain size calculated by means of the model of quantum localisation of the phonon (see text) is indicated by the experimental points. As we have commented previously, only almost null momentum phonons contribute to the scattering with photons leading to the Raman effect. The phonons pseudoparticles extend its position to the whole lattice, which ideally is infinite. But when considering nanoparticles, their position becomes localised and the Heisemberg uncertainty principle becomes important. Therefore, as position is localised, momentum undergoes uncertainty ($\Delta r \Delta q \sim h$). The consequence is that non-null momentum phonons contribute to the Raman effect and, according to the dispersion relations, the frequency of the vibration lightly changes.

To analyse this effect we can consider the first order description of the intensity as function of the frequency ($I(\omega)$),

$$I(\omega) \propto \int_{BZ} |C(q)|^2 \frac{d^3q}{\left(\omega - \omega\ (q)\right)^2 + \left(\Gamma_o / 2\right)^2} \qquad (4.18)$$

Where $C(q)$ are the Fourier coefficients of the vibrational weighting function, $\omega(q)$ is the phonon dispersion curve and Γ_o is the natural linewidth.

In order to describe the localisation of the phonon [Zi,97].Gaussian localisation factor

$$W(r) \propto \exp\left\{\frac{-2r^2}{L^2}\right\} \qquad (4.19)$$

where L represents the average localised size (or grain size). With this formula, the correspondent Fourier transformation gives an expression of the localisation factor in the q-space,

$$W(q) \propto \exp\left\{\frac{-q^2 L^2}{8}\right\} \qquad (4.20)$$

which can be introduced in 4.18 to obtain

$$I(\omega) \propto \int_{BZ} \exp\left\{\frac{-q^2 L^2}{8}\right\} \frac{d^3q}{\left(\omega - \omega\ (q)\right)^2 + \left(\Gamma_o / 2\right)^2} \qquad (4.21)$$

A. Diéguez [Diéguez,99] have calculated the effect of the grain size on both the Raman shift and the FWHM of the A_{1g} vibration by using the dispersion relations of such vibration given by Peercy *et al* [Peercy,73].

By applying the results obtained with this model we have found the grain size of the samples presented in figure 4.47. As in that case, the obtained results are smaller than obtained by other techniques such as XRD or TEM, being the discrepancies discussed in the next section.

4.3.4 Discussion

As we have seen, a regular nanostructural evolution of the samples indicates the presence of a structural effect able to transform some of the sample characteristics. In order to follow a defined line of work, we have introduced hypothesis of the oxygen vacancy diminution with the annealing temperature. Now, our aim is to discuss about the reliability of such hypothesis, in order to give a final conclusion on this phenomenon.

XRD data shows regular bulk phenomena for liquid pyrolysis and microwave samples. Some of these phenomena –such as distortions- has been previously reported [Yu,97]. Other such relative intensities or stress are also undergone by other sets of samples (as we will show in the next chapter). The common characteristic of all these different kinds of tin oxide samples is that they arise form oxygen defective tin oxide; so the easier hypothesis consist on the regular diminution of the oxygen vacancy density with the annealing temperature. However, let us discard other two hypotheses in order to restrict our area of study.

First, let us consider the hypothesis of interstitial tin in tin oxide cassiterite lattice and relaxation effects. Previous results of Agashe *et al* [Agashe,91a] [Agashe,91b] show that this interstitial tin induce an anomalous increase of the (200) intensity, which has never been observed in our samples (figure 4.4).

Otherwise, hydroxyl groups could be considered as origin of such variations in the structural parameters. Despite the difficulty to reject a hypothesis like this, we consider three points that play against it:

✓ If the OH were responsible of the stress, they would be found in substitutional form occupying oxygen sites. The higher bond length of the group (O-H)⁻ (table 4.4, 0.98 Å) with respect the ionic radius of oxygen (0.71 Å) would produce an excess of 0.27 Å per each substitutional site. Due to the ionic character of the hydroxyl groups, this excess should be added in the crystalline place directions for every substitutional site. As consequence, high value of stress would be found for a small

density of substitutional OH; value no corresponding to our measurements. If the excess of 0.27 Å was considered for the strain computation, and no relaxation of stress was possible, only 20 substitutional hydroxyl would be able to reproduce our measured strain on (220) atomic plane. At the contrary, when a vacancy appear in an oxygen position, the character of the matter involved (bosonic or fermionic) will depend on the associated charge (V_O, V_O or V_O). Therefore the redistribution of charge in vacancies, could lead to an easier way to reduce the stress in the matter.

✓ We will show in the next chapter how sputtered samples undergo similar nanostructrual evolution. Such sputtered technology and all the process involved in the production of that samples are dry. Therefore the hypothesis of hydroxyl groups in the lattices in not possible in this samples. If considered that the physics inducing such effects is the same to the presented above, the present samples can not undergo nanostructural evolution effects as consequence of hydroxyl groups.

✓ Finally, we have calculated the theoretical volume of the unit lattice as function of the annealing temperature. It is remarkable to observe the increase of the unit lattice volume. Whereas in the hypothesis of hydroxyl in the lattice, one could expect a diminution of these groups with the annealing temperature and smaller unit lattice volume, in the case of oxygen vacancies, its reduction would lead to higher unit lattice volumes, according with our measurements.

Atomic/ionic bond	Length (Å)
Sn-O in rutile [Rantala,94]	2.0
(O-H) [Goniakowski,96]	0.98
(O-H) in H_2O [Eisenberg,69]	0.957
Ionic species	Radius (Å)
Sn^{4+}	0.71
O^{2-}	1.4
Pd^{2+}	0.8

Pd⁴⁺	0.65
Pt²⁺	0.8
Pt⁴⁺	0.66

Table 4.4 Bond length and ionic radii of different species involved in tin oxide SGS.
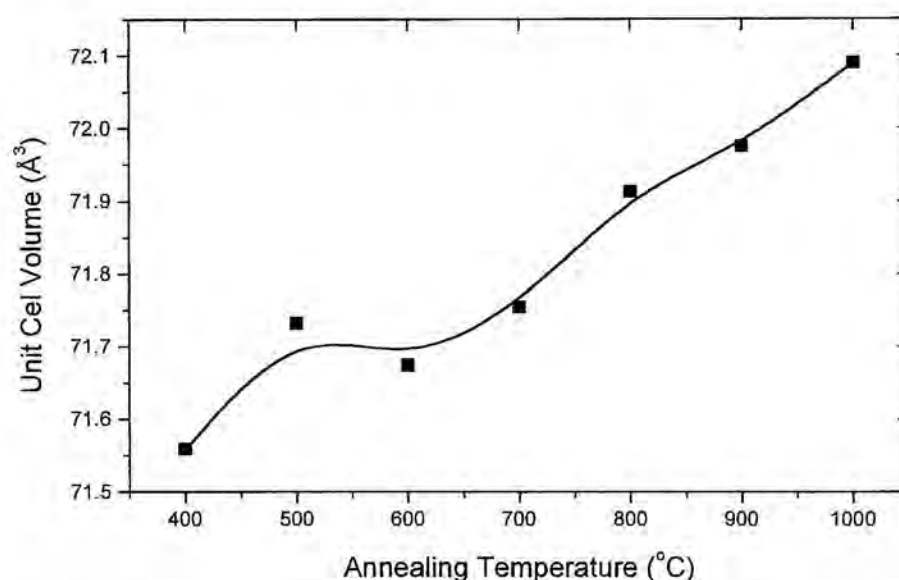

Figure 4.48. Volume of the unit lattice of the liquid pyrolysis samples as function of the annealing temperature. The computation results from $a_{110}(c_{101-110})^2$ that has been obtained using 4.14.

Therefore oxygen vacancy evolution seems to be the most feasible qualitative hypothesis to explain the evolution in the XRD data. However, when calculating the density of vacancies by means of equation (4.8), a density of 10^{21} cm^{-3} is found at 700°C. At lower temperatures the equation gives results without logical sense (densities higher than 10^{23} cm^{-3}). Therefore, despite this equation indicates the tendency of the

relative intensities, is not appropriated for the calculation of the vacancy density. Two reasons are involved in this leak of quantitative description for the equation.

The first consist in the fact that several approximations have been found. Mainly, when considering the scattering factor of a vacancy to be zero ($f_V \sim 0$) and when considering the oxygen vacancies homogeneously distributed in all the oxygen atomic positions. Besides, the equation 4.8 was obtained in the supposition of a very small density of vacancies ($\alpha \rightarrow 1$), whereas the obtained result does not indicate this.

Moreover, the use of XRD is usually accepted to be indicated for the quantification of the induced effects of the atomic related crystallographic defects, such strains, stress, distortions … but XRD is not used to get the density of defects, such as, interstitial atoms, Frenkel defects, vacancies … For this, some works uses Rietveld method based calculation, in example with Fullprof program [Fullprof,98], in order to compare the obtained results with the experimental ones. But even in this case, the results are usually subject of discussion.

Regarding the XPS results, the hypothesis that oxygen vacancies are responsible of energy shift should be compared and analysed with respect a hypothetical band bending leading to similar result.

Before this comparison, let us to introduce the theoretical result of Rantala *et al* [Rantala,94], who showed that an energy shift could be associated to the presence of oxygen vacancies. In a cluster approach based on *ab initio* computations, the authors have found a strong shift of the energy levels originating from tin 5s orbitals due to the change of coordination number of the corresponding tin atom. This result indicates that the presence of oxygen vacancies (leading to changes in the coordination number of tin) should shift the 5s orbital and, therefore, all the electronic bands.

Previous experimental results of Erikson *et al* [Erikson,87] found that the binding energy shift due to the surface band bending associated with the 1x1(110) tin oxide surface reconstruction under reducing/oxidising conditions was always less than

0.12 eV. This value could increase up to 0.2 eV when considering other surface reconstructions [Erikson,87]. In agreement with the variation in the electronic affinity ($\Delta\chi$~0.35 eV) obtained by Cox *et al* [Cox,88] by means of UPS. As the measured binding energy shift in our case is 0.6 eV, further effects have to be considered.

In the same work previously cited, Cox *et al* obtained a work function ($\Delta\phi$) about 0.6 eV, which were related with the creation of surface *in plane* and *bridging* vacancies –see section 2.2.2.4-.

The same authors shows in a posterior work [Cox,89] that at a temperature higher than 423°C the oxygen diffusion from the bulk is responsible of the surface reconstruction observed in reduced SnO_2 surface. These results are in agreement with our hypothesis of the presence of oxygen vacancies in the bulk.

The higher annealing temperature used in our experiences ensures the oxygen vacancy diffusion and uniformly distribution of such vacancies as observed in XRD data. The shallow states related with these vacancies could explain the Fermi level shift observed in XPS.

As suggested previously [Semancik,87], it is possible calculate approximately the increment of conduction carriers due to shift in the Fermi level as,

$$\frac{n(T)}{n_o} = \exp\left(\frac{\Delta E_F(T)}{KT_o}\right) \tag{4.22}$$

Despite in the shift of the Fermi level we would need to rest the effects of the band bending, as suggested in the work [Cox,88], we don't have an idea of this data, therefore let us present the results of (4.22) considering surface flat bands –see table 4.5-.

Annealing temperature (°C)	Binding Energy (eV)	$n(t)/n_o$
300	486.58	10^{10}
400	486.56	$5 \cdot 10^9$

500	486.48	$2 \cdot 10^8$
600	486.34	10^6
700	486.16	10^3
800	*485.98*	*1*
900	486	2
1000	486.16	10^3

Table 4.5. Density of carriers of the liquid pyrolysis samples normalised to the 800°C annealed sample. At this temperature distortions vanish.

Such variations indicate a large influence of the shifts on the density of carriers and probably on the sensing characteristics. Despite measurements of resistivity would be very useful to identify such density of vacancies ($\sigma = e\mu n$), the effects of the Schottky barrier at surface ($\sigma \propto \exp(eV_s / KT)$, see section 2.4.2.1) will represent a large contribution to the conductivity. Moreover, it should be considered that the Schottky barrier (V_s) depends on the grain size, which also varies with the annealing temperature.

Under our view, the most reliable measurements would be those obtained by EPR (*Electronic Paramagnetic Resonance*). It is expected that ($V_o^{\cdot}$) should be measured considering that the existence of one electron in a spin degenerated state becomes a paramagnetic contribution. Besides, the other contributions $V_o^{\cdot}$, $V_o^{\cdot\cdot}$ have to be calculated by means of Saha relations.

With respect the results of Raman spectroscopy, in absence of more accurate models about the lattice dynamics, the hypothesis of oxygen vacancies introduced by the model of [Yu,97] could explain the activation of modes not present in perfect rutile and the shift present in an activated mode in our Raman spectra.

Moreover, quantum localisation effects are observed in our samples, which could be associated with defective regions induced by the presence of oxygen vacancies and surrounding the crystalline perfect region.

As summary, we can conclude that in spite of the wide variety of physical effects that could be considered for such nanostructural evolution of the samples with the annealing temperature, most of data suggest a reduction of the oxygen vacancies with the annealing temperature.

4.4 Verification of the reliability of the obtained powder for sensing applications: microprinted microwave SnO₂ nanopowders on micromachined silicon substrates.

Once presented the main features of the obtained tin oxide, including data about the gas sensitivity of such sensing materials, our aim is to provide an advanced sensor with enhanced performances.

Despite the variety of new technologies presented and the nice effort that would represent to implement everything, some selections have been done to simplify the work.

Thus, in spite of the good nanoscrostructural characteristics of the liquid pyrolysis powders, the improved catalytic activity of the microwave powders, able to distinguish CO and CH₄ when measuring together with a fast and mass procedure, makes this technology suitable for our aim in this section.

The use of substrate becomes an easier selection considering the present state of the art in sensors. As the most advanced laboratories and companies are using nowadays silicon micromachined substrates (those micro hotplates presented in chapter 3), the use of alumina substrates becomes quite *old fashioned*. However, our intention is the use pulsed heating able to measure selectively at every temperature.

Finally, the implementation of the microwave powders on the micromachined substrates will be made by using microprinting. Despite we believe that pulverisation coating will become the most advanced implementation technique in the next future, its used is specially indicated for mass implementation of sensors. As our

aim is to provide a scope of the main features of the some sensors, we have preferred a simplest technique such as microprinting, able to coat encapsulated substrates. See table 4.6 as summary of the used technologies.

	Substrate type	Powder production	Implementation technique
Developed	Alumina type 1, Alumina t. 2, Alumina t. 3, **Silicon micromachined**	Liquid pyrolysis, **Microwave treatments**	Pulverisation coating, **Microprinting**
Main considerations For selection	Low power consumption, integration, CMOS compatibility, pulsed operation.	Improved catalytic activity even reaching active filter properties	Faster implementation, compatibility with encapsulated Si substrates

Table 4.6. Used technologies in this section.

4.4.1 Characteristics of the microprinting of the obtained tin oxide on micromachined substrates

As exposed in section 3.4.1, microprinting is a general technique for the implementation of sensing powders on micromechanised substrates. Mainly it consists on the transference of paste containing the sensing powders from a capillary. However, our application of tin oxide has shown some peculiarities that are remarkable.

The first problem that arise is the difficulty to coat round-shaped drops. Despite the shape of the drop does not influence on the sensing mechanisms or

sensitivity, a round shape is required for easy reproducibility. After a fine control of the
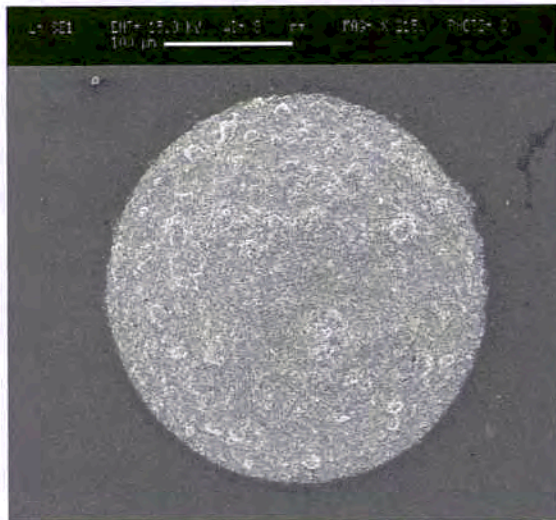
capillary point, round-shaped drops are obtained in the case of microwave tin oxide, as shown in figure 4.49.

Figure 4.49. Planar view in SEM of the drop. Bar rule is 100 μm.

The control of the height of the implemented drop has more influence. A big drop could induce power dissipation in the heater, or temperature discrepancies between different regions of the drop could affect negatively the reproducibility of such technique. This control becomes more difficult. As seen in the figure 4.50, a thickness of about 25 μm is usually obtained.

Figure 4.50. Planar view in SEM of the drop. Bar rule is 50 μm.

Once implemented the drop, the use of this as sensing element in the sensor should be preceded by an ageing treatment to evaporate the solvent
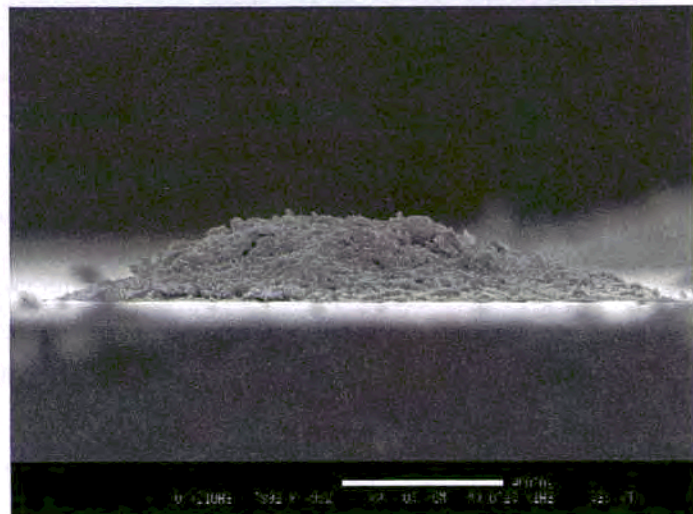
and allow the desorption of surface hydroxyl groups. To avoid crack formation, it is considered that a soft solvent evaporation is required. Then, sensors are kept at 70°C during at least 2 days. After this process, the sensors is selfheated in flowing nitrogen air until it reach about 450°C. At this temperature, Korotchenkov *et al* have shown how the resistance histeresis due to this water compounds on tin oxide surface is removed and sensor stability is enhanced. For this reason, we keep our sensors at this temperature in nitrogen at least during ten hours. It is considered that this process is enhanced by the use of pulsed heating.

Once the sensors is ready for measurement, an ageing of the sensor at the measurement background gas (such as synthetic air with a relative humidity of 50% at 25°C) has been found to be positive for sensing material stabilisation.

Aside these general aspects related with the measurement but conditioned by the use of microprinting, it is remarkable to indicate that some cracks appear in the microdrop after use. We believe this is related with some agglomerate that is in the powders. As consequence of the thermal dilatations of the drop during working life, the agglomerates induce the cracks on the coated drop. To avoid these negative cracks, a sieve process is introduced before the sensing powder paste preparation.

4.4.2 Features of the test device

After the implementation of our microwave tin oxide on silicon micromachined substrates, a gas test have been performed in order to verify the sensing performances of the material. The tested sensing materials, including different catalysation and annealing temperature of the powder are indicated in table 4.7. This stabilised powder has been implemented in the different silicon membranes of the silicon substrate schematised in figure 3.12, however the results presented in this section only corresponds to membrane

S2. Moreover, some measurements in pulsed heating have been performed, but in order to show comparable results, let us use these measurements in the next section.

SnO₂ tested sensors		
Catalisation (% Pt/Sn or Pd/Sn at. nominal)	Annealing temperature of the powder (°C)	Measured in Isothermal/pulsed heating
SnO₂ pure	450	X
SnO₂ pure	800	X
1% Pt	450	X
1% Pt	800	X
10% Pt	450	X
10% Pt	800	X
1% Pd	450	X
1% Pd	600	X
1% Pd	800	X X
10% Pd	450	X X
10% Pd	600	X X
10% Pd	800	X

Table 4.7. Microsensors analysed in this section.

The first measurements have been done at different biasing of the heater in order to obtain the better sensitivities. As shown in figure 4.51, the response of the sensor to alternative pulses of synthetic air (SA)/CO/SA/CH₄/SA during 900s indicate a stable and fast response when biasing higher than 13 V are considered.
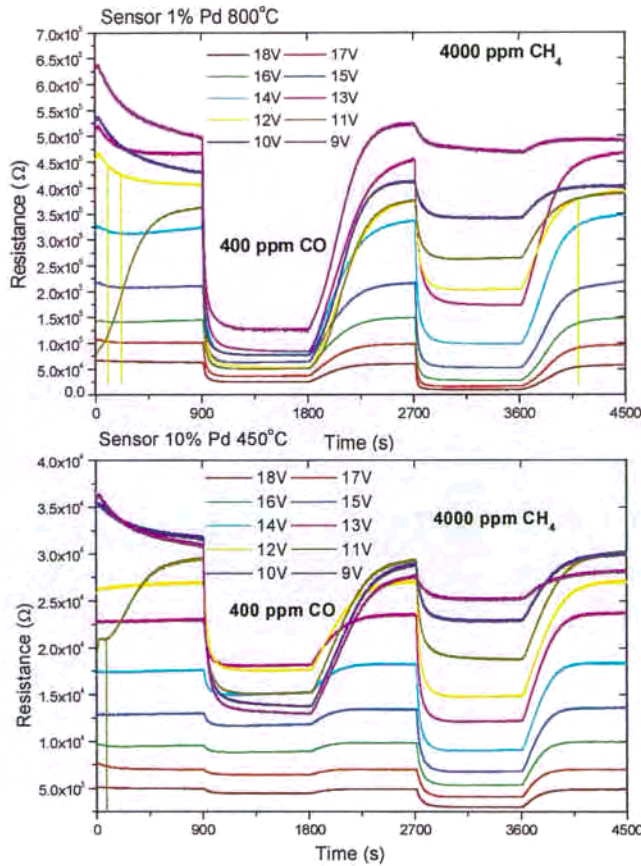
The analysis of such results, presented in figure 4.52, indicates that maximum sensitivity to CO is found at 12-13V and for CH_4 at 17-18V depending on the sensor. It is remarkable to observe how the property of active filter of the 10% Pd catalysed 450°C sensors is reproduced. As seen, higher biasing (i.e. 18V induce null response to CO whereas at lower biasing, such as 11V, the sensor measures both gases).

Figure 4.51. Sensor response after 900 s exposures of CO (400 ppm) and CH_4 (4000 ppm) at 50% RH 25°C. Left, sensor 1% Pd 800°C. Right, sensor 10% Pd 450°C. Colors indicate the biasing of the heater.

Once performed these exploratory measurements, further investigations of the sensing response were obtained from more complete test experiences, such as plotted in figure 4.53. For this, CO exposures were ranged from 40 to 400 ppm and CH_4 from 400 to 4000 ppm. Whereas the exposure time was 30 minutes, one hour was considered for the recovery of the sensor.
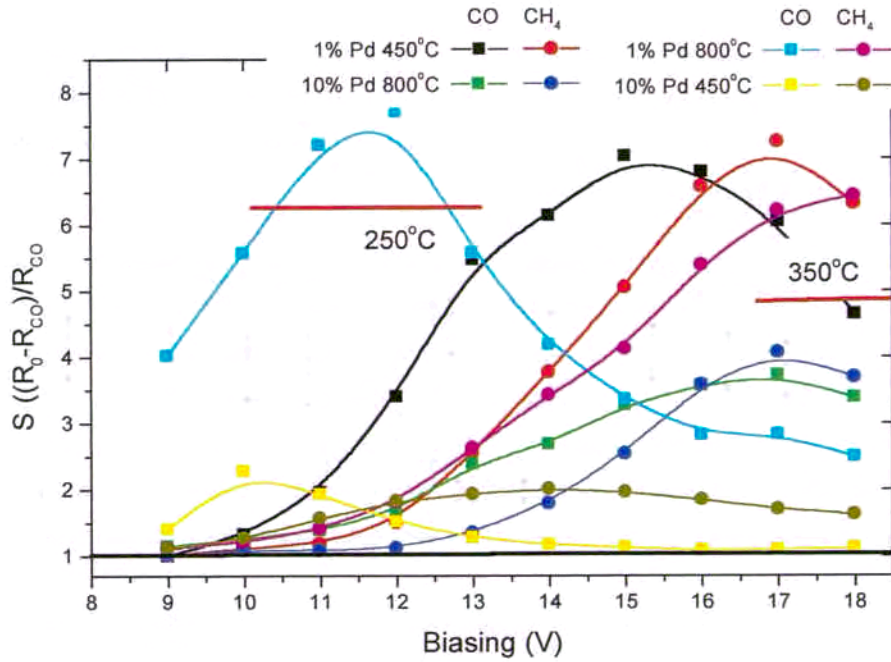
Figure 4.52. Sensitivity versus biasing for different sensors. CO sensitivity is considered for 400 ppm at 50% RH and 25°C. CH₄ for 4000 ppm at the same conditions.
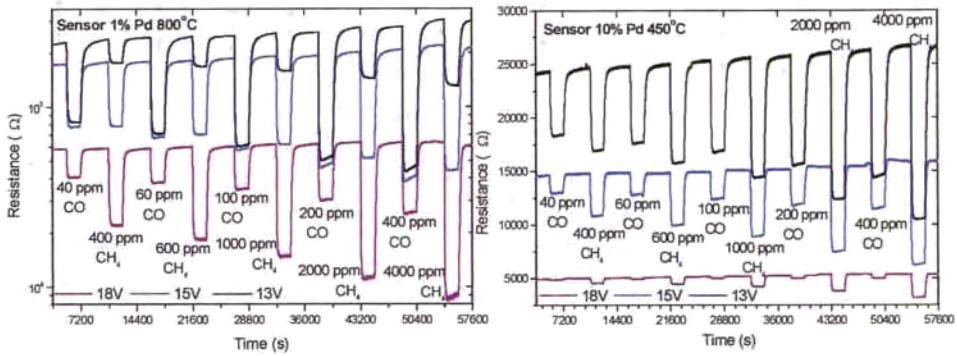

Figure 4.53. Response of the sensor to a CO (from 40 to 400 ppm) and CH₄ (from 400 to 4000 ppm). Color indicates the biasing. Measurements done at 50% RH and 25°C. Left, sensor 1% Pd 800°C. Right, sensor 10% Pd 450°C.

Plotting the obtained sensitivities after these exposures, it is possible to observe good results of sensitivity even for pure tin oxide –as seen in figure 4.54-. However, in both annealing temperatures –450 and 800°C- the selectivity towards CO and CH₄ is low. Thus, when working at 15V, the sensitivity to 40 ppm of CO could be misunderstood with more than 4000 ppm of CH₄.
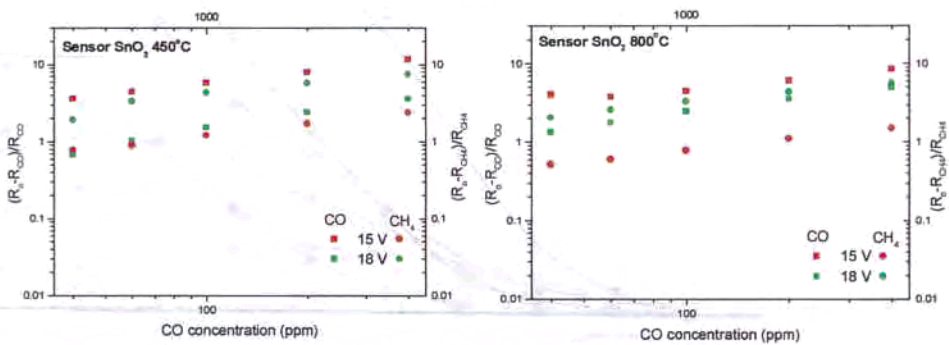

Figure 4.54. Sensitivity versus concentration for pure SnO₂. Left, 450°C annealed tin oxide. Right, 800°C annealed tin oxide.
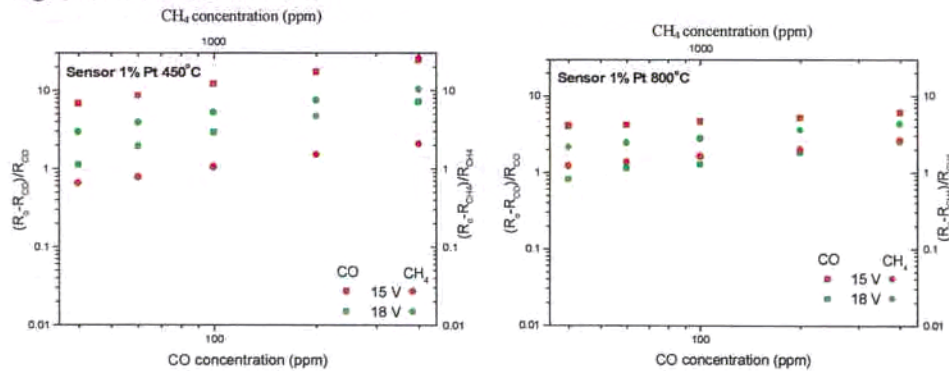

Figure 4.55. Sensitivity versus concentration. Left, 1% Pt 450°C sensor. Right, 1%Pt 800°C sensor.

The introduction of platinum in moderate dose (1%) –shown in figure 4.55 gives better results of selectivity and sensitivity when material is annealed at 450°C. However, at higher annealing (800°C) these properties are lost. This result can be explained by the

capacity of platinum to form clusters, which decreases the surface of the noble metal exposed to gas.

When 1% palladium catalisation is considered, despite the sensitivity is not increased, a selectivity enhancement is obtained. Whereas in the sample annealed at $450°C$, the better selectivity exhibited (working at 13V) is similar to non-catalysed tin oxide, the annealing at $600°C$ leads to a more selective measurement. In this sensor, when working at 18 V, the sensitivity towards CO does not reach 1, whereas the smaller concentration measured of CH_4 increases this value. It is considered that an incipient active filter catalysation is present on these samples, which is responsible for the catalytic combustion of the CO. Under this assumption, this annealing temperature would be the indicated to ensure a good distribution of the palladium on the tin oxide surface, keeping a non-agglomerate state. When higher temperatures are considered, the
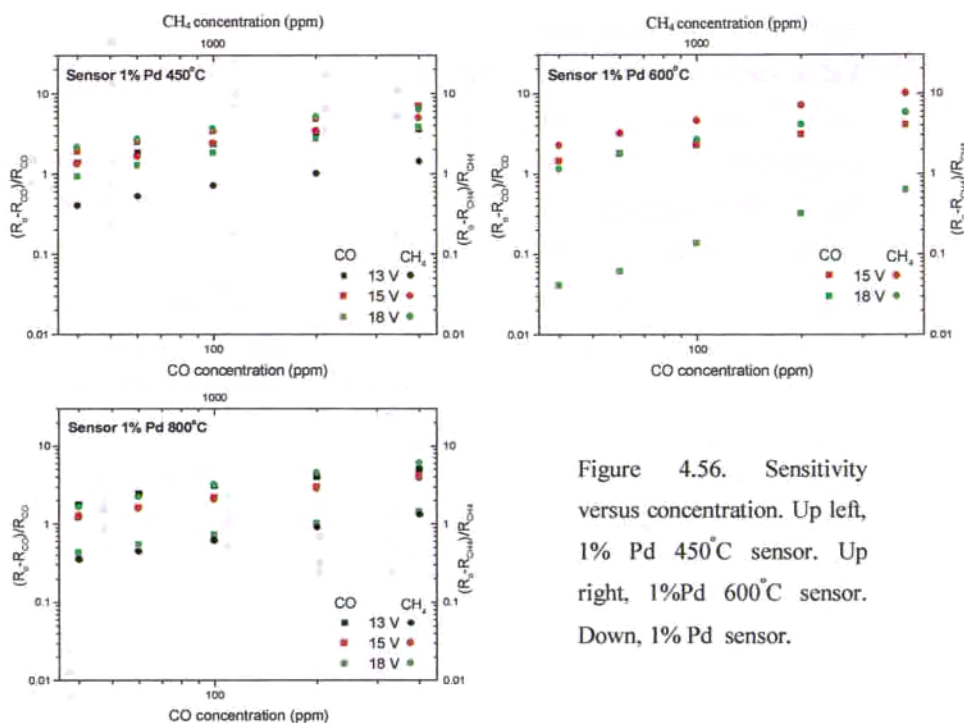

Figure 4.56. Sensitivity versus concentration. Up left, 1% Pd $450°C$ sensor. Up right, 1%Pd $600°C$ sensor. Down, 1% Pd sensor.

selectivity is lost, as result of such process.

However, the most interesting results are obtained when the catalysation is given until the 10% of palladium. Figure 4.57 shows an active filter activity towards CO when working at biasing of 18V, in this case the measurement is still selective to CH_4. According with previous results, the 600°C annealed tin oxide sensor give higher catalytic activity than 450°C. This data, which indicate better selectivity, is in agreement the hypothesis that at this temperature, the diffusion of the palladium on tin oxide surface is enhanced.

Figure 4.57. Sensitivity versus concentration. Up left, 10% Pd 450°C sensor. Up right, 10%Pd 600°C sensor. Down, 10% Pd sensor.
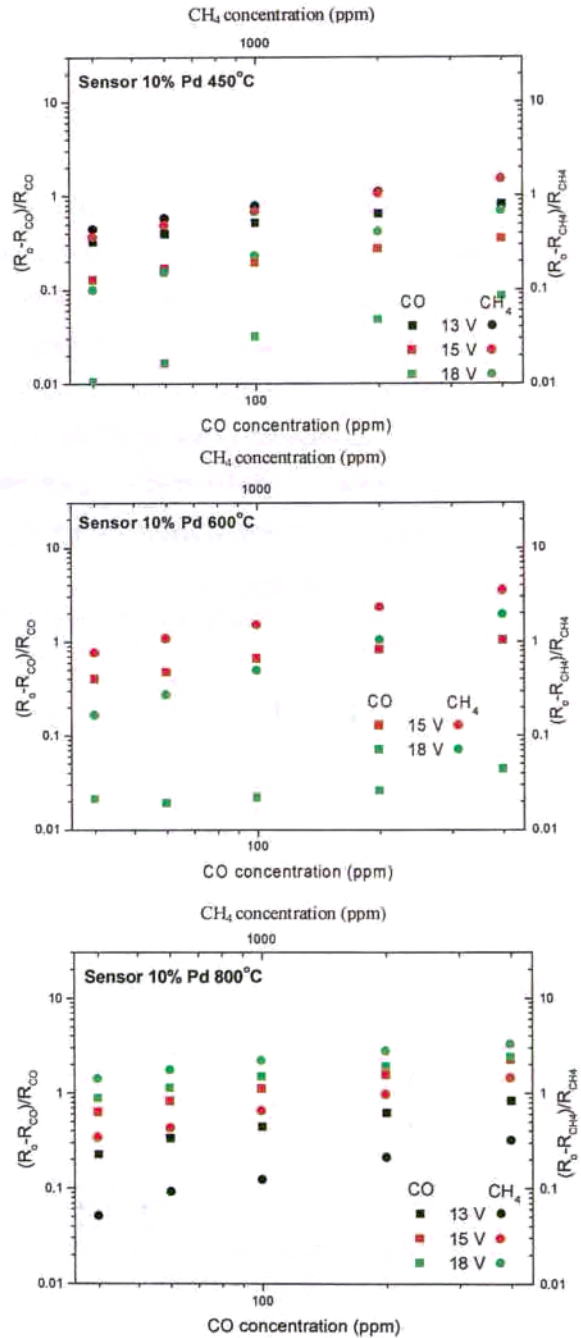
Similar results are obtained with a high catalysation of platinum (10%). The low sensitivity towards CO when working at 18 V observed in figure 4.58 could indicate a combustion of the CO, however some instabilities in the measurement suggest discard this material for further considerations.
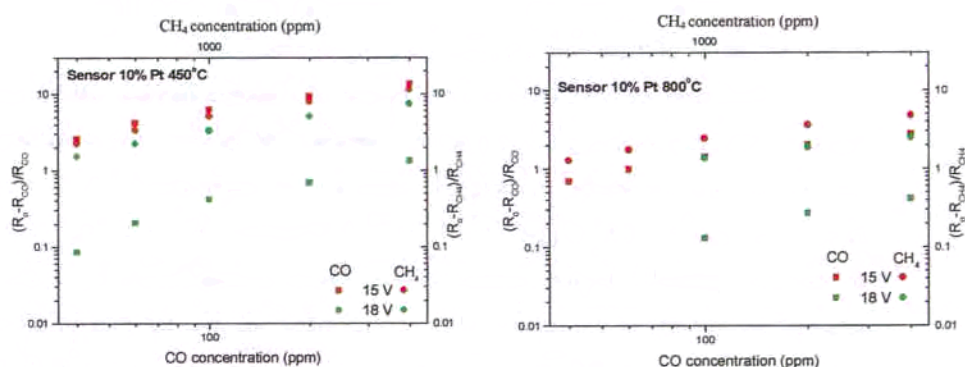

Figure 4.58. Sensitivity versus concentration. Left, 10% Pt 450°C sensor. Right, 10%Pt 800°C sensor.

As summary, the catalytic activity of palladium catalysed samples towards CO is present even when its nominal concentration is lower. This fact could be associated with an improved distribution of the catalytic on the tin oxide surface. In fact, annealing at 600°C the sensing material, the catalytic properties are better than at 450°C. At the contrary, when annealing at 800°C the catalytic activity towards CO is lost.

Consequently a mean annealing temperature (600°C) could be indicated to improve the diffusion of the noble metal on the tin oxide, keeping non-agglomerate state of the metal and the palladium properties.

4.4.3 Sensitivity, selectivity, stability and smart consumption ... putting all together at low cost?

In the previous section we have shown how the developed sensors are reliable and could be used for sensing applications. Thus, the presented results come from a wide variety of sensors, many of them with very good sensing performances.

Until now we have showed how the use of micromechanised silicon substrates together with microprinting allow a *smart consumption*. Besides, the *sensitivity* of the microwave tin oxide sensors is enough to cover a wide range, which has been tested up to 400 ppm of CO and 4000 ppm of CH_4, but it is considered that sensors would be able to measure perfectly higher concentrations. These measurements have shown the appropriate *stability* of the sensors after several weeks of use, for lack of a long-term test. In this context, the Pd catalytic in tin oxide have been presented to show how the active filter property is able to burn the CO and measure CO and CH_4 with *selectivity*. Moreover, all the introduced technologies are *low cost* and results in an easy and fast implementation. Only the micromachining of silicon results expensive for prototype production, but this problem can be overcame when higher series are required.

From an industrial point of view, all the requirements for sensing device prototyping are ready. At this point, only two questions arise. The first is concerning about sensing material selection, and the second about the modulation of the heater temperature.

As showed in the previous section, most part of the studied catalysed and pure materials are sensitive enough for sensing applications. However only those containing a higher quantity of palladium are able to selectively measure. As shown, when annealing is increased until $800°C$, this property is lost, therefore only 450 and $600°C$ annealed material are suitable for selective measurements. Considerations about the stability of the material suggest to use **$600°C$ annealed SnO_2 catalysed with 10%Pd** for our necessities.

With respect the temperature modulation, despite the assumption of Morrison, who stated "... *temperature programming of the sensor is not a common technique used for selectivity* ..." [Morrrison,87], in the recent years the temperature modulation (programming) has became a standard technique for selectivity enhancement.

The most promising temperature modulation of the sensitivity and selectivity has involved the application of a periodic heating to the SGS. Different authors [Sears,89][Reedy,99] suggest several advantages for the application of such oscillating heating. First, the different rates of reaction of the different gases at different temperatures can leads to a selective signal for each gas. Second, as low temperature operation can lead to the accumulation of incompletely oxidised contaminants, periodic higher temperature pulses are appreciated to *clean* the gas sensor surface. Finally, if temperatures in the pulse are properly selected, sensitivity can be enhanced because of the temperature dependence of the sensitivity for each gas.
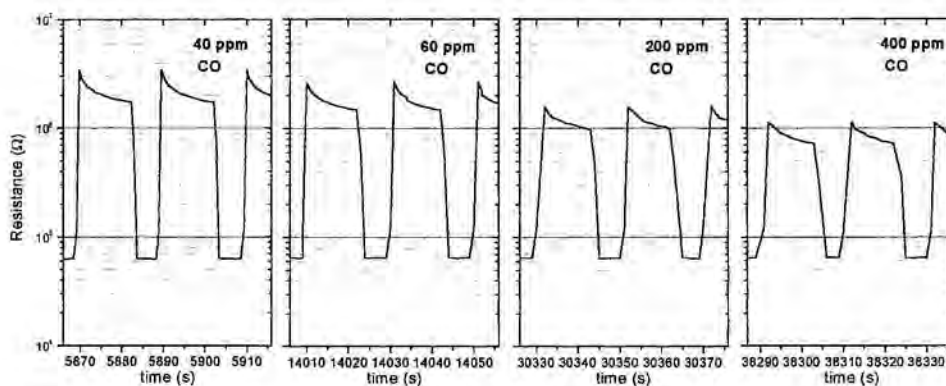

Figure 4.59. Representative pulses of the sensor 10% Pd catalysed (annealed at $600°C$) after CO exposure. Note how high resistance level decreases with CO concentration, whereas low resistance level never is less than 60 kΩ. This limit is called CO/CH_4 threshold (see text).

Therefore, catalyzed sensing powders have been implemented on micromachined hot-plates, but as difference of the previous section membrane S1 (figure 3.12) was used. Some previous measurements suggested applying the pulsed mode keeping at 10V (18.7 mA) the micro-heater for 5s (high biasing) and at 6V (12.4 mA) for 10s (low biasing). These ranges of voltage have been selected for measurement, and consumption (112 mW) need to be still optimized.

Representative pulses of the resistance measurements of the highly catalyzed SnO_2 (annealed at $600°C$) sensor after CO exposures are shown in figure 4.59. High resistance level (low biasing) exhibits a monotonous decrease of the resistance with the CO concentration. Thus, the peak resistance varies from 3.4 to 1.1 $M\Omega$ when the CO concentration is increased from 40 to 400 ppm. However, the low resistance level (high biasing) does not change. This last result is considered to be equivalent to that showed in figure 4.29, where sensor operated at $350°C$ does not exhibit sensitivity to CO.
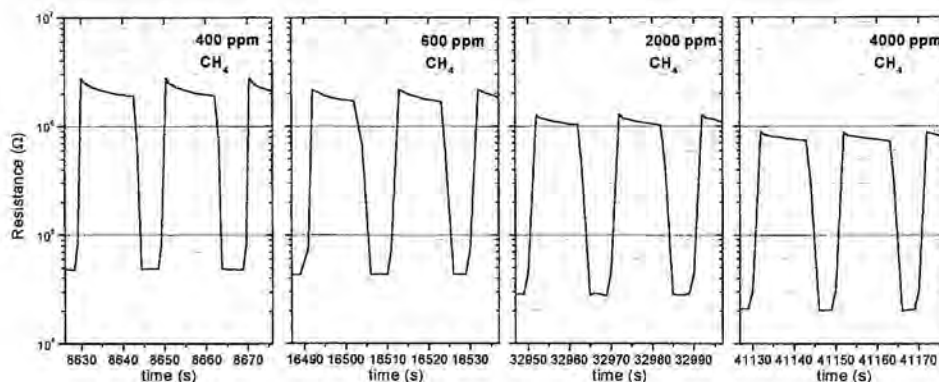

Figure 4.60. Representative pulses of the sensor 10% Pd catalysed (annealed at 600°C) after CH4 exposure. Note in this case how both high resistance level and low resistance level decreases with CH4 concentration. The low resistance level decreases with the CH4 with values under the CO/CH4 threshold.
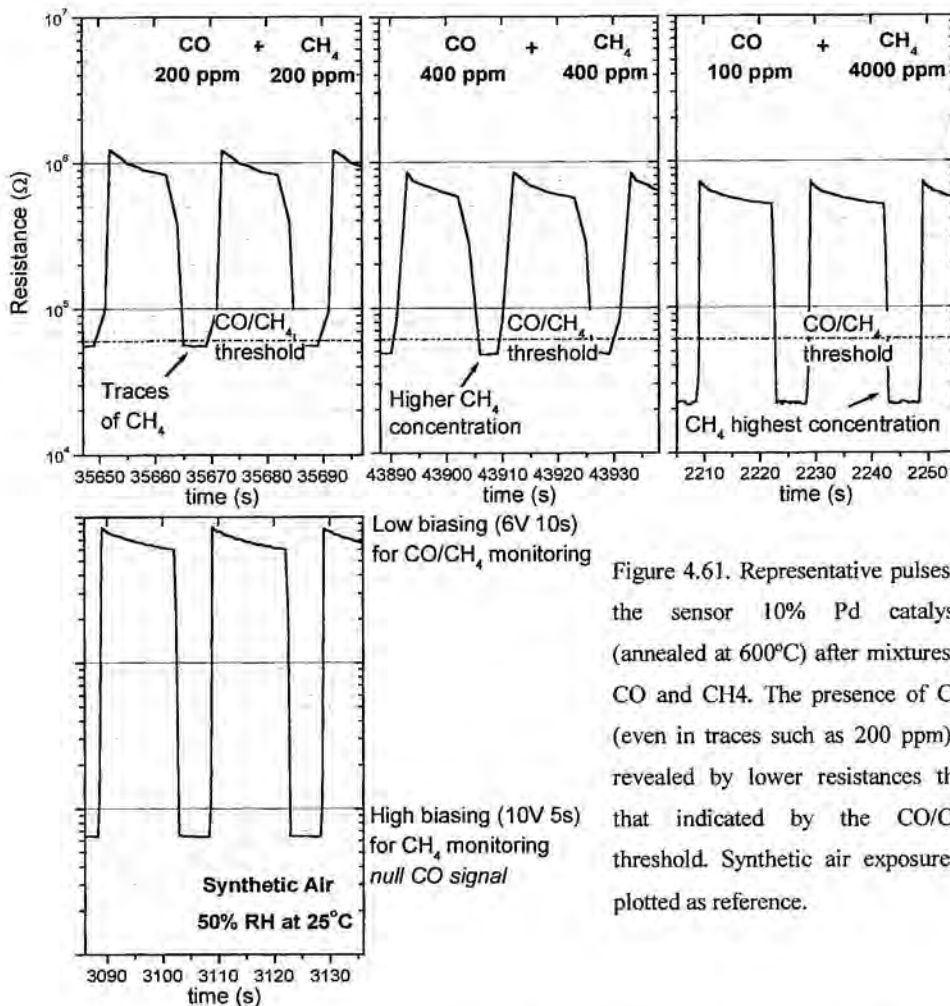
Figure 4.61. Representative pulses of the sensor 10% Pd catalysed (annealed at 600°C) after mixtures of CO and CH4. The presence of CH₄ (even in traces such as 200 ppm) is revealed by lower resistances than that indicated by the CO/CH₄ threshold. Synthetic air exposure is plotted as reference.

When the sensor is exposed to CH₄ high resistance level also decreases. However, low resistance level decreases below the 60 kΩ (see figure 4.60). As under CO exposure the low resistance level of the sensor does not take values under 60 kΩ, it is useful to define a *CO/CH₄ threshold* at this resistance value. In the measured range

and for CO/CH$_4$ mixtures, a low resistance value lower than the CO/CH$_4$ threshold indicates the presence of CH$_4$. When low resistance value is higher than the CO/CH$_4$ threshold, no CH$_4$ is present in the atmosphere.

Sensing measurements under 20 and 60% of relative humidity, have shown similar performances of the sensor.

A simple test of mixture concentrations is shown in figure 4.61. According with previous results, the presence of CH$_4$, even in a small concentration such as 200 ppm, lowers the low resistance value below the CO/CH$_4$ threshold. Besides, higher resistance value decreases as consequence of both CO and CH$_4$.

With this data we have defined a very simple algorithm. For the calibration input, we have used the CO and CH$_4$ exposure data shown in the figure 9 and 10, respectively. As we can see in the figure 4.62, sensitivity data have been fitted according usual expression usual in other works [Hensaw,96]:

$$S = \frac{R_{air} - R_{gas}}{R_{gas}} = k[X]^\beta \qquad (4.23)$$

where [X] is the gas concentration of CO or CH$_4$. Whereas CH$_4$ is fitted both in low and high resistance (high and low biasing, respectively), CO only induce appreciable changes of resistance in low biasing. For test evaluation of the algorithm, we have used data of mixtures shown in figure 4.61.

For this, first we have evaluated the CH$_4$ concentration in high biasing using calibration data and equation (4.23). Predicted concentrations (shown in table 4.8) have an error of about 11.5% for the extreme concentrations (out of calibration data), but keep within 4% of error for the moderate value of 400ppm of CH$_4$.

Once we have obtained this predicted concentration of CH$_4$, we compute the high level resistance values equivalent to a concentration of CH$_4$ without CO (R$_{CH4}$) using the calibration of the CH$_4$ low biasing. With this resistance value, we can compute the sensitivity of CH$_4$ in the low biasing level.
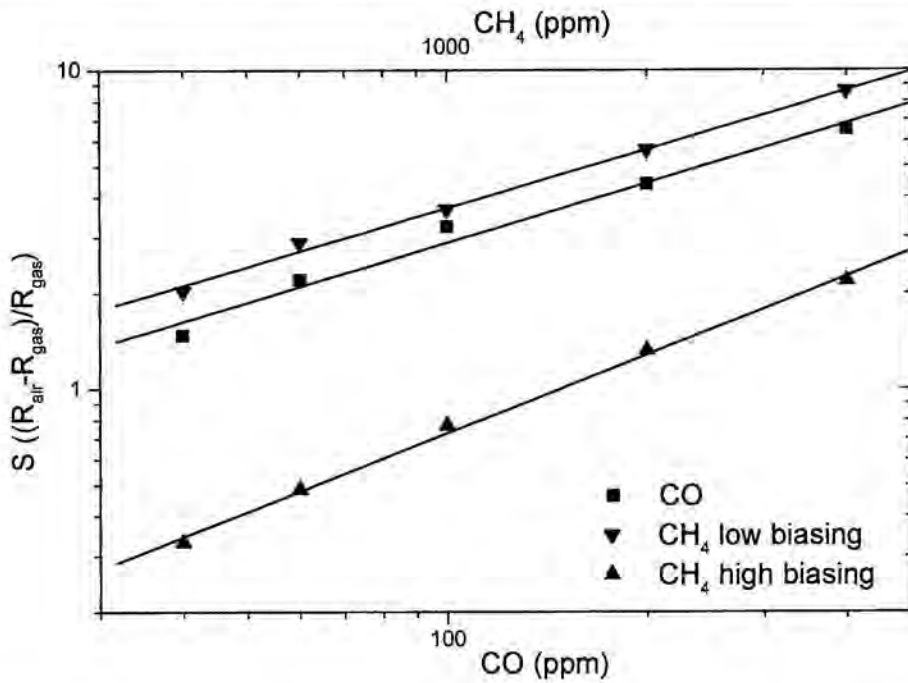
Figure 4.62. Fitting of the sensitivity as function of the gas concentration considering equation (1). Two fittings are considered for CH_4, in low biasing and in high biasing.

Therefore, the actual sensitivity to CO in this low biasing is,

$$S_{CO} = S_{lowbias} - S_{CH4} \qquad (4.24)$$

With the calibration data of the CO and equation 4.23, we can calculate the concentration of such gas. As seen in table 4.8, the predicted concentration of CO is very close to the actual one.

Actual concentration		Predicted concentration	
CO (ppm)	CH$_4$ (ppm)	CO (ppm)	CH$_4$ (ppm)
200	200	189.0 (5.5%)	177.8 (11.1%)
400	400	402.5 (0.6%)	384.7 (3.8%)
100	4000	92.0 (8%)	4116.9 (2.9%)

Table 4.8. Actual and predicted CO and CH$_4$ concentrations using the algorithm described (see text). Relative errors are indicated in parentheses in the prediction concentration columns.

4.5 Conclusions and critic review

In this chapter we have presented the new technologies for the production of nanosized tin oxide and their characterisation. With this sensing material, the study of the nanostructural evolution with the annealing temperature has revealed the oxygen vacancy nature of the material. Finally, the reliability of the obtained tin oxide for sensing application is shown.

The two new technologies for the production of tin oxide give nanosized and stable tin oxide. The material characterisation indicates acceptable grain size values and microstructural characteristics. Thus, whereas in liquid pyrolysis the obtained material exhibit proper material performances and stability even considering short time annealing is one of the major advantages, in the case of the microwave treatments, the low cost approximation for the mass production of the tin oxide should to be considered.

It is remarkable that in both cases the addition of the catalytic has been performed before the annealing. This in-situ catalysation was shown to give good electrical results for sensing applications. In the case of microwave treatments, the addition of palladium, in concentration reaching the active filter properties induces the catalytic combustion of the CO, which allows a CO/CH_4 selective measurement.

The characterisation of the obtained tin oxide allows the study of the nanostructure with the annealing temperature. XRD, XPS and Raman spectroscopy data indicate the presence a density of oxygen vacancies in the tin oxide, which is reduced when the annealing temperature is carried out.

Whereas the XRD results –relative intensities, distortions and strain- suggest a bulk distribution of the vacancies, those results obtained by XPS reveal the surface nature of the observed phenomena. As consequence, certain mobility of the oxygen vacancies with the annealing temperature is introduced.

Once the tin oxide is obtained and studied, its implementation on micromachined silicon substrates is performed by means of microprinting. The reliability of such implementation technique as well as the resulting sensors is studied by means of the electrical test under CO/CH_4 gas exposure.

From the isothermal measurements, microwave active filter Pd-catalysed tin oxide is selected to be considered for further experiences, included pulsed heating. In these measurements, the presented sensor oscillates between a temperature able to burn CO and measure CH_4, and other where both gases are measured. Therefore, the sensor is able to distinguish both gases and a very easy algorithm has shown to be able to quantify the gas concentration of CO and CH_4 with an acceptable error (<10%).

In order to improve the present work, some points would be interested to take into account.

From the point of view of the characterisation, especially that devoted to the nanostructured evolution of the tin oxide with the annealing temperature, once developed the hypothesis of an oxygen vacancy evolution, it would be interesting to obtain a quantification of the oxygen vacancies present in the material. For these measurements, one of the most reliable techniques would be EPR, which is able to quantify paramagnetic defects.

Moreover, Rietveld simulations of the XRD diffractograms would be also interesting and perhaps would be able to give some quantification of the phenomenom. The electrical measurement under usual SGS working conditions would be also interesting.

With respect the test measurements, higher statistics would be appreciated. In this sense, the number of measured sensors is enough to ensure the effect of catalysation, but a higher quantity of measured sensors would be necessary to obtain a statistic dispersion of baseline resistance and sensitivities. Besides, long-term test studies will be necessary for the final reliability assessment of the presented devices.

An important point to improve is the electrical consumption of the sensors. Despite it could be considered low (about 100 mW), this value should improved by means of better heater designs and a thinner microprinted tin oxide drop until reach the standard of the most advanced companies which spend about 40 mW.

References

In chronological order

[Matossi,51] F. Mattosi, "The vibration spectrum of rutile", J. Chem. Phys. 19 (1951) 1543-1546.

[Bartram,67] S. F. Bartram, "Crystallite-size determination from line broadening and spotty patterns", from "Handbook of X-Rays", Eds. E. J. Kaelble, McGraw-Hill, New York (1967).

[Eisenberg,69] D. Eisenberg, W. Kauzmann, "The structure and properties of water", Oxford University Press (1969).

[Fonstad,71] C.G. Fonstad, R.H. Rediker, "Electrical propierties of high-quality stannic oxide crystals" , J. Appl. Phys, 42 7 (1971) 2911-2918.

[Katiyar,71] R.S. Katiyar, P. Dawson, M.M. Hargreave, G.R. Wilkinson, "Dynamics of the rutile structure III. Lattice dynamics, infrared and Raman spectra of SnO_2", J. Phys. C. 4 (1971) 2421-2431.

[Peercy,73] P.S. Peercy, B. Morosin, "Pressure and temperature dependencies of the Raman-active phonons in SnO_2", Phys. Rev. B., 7 6 (1973) 2779-2786.

[Ibers,74] International tables for x-ray crystallography. Volume IV; J.A. Ibers and W.C. Hamilton; Kynock press; Birmingham (1974).

[Bard,76] Encyclopedia of electrochemistry of the elements, editor A. J. Bard, Marcel Dekker Inc., New York (1976).

[Jarzebsky,76] Z.M. Jarzebski, J.P. Marton, "Physical properties of SnO_2 materials (I,II and III)", J. Electrochem. Soc. (1976) 199C.

[Theil,76] B. Theil, R. Heilbig, "Growth of SnO_2 single crystals by a vapour phase reaction method" J. Cryst. Growth 32 (1976) 259-264.

[Windischmann,79] H. Windischmann, P.Mark, "A model for the operation of thin-film SnO_x conductance modulation carbon monoxide gas sensor", J. Electrochem. Soc.: Solid-State Science and Technology 126, 4 (1979) 627-633.

[Wagner,78] C.D. Wagner, W.M. Riggs, L.E. Davis, J.F. Moulder, G.E. Muilenberg, "Handbook of x-ray photoelectron spectroscopy", Perkin-Elmer Corporation, Eden Prairie (1979).

[Gervais,83] F. Gervais, W. Kress, "Lattice dynamics of incipient ferroelectric rutile TiO_2", Physical Review B, 28 6 (1983) 2962-2969.

[Gervais,85] F. Gervais, W. Kress, "Lattice dynamics of oxides with rutile structure and instabilities at metal-semiconductor phase transitions of NbO_2 and VO_2", Physical Review B, 31 8 (1985) 4809-4814.

[Munnix,86] S. Munnix, M. Schmeits, "Electronic structure of point defects on oxide surfaces", Phys. Rev. B 33, 6, (1986) 4126-4144.

[Erickson,87] J. W. Erickson, S. Semancik, "Surface conductivity changes in SnO_2 (110): Effects of oxygen", Surface Science 187 (1987) L658-L668.

[McAleer,87] J.F. McAleer, P.T. Moseley, J.O.W. Norris, D.E. Williams, "Tin dioxide gas sensors", J.Chem.Soc., Faraday Trans. 1 (1987) 87 1323-1346.

[Morrison,87] S. R. Morrison, "Selectivity in semiconductor gas sensors", Sensors and Actuators, 12 (1987) 425-440.

[Munnix,87] S. Munnix, M. Schmeits, "Electronic structure of oxygen vacancies on TiO_2 (110) and SnO_2 (110) surfaces", J. Vac. Sci. Technol. A, 5 (1987) 910-913.

[Cox,88] D.F. Cox, T.B. Fryberger, S. Semancik, "Oxygen vacancies and defect electronic states on the SnO_2 (110)-1x1 surface", Phys. Rev. B 38 3 (1988) 2072-2083.

[Family,88] F. Family, P. Meakin, "Scaling of the droplet-size distribution in vapor-deposited thin films", Phys. Rev. Lett., 61 4 (1988) 428-431.

[Matsushima,88] S. Matsushima, Y. Teraoka, N. Miura and N. Yamazoe, Electronic "Interaction between Metal Additives and Tin Dioxide-Based Gas Sensors", *Jap. J. of App.l Phys.*, 27 10 (1988) 1798-1802.

[Cox,89] D.F. Cox, T.B. Fryberger, S. Semancik, "Surface reconstructions of oxygen deficient SnO$_2$ (110)", Surface Science 224 (1989) 121-142.

[Fryberger,89] T.B. Fryberger, J.W. Erickson, S. Semancik, "Chemical and electronic properties of Pd/SnO$_2$ (110) model gas sensors", Surface and interface analysis, 14 (1989) 83-89.

[Sears,89] W.M. Sears, K. Colbow, F. Consadori, "Algorithms to improve the selectivity of thermally cycled tin oxide gas sensors", Sensors and Actuators, 19 (1989) 333-349.

[Sutton,89] W. H. Sutton, "Microwave Processing of Ceramic Materials", Ceram. Bull., 68 2 (1989) 376-386.

[Sanjines,90] R. Sanjines, F. Lévi, V. Demarne, A. Grisel, "Some aspects of the interaction of oxygen with polycristalline SnO$_x$ thin films", Sensors and Actuators B, 1 (1990) 176-181.

[Semancik,90] S. Semancik, F.B. Fryberger, "Model studies of SnO$_2$ based gas sensors: vacancy defects and Pd additive effects", Sensors and actuators B, 1 (1990) 97-102.

[Agashe,91b] C. Agashe, M. G. Takwale, V. G. Bhide, S. Mahamuni, S. K. Kulkarni, "Effect of Sn incorporation on the growth mechanism of sprayed SnO$_2$ films", J. Appl. Phys. 70 12 (1991) 7382-7386.

[Agashe,91b] C. Agashe, D.J. Goyal, B.R. Marathe, M.G. Tahwate, V.G. Bhide, "Effect of Sn concentration in the precursor solution on the growth of sprayed SnO$_2$ films", Materials Letters, 11 10 (1991) 363-367.

[Grasselli,91] Analytical Raman Spectroscopy, Eds. S. G. Grasselli & B.J. Bulkin, J. Wiley & Sons, inc. New York 1991

[Xu,91] Ch. Xu, J. Tamaki, N. Miura,N. Yamazoe, "Grain size effects on gas sentitivity of porous SnO$_2$-based elements", Sensors and Actuators B, 3 (1991) 147-155.

[Yamazoe,91] N. Yamazoe, "New approaches for improving semiconductor gas sensors", Sensors and Actuators B, 5 (1991) 7-19.

[Kohl,92]   D. Kohl, "Oxidic semiconductor gas sensors", in *Gas Sensors*, G. Sberveglieri (ed.), Kluwer, Dordrecht, 1992.

[Bârsan,94]   N. Bârsan, "Conduction models in gas-sensing SnO_2 layers: grain size effect and ambient atmosphere influence", Sensors and Actuators B., 17 (1994) 241-246.

[Lenaerts,94]   S. Lenaerts, J. Roggen, G. Maes, "FT-IR charactererisation of tin dioxide gas sensors materials under working conditions", Spectrochimica Acta, 51 (1994) 883-893.

[Lin,94]   X.W. Lin, J. Washburn, Z- Lliental-Weber and H. Bernas, "Coarsening and phase transition of $FeSi_2$ precipitates in Si", J. Appl. Phys., 75 (9) (1994) 4686-4693.

[Matsuhata,94]   H. Matsuhata, J. Ej¢nne, J. Taft¢, "A study of the structure factors in rutil-type SnO_2 by high-energy electron diffraction", Acta Cryst. A50 (1994) 115-123.

[Rantala,94]   T.S. Rantala, V. Lantto, T.T. Rantala, "A cluster approach for the SnO_2 (110) face", Sensors and Actuators B, 18-19 (1994) 716-719.

[Göpel,95]   W. Göpel and K.D. Schierbaum, "SnO_2 sensors: current status and future prospects", Sens. and Act. B, 26-27 (1995) 1-12.

[Kövér,95]   L. Kövér, G. Moretti, Zs. Kovács, R. Sanjinés, I. Cserny, G. Margaritondo, J. Pálinkás, H. Adachi, "High resolution photoemission and Auger parameter studies of electronic structures of tin oxides", J. Vac. Sci. Technol. A, 13 3 (1995) 1382-1388.

[Yoo,95]   D.J. Yoo, J. Tamaki, S.J. Park, N. Miura, N. Yamazoe, "Effects of thickness and calcination temperature on tin dioxide sol-derived thin-film sensor", J. Electrochem. Soc., 142 7 (1995) L105-L107.

[Sberveglieri,95]   G. Sberveglieri, "Recent developments in semiconducting thin-film gas sensors", Sensors and Actuators B 23 (1995) 103-109.

[Clark,96]   D.E. Clark and W.H. Sutton, "Microwave Processing of Materials", Annu. Rev. Mater. Sci., 26 (1996) 299-311.

[Cao,96] X. Cao, L. Cao, W. Yoo, X. Ye, "Structural characterization of Pd-doped SnO$_2$ thin films using XPS", Surface and Interface analysis, 24 (1996) 662-666.

[Diéguez,96] A. Diéguez, A. Romano-Rodríguez, J.R. Morante, U. Weimar, M.Schweizer-Berberich, W.Göpel, "Morphological analysis of nanocrystalline SnO$_2$ for gas sensors", Sensors and Actuators B 31 (1996) 1-8.

[Goniakowski,96] J. Goniakowski, M.J. Gillan, "The adsorption of H$_2$O on TiO$_2$ and SnO$_2$(110) studied by first-principles calculations", Surface Science, 350 (1996) 145-158.

[Hensaw,96] G.S. Hensaw, R. Ridley and D. E. Williams, "Room-temperature response of platinised tin dioxide gas-sensitive resistors", J. Chem. Soc. Faraday Trans., 92 18 (1996) 3411-3417.

[Schweizer-Berberich,96] M. Schweizer-Berberich, J.G. Zheng, U. Weimar, W. Göpel, N. Bârsan, E. Pentia and A. Tomescu, "The effect of Pt and Pd surface doping on the response of nanocrystalline tin dioxide gas sensors to CO", Sensors and Actuators B, 31 (1996) 71-75.

[Goniakowski,96] J. Goniakowski, M.J. Gillan, "The adsorption of H$_2$O on TiO$_2$ and SnO$_2$ (110) studied by first-principles calculations", Surface Science 350 (1996) 145-158.

[Harris,97] N. Harris, M. Koch, S. Beeby, N. White and A. Evans, "Thick-film printing of PZT onto silicon for micromechanical applications", Mat. Lett., 31 (1997) 109-112.

[JCPDS,97] JCPDS XRD card 41-1445 (SnO$_2$ Cassiterite synthetic). International Centre for Diffraction Data (1997). Further information can be found in McCarthhy, J. Powder Diffraction 4 (1989) 156. Pd: 05-0681. PdO: 06-0515. PdO$_2$: 34-1101. Pt: 04-0802. Pt$_3$O$_4$: 21-1284. PtO: 43-1100. PtO$_2$: 43-1045. α-PtO$_2$: 38-1355. β-PtO$_2$: 37-1087.

[Lide,97] Handbook of chemistry and physics, editor D. R. Lide, CRC Press, New York (1997).

[Sangaletti,97] L. Sangaletti, L.E. Depero, A. Diéguez, G. Marca, J.R. Morante, A. Romano-Rodriguez, G. Sberveglieri, "Microstructere and morphology of tin dioxide multilayer thin film gas sensors", Sensors and Actuators B, 44 (1997) 268-274.

[Yu,97] K.N. Yu, Y.Xiong, Y. Liu, C.Xiong, "Microestructural change of nano-SnO_2 grain assemblages with the annealing temperature", Physical Review B, 55, 4 (1997) 2666-2671.

[Zi,97] J. Zi, K. Zhang, X. Xie, "Comparison of models for Raman spectra of Si nanocrystals", Phys. Rev. B, 55 15 (1997) 92623-92266.

[Fullprof,98] Fullprof and WinPlotr programs for Rietveld simulations. Both available at ftp://charybde.saclay.cea.fr/pub/divers/fullprof.98/windows/winfp98.zip

[Martin,98] L.P. Martin, D. Dadon, M. Rosen, D. Gershon, K.L. Rybarkov, A. Birman, J.P. Calame, B. Levush, Y. Carmel and R. Hutcheon, "Effects of anomalous permitivity on microwave heating of zinc oxide", J. Appl. Phys., 83 1 (1998) 432-437.

[Tinga,98] W.R. Tinga, "Fundamentals of microwave-material interactions and sintering, *from* Microwave Processing of Materials", MRS proceedings, 124 (1998) 33-43.

[Vriezinga,98] C.A. Vriezinga, "Thermal runaway in microwave heated isothermal slabs, cylinders, and spheres", J. Appl. Phys. 83 1 (1998) 438-442.

[Bârsan,99] N. Bârsan, J.R. Stetter, M. Findlay, W. Göpel, "High-performance gas sensing of CO: Comparative tests for semicondcuting (SnO_2-based) and for amperometric gas sensors", Anal. Chem. 71 (1999) 2512-2517.

[Blaustein,99] G. Blaustein, M.S. Castro, C.M. Aldao, "Influence of frozen distributions of oxygen vacancies on tin oxide conductance", Sensors and Actuators B, 55 (1999) 33-37.

[Lee,99] A.P. Lee, B. J. Reedy, "Temperature modulation in semiconductor gas sensing", Sensors and Actuators B, 60 (1999) 35-42.

[Cirera,99] A. Cirera, A. Dieguez, R. Diaz, A. Cornet and J.R. Morante, "New method to obtain stable small-sized SnO$_2$ powders for gas sensors", Sensors and Actuators B, 58 (1999) 360-364.

[Diéguez,99a] A. Diéguez, "Structural analysis for the improvement of SnO$_2$-based gas sensors", PhD thesis at the University of Barcelona (1999).

[Korotchenkov,99] G. Korotchenkov, V. Brynzari, S. Dmitriev, "Electrical behavior of SnO$_2$ thin films in humid atmosphere", Sensors and Actuators B, 54 (1999) 197-201.

[Wöllenstein,99] J. Wöllenstein, M. Jägle, P. Roetsch, H. Böttner, W.J. Becker, E. Wagner, "The influence of Pt-clusters at the surface of highly dense SnO$_2$ nano-films on the NO$_2$/CO sensitivity" Proceedings of Transducers 99 (1999).

[Cabot,00] A. Cabot, J. Arbiol, J. R. Morante, U. Weimar, N. Bârsan, W. Göpel, "Analysis of the noble metal catalytic additives introduced by impregnation of as obtained SnO$_2$ sol-gel nanocrystals for gas sensors", Sensors and Actuators B, accepted for publication.

[Capone,00] S. Capone, P. Siciliano, L. Vasanelli, N. Bârsan, U. Weimar, "Application of a micro-hotplate gas sensor array to the analysis of CO/CH$_4$ gas mixtures by pattern recognition and multicomponent analysis methods", Proceedings of Eurosensors XIV (2000) 45-49.

[Hahn,00] S. Hahn, N. Bârsan, U. Weimar, "Impact of different feature extraction methods on signal evaluation of sensors coated with differently doped SnO$_2$", Proceedings of Eurosensors XIV (2000) 61-62.

[Khatko,00] V.V. Khatko, R.E. Soltis, J.R. McBride, K. E. Nietering, "Catalytic property of Pd/Al$_2$O$_3$ and Pt/Al$_2$O$_3$ multilayer stacks", Proceedings of Eurosensors XIV (2000) 97-98.

[Montméat,00] P. Montméat, C. Pijolat, G. Tournier, J.P. Virecelle, "The effect of metallic membranes on SnO$_2$ thin films sensing properties", Proceedings of Eurosensors XIV (2000) 209-210.

5. Applied characterisation for thin film based sensors